Development of in-situ optical sensor-based monitoring methodologies for Additive Manufacturing processes

Development of in-situ optical sensor-based monitoring methodologies for Additive Manufacturing processes / Lafirenza, M.. - ELETTRONICO. - (2025). [10.60576/poliba/iris/lafirenza-marco_phd2025]

DOI:10.60576/poliba/iris/lafirenza-marco_phd2025

Publisher: Politecnico di Bari

Department of Mechanics, Mathematics and Management
MECHANICAL AND MANAGEMENT ENGINEERING
Ph.D. Program
SSD: IING-04/A–Manufacturing Technologies and Systems

Final Dissertation

Development of in-situ optical sensor-based monitoring methodologies for Additive Manufacturing processes

by
LAFIRENZA Marco

Supervisors:
Prof. Luigi Maria GALANTUCCI.
Prof. Fulvio LAVECCHIA.

Coordinator of Ph.D. Program:
Prof. Giuseppe CASALINO.

Course n°37, 01/11/2021-31/10/2024

LIBERATORIA PER L'ARCHIVIAZIONE DELLA TESI DI DOTTORATO

Al Magnifico Rettore
del Politecnico di Bari

Il/la sottoscritto/a Marco Lafirenza nato/a a Acquaviva delle Fonti il 11/02/1995

residente a Adelfia in via Dossetti 15 e-mail marco.lafirenza11@gmail.com

iscritto al 3° anno di Corso di Dottorato di Ricerca in Ingegneria Meccanica e Gestionale ciclo XXXVII

ed essendo stato ammesso a sostenere l'esame finale con la prevista discussione della tesi dal titolo:

Development of in-situ optical sensor-based monitoring methodologies for AM processes

DICHIARA

1) di essere consapevole che, ai sensi del D.P.R. n. 445 del 28.12.2000, le dichiarazioni mendaci, la falsità negli atti e l'uso di atti falsi sono puniti ai sensi del codice penale e delle Leggi speciali in materia, e che nel caso ricorressero dette ipotesi, decade fin dall'inizio e senza necessità di nessuna formalità dai benefici conseguenti al provvedimento emanato sulla base di tali dichiarazioni;
2) di essere iscritto al Corso di Dottorato di ricerca In Ingegneria Meccanica e Gestionale ciclo XXXVII, corso attivato ai sensi del "*Regolamento dei Corsi di Dottorato di ricerca del Politecnico di Bari*", emanato con D.R. n.286 del 01.07.2013;
3) di essere pienamente a conoscenza delle disposizioni contenute nel predetto Regolamento in merito alla procedura di deposito, pubblicazione e autoarchiviazione della tesi di dottorato nell'Archivio Istituzionale ad accesso aperto alla letteratura scientifica;
4) di essere consapevole che attraverso l'autoarchiviazione delle tesi nell'Archivio Istituzionale ad accesso aperto alla letteratura scientifica del Politecnico di Bari (IRIS-POLIBA), l'Ateneo archivierà e renderà consultabile in rete (nel rispetto della Policy di Ateneo di cui al D.R. 642 del 13.11.2015) il testo completo della tesi di dottorato, fatta salva la possibilità di sottoscrizione di apposite licenze per le relative condizioni di utilizzo (di cui al sito http://www.creativecommons.it/Licenze), e fatte salve, altresì, le eventuali esigenze di "embargo", legate a strette considerazioni sulla tutelabilità e sfruttamento industriale/commerciale dei contenuti della tesi, da rappresentarsi mediante compilazione e sottoscrizione del modulo in calce (Richiesta di embargo);
5) che la tesi da depositare in IRIS-POLIBA, in formato digitale (PDF/A) sarà del tutto identica a quelle **consegnate**/inviate/da inviarsi ai componenti della commissione per l'esame finale e a qualsiasi altra copia depositata presso gli Uffici del Politecnico di Bari in forma cartacea o digitale, ovvero a quella da discutere in sede di esame finale, a quella da depositare, a cura dell'Ateneo, presso le Biblioteche Nazionali Centrali di Roma e Firenze e presso tutti gli Uffici competenti per legge al momento del deposito stesso, e che di conseguenza va esclusa qualsiasi responsabilità del Politecnico di Bari per quanto riguarda eventuali errori, imprecisioni o omissioni nei contenuti della tesi;
6) che il contenuto e l'organizzazione della tesi è opera originale realizzata dal sottoscritto e non compromette in alcun modo i diritti di terzi, ivi compresi quelli relativi alla sicurezza dei dati personali; che pertanto il Politecnico di Bari ed i suoi funzionari sono in ogni caso esenti da responsabilità di qualsivoglia natura: civile, amministrativa e penale e saranno dal sottoscritto tenuti indenni da qualsiasi richiesta o rivendicazione da parte di terzi;
7) che il contenuto della tesi non infrange in alcun modo il diritto d'Autore né gli obblighi connessi alla salvaguardia di diritti morali od economici di altri autori o di altri aventi diritto, sia per testi, immagini, foto, tabelle, o altre parti di cui la tesi è composta.

Luogo e data Bari, 03/02/2025 Firma

Il/La sottoscritto, con l'autoarchiviazione della propria tesi di dottorato nell'Archivio Istituzionale ad accesso aperto del Politecnico di Bari (POLIBA-IRIS), pur mantenendo su di essa tutti i diritti d'autore, morali ed economici, ai sensi della normativa vigente (Legge 633/1941 e ss.mm.ii.),

CONCEDE

- al Politecnico di Bari il permesso di trasferire l'opera su qualsiasi supporto e di convertirla in qualsiasi formato al fine di una corretta conservazione nel tempo. Il Politecnico di Bari garantisce che non verrà effettuata alcuna modifica al contenuto e alla struttura dell'opera.
- al Politecnico di Bari la possibilità di riprodurre l'opera in più di una copia per fini di sicurezza, back-up e conservazione.

Luogo e data Bari, 03/02/2025 Firma

Department of Mechanics, Mathematics and Management

MECHANICAL AND MANAGEMENT ENGINEERING
Ph.D. Program

SSD: IING-04/A–Manufacturing Technologies and Systems

Final Dissertation

Development of in-situ optical sensor-based monitoring methodologies for Additive Manufacturing processes

---

by

LAFIRENZA Marco :

Referees:

Prof. Gianni CAMPATELLI

Prof. Michela SIMONICNI

Supervisors:

Prof. Luigi Maria GALANTUCCI

Luigi Maria Galantucci firma

Prof. Fulvio LAVECCHIA

Fulvio Lavecchia firma

Coordinator of Ph.D Program:

Prof. Giuseppe CASALINO.

Casalino *firma*

Course n°37, 01/11/2021-31/10/2024

Abstract

Process monitoring has proven to be essential in manufacturing fields, where quality and precision are paramount. The introduction of AM techniques has enabled the production of complex parts but has also increased the complexity of manufacturing systems. This has led to the demand for monitoring systems able to provide significant information about the process while it is running as well as give real-time insights to detect and prevent, when possible, process anomalies. Reliable monitoring systems provide a window into the process dynamics, allowing for process parameters adjustment that could maintain product quality and reduce waste of materials and energy. Despite the numerous advantages introduced by monitoring systems, widespread traditional solutions remain limited, prompting significant effort from researchers and industries in this direction. This thesis addresses the current critical gaps in terms of monitoring purposes by proposing innovative and cost-effective in-situ optical-based monitoring methodologies for three key AM processes: Material Extrusion Additive Manufacturing, Laser Powder Bed Fusion and Direct Energy Deposition. Material Extrusion showed to be lacking adequate metrics able to describe the process, together with the absence of solutions exploiting profilometers as monitoring sensors. The monitoring activities on L-PBF were driven by the lack of robust monitoring systems able to characterize lattice structures. Finally, the monitoring activities on L-DED were led by the current absence of real-time monitoring system capable of monitoring more than one direction, since the majority of the system focused on single direction thin wall monitoring. First, two layerwise monitoring approaches for MEX, based on a high-resolution blue laser line profilometer embedded within a consumer grade MEX printer, were presented to characterize the surface quality, to detect defect occurrence layer-by-layer and to expand the metrology field related to the MEX process, which is currently lacking, by proposing new metrics. The three proposed quality indexes (AD_{LH}, RAD and slope s) proven to be representative of the layer height accuracy, the occurrence and distribution of surface defects, such as over/under-fill, and, also, the process stability respectively. In the second approach, functional analysis tools were successfully used to detect, localize, and characterize the topology of common surface defects caused by over-extrusion and under-extrusion conditions. An optical-based monitoring procedure was also developed and applied for layerwise in-situ monitoring of complex geometries produced by L-PBF through a tailor-made image processing algorithm. Based on High-Resolution Optical Tomography (HR-OT), this procedure effectively detected geometric distortions and, at the end of the process, provided a 3D reconstruction of the lightweight structure suitable for post-process quality assessment. Finally, a preliminary study on a cost-effective off-axis dual-camera real-time 3D monitoring method for L-DED process was conducted. The aim was to enable a reliable measure of the melt pool height regardless of the laser head scanning direction. Results showed that the proposed methodology was able to provide acceptable melt pool height measures for all the scanning direction tests. By introducing robust process signatures and defect metrics, this work significantly advances the metrology of AM processes. The comprehensive monitoring methodologies developed during the research activities not only improve in-process quality evaluation and process stability but also pave the way for real-time, closed-loop corrective actions.

Acknowledgment

I would like to express my sincere gratitude to all those who supported me during my Ph.D. journey. I am deeply grateful to my tutors, Prof. Ing. Luigi Maria GALANTUCCI, Prof. Ing. Fulvio LAVECCHIA, and Ph.D. Ing. Maria Grazia GUERRA, whose invaluable guidance and support over these three years have been instrumental in my academic and personal development. I also wish to thank Ing. Rosario GALANTE, the expert at the Rapid Prototyping and Reverse Engineering Laboratories, for his constant assistance and technical expertise.

Additionally, I am profoundly thankful to my host at University of California Davis (UC Davis), Prof. Masakazu SOSHI, for welcoming me at ARMS Laboratories and providing the opportunity to complete my research activities abroad. His mentorship and the enriching experience at ARMS Lab have significantly contributed to the advancement of my work and my expertise.

I also would like to thank The Rotary Foundation, Rotary Club Bari, Rotary Club Bari Castello, Rotary International District 2120 and Rotary Club Davis, for their support during my period abroad.

Contents

Nomenclature

AM	Additive Manufacturing
3DP	3 Dimensional Printing
NDT	Non Destructive Technique
NDE	Non Destructive Evaluation
GD&T	Geometric Dimensioning and Tolerancing
CMM	Coordinate-Measuring Machine
CT	Computed Tomography
XCT	X-ray Computed Tomography
SEM	Scanning Electron Microscope
CCD	Charged Coupled Device
CMOS	Complementary Metal-Oxide-Semiconductor
IR	Infrared
NIR	Near Infrared
L-DED	Laser-Direct Energy Deposition
L-PBF	Laser-Powder Bed Fusion
MEX	Material Extrusion
ISO	International Organization for Standardization
ASTM	American Society for Testing and Materials
HR-OT	High Resolution-Optical Tomography
SAXS	Small-Angle X-ray Scattering
LIBS	Laser-Induced Breakdown Spectroscopy
OES	Optical Emission Spectroscopy
SVR	Support Vector Regression
MJ	Material Jetting
BJ	Binder Jetting
LOM	Laminated Object Manufacturing
VIS	Visible
A&V	Acoustic & Vibrating
AE	Acoustic Emission
UT	Ultrasonic Testing
CAD	Computer-Aided Design
FMT	Fourier-Mellin Transform
Q-Q	Quantile-Quantile
EWMA	Exponential Weighted Moving Average
SVM	Support Vector Machine
DIC	Direct Image Correlation
ML	Machine Learning
DL	Deep Learning
AES	Acoustic Emission Spectroscopy
HAZ	Heated Affected Zone
SISO	Single Input Single Output
FPGA	Field Programmable Gate Array
LAAM	Large Area Additive Manufacturing
OT	Optical Tomography
FoV	Field of View
HOG	Histogram of Oriented Gradient
LBP	Local Binary Pattern
CNN	Convolutional Neural Netwrok
EPMP	Enhanced Phase Measuring Profilometry
μCT	micro Computed Tomography
ANN	Artificial Neural Network
ABS	Acrylonitrile Butadiene Styrene
PLA	Polilactic Acid
RAD	Residual Average Deviation
AD_{LH}	Layer Height Average Deviation
EAS	Ellipse Angle Sum
DSA	Deposition Scanning Angle
BLP	Blue Laser Profilometer
SL	Structured Light (scanner)
AHPE	Average Height Percentage Error
LP	Laser Power
PFR	Powder Flow Rate
FR	Flow Rate
C.F.	Conversion Factor
AC	Acceptable Range
LR	Lower Region
UR	Upper Region
PPA	Projected Percentage Area
VV	Volume of Void
VM	Volume of Material

1. Introduction

Additive Manufacturing (AM), also known as 3D printing (3DP), is transforming manufacturing by enabling the creation of three-dimensional objects directly from digital designs. Unlike traditional chip removal technologies, which rely on material subtraction processes to shape a workpiece, AM builds objects layer-by-layer, offering significant advantages:

- *Design Freedom*: AM removes many geometric constraints imposed by traditional manufacturing, allowing for the creation of highly complex designs with intricate internal features and customized geometries [1].
- *Material Efficiency*: AM typically uses only the material required for the functional part [2], minimizing waste compared to subtractive methods that generate significant material offcuts.
- *Tool-less Manufacturing*: AM often eliminates the need for expensive and time-consuming tooling, such as molds or dies, enabling rapid prototyping and cost-effective customization.
- *Lightweighting Opportunities*: AM facilitates the production of lightweight components with optimized material distribution, contributing to fuel efficiency and performance improvements in various industries [3].
- *Functional Integration*: AM enables the integration of multiple components and functionalities within a single part, simplifying assembly and potentially enhancing product performance.

These advantages make AM a game-changer in various sectors, including aerospace [4,5], automotive, healthcare [4,6], and consumer goods. While AM offers tremendous potential, ensuring the reliability and quality of AM-produced parts remains a critical challenge. The dependence of AM on several internal and external factors decreases process stability and repeatability, which can lead to defect formation in the printed part. Defects can form either on the external surface of produced part, in the sub-surface, or internally, affecting the part's integrity and mechanical properties. Integration of monitoring methods in the AM process can help in continuously evaluating the quality of the manufacturing process and in developing intervention methods for correcting the defects as soon as they start to evolve. But, given the absence of metrological standardization to assess the 3D printed product quality [7], developing reliable monitoring systems remains a challenging task that many researchers are trying to solve [8]. In general, monitoring methodologies have been applied to all seven AM categories [9], first, to characterize defect formation mechanisms and, after, to provide quality evaluation of printed parts, by enabling defects detection and, where possible, a means of correction to reduce waste of time and materials. Monitoring systems can be categorized into different groups based on their methods and practice[9], and their advantages and disadvantages are summarized in Table 1:

- *Contactless/contact:* Contactless systems can be considered as all the measuring instruments that can measure quantities without touching the part under examination. While contact instruments need to touch the surface to gather information.
- *Real-time/Off-time:* Real-time systems are able to acquire internal and external data during the AM process, enabling instant feedback about deposition and consolidation processes, defect formation and correction, through either printing parameters variations [10] or hybrid manufacturing solutions [11]. Off-time systems usually evaluate the part at the end of the process or at predetermined intervals, offering a deeper investigation into external and internal part quality and performance and setting the basis for post-processing.
- *Destructive/non-destructive*: Destructive techniques involve the part to be broken to study internal features and defects, while non-destructive techniques/evaluation (NDT/NDE) can obtain comprehensive data about the part without destroying it. From a NASA report [12], it is identified the need for real-time NDT/NDE for AM processes to reuse the tested parts and acquire real-time information, saving material and time.
- *In-situ/ex-situ:* In-situ systems refer to the techniques used to gather data directly at the location of interest, so they are integrated within the machine, and they can provide real-time feedback about the part and the process. Ex-situ systems, on the other hand, involve detailed and comprehensive analysis of parts at a different location. In other words, the part needs to be moved from the printer because the measuring instrument is not embedded inside the machine.

From Table 1 it is shown that the same instrument/sensor can be part of different categories contemporarily and, therefore, it can be used for different purposes. For example, optical sensors, which are widely used for MEX monitoring [13] and for monitoring metal AM [14], can be considered as contactless, NDT, real-time sensors and their versality make them suitable for both in-situ or ex-situ approaches, depending on whether they are mounted within the machine or externally. A variety of sensor technologies have been explored for monitoring AM processes, each offering a unique perspective on the as-built part, on the process and on the machine state[9,15]. Thermal sensors, such as thermal cameras, pyrometers, and thermocouples, capture temperature distributions and fluctuations within the melt pool and surrounding areas[7], providing insights into heat flow, cooling rates, and potential defects related to thermal stresses or insufficient melting. These types of sensors are mostly used when high heat exchange phenomena occur during the deposition, as usually happens when metal components are printed. Acoustic and vibrating sensors[16], such as microphones, acoustic emission and accelerometer sensors, detect waves generated during the build process. These wave signatures can reveal information about melt pool dynamics, powder flow, and the formation of defects such as cracks or porosity but can also reveal abnormal process conditions [17]. Load cells, on the other hand, measure forces and stresses experienced by the build platform or deposition head during the AM process [18], which can indicate issues with part adhesion, warping, or other structural instabilities. Optical sensors[13,15,19,20], such as IR/NIR/visible cameras, interferometers, profilometers, 3D scanners and so on, capture images and analyze light emitted or reflected from the build area.

Table 1: Monitoring systems characterization based on different principles with advantages and disadvantages. The sensors/instruments column considers only the most common devices used for monitoring purposes in additive manufacturing processes.

Monitoring system categories	Feedback	Purpose	Advantages	Disadvantages	Instrument/sensors
Contact-based	During/After AM process	Dimensional and geometric validation, tactile surface roughness measurement	High precision for geometrical (GD&T) and physical dimensions	Limited to external features and time-consuming when used for complex geometries	Calipers, micrometers, CMMs, thermocouple
Contactless	After/During AM process	Geometry, heat or structural monitoring without interfering with the part	Faster and less intrusive: suitable for complex geometries	Less measurement resolution than contact instruments. High dependance of the final result from material optical properties and on the environment lighting conditions, which are changing during the process.	CT scanner, thermal cameras, 3D scanners, SEM
Real-time	During AM process	Immediate defect detection and process adjustment	Reduce waste of material and time by addressing problems at an early stage; support closed-loop control	Require advanced sensors and fast data processing	Thermal/CCD/CMOS camera, stereo cameras, acoustic emission sensors, laser profilometer, pyrometers, load cells, sensor fusion
Off-time	After AM process	Provide comprehensive data for quality inspection, validation and post-processing	Deliver accurate and detailed analysis useful for post-processing techniques	Time-consuming and costly: no real-time feedback	CT scanner, profilometers, tensile machine, CMM, structured-light scanners
Destructive	After AM process	Analyze internal or material properties by sectioning	Enable thorough material or structural analysis	Destroy or compromise part integrity: increase of material waste and production time	Tensile or fatigue machines, SEM, micro-sectioning
NDT/NDE	After/During AM process	Verify quality without part damaging	Suitable for preserving functional parts	May not detect all internal defects or material inconsistencies	Optical/CT/3D scanners, ultrasonic imaging, CMM, cameras
In-situ	During AM process	Ensure process stability and early defect detection and mitigation	Provide off-time/real-time internal/external feedback suitable for adaptive and closed-loop control	May be affected by environmental or process disturbances (noise, spatter, high reflections, dimension of the building volume and so on)	Thermal sensors, High-speed/CCD/CMOS camera, stereo cameras, acoustic emission sensors, laser profilometer, optical scanners, load cells, sensor fusion
Ex-situ	After AM process	Ensure final part quality and compliance with standards	High precision and detailed examination of internal and external features	Not suitable for closed-loop controls: time-consuming and costly	CT scanner, profilometers, tensile machine, CMM, structured-light scanners

Optical techniques offer high spatial and temporal resolution, enabling the monitoring of melt pool geometry, powder bed dynamics, and surface characteristics[21] for metal laser-based technologies (Laser-Direct Energy Deposition L-DED and Laser-Powder Bed Fusion L-PBF). Optical sensors in MEX can help to acquire data about part geometry and surface without interfering with the deposition process and, furthermore, images, either alone or combined with output from other sensors, are widely used to feed different types of neural networks to enable closed-loop monitoring systems able to classify good/defective conditions during the deposition process [22]. The need to better understand AM process dynamics pushed toward a different approach to collect data. Such lack of knowledge led to the current tendency to capture as much information as possible, by equipping AM machines with an increasing number of heterogeneous sensors and by combining the data gathered from different sensors, an example is found in [23]. This approach takes the name of '*sensor fusion*'. The volume of information that can be generated, even during the fabrication of a single part, is rapidly increasing. The identification of what variables should be monitored and how involves significant research efforts going ahead, both in terms of process and material understanding, and data mining.

Process monitoring is paramount to successful widespread implementation of AM because it could provide a real-time window into the complex physical phenomena occurring during the build process, enabling manufacturers to ensure part quality, optimize process parameters, and ultimately move towards the reliable and repeatable production of high-value components. AM technologies are highly diverse, differing in operating principles, materials and industrial applications and seven macro-categories have been highlighted by the ISO/ASTM Committee F42 inside the ISO/ASTM 52900:2021 [24]. *Vat Polymerization (VAT)* uses a liquid photopolymer resin that cures and solidifies upon exposure to ultraviolet light. *Material Extrusion (MEX)*, extrudes a thermoplastic filament through a heated nozzle, depositing it layer-by-layer to create the object. *Powder Bed Fusion (PBF)* utilizes a heat source, typically a laser or electron beam, to selectively melt and fuse layers of powdered material. *Material Jetting (MJ)* involves jetting droplets of photopolymer resin or molten material onto a build platform, where they solidify and bond together. *Binder Jetting (BJ)* employs a liquid binder to selectively join layers of powdered material. The green part is then cured or sintered to achieve its final properties. *Directed Energy Deposition (DED)* uses a focused energy source, such as a laser or electron beam, to melt material, powder or wire, as it is deposited onto the build platform. Finally, *Sheet Lamination (LOM)* bonds and cuts thin sheets of material, typically metal, to create the desired three-dimensional shape.

This diversity makes it very hard to categorize monitoring methods solely based on the sensor used, because not all sensors can be applied across all AM technologies. Moreover, the same sensor can measure different process signatures depending on the technology, for example, the melt pool is a signature unique to powder/wire-based processes, as it results from the high-temperature interaction between the energy source (laser or beam) and the material, which melts and solidifies rapidly. Consequently, monitoring the melt pool is not applicable in processes like MEX, where such phenomenon does not occur.

It is important to say that not all AM technologies have been considered in this thesis. The monitoring activities were performed on three AM processes that are MEX, L-PBF and Laser-DED (L-DED). These three technologies represent a significant portion of the AM landscape, each offering unique capabilities and addressing a wide range of applications. MEX is one of the most widely used AM categories due to its simplicity, relatively low-costs and large variety of feedstock materials [25], such as polymer [26], composite materials [27] and metals [28], but it can also be used with ceramic filaments and copper. The latter two categories are well suited for metal powder/wire processing [29] and lightweight structures production [3], and for this reason are very popular among industry environments where high-performance parts or functionally graded material are requested [30,31] (i.e. Automotive, aerospace, biomedical). In particular, given the challenges arose during each AM process and current state of monitoring systems, the focus in this work will be on monitoring setup and methods and their advantages and criticality. A more comprehensive overview of the AM monitoring state of art can be found in [9].

1.1. About this work

After reviewing the state of art of monitoring systems for AM processes [15,19,32], it appears that, despite several studies on this topic, significant gaps remain in the development of reliable monitoring systems and methodologies across different AM technologies. As highlighted in [14], one of the biggest challenges for in-situ metrology and monitoring lies in the choice of process variables that should be measured. Understanding of process performance and behavior still needs to be improved and as a result, it is often unclear which process variables should be prioritized for monitoring purposes.

The main objective of this thesis is to address the challenges of reliable monitoring and quality assurance in AM based on novel signatures. This is achieved through the study, development, and validation of innovative monitoring setup and methodologies tailored to the most common AM technologies. By leveraging advanced optical sensors and high-resolution cameras, this work aims to bridge the gap between the lack of in-situ metrology and the growing demand for reliable and repeatable AM processes. This concept will be further expanded for each AM technology in subsequent paragraphs.

As already mentioned, the key AM technologies considered are three. This thesis investigates monitoring methodologies tailored to these three processes, each presenting unique challenges and opportunities for quality assurance. The monitoring methodologies developed to address these challenges are outlined below:

- **Material Extrusion (MEX)**: Two different monitoring methodologies were explored by using the same sensor (laser line profilometer) and setup. First, a set of quality indexes was introduced to detect surface defects, enabling rapid identification of anomalies. Second, the sensors data were analyzed through a unique methodology based on layer height and functional analysis tools, providing a detailed characterization of surface and defect topology. These complementary approaches aimed to enhance the accuracy and robustness of in-situ layerwise monitoring in MEX processes.
- **Powder Bed Fusion (PBF)**: Building upon a previously introduced framework [33], this work improved (by increasing its spatial resolution) and evaluated the High-Resolution Optical Tomography effectiveness by applying it to complex lattice structures production. The lightweight structure monitoring is challenging due

to the complex geometry to be produced and successfully evaluating both internal and external features would significantly improve in-situ monitoring of complex geometries. By subjecting the monitoring system to a "stress test," the capacity to handle intricate shapes and accurately detect possible defects was demonstrated, underscoring the system's suitability for next-generation L-PBF applications.

- **Laser-Direct Energy Deposition (L-DED)**: A tailor-made setup and an image processing algorithm were developed to enable 3D monitoring of melt pool height along multiple directions. This system provided accurate measurements of the height across various scanning paths, laying the groundwork for real-time, closed-loop control. The effectiveness of this method was further corroborated by a predictive model to estimate the measurement error introduced by the off-axis dual camera-based configuration of the proposed monitoring system, confirming the robustness of the proposed approach for enhanced process control in L-DED.

During experimental activities, optical sensors have been chosen as the core for monitoring systems and methodologies across all the considered AM technologies. While the used sensors and the setup can vary depending on the requirements of each technology, such as the dimension of the machine, the light reflection generated, the material considered and the purpose of the monitoring system, they can all be grouped within the broader category of optical sensors. This choice is motivated by the numerous advantages inherent to optical methods, making them well-suited for AM process monitoring. Their contactless nature allows for measurements without interfering with the process's dynamics or risking damage to the sensor itself. Furthermore, optical sensors often exhibit high sensitivity and accuracy, enabling the detection of subtle changes in light intensity, wavelength, or phase, which can be correlated with critical process parameters and signatures. The optical techniques can capture a wide range of process signatures regardless of the technology considered, from melt pool dimensions and temperature distributions to powder flow behavior and surface roughness when high thermal exchange occurs (L-PBF, L-DED), and from single track features to surface quality and defect topology (MEX) when the heat transfer is low , highlighting both the versality of optical sensors and their ability to provide a comprehensive overview of the build process. Moreover, optical sensors can provide continuous data acquisition, in some cases, allowing for real-time evaluation of the build process and enabling early defect detection.

In section 2, the main defects that commonly occur during each different deposition process and that will be analyzed during the experiments are presented. Due to different nature of the monitored AM processes, defects are categorized based on the specific AM process considered, such as MEX and Laser-based AM processes. In section 3 the discussion of literature advancements about monitoring solutions divided by AM technologies is explained. In this discussion, for each technology, monitoring systems will be divided by type of measured signal (like thermal, acoustic and optical signals) to simplify data presentation, and the gaps highlighted from the literature review will be presented. After the literature review, the discussion will focus on the research activities conducted and the results obtained from the proposed methodologies as follow: section 4 will focus on MEX monitoring, section 5 will discuss about L-PBF monitoring and section 6 will talk about L-DED monitoring. For each section will be described the proposed monitoring setup used during the experiments. After that, the monitoring methodologies developed will be presented and their findings will be discussed in the results section, for each technology. Furthermore, the main highlight will be resumed in the conclusion part and the main limitation and the topic that must be addressed in future works will be discussed at the end of each sections (section 4, 5, 6). Finally, in section 7 the conclusion will be presented.

2. AM process defects

An essential aspect of process monitoring in AM is its ability to identify and mitigate defects that can arise during the build process. Defects, whether they occur on the external surface, within the sub-surface, or internally, directly impact the mechanical properties and functionality of the final part, making their understanding and detection paramount for quality assurance. Each AM technique introduces unique defect formation mechanism influenced by its material deposition strategy and energy source.

To provide a comprehensive foundation for discussing monitoring techniques, it is critical to first categorize and analyze the types of defects associated with the three AM technologies considered in this thesis. MEX presents a distinct set of challenges due to its extrusion-based deposition process and to its low heat exchange during the heat source-material interaction, while L-PBF and L-DED share certain defect characteristics owing to their reliance on high-energy heat sources (the heat source for these two technologies is a high-energy laser beam) for material consolidation. By exploring these defects in detail, this chapter creates the context for understanding how process monitoring can address the specific quality control needs of each technology.

2.1. MEX main defects

Material Extrusion (MEX) is a widely adopted additive manufacturing technology recognized for its accessibility, versatility, and cost-effectiveness. Its speed and affordability make it ideal for rapid prototyping, allowing designers and engineers to quickly create tangible models to test designs and functionality. MEX finds applications in a diverse range of fields [25]. It boasts a relatively low cost of entry compared to other additive manufacturing technologies, making it an attractive option for startups, small businesses, and educational institutions. While often associated with prototyping, Material Extrusion is also gaining traction in the fabrication of tooling and fixtures, such as jigs and molds, used in various manufacturing processes. However, like any technology, Material Extrusion also has its limitations. Parts produced through this method may exhibit lower strength and durability compared to those manufactured using other additive manufacturing techniques, particularly those involving metals [25,34]. Moreover, due to the anisotropic nature of the layered structure, parts may exhibit different mechanical properties in different directions, which need to be considered during the design phase[35].

The dependance of MEX on several printing parameters [25], such as number of outer layers, infill degree, infill pattern, sample orientation on the build platform, layer thickness, printing speed and temperature and many others, make this process prone to defects that can arise during the layer-by-layer deposition process. As already mentioned, these defects can affect the final part's aesthetic, dimensional accuracy and mechanical properties and the relationship between process parameters and defects have been deeply explored in literature [8,13,25,36]. Common defects for MEX are shown in Fig. 1, and they include:

- *Under/Over-fill* (Fig. 1, a-c and e, f): These are related to inconsistent extrusion volume of material. Underfill is characterized by lack of material inside the part, and it can lead to void and delamination, while overfill can be considered as the opposite condition, and can lead to mechanical stresses, residual strains and warping [22].
- *Stringing/Oozing* (Fig. 1, c and d): Thin strands of material appearing between separated features are often caused by the filament oozing out of the nozzle while not extruding, because of the gravity force[13].
- *Surface texture defects* (Fig. 1, e): A very uneven surface texture can occur because of the high number of printing parameters to control. These include layer height, nozzle feed rate, and diameter and filament quality are just some of the parameters to control during the deposition process[13].
- *Delamination* (Fig. 1, g): This occurs when layers of the printed part fail to bond properly, resulting in weakness and potential separation. Inconsistent extrusion rates and insufficient temperature can contribute to this error[22].
- *Warping* (Fig. 1, h): Usually, this occurs when the part curls upwards or distorts at the edges because of non-homogeneous cooling rates and the material's thermal contraction. Bed adhesion, printing temperature and cooling rates significantly influence warping[22].
- *Shrinkage*: Dimensional reduction of the printed part as it cools and solidifies after deposition. This defect occurs due to the thermal contraction of the material and can lead to warping, internal stresses and geometric deviation. It is a common defect that occurs when metal parts are printed.

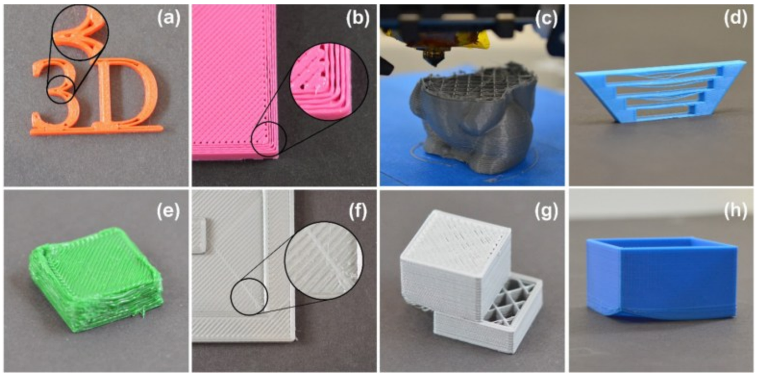

Fig. 1: Common MEX defects[37]: a-c) Underfill defects -a) gaps between walls, b) under-extrusion, c) clogged nozzle- d) stringing; e)-f) over-extrusion defects; g) delamination; h) warping.

2.2. Defects related to Laser-based metal AM technologies

Laser-based metal AM technologies, such as L-PBF and L-DED, share key thermal and material phenomena because of their reliance on the same fundamental working principle: melting and solidifying metal powder using a laser heat source. Unlike MEX process, which typically involves melting polymers at lower temperatures compared to metals, L-PBF and L-DED involve high-temperature operations, resulting in high heat exchange phenomena. Both technologies rely on a layer-by-layer material deposition approach, in accordance with AM paradigm, enabling the creation of complex geometries and high-performance components, which are hard or impossible to construct with traditional machining processes and one important example is represented by lattice structure production [38]. However, despite their similarities, L-PBD and L-DED differ significantly in their implementation, capabilities and typical industry applications[39].

L-PBF operates within a controlled environment where a laser beam selectively melts powder spread across an entire layer, the so-called "*powder bed*", which explains the name of the technology (Laser – Powder Bed Fusion). This powder bed-dependent approach restricts the build chamber and limits building volumes but is highly precise and suited for producing small and complex parts with better surface finishes and details, compared to L-DED produced parts. This, combined with the material palette, makes L-PBF appreciated by industry, such as aerospace, healthcare and tooling, through the production of lightweight structures, tailor-made implants and prosthetics, prototype and mold and dies with intricate internal cooling channel production, respectively. On the contrary, L-DED employs a focused laser beam to melt the powder as it is simultaneously expelled from the nozzle and deposited onto a substrate. This technology is not restrained from a powder bed so higher deposition rates and larger building volumes are enabled, making L-DED ideal for fabricating large parts and Near Net Shape components characterized by a comparatively lower surface finish quality and precision. Moreover, L-DED's ability to process complex geometries, repair and coating existing parts offer important advantages in aerospace and energy industrial applications. The main current usage of L-DED process is for damaged turbine blades repair and for coating purposes.

However, the aforementioned technologies face challenges primarily related to defect formation, arising from their dependency on a multitude of process parameters, and an example is presented in Fig. 2 for an L-PBF process, and the complexity of thermal and material interactions during production. Understanding the defects that occur during these laser-based technologies is critical for developing robust and reliable monitoring systems and control strategies. This understanding provides a foundation for implementing real-time control strategies that minimize defect occurrence and improve overall part quality. Detailed description of relationship between defects and process parameters can be found in literature [19,20,40] and the main defects encountered during L-PBF and L-DED are listed below, and shown in Fig. 3:

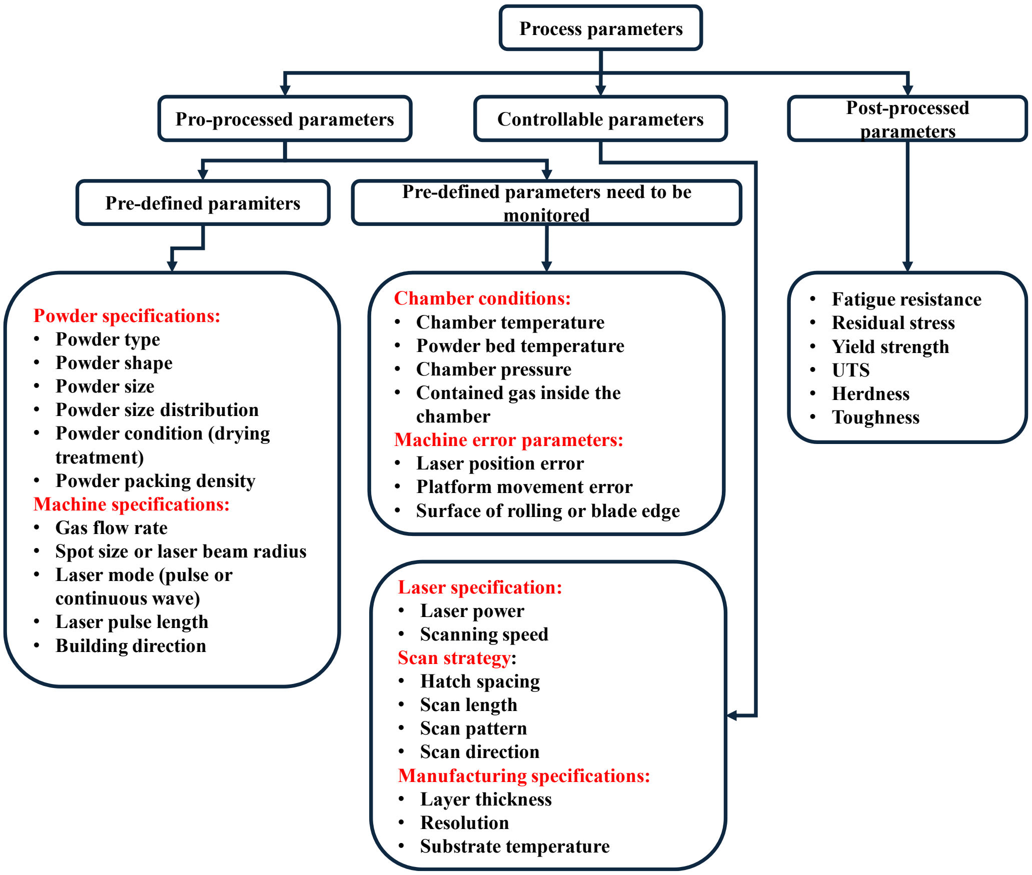

Fig. 2: L-PBF process parameters [20].

- *Porosity* (Fig. 3, a): Voids inside the material that are often attributed to trapped gas, inadequate powder melting due to insufficient laser energy, or evaporation phenomena during the process[3].
- *Lack of Fusion* (Fig. 3, a): This defect occurs, usually, when insufficient melting occurs between adjacent layers, leading to weak point in the structure. This could be caused by inconsistent powder layers, improper laser power or part geometry complexities[19].
- *Residual stresses and Distortion*: Fast cycles of heating and cooling can lead to significant residual stresses inside the deposited part. These stresses can cause also defects such as warping (Fig. 3, c) and part distortion, compromising its dimensional accuracy and leading to cracking or delamination (Fig. 3, b) [40].
- *Surface Roughness* (Fig. 3, d): Both technologies exhibit high surface roughness due to layer-by-layer deposition and their powder-based nature, but L-DED parts usually exhibit rougher surface finish because of the larger melt pool and the less controlled material deposition process. Surface roughness can affect mechanical properties and need post-processing operations[40].
- *Microstructural defects* (Fig. 3, e): Monitoring the microstructure of the part gives information about the dynamics of deposition and microstructural evolution. These are defined as undesirable structural features in the microstructure that affects mechanical properties[40].

- *Balling* (specific to L-PBF, Fig. 3, f): The molten pool can divide into small spheres due to poor wetting behavior, high residual stresses on the surface or inconsistent powder bed surface[19].
- *Powder bed-related issues* (specific to L-PBF, Fig. 3, g): Variability in powder layer density or contamination in the powder bed can be detrimental to the melting process.
- *Overheating and substrate damage* (specific to L-DED): Due to focused energy source, excessive heat can damage the substrate or lead to material evaporation

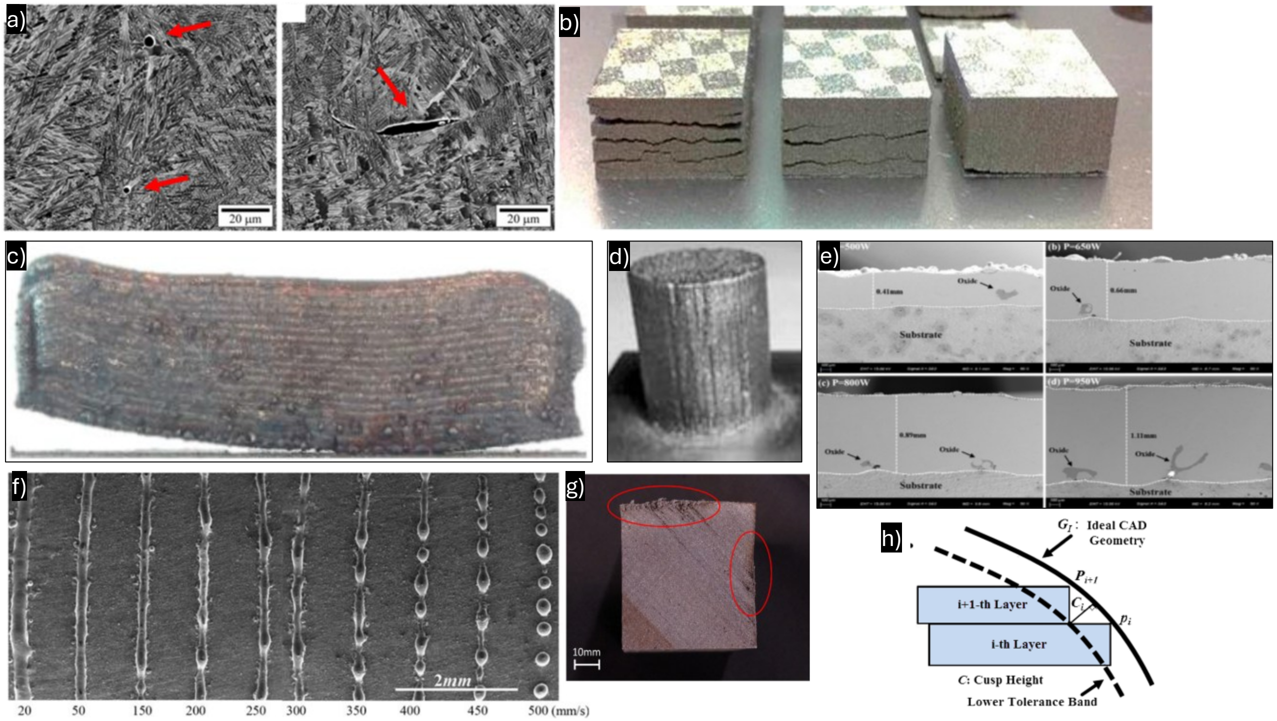

Fig. 3: a) spherical pores and acicular pores[19]; b) delamination due to cracks[19]; c) geometric distortions and warping[40]; d) high surface roughness[40]; e) microstructural defects with different laser powers[19]; f) balling at different laser feed rates[19]; g) poor edge accuracy because of powder bed inconsistencies[19]; h) staircase effect [20], which is common to AM technologies.

2.2.1. ***Process signatures***

Due to the dependency of L-PBF and L-DED on numerous process parameters and intricate interactions between these parameters and the complex thermal physics involved, defects are prone to occur. To mitigate these challenges and ensure part quality and process reliability, it is essential to identify and monitor the so-called process signatures. These are defined as measurable features that reflect the real-time state of the process and can be correlated with specific phenomena or part characteristics, providing useful insights for interpreting experimental results and optimizing process parameters [20]. It is important to point out that these signatures are the most common features observed by monitoring systems to study and control the processes and some of them will be analyzed during the research activities conducted and described in this thesis:

- *Melt Pool Geometry* (Fig. 4, a): The melt pool refers to the localized region of molten material created during the interaction between the laser source and the metal powder. The size and shape of the melt pool are critical indicators of energy input and powder melting dynamics. A stable melt pool, typically characterized by a specific width, depth, and aspect ratio, is crucial for achieving consistent fusion between layers and preventing defects like lack of fusion or porosity. Monitoring melt pool geometry allows for real-time adjustments to laser power, scan speed, or spot size to maintain optimal melting conditions [19].
- *Melt Pool Temperature* (Fig. 4, b): The temperature of the melt pool directly influences the metallurgical properties of the solidified material, affecting microstructure, grain size, and ultimately, mechanical properties. Monitoring melt pool temperature helps ensure it remains within a specific range to avoid issues like overheating, vaporization, or lack of fusion, which can lead to more severe defects and compromised part quality.
- *Light Emissions from the Melt Pool*: The intensity and spectral characteristics of the light emitted by the melt pool provide valuable information about the melting process and material behavior. Analyzing these emissions can reveal insights into melt pool temperature, chemical composition, and the presence of impurities or defects[38]. This information can be used for real-time process control and quality assurance.
- *Powder Bed Density*: The density and uniformity of the powder bed before melting significantly impact the consistency of energy absorption and melt flow. Variations in powder bed density can lead to uneven melting, porosity, and dimensional inaccuracies in the final part. Monitoring powder bed characteristics helps ensure a consistent and repeatable build process[41].
- *Part Surface Features*: Analyzing the surface characteristics of the manufactured part, such as roughness, texture, and the presence of defects, provides valuable feedback on the overall process stability and part quality. Surface defects like balling, cracking, or excessive roughness can indicate issues with process parameters, powder characteristics, or environmental factors [20].

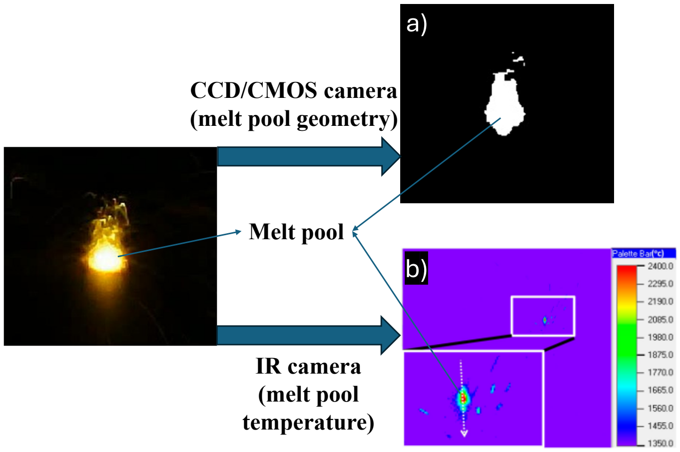

Fig. 4: Melt pool obtained from different sensors: a) Melt pool geometry obtained by thresholding a VIS camera frame; b) Melt pool temperature profile from an IR camera [42].

As will be discussed in subsequent paragraph, during the experimental activities conducted, the melt pool geometry and the light emitted from the melt pool were chosen as monitored process signature.

2.2.2. ***Lattice structures main defects***

Lightweight structures, which include both foam and lattice, are engineered cellular structures characterized by the repetition of unit cells within the three-dimensional space [43], as it is shown in Fig. 5.

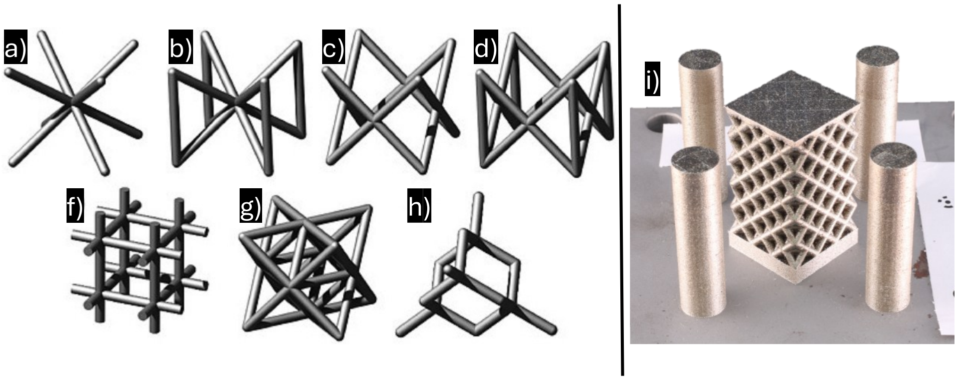

Fig. 5: Different types of unit cells for strut-based lattice structures [3]: a) BCC; b) BCCZ; c) FCC; d) FCCZ; f) cubic; g) Octet-truss; h) diamond. In i) example of Octet-truss (g) lattice structure.

These structures have gained significant attention, particularly in sectors such as aerospace and healthcare [3], where achieving the optimal balance between lightweight and high-strength components is critical. The design flexibility of lattice structures allows applications demanding low weight, excellent mechanical performance, and enhanced thermal properties. This design freedom puts lightweight structures inside the category of *meta-materials [44],* which entails structures that gain their functional properties from their geometry rather than inheriting them directly from the material used to produce them. The open-cell configuration brings other advantages to these components, such as high strength-to-weight ratio, good heat dissipation and good energy absorption.

Lattice structures are known to be difficult to fabricate using conventional subtractive manufacturing technologies due to their geometric complexity. The advent of Industry 4.0 paradigm and AM technologies, particularly L-PBF, has overcome these limitations. In fact, L-PBF enables the production of highly complex and lightweight structures with exceptional geometric control, unlocking new possibilities in design and performances. However, as already mentioned, L-PBF, and all AM technologies, remain susceptible to the occurrence of defects during production because of the high number of interdependent parameters that influence the process itself and the incomplete understanding about the underlying process dynamics. Consequently, as the adoption of L-PBF for lattice production grows, understanding the impact of printing parameters on critical outcomes such as dimensional and geometrical accuracy, mechanical and chemical properties and defect formation becomes essential. Indeed, variability in these factors affect significantly the performance and reliability of lattice structures, emphasizing the need for deeper insights and robust monitoring strategies.

In chapter 3.2, the monitoring activities related to L-PBF will be explained, where a lattice structure was produced to evaluate the reliability of the monitoring system. Therefore, it is important to introduce lattice structure and highlight their importance in industrial applications. But, considering the focus of this work on monitoring systems and methodologies for AM technologies, it is necessary to discuss common defects that affect lattice structures. This discussion lays the foundation for understanding how to evaluate and characterize the reliability of monitoring methodologies. Usually, lightweight structures are produced by means of L-PBF due to its capability to handle intricate geometries with relatively high precision. However, it is important to emphasize that lattice structures proved to be prone to additional geometrical defects unique to their architecture [45,46], alongside those typically induced by the manufacturing process, described in chapter 2.2. These geometrical defects are outlined below and shown in Fig. 6:

- *Strut Thickness* (Fig. 6, b): This parameter is considered as the smallest cross-sectional diameter of each strut, measured layer by layer throughout the structure. Variation in strut thickness can indicate deviations in geometric quality, directly affecting the structural integrity and mechanical performance of lightweight structures.
- *Strut Waviness* (Fig. 6, a): The strut waviness is defined as the deviations in the position of struts' axes; thus, the central axis of the built strut is not collinear with the central axis of the nominal strut. Significant waviness can lead to eccentric loading, premature structural collapse undern nominal loads, and reduced energy absorption capabilities.

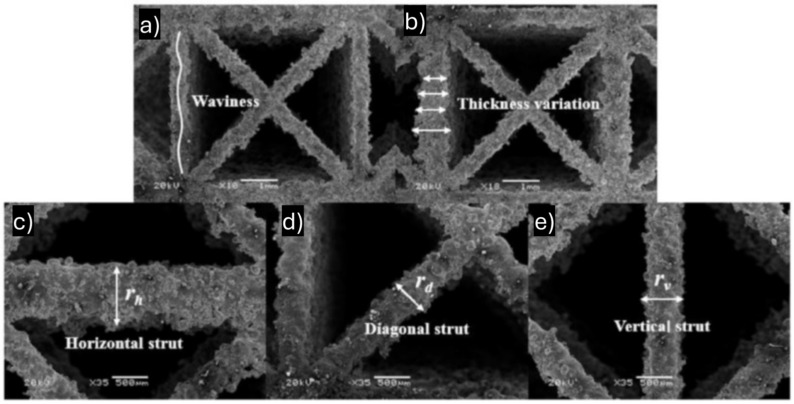

Fig. 6: SEM images representing a) strut waviness; b) strut thickness variation; c) horizontal strut; d) diagonal strut; e) vertical strut. [45]

3. State of art: AM process monitoring

Process monitoring is paramount to the successful wide implementation of AM technologies. It can provide a real-time window into the complex physical phenomena occurring during the build process, enabling manufacturers to ensure part quality, optimize process parameters, and ultimately move towards the reliable and repeatable production of high-value components. Without robust monitoring, AM processes are prone to inconsistencies and defects that can compromise the mechanical properties, dimensional accuracy, and overall integrity of the final part.

Effectively monitoring AM processes presents inherent difficulties due to the dynamic nature of the build environment [47,48], the harsh conditions involved [49,50], and the complexity of the data generated [51,52]. The rapid heating and cooling cycles, intricate melt pool dynamics, and constantly evolving part geometries create a highly dynamic environment that is challenging to monitor accurately. Furthermore, the high temperatures, intense light emissions, and potential presence of spatter or fumes can pose significant challenges for sensor operation and reliable data acquisition. Adding to these challenges, AM monitoring systems typically generate vast amounts of high-dimensional data from various sources, necessitating sophisticated data processing and analysis techniques to extract meaningful information. By providing real-time information about the build process, reliable monitoring systems can enable the early detection and prevention of defects, ensuring the production of high-quality parts. Moreover, monitoring systems can provide valuable data for process optimization, leading to improved efficiency, reduced waste, and enhanced material properties.

Given these challenges, it becomes crucial to explore existing research on monitoring systems tailored for different AM technologies. This chapter reviews the existing literature, at the best of author knowledge, on monitoring systems and methodologies for AM technologies, by organizing the discussion by the three considered AM processes (MEX, L-PBF and L-DED), and at the end of each subparagraph a panoramic of research gaps to be filled is presented. This is of paramount importance because it will help contextualize the research activities conducted in this thesis. The purpose of these paragraphs is focused on key advancements in AM monitoring field, by showing representative examples for each application to illustrate the progress made and the challenges to address.

3.1. MEX in-situ monitoring

Material Extrusion (MEX), one of the most widely utilized additive manufacturing (AM) technologies, has obtained significant attention due to its simplicity, cost-effectiveness, and versatility in fabricating complex geometries. By depositing a large variety of materials, usually thermoplastic materials, layer-by-layer, MEX offers exceptional flexibility for producing tailor-made and small-batch components for various industries, including aerospace, automotive, and healthcare. In accordance with Oleff et al. [13], MEX process monitoring is the most developed topic in literature so far. Despite this interest in this technology, ensuring part quality and process consistency remains a persistent challenge. As discussed in paragraph 2.1, a lot of defects can occur during the extrusion process, and this is due to the several parameters that influence the process, as better explained in Fig. 7 where the main process parameters are presented. It comes that dependency on a very high number of parameters makes the process very complex and prone to defect occurrence, because of the lack of systems able to control and optimize process parameters.

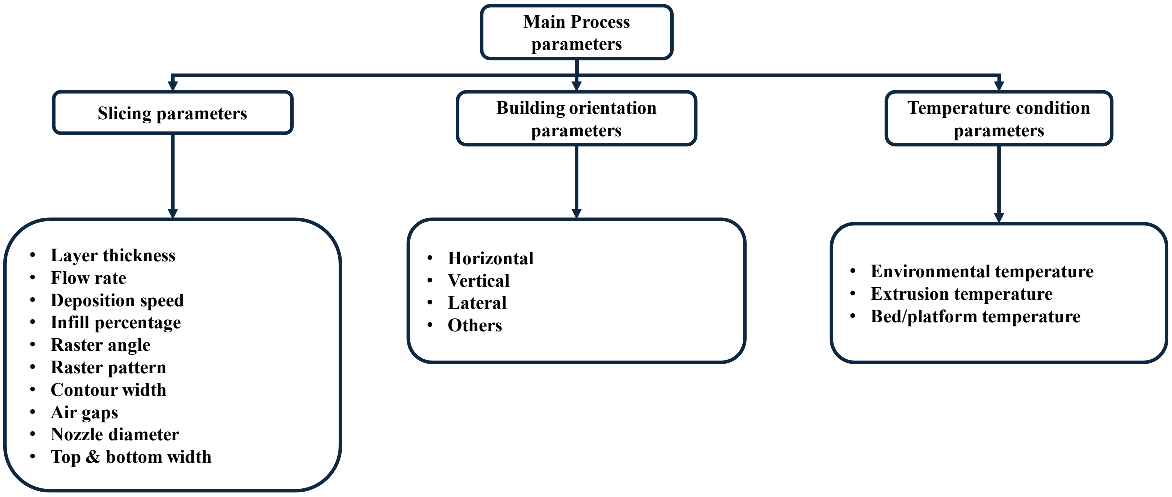

Fig. 7: MEX main process parameters.

In-situ monitoring emerges as a critical solution to address these challenges, offering real-time insights into the dynamic nature of the MEX process. By providing continuous feedback on process conditions, in-situ monitoring facilitates early detection of defects, enabling corrective measures to be implemented before they compromise the integrity of the final part. This is possible because the relationship between parameters and defective condition has widely been studied [25,34,53]. Furthermore, monitoring systems contribute to a deeper knowledge of the process dynamics, optimizing process parameters, reducing material waste, and enhancing overall production efficiency. In this chapter, in-situ monitoring systems for MEX will be categorized based on the measured signal type used to acquire process information: acoustic, thermal, and optical. Acoustic systems detect vibrations and sound emissions to identify anomalies such as nozzle clogging or mechanical failures [17,54]. Thermal systems utilize temperature sensing devices to monitor heat distribution and ensure proper layer adhesion [13]. Optical systems, ranging from high-resolution cameras to laser profilometers, enable detailed inspection of geometric and surface features in real-time, thanks to the application of different machine learning approaches [22].

The following sections provide a comprehensive review of these in-situ monitoring methodologies, exploring their underlying principles, applications, and limitations. The discussion aims to highlight the advancements achieved in in-situ monitoring for MEX while identifying opportunities and gaps to contextualize and explain the research activities conducted in this thesis.

3.1.1. *Acoustic and vibrating monitoring methods*

Acoustic and vibrating (A&V) sensors can transform sound waves, vibrations, and pressure waves to electrical signals, making it possible to measure these quantities and provide useful information about the condition of the process. These sensors can acquire response after generating an acoustic wave (active sensors) or can measure directly the waves generated by the measured object (passive sensors) [15]. The signals measured by these sensors are then analyzed through different algorithms to identify anomalies in the process that may compromise the quality of the printed part. In general, based on this, it is possible to categorize mainly in three MEX monitoring method groups, based on the analyzed signal: Acoustic Emission (AE), Vibrations emission or Ultrasonic testing (UT).

Acoustic Emission (AE) monitoring is a methodology for in-situ monitoring in Material Extrusion (MEX) processes that leverage high-frequency stress waves generated during rapid stress release in materials [55]. These waves contain valuable information about machine status and defect formation. Several studies have demonstrated the efficacy of AE sensors in monitoring the extrusion process and identifying anomalies. For instance, Wu et al. [54] attached an AE sensor to an extruder using vacuum grease, enabling the classification of extruder states, such as material loading/unloading, idle, and normal extrusion, using a hidden semi-Markov model. This setup achieved a classification accuracy of over 90%, highlighting its potential for precise defective condition detection. In another study, Wu et al. [56] mounted an AE sensor on the build platform next to the part, allowing detection of detachment from the platform and deformations during printing. These defects resulted in altered acoustic emissions, indicating contact between the defective part and the nozzle. Moreover, Chhetri et al. [57] employed an external AE monitoring setup to capture acoustic signals from the printer's axes and motors. By reconstructing the geometry of the layers from these emissions and comparing it with the original G-code, they successfully detected cyberattacks that modified the geometry of printed parts. AE sensors are cost-effective, sensitive, and non-intrusive, making them highly suitable for in-situ MEX monitoring applications. Researchers have utilized them to detect filament breakage, nozzle clogging, and other defects that compromise the printing process. AE monitoring systems generate a big amount of data during the record phase. For this reason, these sensors have been coupled with ML algorithms, which have the possibility to process a big quantity of data without human efforts and classify the process if defective or not. More detailed information about AE monitoring systems based on ML and DL approaches proposed in literature can be found in [15,55].

Another important category of monitoring systems for MEX are the ones exploiting vibrating sensors. Vibration monitoring systems operate by measuring mechanical oscillations around the equilibrium position of machine components during the manufacturing process. These oscillations are captured using vibration sensors, which convert the mechanical movements into electrical signals. Accelerometers, the most used vibration sensors in AM, are preferred for their affordability, durability, and sensitivity to abnormal signals. In MEX, vibration sensors can be strategically installed on components like the extrusion head or substrate to monitor vibrations that may indicate machine faults or defects in the printing process. Several studies have demonstrated the application of vibrating monitoring systems in MEX. Tlegenov et al. [58,59] attached an accelerometer to the extruder to assess nozzle clogging by measuring effective nozzle diameter. They observed a nonlinear increase in vibration amplitude as the effective nozzle diameter decreased. Their analytical model for amplitude determination showed strong agreement with experimental results across different extruder types, including Bowden and direct extruders. In another study

[16], sensors were mounted on both the extrusion head and build platform to detect part deformations and defective extruder conditions. This setup enabled effective identification of mechanical issues in the MEX system. Yen and Chuang [60] extended this work by focusing on the detection of defects specifically in the mechanical components of MEX machines, highlighting the versatility of vibration monitoring for ensuring machine reliability. These studies underscore the importance of vibrating monitoring systems in identifying machine-related issues, such as nozzle clogging and mechanical deformations, thereby contributing to enhanced process stability and defect prevention in MEX.

Ultrasonic Testing (UT) is a promising NDE method used for defect detection in MEX processes. UT is a method where ultrasonic waves are actively generated by a transmitter, interact with the material, and are captured by a receiver. These waves were found reflective of some defective condition, especially for L-PBF monitoring as will be further discussed in chapter 3.2.1. Literature about UT monitoring system for MEX is very short. Cummings et al. [61] demonstrated a UT setup with four piezoelectric transducers (one transmitter and three receivers) positioned around a part on the print bed of a MEX machine. They analyzed frequency responses to detect delamination, comparing the frequency characteristics of normal printing and extrusion-free states as baselines. Quality indicators derived from these responses allowed effective defect prediction. Another advanced approach involves laser ultrasonic systems, as shown in [62]. Authors employed a piezoelectric transducer as a pulser on the print bed and used a laser Doppler vibrometer to scan the part surface. Defect detection was based on wavenumber spectroscopy, where large wavenumbers and abnormal response magnitudes indicated damage. In conclusion, UT monitoring systems provide high sensitivity for detecting sub-surface defects and enabling real-time quality assessment.

Despite these advantages, A&V monitoring systems for MEX face several limitations. One significant drawback is their primary focus on monitoring the state of the machine rather than the part itself. Most studies relate machine conditions, such as vibrations, extrusion head motion, or motor performance, to defective states without directly assessing the quality of the printed layers or the structural integrity of the part. This indirect approach can limit the ability of A&V systems to detect defects that arise independently of machine anomalies, such as material inconsistencies or layer delamination. Additionally, A&V signals are highly sensitive to environmental noise and other disturbances, which can complicate data interpretation. The complex acoustic environment of MEX processes, including noise from motors, fans, and other moving parts, may mask or mimic defect-related signals [8,13,55]. Accurate calibration and advanced signal processing techniques are necessary to distinguish meaningful signals from background noise, which adds to the system's complexity and cost. Furthermore, while A&V systems excel in detecting anomalies, they are less effective in providing detailed insights into defect mechanisms or part geometry. This limitation makes them less suitable as standalone tools for comprehensive quality control. Integration with other monitoring modalities, such as optical or thermal sensors, is often required to achieve a deeper understanding of the process and part quality.

3.1.2. *Thermal monitoring methods*

Thermal monitoring methods have been explored as a means in ensuring the quality of MEX part processes, because of their inherent thermally driven nature. Compared to laser-based AM technologies, thermal phenomena are way less crucial to the quality of the final part, but they were found worth studying because they are related to defective conditions caused by non-correct polymer diffusion and adhesion between deposited layers. Knowing the relationship between thermal phenomena and part integrity can help in optimizing interlayer bonding and in minimizing temperature-related defects [63]. A deeper analysis on the influence of thermal factors, such as nozzle temperature, bed temperature and cooling rates, can be found in [63], but will be omitted in this work because the focus is on thermal monitoring methods and systems. The main sensors applied to perform thermal monitoring for MEX are IR cameras and thermocouple. IR cameras offer insight into cooling rates and thermal gradients over the external surface of the part, while thermocouples, on the other hand, measure localized temperature profiles at specific points, usually at the interface between subsequent layers, but they need to be in contact with the part to measure the temperature.

In terms of IR cameras monitoring, Seppala et al. [64] proposed the use of IR thermography to measure the temperature profiles of filaments during MEX under various printing conditions. Their setup focused on the weld zone, capturing in-process temperature data to estimate the extent of sublayer heating within the melting zone. They later extended this work [65] by developing an experimental framework that integrated thermal, rheological, and fracture mechanics analyses to study weld formation during material extrusion. Their findings demonstrated a steady increase in weld strength with extended weld times, although they highlighted the need for further investigation into these observations. Compton et al. [66] investigated temperature evolution in large-scale thermoplastic polymer composites using a combination of experimental and numerical approaches. They recorded the temperature profiles of deposited layers using thermal imaging and applied the results to a one-dimensional finite difference heat transfer model. Their study revealed that cooling rates decreased with reduced distances from the build platform and identified the temperature of the topmost layer before new deposition as a critical indicator of warping and cracking risks. Prajapati et al. [67] monitored the filament temperature distribution in the stand-off gap between the liquefier and platform, employing a model that accounted for heat loss. Their results demonstrated strong alignment between experimental and predicted temperature profiles, validating the robustness of their approach. Ferraris et al. [68] employed IR-based setups to record spatial and temporal temperature variations in vertical walls. Although they validated their experimental results using a finite difference method, significant discrepancies were observed between numerical and experimental peak temperatures, emphasizing the complexities involved in accurately modeling heat transfer during MEX. Kuznetsov et al. [69] examined the impact of process parameters on interfacial temperature variations between adjacent layers, using an IR camera to record the temperature distribution on rectangular tube-shaped samples. Their analysis linked temperature variations to the mechanical strength of the fabricated parts. Lepoivre et al. [70] investigated heat transfer and adhesion by using IR cameras to experimentally record the temperature profiles of vertical walls, complemented by a 2D transient heat transfer model. Their results demonstrated a strong agreement between experimental and numerical findings, emphasizing the role of heat transfer in determining adhesion quality. Basgul et al. [71] proposed a non-isothermal healing model for interfacial strength, integrating experimental IR-based temperature measurements of vertical walls with a one-dimensional heat transfer model. Discrepancies between experimental data and model predictions indicated the need for further refinement.

MEX monitoring based on thermocouple was also explored in literature. Yin et al. [72] investigated the interfacial bonding during multi-material MEX by focusing on interfacial temperature profiles. Their setup incorporated K-type thermocouples embedded within the layers to measure temperature evolution during the process. The experimental data were validated using a three-dimensional transient heat transfer model. While their results indicated good agreement between experimental and modeled data, notable discrepancies in the onset of temperature peaks highlighted challenges in accurately capturing dynamic thermal behaviors. Xu et al. [73] analyzed the temperature evolution of filaments during the fabrication of thin walls using T-type thermocouples. Their setup also involved validating experimental data against a pre-established model. Although the results demonstrated strong consistency between the recorded and predicted data, the need to pause the process to place the thermocouples was a significant limitation, potentially affecting the thermal profile of the printed part. Vanaei et al. [74] proposed an innovative approach to local in-process temperature monitoring during thin wall fabrication. They utilized ultra-small K-type thermocouples (diameter = 80 µm) to measure temperature variations without interrupting the printing process. Their setup achieved excellent agreement between experimentally recorded data and numerical predictions, successfully capturing key temperature characteristics such as the onset, relative magnitude, and breadth of temperature peaks. This non-intrusive methodology addressed prior limitations, offering a more accurate representation of the dynamic thermal environment in MEX.

In conclusion, Infrared (IR) cameras can capture surface temperature profiles over complex geometries. However, these systems are unable to measure temperatures at specific locations, such as the interfaces between adjacent filaments, where interlayer bonding occurs, and they also have lower resolution than visible cameras. Additionally, the presence of other heat sources, such as radiation from surrounding components, can lead to over-estimated temperature values, reducing the reliability of the recorded data. While thermocouples, widely used in local thermal monitoring, provide high precision in measuring temperatures at specific points, such as interfacial zones, their application introduces notable challenges. Traditional thermocouple setups often require interruptions in the printing process to position sensors, which can alter the thermal environment and affect the results. Moreover, their limited spatial coverage restricts their ability to capture broader temperature distributions across the part. Both global and local approaches face difficulties in accounting for dynamic thermal phenomena inherent to the MEX process. This is because the discussed monitoring systems relay on tailor made models, which are still too simple for the phenomena they are supposed to represent, and this can be seen from the discrepancies between experimental data and numerical predictions.

3.1.3. *Optical monitoring methods*

Optical monitoring methods for MEX include most of the monitoring approaches proposed for this technology [13]. Optical systems offer several advantages that widen their usage in real-time control and quality assessment by leveraging advanced imaging techniques without touching the part under exam. This enables geometry, dimensions, surface and defects topology monitoring and, lately, started to provide valuable input to ML algorithms, which have proven to be essential to implementation of closed-loop monitoring systems [15]. In the context of MEX monitoring, optical methods are broadly categorized into 2D image-based methods and 3D scanning methods.

The 2D image-based techniques primarily generate two-dimensional images, offering insights into part geometry and dimensions. These methods are relatively straightforward and cost-effective, but they are inherently limited by their inability to capture depth information [75,76]. Li et al. [77] developed a vision-based monitoring system using a single camera mounted above the MEX 3D printer to capture images of each printed layer. These images were compared with simulated layer images generated from CAD models using G-code. The system employed background subtraction and Fourier-Mellin Transform (FMT) to evaluate layer dimensions, profile accuracy, and infill patterns. Experimental results demonstrated the system's ability to detect print deviations, such as dimensional errors and profile inaccuracies, with high precision, ensuring reliable quality assessment during the printing process. Moretti et al. [23] conducted a comprehensive evaluation of defect detection capabilities by mounting various sensors on a low-cost MEX printer. They demonstrated the effectiveness of 2D image acquisition for detecting cohesion issues between infill and walls, defects that were otherwise undetectable by the other sensors used. In a subsequent work [78], the authors utilized a digital microscope to capture 2D images, which were analyzed with machine learning classifiers to identify surface defects, including voids between walls and rasters. Additionally, they integrated a digital twin of the printer [79], allowing the ideal contour of the printed part to be compared with the actual contour derived from the microscope images, enabling precise in-process defect detection. Liu et al. [80] introduced a dual-camera setup using borescopes mounted on opposite sides of the nozzle to monitor surface conditions. Their image textural analysis algorithm successfully identified under-fill, over-fill, and normal conditions, demonstrating the utility of 2D imaging systems coupled with ML classification algorithms for monitoring material deposition quality in real time. Nuchitprasitchai et al. [75] proposed two distinct in-process monitoring systems: one using a single camera and the other employing a dual-camera setup mounted on the side of the 3D printer. By comparing binarized images from the cameras with ideal ones derived from the CAD model, their systems effectively detected surface flaws during printing. Huang et al. [81] implemented a statistical process monitoring technique based on 2D images obtained from a digital camera mounted above the printer. This method allowed for the detection of under-fill and over-fill conditions on the layer surface, showcasing the effectiveness of straightforward camera setups in MEX monitoring. Similarly, He et al. [82] presented an optical monitoring system designed to monitor geometric deviations in MEX parts using profile monitoring techniques. A CCD camera, mounted above the printing bed, captured images of each layer. Geometric profiles were extracted and deviations from ideal CAD data were computed. Deviations were transformed into linear profiles using Quantile-Quantile (Q-Q) plots, which were subsequently monitored with Exponentially Weighted Moving Average (EWMA) control charts. This method effectively identified geometric defects such as dislocation, staircase variations, and gradual changes in layer geometry, ensuring detailed monitoring of the entire manufacturing process. Delli et al. [83] conducted a comparative analysis between images of an ideal, defect-free part and those of the actual manufactured part. They employed a combination of a simple thresholding technique and a support vector machine (SVM) classifier to evaluate the part's quality. Based on the analysis, the system categorized the part into one of two classes: acceptable or defective. In addition to part inspection, some 2D vision systems focus on monitoring the mechanical components of the printer itself. An example can be found in the works of Greeff et al. [84,85] that used a digital microscope to observe the filament delivery mechanism within the extrusion head. By measuring the filament's speed and width, they calculated the volume flow and compared it with the feeding gear speed to identify potential slippage effects. These approaches highlight the versatility of 2D imaging systems in assessing not only the printed part but also the functionality and accuracy of the printer's mechanical components. Although 2D vision monitoring systems are widely used in MEX monitoring for their simplicity, cost-effectiveness, and ability to detect defects, they still exhibit important limitations that restrict monitoring capabilities. One of the primary drawbacks is the inability to capture height or depth information, which is crucial for analyzing topological features and identifying 3D defects such as layer misalignment. Additionally, the performance of 2D vision-based monitoring system heavily depends on environmental lighting conditions. Indeed, variations in illumination can introduce inconsistencies and noise in the acquired data, reducing the reliability of defect detection. Another important limitation is their inability to provide quantitative metrics for the identified defects. This is particularly true when neural networks are used to process processed images. These networks work as black-boxes and they can classify when a defective condition occurs, but, often, without providing further quantitative data about the defect, limiting the utility of 2D vision-based monitoring systems for MEX for precise diagnostic and corrective actions. Furthermore, these systems struggle to provide comprehensive monitoring when parts with complex geometries are produced.

These needs have brought researcher to explore also different methodologies based on optical sensors. 3D scanning methods, which include stereo-cameras, laser-based and structured-light systems, deliver a richer set of topological data by capturing three-dimensional representations of the part. These systems are particularly valuable for detecting surface defects and analyzing part topology in detail. However, their implementation typically demands higher investment in equipment and computational resources for data processing [52]. An advanced and interesting application of 3D reconstruction algorithms, based on a single camera monitoring set up, was proposed by Malik et al. [86]. They developed an innovative 3D vision-based monitoring system for MEX using a single camera mounted above the build plate of a PRUSA i3 MK3 printer. This system acquires images layer-by-layer during the printing process, which are processed to construct a 3D model of the printed part in real time. The methodology involves aligning captured images with G-code simulations to segregate layer information and reconstruct the geometry of the current layer. These reconstructed models are then converted into 3D file formats for further analysis. One of the significant advancements of this system is its integration with augmented reality (AR) using HoloLens. The reconstructed 3D models can be visualized in a mixed-reality environment, allowing users to inspect both surface and internal defects layer-by-layer using hand gestures and voice commands. The experimental results demonstrated their ability to detect defects, such as geometric inaccuracies and embedded imperfections, during the build process, thereby enhancing decision-making and defect mitigation capabilities in real time. Holzmond et al. [87] presented an innovative 2D imaging approach using 3D-Digital Image Correlation (3D-DIC). This is an optical technique used to measure and analyze deformations, displacements and surface geometry. It involves capturing a series of 2D images, typically using multiple cameras, during the manufacturing process to generate point clouds or surface height maps. In their work [87], by mounting two cameras on a 3D printer, they captured images of each printed layer. These images were processed to generate a point cloud for each layer, which was then compared with an ideal point cloud derived from the CAD model. This approach effectively identified surface defects such as holes and blobs by analyzing height differences between the two point clouds. Ye et al. [88] demonstrated the application of a structured-light scanner mounted on a low-cost 3D printer. By utilizing a deep cascade model, they compared point clouds from the 3D scans with reference models to evaluate the effects of varying printing parameters on layer quality. This approach highlighted the capability of structured light scanning to capture detailed geometric information, enabling precise quality control. Similarly, Charalampous et al. [89] used a structured-light scanner integrated with a consumer-grade 3D printer to compute the geometric deviation between scanned layers and theoretical layers derived from G-code. Their methodology, which involved the calculation of root mean square error and mean absolute error, proved effective in identifying geometric inaccuracies. To mitigate the computational demands of analyzing dense point clouds, some researchers have proposed rasterizing point cloud data into depth images. These images can then be compared with nominal depth images derived from simulations or G-code. For example, Lin et al. [37] employed a laser line scanner to monitor depth variations by subtracting theoretical depth images from real ones, effectively detecting over-fill (OF) and under-fill (UF) conditions on layer surfaces. Lyu et al. [90] expanded on this approach by feeding rasterized images from a red-light profilometer into a convolutional neural network. Their model successfully classified defective and non-defective regions based on point height values, showcasing the potential for integrating neural networks into 3D monitoring workflows.

3.1.4. ***Research gaps: metrology and 3D scan monitoring in MEX***

The field of metrology in additive manufacturing (AM) faces significant challenges, particularly in Material Extrusion (MEX) processes [9]. A key issue is the lack of robust, standardized, and reliable metrics to evaluate part quality during manufacturing. Traditional metrological approaches struggle in addressing the novel and unique requirements of AM produced parts, which demand in-situ monitoring systems capable of delivering real-time, high-resolution assessments of layer quality, defect topology, and process consistency. This deficiency is exacerbated by the absence of universally recognized process signatures that could serve as benchmarks for quality assessment and corrective actions. Establishing these process-specific metrics is essential for ensuring reproducibility and precision in AM [14]. In other words, a critical gap lies in the lack of a well-defined framework for determining what process parameters should be measured during the MEX process. Without clear guidelines, establishing process stability and quality control becomes increasingly challenging. This ambiguity not only complicates metrological practices but also hampers the development of reliable in-situ monitoring systems. Moreover, while functional surface analysis has recently been proposed successfully for evaluating surface morphology and defect topology in MEX processes [91], its integration into in-situ monitoring systems has yet to be investigated. Functional analysis is a method used to characterize the geometric and physical properties of a surface by evaluating its height distribution and related parameters. Applied to MEX as a monitoring method, such tools could enhance understanding of layer bonding, dimensional accuracy, and mechanical integrity, by detecting the occurrence of defects, providing actionable insights about part performance and process optimization. Despite the promising results, literature about functional analysis applied as a monitoring tool for AM, in general, needs to be expanded.

In terms of sensors and methods used in monitoring systems for MEX, 3D scanning methods, particularly laser line profilometers, offer significant potential for detailed surface analysis, layer surface functional analysis and real-time defect quantification. These systems can rapidly acquire extensive topological data, which is vital for in-depth analysis of layer morphology. However, as discussed in chapter sed in chapter 3.1.3, much of the existing research focuses on rasterized depth images derived from point clouds, often leading to the loss of critical surface details and defect morphology. The exploration of high-resolution raw point cloud, which could provide more precise in-situ defect characterization and enable real-time corrective methodologies, remains notably limited and it also opens possibilities to perform functional analysis, thanks to the high resolution of profilometers.

To address these gaps, a laser line scanner able to retrieve both 2D profiles and 3D point clouds will be employed as a primary sensor in a custom monitoring setup. The high-resolution system enables the acquisition of detailed surface data, facilitating the use of functional analysis tools for surface morphology and defect topology evaluation. From this analysis, robust and quantitative indexes will be developed, serving as a potential process signature for MEX. The goal is not only to improve real-time monitoring and process signatures but also to contribute to advancing metrological practices in AM by providing reliable metrics for quality assessment.

3.2. L-PBF in-situ monitoring

L-PBF is an appealing metal AM technique, and it has obtained significant interest due to its ability to fabricate complex, near-net-shape components with high material efficiency [3]. However, as already discussed in chapter 2.2, the high number of parameters influencing the process (Fig. 2) introduces challenges in maintaining part quality and reliability. Indeed, process monitoring is essential to address these challenges because it enables real-time defect detection and process control and optimization. In accordance with [92], and the same as did for MEX, it is possible to classify in-situ monitoring for L-PBF in three categories based on the processed signal: acoustic, thermal and optical methods.

3.2.1. *Acoustic monitoring methods*

Acoustic-based monitoring methods rely on measuring the transmitted or reflected wave intensities propagated through the part to determine part properties. Mainly, two techniques have been explored so far for L-PBF monitoring, which are ultrasonic testing (UT) and the acoustic emission spectroscopy (AES) techniques.

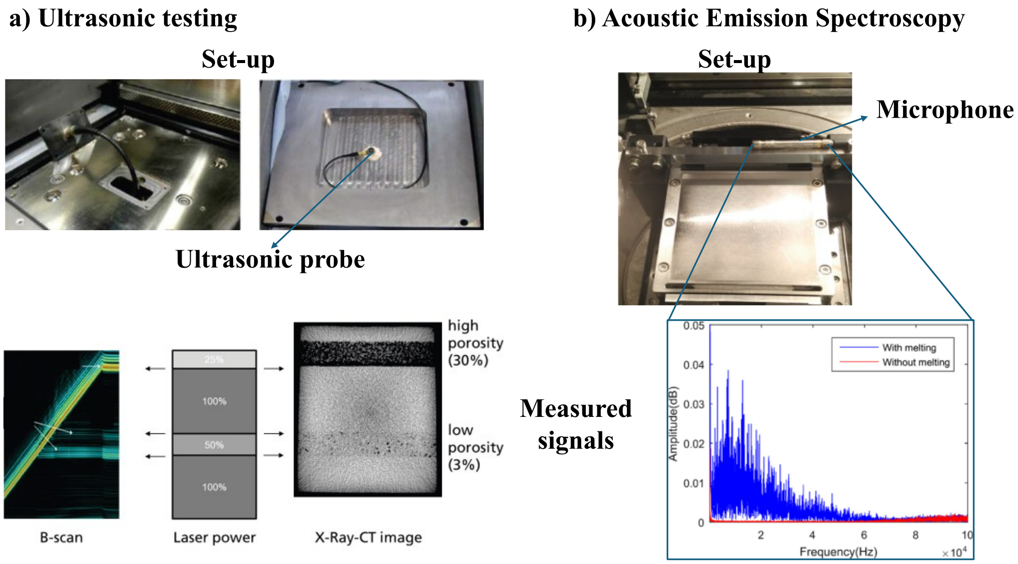

Fig. 8: a) UT monitoring system with the ultrasonic probe mounted below the building platform, and the waves reflected are associated to the internal porosity of the part [93]; b) AES monitoring system based on a microphone mounted inside the building volume and below an example of acoustic measured signal is displayed. Acoustic signals were demonstrated to be sensitive to melt and no melt conditions [94].

Currently, UT is widely used in industrial contexts as NDT to evaluate the fatigue performances of a part during its lifecycle. For L-PBF monitoring purposes, an ultrasonic transducer is mounted below the build plate and the ultrasonic waves are transmitted through this to the part. The waves reflection is recorded by a combined pulser/receiver unit. UT was found to be able to detect the presence of voids/porosity within layers [93,95] by looking at the ultrasonic wave reflections (Fig. 8, a). Despite these sensors offer high sensitivity to characterize internal defects, they are challenging to implement. On the other hand, AES detects high-frequency sound waves generated by rapid thermal and mechanical events during the printing process, usually through a microphone with specific frequency response. Ye et al. [96] were able to propose an in-situ monitoring system that relates AES signals with five different defective states of the part, such as balling, slight balling, normal state, slight overheating and overheating state. Due to the complexity of the recorded signals and to their dependance on multiple factors, often, acoustic signals are analyzed by means of machine learning approaches. An example can be found in [94], where the part quality classification (poor, medium and high quality) was made by a ML algorithm, based on the part porosity. The part porosity was measured thanks to the AES technique (Fig. 8, b) and the monitoring system showed 80% of accuracy in part quality evaluation. In general, acoustic techniques are sensitive to environmental noise and they need to be filtered because of the high amount of data produced. These limitations limit the wider usage of acoustic sensors for in-situ and real-time L-PBF monitoring applications, despite the fact that they have been found to be well-suited for internal defect detection.

3.2.2. *Thermal monitoring methods*

Thermal monitoring is a common measuring approach for advanced high-heat exchange processes, particularly used when a laser is used as energy source, as in the case of welding, L-PBF or L-DED. In this case, by measuring the thermal radiation emission obtained from the interaction between the powder bed or the melt pool and the laser, it is possible to gain insight into the thermal gradients present in the L-PBF process because it can have significant influence in final part properties, as it is widely discussed in literature [20,92,97].

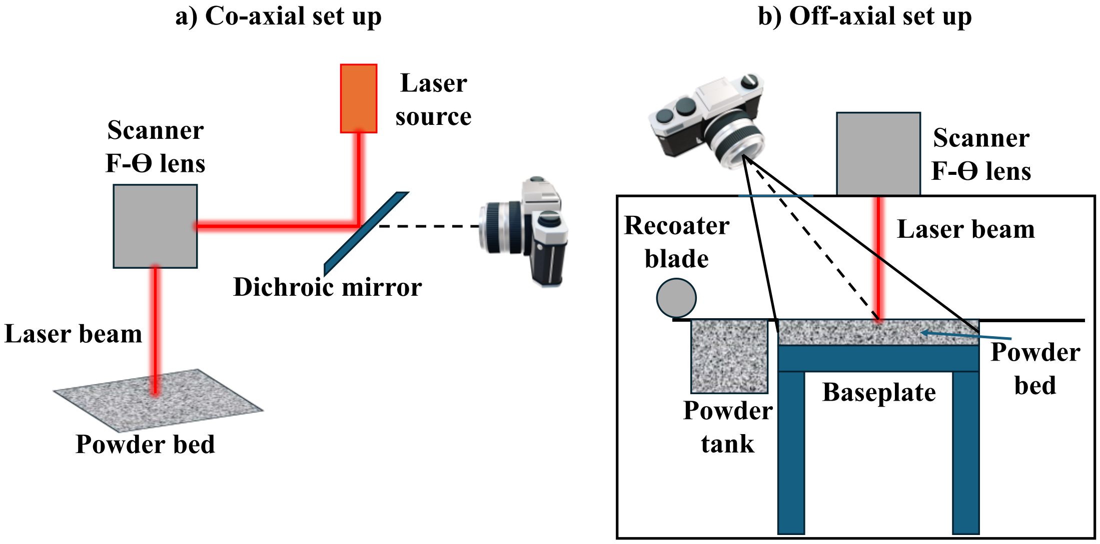

Fig. 9:Different thermal imaging configuration for L-PBF monitoring: a) Co-axial set-up; b) Off-axial set-up.

In general, it is possible to divide thermal monitoring systems into contact-based and contactless. Contact-based sensors, such as thermocouples, are mainly exploited as references to calibrate contactless thermal monitoring systems, an example was discussed in [98]. Indeed, thermocouples can effectively measure the real-time temperature variations of the part, and by measuring the temperature of the building platform or surrounding areas, they can provide reference data that can be used to adjust IR camera readings; by considering factors like emissivity variations and atmosphere transmittance but they are limited due to their small spatial coverage and their invasive nature. Very few examples of in-situ monitoring systems are discussed in literature. An example was discussed by Dunbar et al. [99] that proposed an eclosed system for L-PBF thermal and distortion monitoring through implementing K-thermocouples beneath the substrate and the system was able to detect part distortion based on the thermal cycles of the substrate.

Based on the Plank's law that relates a blackbody to the wavelength at a certain temperature, contactless sensors, such as pyrometers and IR/NIR thermal cameras, are widely explored as monitoring devices for metal AM. According to [19], these type of monitoring systems can be divided into *co-axial* and *off-axial* sensing, as shown in Fig. 9. Specific to L-PBF process, in the co-axial configuration (Fig. 9, a), the sensors share the optical path of the laser source, while in off-axial configuration (Fig. 9, b) the sensor is placed with a given angle-of-view with respect to the region of interest.

Co-axial thermal monitoring systems proved to give valuable insights into the process dynamics, but they are limited to melt pool observation because of the configuration of this monitoring system. Early contributions include the work of Berumen et al. [100], and Craeghs et al. [101,102], who developed a coaxial thermal monitoring setup utilizing a photodiode and a high-speed NIR CMOS camera. This system captured melt pool radiation and enabled the determination of both temperature distribution and melt pool geometry. Clijsters et al. [103] further extended this work, integrating the same optical system with a partially reflective mirror that reflected the laser beam wavelength (1064 nm) while allowing thermal radiation to pass through to the sensors. The use of a high-speed CMOS camera and photodiode operating at a sampling rate of 10 kHz provided critical insights into the thermal dynamics of the melt pool during LPBF. Indeed, the proposed system was able to give information about the melt pool geometry and thermal behavior, temperature distribution and to correlate defect occurrence, such as balling or lack of fusion, with thermal variations. Doubenskaia et al. [104] and Chivel [105] introduced co-axial thermal monitoring using a two-wavelength pyrometer to measure melt pool intensity and temperature distribution. Their system, equipped with photodiodes, enabled temperature measurements. By integrating a CCD camera to capture brightness of profiles, this system achieved a sampling frequency of 20 kHz, which allowed precise thermal characterization of the melt pool during the deposition process. Further advancements in thermal monitoring include work by Thombansen et al. [106], who incorporated a coaxial laser illumination system alongside thermal sensor. Their systems enhanced visualization and detection of the melt pool temperature while minimizing optical distortions due to chromatic aberrations. Additionally, a high-speed IR camera was used to measure the melt pool temperature distribution and analyze heat radiation patterns during the L-PBF deposition process. Once again, temperature anomalies were correlated with defective conditions, such as lack of fusion or over-melting. Significant results were found by Mohr et al. [107], who investigated a coaxial monitoring set-up combining infrared thermography and optical tomography (OT). The study integrated both techniques as real-time in-situ voids and pores detection. Thermography proved to be suitable to pores detection based on the temperature distributions while OT struggled in pores detection but was reliable in terms of melt pool geometry and surface features observation. The findings highlight the advantages of combining these two sensor systems, offering a comprehensive approach for identifying potential defects both thermally and geometrically. However, the study also notes limitations related to data processing speed and sensitivity to environmental noise.

Despite the important information gathered thanks to coaxial thermal monitoring systems about the melt pool, a significant limitation related to these systems is their limited capability to monitor only melt pool-related signature. But, as discussed in chapter 2.2.1, there are other process signatures alongside the melt pool that are related to defect formation and are worth investigating to understand better the process and defect formation mechanism. Due to the limitation on process signatures that can be measured with coaxial monitoring systems, off-axial monitoring systems have been also developed and related to defective conditions. Usually, these systems are of easier implementation compared with coaxial systems because they are mounted outside the building volume and optical filters are used to reduce noise phenomena. This makes these systems able to acquire information about the laser scanning path, the entire layer surface, the spatter production and the powder bed after the deposition of a new layer of powder and correlate with common defects. Krauss et al. [108,109] and Lane et al. [110] used IR cameras positioned off-axially to monitor the heat-affected zones and areas surrounding the scan path. These studies demonstrated that thermal videos could be used to identify defects caused by irregular energy distribution, such as lack-of-fusion and overheating. An example of pyrometers used for powder bed monitoring can be found in Islam et al. [111] highlighted the role of temperature variations in identifying uneven powder bed deposition, which is an indicator to layer non-uniformity and lack-of-fusion defects. The pyrometer enabled the precise detection of spatial temperature gradients. Schwerdtfeger et al. [98,112] used an IR camera to detect surface flaws and irregularities in scanned slices, linking temperature anomalies to incomplete melting and porosity formation. Similarly, Rodriguez et al. [98] analyzed the temperature distribution across the build platform to detect subsurface defects, such as porosity and thermal-induced cracking. A significant result was proposed by Grasso et al [113] that used a high-speed camera to infer local pixel intensity as a representation for temperature, enabling the identification of overheating regions that could compromise dimensional accuracy. This method proved effective for identifying overheating defects during slice development, which can compromise dimensional accuracy and result in warping or distortion. Cheng et al. [42] employed a near-infrared (NIR) thermal imager to capture the temperature distribution and melt pool characteristics. The imager allowed the identification of melt pool dimensions by analyzing the liquidus-solidus phase transition. This study demonstrated the feasibility of linking thermal signals to defect-related phenomena, which are directly related to melt pool variation in geometry and temperature as discussed above, such as irregular heat input causing porosity or lack of fusion. Despite this, they highlighted the limitation of the system in measuring the real absolute temperature because of the several factors that affect the temperature measurements and the difficulty performing the calibration method.

These contributions highlight the importance of thermal monitoring systems in identifying defect-related conditions, ensuring process stability, and enabling improved part quality in L-PBF processes but an important limitation to take into account of thermal cameras is their limited spectral sensitivity, their sensitivity to light reflection and radiation caused during the deposition process and low spatial resolution and field of view (FOV), their higher cost with respect to visible high-resolution cameras and the challenges related to the calibration process.

3.2.3. ***Optical monitoring methods***

An important group of monitoring systems and methods discussed in literature is represented by optical monitoring systems. They have been widely explored for their ability to capture melt pool dynamics, surface features, and powder bed quality during the L-PBF process. It is important to point out that optical sensors have been used also for thermal monitoring as was discussed in the previous chapter, but they are not limited to just temperature measurement, as will be discussed below. In this paragraph, the state of art of different types of optical sensors will be presented by grouping monitoring system that exploits the same sensor to gather data.

High-speed cameras are integral to L-PBF monitoring, offering very high frame rates for capturing transient melt pool behaviors and spatter dynamics. These systems can be mounted in co-axial configurations along the laser optical path or in off-axial setups outside the build chamber. Co-axial high-speed camera setups, as demonstrated in [103,114], allow the melt pool to appear stationary within a limited field of view (FoV) during laser scanning, focusing on precise melt pool geometry, as already discussed for thermal coaxial monitoring systems. However, they require integration into the laser scanning system and calibration to address perspective distortions. Off-axial configurations [115–119] provide a broader FoV, capturing additional process information such as spatter and plume behavior, but require techniques like coordinate transformation to track the rapidly moving melt pool. High-speed cameras have been used to extract key process signatures, such as melt pool width, height, area, aspect ratio, and penetration depth [119,120]. Kruth et al. [121] identified that excessive melt pool aspect ratios indicate a tendency for balling defects, while large melt pool areas in loose powder regions correlate with overheating, elevated edges, and poor down-facing surface quality [113]. Machine learning (ML) techniques have further enhanced the utility of high-speed imaging monitoring systems by enabling automated defect prediction. For instance, k-means clustering and support vector machines (SVMs) have been employed to classify defects based on melt pool dimensions and thermal anomalies [113,116].

Interferometry-based monitoring systems rely on the interference phenomenon caused by super-position of waves. In terms of L-PBF monitoring optical coherent tomography (OCT) have been explored. The interferometry sensor was installed coaxially with the laser beam while the camera can be placed off-axis, and the interference is only possible if optical paths are matched to be equal in length within the short coherence length. Those systems have been exploited for detailed geometric and subsurface monitoring. Indeed, OCT systems provide depth profiles by analyzing interference patterns generated by light reflected from the melt pool and the powder bed. Kanko et al. [122] utilized OCT to characterize scan track geometry and detect denudation zones, while Guan et al. [123] extended its application to subsurface defect detection, identifying voids and measuring their dimensions up to 400 μm below the part surface.

High-resolution imaging monitoring techniques play a crucial role in monitoring the quality of parts produced via L-PBF. A typical setup involves a high-resolution camera mounted above the build platform, enabling the capture of detailed layer-wise images after powder spreading and fusion processes. This configuration allows for the inspection of powder bed uniformity and part surface quality, with proper illumination being a critical factor to enhance contrast in elevated regions and surface textures [124–127]. Zur Jacobsmuhlen et al. [124] proposed a monitoring system made from an off-axis high-resolution CCD camera and different light source placed in different spots inside the building chamber. They proved that, by observing the powder bed and the fused layers, defective conditions, such as super-elevated edges, surface irregularities and other defects, were highly dependent on illumination directions since proper illumination can enhance the contrast of elevated regions and part surface texture. The latest researches have proven the great compatibility of imaging monitoring systems with machine learning algorithm for real-time data processing. Based on this, High resolution-based monitoring techniques can be divided into two primary approaches that have been developed for defect detection using high-resolution imaging: classification-based methods and segmentation-based methods. Classification-based methods rely on extracting representative image features, such as Histogram of Oriented Gradients (HOG), DAISY, and Local Binary Patterns (LBP), which are then processed by machine learning classifiers like Random Forest, Support Vector Machines (SVMs), and Stochastic Gradient Descent to identify defect regions [127]. Supervised feature extraction techniques have also been proposed to reduce high-dimensional data for more efficient classification [128]. Caggiano et al. [129] utilized a bi-stream Convolutional Neural Network (CNN) to analyze powder bed and part fusion images, achieving a surface condition classification accuracy of 99.4%, underscoring the effectiveness of deep learning in defect detection and real-time application. Segmentation-based methods provide a more detailed analysis by classifying individual image patches or pixels into defect categories [130–132]. This approach enables not only the determination of defect occurrence, like cracks, voids or surface irregularities but allows for precise measurement of the size, shape and the extent of the defect. They also provided image distortion correction algorithms, to compensate for non-correct measure because of the perspective (as it happens when the camera is mounted off-axis) and the camera lens distortion. In other works, Gobert et al. [133] and Lu et al. [134] stacked layer-by-layer detection results in constructing a 3D defect model, which was validated against computed tomography (CT) scans. Their method involved reducing perspective distortion because of the off-axial nature of the monitoring setup, extracting fusion areas using graph-based [135] and active contour methods [136,137], and localizing defects layer by layer. This process allowed for accurate defect volume estimation, offering an advantage over traditional classification-based methods.

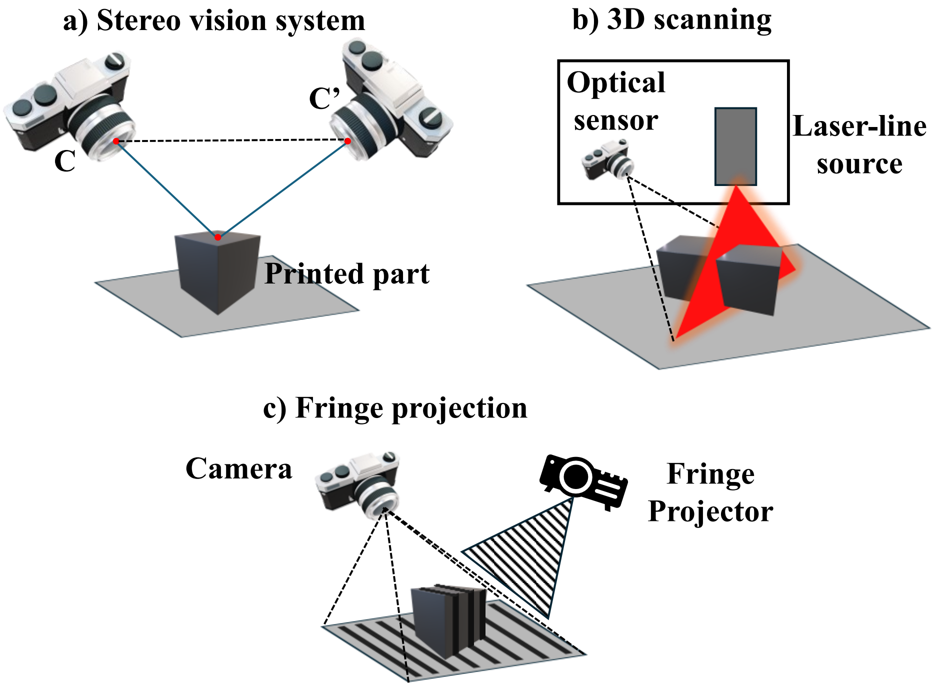

Fig. 10: Main 3D reconstruction techniques: a) Stereo-vision system; b) 3D scanning and c) Fringe projection system.

3D reconstruction techniques have become interesting for L-PBF monitoring applications due to their ability to provide precise spatial data about printed layers, enabling the detection, localization, and quantification of defects. Techniques such as stereovision, fringe projection, and digital image correlation (DIC) have been explored for their high spatial resolution and insights into process dynamics. In Fig. 10 the main 3D reconstruction techniques used for AM monitoring are shown. On the contrary of MEX technology, 3D scanners have been barely explored as L-PBF monitoring systems. An example of 3D scanner applied for PBF monitoring is proposed in [138] where a 2D displacement sensor (Fig. 10, b) was applied to monitor the 3D powder bed topography. The sensor relays on the triangulation principle to obtain the 3D coordinate of the scanned points and the scanned surface flaws were detected with a good resolution and related to bed inhomogeneities. The same triangulation principle is exploited by stereovision monitoring systems by using multiple cameras to reconstruct 3D geometries. In terms of monitoring related to L-PBF promising results have been found by applying direct image correlation (DIC) algorithms. In this context, Bartlett et al. [139] proposed a system where two high-resolution CCD cameras were mounted stereoscopically in an off-axis configuration within an EOS M290 machine. The cameras provided a field of view large enough to capture the full surface of the build platform, enabling precise monitoring of residual stress development. Using the natural surface texture of the printed parts, DIC measured deformations caused by thermal cycles, revealing the heterogeneous distribution of residual stresses. These stresses were shown to depend on laser scanning strategies and layer-by-layer thermal gradients. The system provided valuable insights into stress accumulation mechanisms, validated with X-ray diffraction to a high degree of accuracy. In another study, Bartlett et al. [140] expanded on this concept to focus on powder bed anomalies. The system, also mounted in an off-axis configuration, utilized DIC to detect irregularities such as insufficient powder spreading and pileups. These powder bed anomalies were strongly correlated with defect formation in the final parts, including lack of fusion defects. The ability to predict defect formation through powder bed monitoring demonstrated the potential of stereovision systems combined with DIC algorithms for real-time quality assurance in L-PBF processes. Another important 3D reconstruction-based monitoring system is the fringe projection method (Fig. 10, c). Fringe projection offers a monitoring approach for reconstructing layer geometries and monitoring defects geometry. By projecting grating fringes onto the surface of the powder bed or fused layers and analyzing the modulated patterns captured by a high-resolution camera, mounted with an angle relative to the projector, this method provides precise height measurements. Zhang et al. [141] proposed a fringe projection system integrated into an L-PBF testbed developed by Edison Welding Institute. Their setup included a digital fringe projector, inclined at a relative angle to the camera, and a high-resolution machine vision camera (PointGrey Flea3, 4096 × 2160 pixels) mounted on top of the powder bed. The camera, positioned approximately 200 mm above the powder bed at an oblique angle of 35°, captured sinusoidal light patterns projected onto the surface. The system provided detailed insights into process signatures, including powder bed flatness, height variations in fused regions, edge roughness, and spatter distributions. It demonstrated the capability to track layer-by-layer changes in surface characteristics, offering critical data for quality control despite the shape of the printed part. However, challenges included optimizing the projector and camera alignment and addressing specular reflections from metallic surfaces, which could interfere with accurate measurements. An example of fringe projection and stereo vision combination was explored by Li et al. [41] that proposed a fringe projection-based monitoring method by employing a binocular stereo vision system combined with Enhanced Phase Measuring Profilometry (EPMP). Their setup featured two high-resolution CCD cameras positioned at calibrated angles to the powder bed, paired with a fringe projector. This configuration allowed for capturing fringe images during both the powder spreading and laser fusion phases of L-PBF. The EPMP method enhanced efficiency by requiring fewer images for accurate reconstruction, while a slice model-assisted contour detection algorithm improved precision and reduced processing time. This system enabled quantitative analysis of defects such as recoater grooves, insufficient powder deposition, and warping. Additionally, the layer-by-layer reconstruction of 3D contours facilitated detailed evaluation of surface quality and slice geometry, making it a robust tool for defect monitoring. While fringe projection systems offer significant advantages in providing high-resolution topographical data, they are not without limitations. The accuracy of 3D reconstructions heavily depends on precise calibration of the projector and camera, which can be a hard process because of the limited dimension of building chambers. Specular reflections from metallic surfaces in L-PBF can distort the captured patterns, reducing measurement reliability. Most of all, the computational cost associated with processing high-resolution data for real-time applications remains a challenge that prevents these systems from being widely used. As discussed, the 3D reconstruction during the monitoring provides important information about the part quality, which can speed up post-processing applications because it would help in the part characterization without using off-line high-cost and time-consuming measuring instruments, such as CT scanner for example. An interesting approach for L-PBF monitoring is the so-called Optical Tomography (OT).

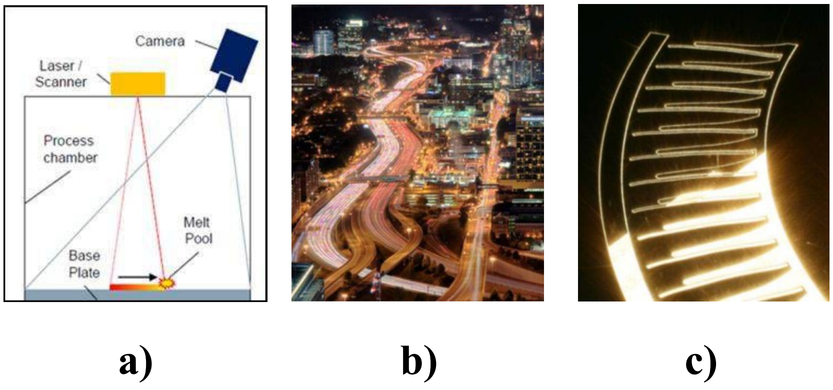

a) **b)** **c)**

Fig. 11: a) Principle of OT technique; b) Long-time exposure of traffic at night; c) long-time exposure of single layer production during L-PBF process [142].

This technique is an advanced contactless monitoring technique that captures the spatial and temporal distribution of emitted or reflected light from a laser-powder interaction zone during the LPBF process by sampling increasing the exposition time, as it is shown in Fig. 11. It uses industrial cameras, often in the near-infrared (NIR) or visible range, to monitor the entire build area or specific regions. By analyzing the captured light intensity and distribution, optical tomography can detect process signatures and, one of its main advantages lies in providing layer-by-layer insight into process stability and part quality without interrupting the manufacturing process. Furthermore, the OT provides a valid means to extract the 3D geometry of the part by only using a single camera, reducing high computational time compared with 3D reconstruction monitoring systems discussed above. Bamberg et al. [142] proposed the first OT approach as an in-situ process monitoring system. They showed how this method was possible to detect size and location of defects, due to induced lack of fusion, and part geometry in-process. They also proved that by combining statistical evaluation with the output images obtained from the camera it was possible to apply OT as reliable in-situ monitoring system for L-PBF. More recently, Guerra et al. [33] proposed a refined OT approach, named High Resolution Optical Tomography (HR-OT). The setup utilized a single off-axis high-resolution camera and a specialized lens configuration capable of achieving a resolution of 26 μm/pixel over a field of view of approximately 160 × 105 mm. This setup allowed the entire working area to be monitored with better detail, outperforming typical configurations found in the literature. Results showed that HR-OT effectively captured the onset of deformations and offered a robust overlap with data from post-process photogrammetric 2D/3D analyses, validating the system's accuracy. While in previous work [142] the OT was used for detecting volumetric defects like lack of fusion and keyhole porosity, this study demonstrated the technique's potential for monitoring geometric distortions, caused by overhanging surfaces. Additionally, HR-OT high resolution and field of view reduced the computational burden often associated with 3D reconstruction systems, offering a more efficient solution for real-time monitoring.

3.2.4. ***Research gaps: Lattice structures monitoring methods***

Despite the big extend of monitoring systems and techniques discussed so far in literature, lattice structures, due to their complex geometry and small feature details, present significant challenges for in-process monitoring in Additive Manufacturing (AM). Lightweight structures printed by L-PBF are highly prone to defect occurrence because of several factors. First of all, the fine dimensions of their struts result in a very small thermal mass, which means they rapidly heat up and cool down. These rapid thermal cycles can lead to high thermal gradients and, as consequence, residual stresses, increasing the possibility for incomplete fusion or residual porosity. Moreover, their complex geometries, featuring numerous overhanging surfaces, make it challenging to achieve uniform energy distribution during laser exposure. These inconsistencies can often result in lack of melting in some regions, balling phenomena and microstructural inhomogeneities. Furthermore, the powder bed itself provide less effective heat conduction compared to a solid substrate, making the cooling process more complicated. The combination of these contribute to the high defect susceptibility of lattice structures in L-PBF processes.

Traditional methods such as X-ray computed tomography (XCT), optical microscopy, and Scanning Electron Microscopy (SEM) have been used for post-process defect detection, focusing on dimensional accuracy, surface quality, and porosity [143]. Among these, XCT has proven to be the most effective for assessing both external and internal defects within lattice structures [14] without compromising part integrity. Several studies have focused on using XCT for analyzing lattice structures. For instance, Lozanovsky et al. [47] analyzed the geometrical and internal properties of a Face-centered cubic (FCC) lattice structure through X-ray microcomputed tomography (μCT) cross-sectional images. They used a custom tool capable of classifying the nodal geometry and its relative defects, providing valuable insights into the structural integrity of lattice designs. Jost et al. [48] used XCT to study the evolution of global and local deformation during a compression test of an Octet-Truss (OCT) lattice structure, which helped them better understand the failure mechanisms occurring during a loading process. Colosimo et al. [44] proposed a novel methodology for statistical quality monitoring of lattice structures, detecting out-of-control geometrical distortions by analyzing local variations within the part. While their approach was useful for in-situ monitoring data analysis, it still relied on XCT for data acquisition. A big limitation is that XCT is costly, time-consuming, and offline, making it impractical for real-time monitoring during the manufacturing process. This limitation is particularly problematic in AM, where process defects, which are very likely to occur, especially when complex geometries characterized by several overhanging walls such as lattice structure, can lead to material and energy waste, delays during production phases, and cost inefficiencies because the process is not optimized.

With the increasing adoption of L-PBF for lattice structure fabrication, there has been a growing need for in-process monitoring systems capable of detecting geometric and dimensional inaccuracies as they occur. Current research on lattice structure monitoring has highlighted the necessity of real-time defect detection, particularly for complex geometries such as strut diameter, inclination angle, and axis waviness, which significantly impact the mechanical properties of the structures [45]. To cope with this lack of reliable in-situ monitoring systems, in this thesis, research activities trying to address and propose a robust and reliable solution to this need were done and will be discussed in detail in chapter 5, by exploiting and improving a promising HR-OT monitoring system.

3.3. L-DED Monitoring

L-DED is an interesting AM technique that provides significant advantages in terms of material utilization and production flexibility. One of the key advantages lies in its ability to create dense, high-quality deposition layers with minimal dilution between the substrate and the deposited material, which ensures robust bonding and good structural integrity, even in complex geometries. L-DED is particularly effective for working with a wide range of materials, such as metal alloys and composites, allowing for tailored solutions to meet custom mechanical and chemical feature requirements. Moreover, the technology is highly adaptable in different applications, like coating, repairing and rapid prototyping of large components, making L-DED suitable for aerospace, automotive and biomedical industries, where high material efficiency, performance and customization are required.

Unlike L-PBF, which is characterized by a highly localized and transient melt pool, L-DED employs a larger melt pool and slower movement speeds, facilitating different monitoring approaches [29,144]. Additionally, the coaxial powder feed system in L-DED introduces complexities such as powder-flow interaction, necessitating specialized monitoring methods [144] and the space available to mount monitoring setup is usually bigger compared to the other two considered AM technologies. Monitoring in L-DED, same as already discussed for MEX and L-PBF, plays a crucial role in ensuring part quality, process stability and defect detection and prevention. Unlike MEX and L-PBF monitoring, which primarily focus on acoustic/vibrating, thermal and optical signals, L-DED monitoring encompasses a broader range of signal categories. These include X-ray signals for subsurface defect characterization, plasma spectral analysis for material composition and process dynamics, acoustic emission waves for crack detection, thermal data for temperature distributions, and optical systems for morphological measurements and real time control. For this reason, the discussion on monitoring methods for L-DED will be structured around these five categories of signals. This approach aims to highlight the advancements in each area while addressing the challenges posed by L-DED process, thus providing an overview of in-situ monitoring systems and presenting research gaps left open from the current literature.

3.3.1. *X-ray monitoring methods*

X-ray imaging is an advanced and effective technique for in-situ monitoring of L-DED processes. It provides critical insights into the internal structure of materials and the dynamics of defect formation [145]. When a polychromatic X-ray beam passes through the part under inspection, a scintillator converts the beam into visible light, which is captured by a high-speed camera to generate detailed visualizations. This enables real-time analysis of melt pool behavior, powder flow, and defect evolution [146,147]. For instance, Wolff et al. utilized two X-ray imaging monitoring setups [145,148] to investigate the effects of different powder flow rates on melt pool fluctuations and porosity. Their experiments revealed that lower powder flow rates resulted in porous structures, while higher flow rates led to more pronounced surface fluctuations on the melt pool. In subsequent work, high-speed X-ray imaging was used to classify pore-generation mechanisms, offering valuable data to inform process improvements. Lindenmeyer et al. [149] introduced an innovative monitoring approach using an edge-image template combined with Bayesian inference to automatically extract the shape and size of the melt pool. This technique mitigated the labor-intensive task of manual data analysis, though it remained susceptible to noise interference, highlighting areas for further optimization. Chen et al. [150] employed synchrotron X-ray-based monitoring technique to examine how laser power, powder feed rate, and scanning speed influence melt pool morphology in titanium alloy deposition. Their monitoring method was also able to capture information such as powder sintering and pore formation. Same authors in a different work [151] involved quantifying key deposition features using X-ray diffraction, enabling the isolation of melt pool temperature gradients and phase transition sequences, thereby providing deeper insight into the stress states of L-DED deposited layers.

X-ray-based monitoring continues to gain traction due to its unmatched ability to visualize internal defects and capture real-time kinetic interactions in the deposition process, fostering a deeper understanding of the process and supporting the development of more reliable and efficient manufacturing solutions. Furthermore, alongside imaging, other X-ray techniques, such as X-ray diffraction and Small-Angle X-ray Scattering (SAXS), have been applied to study solidification kinetics and precipitation behavior during L-DED [152]. While these methods show significant results for online monitoring, their implementation is hindered by the high cost and complexity of equipment, and strict safety requirements associated with X-ray systems. Custom-designed setups are often necessary to integrate X-ray monitoring effectively into L-DED.

3.3.2. *Plasma spectral monitoring methods*

Plasma spectral monitoring is an advanced technique for in-situ analysis of L-DED processes. This approach leverages the emission of plasma generated during laser-material interactions to gather critical information about the material composition at an atomic level, melt pool dynamics, and defect formation. Plasma spectral signals, characteristic of the atomic species and excitation states, offer low dependance on background noise compared to image- and temperature-based monitoring methods [153,154] and can provide rich physical data at the atomic level alongside high degree of versatility and adaptability [155,156].

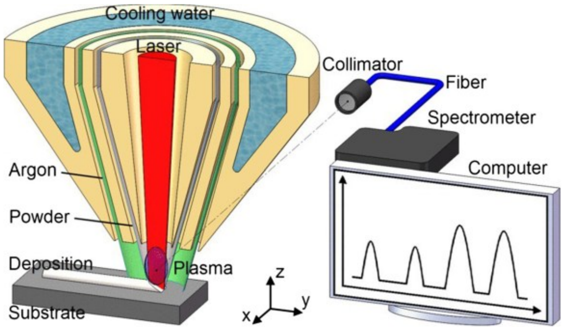

Fig. 12: Diagram of the detection of laser-induced plasma.[157]

Two primary sensors are commonly used in plasma spectral monitoring for L-DED: photodiodes and spectrometers, with an example of the set up showed in Fig. 12. Photodiodes, known for their fast response times and simplicity, are often used to monitor the intensity of light signals emitted from the melt pool. For instance, Miyagi et al. [158] employed photodiodes integrated within the laser head to measure the intensities of thermal radiation, plume emissions, and laser reflections. By correlating these intensities with process parameters such as laser power and melt pool width, a feedback control system for thermal radiation was established. Similarly, Lin et al. [159] and Bi et al. [160,161] utilized photodiodes to monitor thermal radiation energy, establishing its relationship with melt pool temperature. Spectrometers provide a more detailed analysis by capturing light signals across multiple wavelengths, enabling elemental composition characterization. Spectrometers have been used to propose a novel monitoring methodology for L-DED, named Laser-Induced Breakdown Spectroscopy (LIBS), which is one of the most widely used. LIBS has gained prominence for its ability to perform contactless, real-time analysis of plasma. Lednev et al., in two subsequent works [162,163], developed a LIBS-based monitoring system mounted off-axis to analyze melt pool plasma, distinguishing between optimal and defective depositions through spectral intensity differences. These findings underscored the technique's ability to identify defects such as cracks and pores in real time. However, the system required offline calibration, and its application to processes like L-PBF was constrained by challenges due to the limited space inside the building volume. Ni et al. [164] used LIBS to study the spectral intensity of aluminum ions during high-entropy alloy deposition under varying scanning speeds. Their results demonstrated that spectral intensity could effectively represent the depth of the deposition layer, highlighting LIBS's potential for process optimization in L-DED. Sdvizhenskii et al. [165] extended this methodology by focusing on the metal powder flow instead of the melt pool, reducing interference from blackbody radiation and laser reflections. However, their study revealed that the heterogeneous powder density necessitated continuous optimization of LIBS sampling points through two-dimensional mapping.

Another promising technique is Optical Emission Spectroscopy (OES), which offers higher spectral resolution than LIBS and allows for the analysis of subtle changes in material composition at greater depth than LIBS. However, OES generates large volumes of data, complicating the extraction and categorization of meaningful information [166,167]. Wang et al. [168] addressed these challenges by developing calibration models for spectral line intensity ratios to compensate for deviation caused by vapor pressure variations during the metal powder deposition for the L-DED process, which was studied in [169]. Similarly, De Baere et al. [170] confirmed the absence of detectable plasma information under low energy conditions, emphasizing the need for adequate laser power in plasma spectroscopy for reliable online monitoring systems for L-DED processes. Song et al. [157] developed a monitoring system using a support vector regression (SVR) model to predict elemental concentrations based on spectral intensity ratios and integral features. Their experiment demonstrated that high-dimensional features provided better prediction accuracy, particularly in low-concentration regions, compared to simpler models.

Overall, plasma spectral monitoring offers significant advantages for L-DED, providing detailed insights into elemental composition and melt pool behavior while enabling the detection of defects and process inconsistencies. As research continues, improvements in data processing and equipment design are expected to enhance the feasibility and reliability of this technology for real-time quality control in L-DED. Despite its potential, plasma spectral monitoring in L-DED faces challenges, including the high cost and complexity of the required equipment. Additionally, variations in vapor pressure above the melt pool can cause deviations in measured elemental compositions, necessitating calibration models such as those developed by Wang et al. to improve accuracy [169]. These calibration efforts are critical for addressing errors in low-concentration regions and for expanding the applicability of spectral monitoring to advanced alloys and refractory materials [170].

3.3.3. *Acoustic emission monitoring methods*

Acoustic Emission (AE) monitoring is a well-established technique used to assess material behavior, defect formation and machine state, as already discussed in 3.1.1 and 3.2.1. Also, for L-DED processes, AE sensors have been used to propose monitoring systems and methodologies, which will be analyzed in this paragraph. By detecting minute acoustic wave signals generated by the material under stress, temperature or pressure [76], AE monitoring methods proved valuable insight into the internal features of the printed part. These signals, which are generated by events such as cracking, pore formation, material deformation and defective machine states [171–173], are captured using highly sensitive contact [174] or contactless [175] sensors. Contact sensors, typically more affordable, are mounted directly on the substrate or on the uppermost surface of the part to measure acoustic signals. However, their usage in high-temperature processes, as happens for L-PBF or L-DED, requires additional cooling systems, such as waveguide rods or water circulation. Contactless sensors, such as laser vibrometer and optical microphones, offer NDT but are more expensive and sensitive to environmental conditions than contact-based sensors. Gracia de la Yedra et al. [175] used a laser vibrometer and an optical microphone to monitor layer cracking caused by thermal stress and heat-affected zone (HAZ) cracking. Their approach validated crack analysis using normalized acoustic energy images and identified correlations between cracks, coating area, thickness and cooling rates. Strantza et al. [176] focused on AE-based crack extension monitoring method, by linking AE parameters, such as amplitude and duration, to the location of the crack formation. Gaja et al., in subsequent works [171,172] collected AE signals during mixed-metal powder deposition process and differentiated between signals generated by pores and cracking, by using ML models like K-Means clustering algorithms, further validating the utility of AE monitoring for defect diagnosis [174]. Li et al., in multiple works [173,177] explored the relationship between process and parameters and AE signals, constructing a deep learning model named SRCD to detect crack defects with an accuracy of 99.76%. Additionally, using the t-SNE algorithm, they optimized both time and frequency domain, achieving classification accuracy above 89% under different process parameters. Whiting et al. [178] developed a powder mass flow monitoring system by integrating a contactless AE sensor into the powder feed line. Their system demonstrated a strong correlation (0.985) between AE signals and powder flow rates, emphasizing the versatility of AE monitoring systems process stability characterization.

In summary, AE monitoring proved to be a powerful tool also for L-DED in-situ real time monitoring and detecting defects like cracks and pores, especially if ML algorithms are used. However, the weak nature of AE signals requires a highly sensitive and often costly setup for reliable acquisitions. Environmental noise and interference can also compromise signals accuracy, particularly for contactless sensors. Furthermore, contact sensors face challenges in adapting to the high-temperature conditions of L-DED processes, necessitating complex cooling mechanisms that add system complexity and cost [173–175].

3.3.4. ***Thermal monitoring methods***

Thermal monitoring is a critical aspect of Laser-Directed Energy Deposition (L-DED) processes, where high temperatures and complex heat exchange phenomena occur during the interaction between the laser and powder. For instance, the melt pool is created after the interaction of the laser beam with the metal power in a localized area [179]. These thermal dynamics are necessary to understand melt pool behavior, material bonding, and defect formation, like the thermal monitoring methods observed in L-PBF. Effective thermal monitoring provides insights into temperature distribution, cooling rates, and microstructural changes, which are essential for ensuring part quality and process consistency.

To perform thermal monitoring for L-DED, as already discussed in 3.2.2, several sensors are commonly used for thermal monitoring in L-DED, each offering unique capabilities. Contact-based sensors, such as thermocouples, are often used to measure substrate temperature but are unsuitable for directly monitoring melt pools due to their limited temperature range and slower response times [180]. These are well suited for capturing thermal history over long periods but are less effective for high gradient, dynamic melt pool monitoring. For instance, Thawari et al. [181,182] used type K thermocouples and laser displacement sensors to monitor substrate temperature and deflection during clad deposition. Their studies revealed that substrate fixation methods significantly impacted deflection and temperature gradients, with preheating substrates improving thermal gradients and deposition performance. However, their analysis lacked validation of the mechanical properties of the deposition layers. Contactless sensors, including pyrometers and IR thermography cameras, are preferred for in-situ monitoring the high-temperature, dynamic melt pool. These devices measure temperature based on one or more infrared radiation wavelength and can provide detailed spatial and temporal data on temperature distributions of the surface [183,184]. Muvvala et al. [185,186] recorded thermal cycling during L-DED using a single-spot, monochromatic pyrometer. They examined the effects of scanning speed and laser power on cooling rates and melt pool behavior. Their findings demonstrated that slower cooling rates, induced by lower scanning speeds, led to the decomposition of TiC and the formation of brittle structures with poor wear resistance. The study also explored different laser waveforms, showing that modulated power signals could refine particle coatings and improve material properties.

IR cameras are divided into two main types: photon detectors, which directly convert IR photons into electrical signals, and thermal detectors, which absorb heat to generate electrical signals. Photon detectors offer higher sensitivity and frame rates but require advanced cooling techniques, like cryogenic cycles, making them very expensive. Thermal detectors, even if less sensitive, are generally sufficient for monitoring the high temperature variations characteristic of metal AM processes. Bi et al. [161] investigated the relationship between temperature signals and the main process parameters, including laser power, powder feed rate, and scanning speed. Their results showed a strong correlation between temperature distribution and dilution, indicating that in-situ temperature monitoring could directly reflect powder-matrix bonding and influence part properties, in accordance with what found in [187]. Doubenskaia et al. [188] measured brightness temperature in the melt pool using infrared thermography, applying the gray-body assumption to determine true temperature distributions. Their results revealed that increasing laser power expanded the heat-affected zone (HAZ) and track width, emphasizing the role of thermal monitoring in optimizing laser parameters for uniform deposition.

Thermal monitoring remains a fundamental tool for understanding and controlling L-DED processes. Continued research into advanced sensing technologies and hybrid monitoring methodologies is essential for addressing current limitations and enhancing the precision and reproducibility of additive manufacturing. Recent advancements in senor fusion monitoring systems have combined thermal imaging with other sensing techniques to overcome these challenges. For instance, Xu et al. [189] developed a multi-source image monitoring system integrating infrared thermography and high-speed cameras. By extracting complementary features from both sensors, they achieved a classification accuracy of 99.5% for melt pool and splash characteristics, demonstrating the potential of integrated thermal monitoring systems in improving process reliability and defect detection. Other examples were proposed and discussed by Tang et al. [190] and Song et al. [191,192] that introduced advanced monitoring and control systems to enhance the accuracy of L-DED processes based on sensor fusion. Tang et al. [190] developed a layer-to-layer control strategy, while Song et al. proposed a multi-source hybrid monitoring system that integrated temperature data from cameras. Both approaches demonstrated significant improvements in the dimensional precision of printed parts. However, despite their advantages, thermal monitoring techniques face limitations mostly related to emissivity. Pyrometers provide high response rates but lack the ability to visually characterize internal defects, and single-input-single-output (SISO) systems relying solely on temperature data struggle to ensure consistent track morphology across multiple layers. Cameras, while offering visual process information, are sensitive to environmental noise, reflections, plasma arcs, and powder flashes, which can affect image quality and data accuracy [193,194]. Indeed, the emissivity of a surface, which affects the accuracy of temperature readings, varies with temperature and material state. In L-DED where temperatures can fluctuate dramatically, assuming a constant emissivity can introduce errors. For this reason, calibration techniques, such as correlating emissivity at know solid temperatures, are often employed to improve accuracy, but introducing complexity into the thermal monitoring system [195].

3.3.5. *Optical monitoring methods*

Optical monitoring methods are paramount in L-DED monitoring because of their contactless nature and ability to capture high-resolution data about melt pool, clad geometry and surface conditions [196]. These methods are supposed to ensure part quality and process control by providing real-time feedback during manufacturing. Unlike other monitoring approaches, optical systems can simultaneously offer detailed spatial and temporal information, making them particularly well-suited for the dynamic and high-temperature environment of L-DED. This section focuses on optical monitoring techniques, categorized into coaxial and off-axis-based methods. The main sensors used for optical monitoring are charge-coupled device (CCD) and complementary metal oxide semiconductor (CMOS) cameras [197]. CCD cameras use a photosensitive element to convert visible light into an electrical signal, which is further converted into a digital image signal by an A/D converter; CMOS cameras use each pixel unit on the image sensor and internal integrated circuits to convert the signal, and are more highly integrated than CCD cameras, with lower power consumption and cost, but are usually less sensitive than CCD cameras. These sensors are used to develop optical monitoring systems both coaxial and off-axis.

Coaxial monitoring setups have been studied in L-DED due to their ability to capture detailed information about the melt pool and its surroundings. In these configurations, the optical axis of the monitoring system coincides with the laser beam path, allowing light reflected from the surface to be redirect through semi-transparent mirrors or filter-mirror combinations to the optical sensor [100]. This setup ensures precise alignment with the process zone, enabling localized, high-resolution monitoring of critical parameters such as melt pool size, shape and dynamics. Moralejo et al. [198] employed a coaxial CMOS camera to monitor the melt pool size, with the captured data calibrated and processed to extract dimensional features. These features were then used as control parameters for a feedforward controller, optimizing laser power to mitigate issues such as excessive dilution caused by thermal accumulation. Similarly, Hofman et al. [199,200] explored the correlation between melt pool width and dilution rate, using a CMOS camera to fit the melt pool shape as an ellipse. This data was integrated into a feedback control loop, using melt pool width as a control parameter to ensure process stability. However, as melt pools often deviate from standard elliptical shapes, Lei et al. [201] improved dimension extraction accuracy by employing a region-based active contour method to identify melt pool boundaries more precisely. In another study, Colodròn et al [196] developed a system for measuring melt pool width using a field programmable gate array (FPGA). This system significantly enhanced processing speed, nearly then times faster than traditional PC-based methods, without compromising performance. Additionally, Sampson et al. [202] introduced an adaptive exposure technique for coaxial CMOS cameras to reveal true edge features of the melt pool, subsequently designing an innovative edge detection algorithm that was independent of material emissivity, further improving detection accuracy. While coaxial configurations offer several advantages, including precise alignment with the process zone, they also present limitations. One significant constraint is the method of light direction through mirrors and filter-mirror combinations that exclude certain wavelengths. Even if this is beneficial in terms of optical sensors protection, it could affect the sensor's measurement [100]. Another notable limitation is the constrained field of view inherent to coaxial setups. These systems typically monitor a small region surrounding the process zone, which varies depending on the machine design, working distance, and nozzle aperture. While this localized focus is effective for tracking melt pool dynamics, it is less suited for monitoring the quality of entire build layers, such as identifying powder spreading inconsistencies. However, the localized nature of the captured images simplifies the recordings and localization of defects during production, ensuring precise identification and correction when defects occur [100]. These limitations highlight the trade-off in using coaxial systems, emphasizing the need for off-axial mounting systems.

Off-axis optical monitoring systems, where cameras are positioned at angles relative to the process zone, provide broader views and more comprehensive layer-wise information compared to coaxial setups. Monocular systems encompass challenges related to the resulting images due to perspective distortions and focal inconsistencies because of the wider field of view (FOV) compared to coaxial systems. Moreover, off-axis systems suffer from blind spot caused by obstruction such as the already deposited track. In this context, single-camera monitoring systems for L-DED usually mount the camera directly on the head of the machine. This way it is possible to avoid obstruction problems and make the perspective correction and image undistortion easier to implement. An example can be found in the work from Zhou [10] et al., which developed a single-camera system mounted on a moving head with an integrated height control mechanism. This setup maintained a consistent standoff distance between the nozzle and substrate, improving geometric accuracy. However, its application was limited to 2D thin-wall geometries, with height compensation applied only every two layers, restricting its effectiveness for complex 3D structures. To address the limitations of single-camera systems, multi-camera setups are often employed. For example, Hsu et al. [203] utilized a trinocular CCD camera arrangement to monitor melt pool height and deposition boundaries from an overhead angle. By incorporating a calibration bar, the system compensated for FOV effects and see-through phenomena, achieving a deviation of only 2.3% and significantly reducing costs. Multi-camera setups can also be used to generate valuable three-dimensional in-situ monitoring techniques about the melt pool and the surrounding areas. Mazzarisi et al. [204] used a three-camera system to monitor the spatial evolution of the melt pool and generate 3D point clouds for each layer. While highly accurate, this approach required substantial computational resources, limiting its practicality for real-time monitoring and control. In addition to multi-camera setups, Donadello et al. [205] employed a triangulation method for melt pool height measurement on a modified coaxial device, achieving sub-millimeter accuracy suitable for closed-loop control systems. This method offered a balance between sensitivity and practical application. Other optical sensors based on 3D reconstruction have been used for off-axis monitoring such as structured light scanner combined with a coaxial camera [206,207] to obtain 3D height profile of the clad, while laser profilometer have been widely explored because of their good ability to measure geometric features directly on high-temperature metal parts, their ease of use and mounting on the laser head. These profilometers enable detailed point cloud acquisition of layer geometry, allowing for advanced dimensional corrections and in-situ monitoring techniques. Xu et al. [173] proposed a laser line scanning system integrated into a robotic LAAM (Laser Aided Additive Manufacturing) system for in-process dimensional corrections. This method relied on 3D point cloud acquisition to detect deviations in layer geometry and adapt the deposition tool path accordingly. Unlike traditional CAD-based correction methods, this system directly used point cloud data, bypassing computationally expensive CAD reconstructions. Their results demonstrated a significant improvement in dimensional accuracy, with errors reduced by over 80%, showcasing the efficiency of point cloud-based adaptive corrections. However, sensitivity to surface conditions and environmental factors like powder adherence and light reflectivity were noted as limitations. Chen et al. [173] extended the application of laser line scanning by combining it with in-situ point cloud processing and machine learning techniques to identify surface defects during L-DED. Their setup used a laser line scanner mounted on the laser head to acquire high-resolution 3D point clouds of the part's surface in real-time. Defects such as under-fill and over-fill were identified using feature extraction algorithms, which were further refined through machine learning models for rapid defect classification. While the system demonstrated high accuracy and robustness, its computational requirements and dependence on effective point cloud filtering were highlighted as key challenges. Jeon et al. [173] integrated a laser line scanner into a L-DED system with an IR camera to monitor the geometry of the melt pool and deposited layers. These inputs were used to train an artificial neural network (ANN) to estimate the melt pool depth in real time with high accuracy. Despite its potential, the system faced challenges such as an 8-second delay between laser scanning and thermal imaging due to spatial offset, which could be minimized with improved sensor placement. Binega et al. [173] employed a similar laser line scanning setup to monitor and correct surface geometry deviations in real time. Their study focused on integrating the scanning system into a feedback loop that dynamically adjusted deposition parameters to ensure uniform layer geometry. This approach not only enhanced dimensional accuracy but also minimized material wastage. However, limitations included sensitivity to environmental conditions and alignment precision between the scanner and the deposition zone.

Off-axis systems discussed so far provide significant advantages in reducing measurement errors and enabling broader monitoring and control capabilities. However, their effectiveness depends on careful calibration and the development of robust image processing algorithms to ensure reliability in diverse and complex L-DED scenarios. Indeed, these monitoring systems face challenges in image processing due to the complexity of the L-DED process and the dynamics of the process signatures. Techniques such as image filtering, threshold segmentation, and edge detection are commonly applied to enhance melt pool contour extraction. However, these methods often rely on manual tuning or fixed algorithms, which can struggle in adapting to complex scenario.

3.3.6. *Research gaps: real-time complex geometry height monitoring*

In this described scenario of monitoring systems for L-DED, it was demonstrated that plenty of different techniques, relying on different sensors and algorithms, have been exploited. ML approaches have been increasingly proposed in order to develop closed-loop systems able to adjust some of the several process parameters in real-time during the powder deposition. Furthermore, it arose from some studies that real-time closed loop monitoring system, because of the high computational time, cannot perform the printing parameters correction every layer, but they work with certain intervals, as in the case of [10] where the control is executed every two layers. From here, it emerges the need to have monitoring systems fast enough to measure the process signature every layer and capable of correcting defects when they are detected from the detection algorithm. To speed up the computation time, many different ML approaches have been proposed. Typically, these in-situ real-time monitoring systems exploit inputs from optical sensors, which are processed by computer vision algorithms to isolate the process signature before being sent to the neural network. The quantity that is measured more often is the clad because it can be easily related with both defect occurrence and process parameters. Then, the decision whether the measured value is satisfying or not is completely left to the ML algorithm and the monitoring is executed.

Despite many working systems have been proposed, a big limitation consists of the geometry that these systems can effectively monitor. Usually, the part under examination is restricted to 2D-single direction thin wall geometry but these are far from real L-DED applications produced parts where complex and multi-directional geometries are typically required. The challenge lies in developing a fast and robust monitoring system, based on simple image processing algorithms, that can measure clad height and detect and correct defects in real-time when relevant industrial shapes are produced.

4. MEX metrology and monitoring based on a blue laser line profilometer

Following the discussion started in 3.1.4, the need for improving the metrology related to MEX processes, because of the lack of robust, standardized, and reliable metrics for evaluating part quality during production, combined with the necessity of expanding the literature about functional analysis-based monitoring systems led the research activities of this thesis to exploit a laser line scanner as monitoring sensor. A key issue is the absence of universally recognized process signatures that could serve as benchmarks for quality assessment and corrective actions. Furthermore, while functional analysis has shown promising results in evaluating surface morphology and defect topology in AM, its integration as in-situ monitoring technique remains largely unexplored. The MEX-related activities will be explained by illustrating the proposed setup and the metrology indexes used as quality indicator. After introducing the indexes, a preliminary test of the monitoring methods based on these indexes will be discussed to prove their effectiveness. Two experiments were conducted. After explaining the methodology, the results will be discussed for both experiments.

4.1. Laser line scanner

The system is based on the MicroEpsilon scanControl 2900–50 BL (Fig. 14), a high-resolution blue laser line profilometer (BLP) designed for precise, non-contact surface measurement. This sensor operates on the principle of laser triangulation [208], projecting a laser line onto the object's surface while a CCD sensor detects the reflected light to reconstruct the surface profile. The projection of the laser onto the surface is recorded and the X and Z coordinates of the point belonging to the line are gathered and a profile is generated. By adding a movement to the sensor along the Y direction and knowing the scan speed, it is possible to stack multiple profiles to achieve a 3D point cloud of the measured surface. Lately, triangulation sensors have been widely used as in-situ measurement instruments to measure complex geometries [209].

The blue laser line features are shown in Table 2. The scanning parameters have been selected after testing various combinations. In general, the primary requirement that they had to respect was that the exposure time had to be short enough to enable fast layer surfaces measurements, ensuring feasibility for future real-time applications. Consequently, the other parameters were adjusted and optimized leading to the current configuration. The profilometer outputs profiles via an Ethernet connection (UDP/Modbus TCP), allowing for rapid data exchange and real-time control. While the sensor is limited in capturing overhang and vertical walls, its high resolution and advanced capabilities make it particularly effective for monitoring horizontal cross-sections, such as those encountered in AM processes. Furthermore, usually, laser line sensors use red-light lasers but in this work a blue laser was employed. The blue laser technology ensures reduced influence from ambient light and minimizes material scattering, which is critical when measuring materials such as semi-transparent polymers or metals. Its versatility allows it to be used in both polymer-based and metal-based additive manufacturing processes, such as L-DED and L-PBF. Although the sensor cannot monitor overhangs and vertical walls, because of the occlusion phenomena explained in Fig. 13, it excels in measuring horizontal cross-sections with high resolution, making it an invaluable tool for detailed metrology and a solid foundation for improving measurement practices in additive manufacturing.

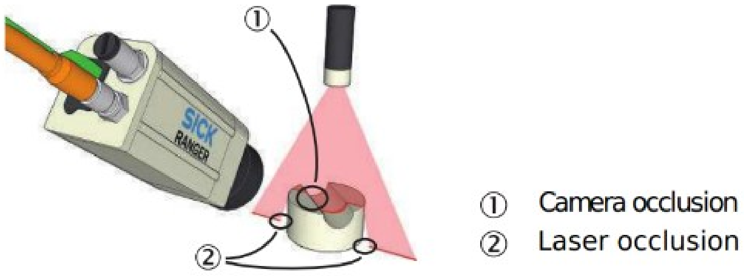

Fig. 13: Occlusion phenomena for a laser line scanner: 1) camera occlusion happens when the camera is not able to see the laser onto the surface; 2) laser occlusion occurs when the laser is not reflected into the CCD sensor.

Table 2: Blue laser line specifications.

Parameters	***Value***	***Parameters***	***Value***
Wavelength	405 nm (blue light)	**Optimal working distance**	95 mm
Measuring Range	50 mm (X,Z axis)	**Profile points**	1280 points per profile
Resolution (Z-axis)	4 µm	**Profile Frequency**	135 profile/s
Resolution (Y-axis)	39 µm	**Scanning speed**	5 mm/s
Resolution (X-axis)	37 µm	**Exposure time**	20 ms

Fig. 14: Blue laser line sensor

4.2. Monitoring setup

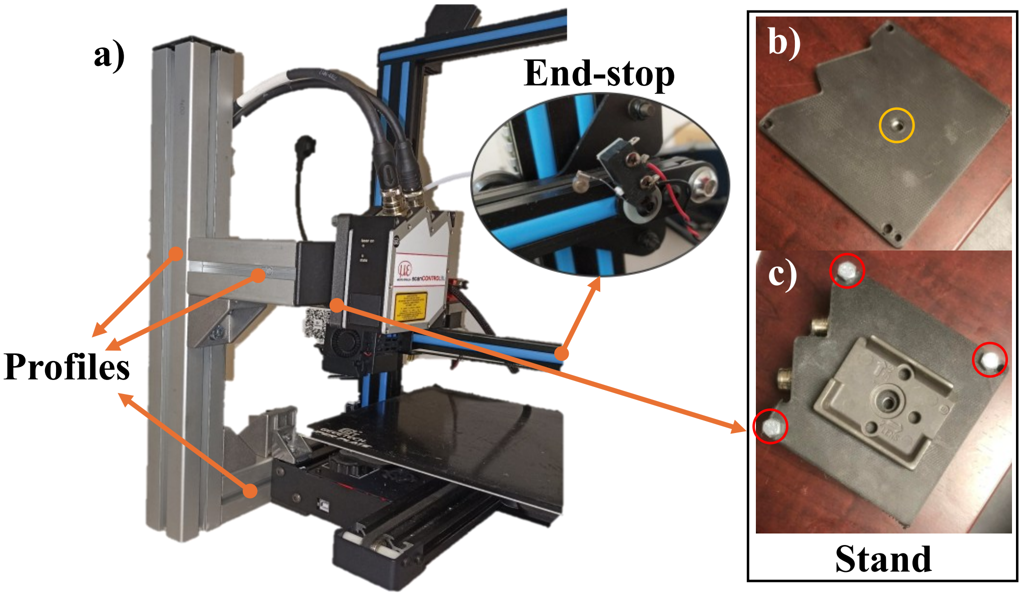

Fig. 15:a) BLP-based monitoring system setup; b) and c) show a representation of the sensor mount. The yellow circle in b) highlights the embedded nut inside the mount that will be screwed to the frame, while in c) the red circles indicates the screws used to attach the BLP to the mount.

Two MEX in-situ monitoring methodologies were conducted during the thesis [210,211] and both exploited the same setup, which was tailored to meet the specific requirements of the 3D printer. The machine used for the analysis was a Geetech A10, which is a Cartesian machine characterized by direct architecture with a building volume of 220x220x260 mm^3. The extruder moves on a gantry along the X and Z axis, while the printing bed moves along the Y direction. The heated bed can reach up to 100 °C, the extruder can reach 250 °C as maximum temperature with a nozzle diameter of 0.4 mm. From manufacturer specification, the maximum printing speed is 180 mm/s, but in the proposed experiments it was kept lower to maintain control over the printed part.

Based on the requirements and the scanning parameters emerged from the sensor, four custom features were added to the printer to create the monitoring setup.

- Tailor made adjustable structure for sensor holding and placing purpose.
- Custom mount to attach the sensors to the frame.
- End-stop switch integration into the printer to automate point cloud acquisition process.
- Optical properties of the printing bed surface optimization to simplify the scanning process.

Thanks to the architecture of the printer, it was possible to create a custom structure to support the optical sensor that was used to perform measurements. The structure was fabricated using aluminum X-cross profiles, providing a light and stable base for the integration of additional components. From Fig. 15, a it is possible to observe the profiles screwed to the printer that helped to mount the profilometer on the printing bed. Another component designed and 3D printed was the sensor mount, which is shown in Fig. 15, b and c. The mount was made by replicating the shape of the profilometer and acted as an interface between the sensor and the frame. The material used to produce this part was Onyx, which is a combination of nylon reinforced with carbon fibers, to provide high structural stability and precision alignment of the sensor, and the printer used was a Mark Two 3D printer by Markforged. Furthermore, an end-stop switch was also fixed at the end of the printer's x-axis gantry. Again, the connector to fix the switch was 3D printed in PLA and helped in correctly positioning the end-stop, as it is shown in Fig. 15, a. The end-stop was connected to the profilometer, and it was supposed to work as a mechanical scan trigger. Thus, when the circuit was closed, it triggered the sensor to acquire multiple profiles. This operation had two main goals: the first one was automating the acquisition phase at the end of each layer and aligning subsequent layer point clouds. This latter operation was guaranteed by the G-code modification that will be discussed in section 4.3. Finally, the last modification to the setup was coating the printing bed, which was a transparent glass plate. It is known that transparent surfaces are hard to scan and can generate very noisy data, making the measure not reliable, but for monitoring purposes it was important to have a correct profile of the bed alongside the layer profiles because the bed point cloud was supposed to work as the reference from where point heights are measured. The monitoring methods relied on the correct measure of height, so it turned out necessary to tape the bed sheet. An aluminum white tape was chosen to cover the surface because it is very easy to scan, providing a clean and smooth dataset as it is displayed in Fig. 16.

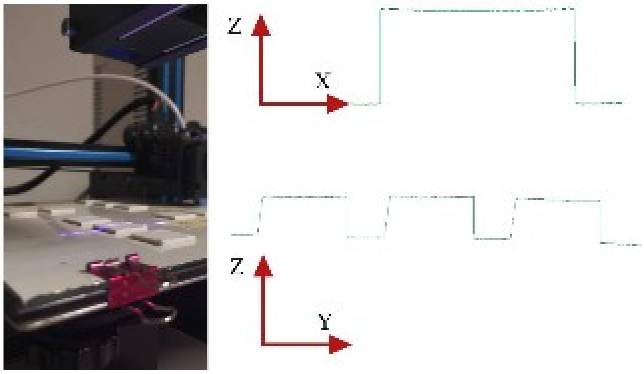

Fig. 16: 2D profile resulted from the BLP sensor after coating the printing bed with white aluminum tape.

4.3. G-code customization

G-code is the language with which 3D printers usually use to receive commands from laptops. This code type is like the code used to control conventional chip removal machines, such as turning and milling machines. This code is generated automatically after preparing the 3D model on software called slicers. These programs literally slice the 3D model in layer and generate the toolpath that the deposition system will follow to complete the process. Together with the design of the setup to mount the profilometer, the second fundamental operation done before starting the experiments was the customization of the G-code. This customization enabled the 3D point cloud acquisition phase to be consistent and independent of human intervention, thereby minimizing potential inaccuracies in the measurements. Furthermore, as explained in section 4.1, the 3D point cloud, which is the input element of the proposed monitoring methods, can be obtained only if there is a relative movement between the profilometer and the part to be scanned in the direction perpendicular to the laser line. This relative movement was added thanks to the custom G-code. Because of the setup configuration, the laser line scanner was fixed in its position, so the only way to move the object under the laser was to add a movement to the printing bed. These requirements were translated into the following g-code lines, and, subsequently, were added through a plug-in already existing in the software used to do the slicing (Ultimaker CURA):

N1 G91; relative coordinates working mode

N2 Z5; rise extruder 5 mm up

N3 G90; absolute coordinates working mode

N4 G00 Y190; moving the printing bed to its starting scanning position

N5 G00 X230; moving extruder to activate the end-stop switch and start the scanning

N6 G01 F300 Y90; moving the printing bed toward its final scanning position

N7 G91;

N8 Z-5; lowering extruder to the correct working height

N9 G90;

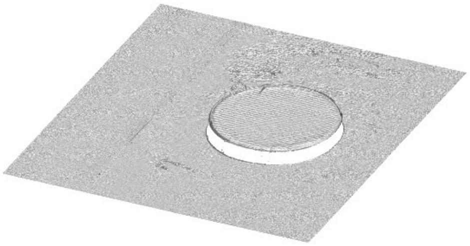

Fig. 17: 3D point cloud obtained after a layer scan.

In other words, at the end of each layer, the extruder was lifted 5 mm from its current position to avoid possible collision with the upmost surface of the printed part, and after that the printing bed was moved to its starting scanning position which was previously decided based on the location of the printed part on the bed. The extruder travelled along the X axis to activate the end-stop switch. Once the circuit was closed, the sensor began recording the video while the printing bed was moved towards its final scanning position at the speed of 300 mm/min (5 mm/s). Once finished, the extruder was brought back to its original height and the process could start again. The output after this operation was the 3D point cloud of the layer surface as it is demonstrated in Fig. 17 where the cross section of a cylindrical part with part of the printing bed were acquired.

4.4. Printer’s stepper calibration and point cloud correction factor

Before conducting the experiments, it turned out necessary to calibrate the stepper motors of the 3D printer to ensure accurate movements along the axes. This calibration was critical due to the nature of the printer, a consumer-grade device known to have declared uncertainty, from the manufacturer, on each axis of 100 microns. Consumer printers are particularly sensitive to environmental, like dust, room temperature and humidity, and mechanical disturbances, such as movements or collisions, which can cause the motors to lose steps or the printer not to work correctly. This phenomenon results in the axes moving more or less than expected or operating at speeds different from those specified. Given that the printer had to be moved and adjusted during the setup of the monitoring system, performing this calibration was essential to avoid potential inaccuracies in the experimental results. The calibration process was performed using a digital comparator and the Ultimaker Cura software, which enabled direct control of the printer's movements. Initially, the printer was connected to a computer via USB, and the movements of each axis were controlled manually and monitored through the comparator. The actual travel distance of each axis was measured using the comparator and compared with the theoretical distance commanded through the software, as explained in Fig. 18. Any discrepancies were attributed to inaccuracies in the step/mm values assigned to the stepper motors. To correct these discrepancies, the actual and theoretical measurements were used to calculate the corrected step/mm values which were then updated in the printer's firmware, following the equation (1):

$$x_{new} = x * \frac{L_{nom}}{L_{meas}} \qquad (1)$$

Where x_{new} is the corrected step/mm value, x is the initial value stored in the printer firmware, L_{nom} is the theoretical distance the axis is supposed to travel, while L_{meas} is the real distance the axis moved. Three measurements were performed for each axis to ensure reliability. It was found that the Y-axis required no adjustments, whereas the X and Z axes showed significant deviations that necessitated calibration. Corrected values are omitted because not the purpose of this thesis but, as will be demonstrated in section 4.5.5, this calibration played a fundamental role in compensating errors induced by the non-optimal machine conditions ensuring reliable, accurate and robust measurements.

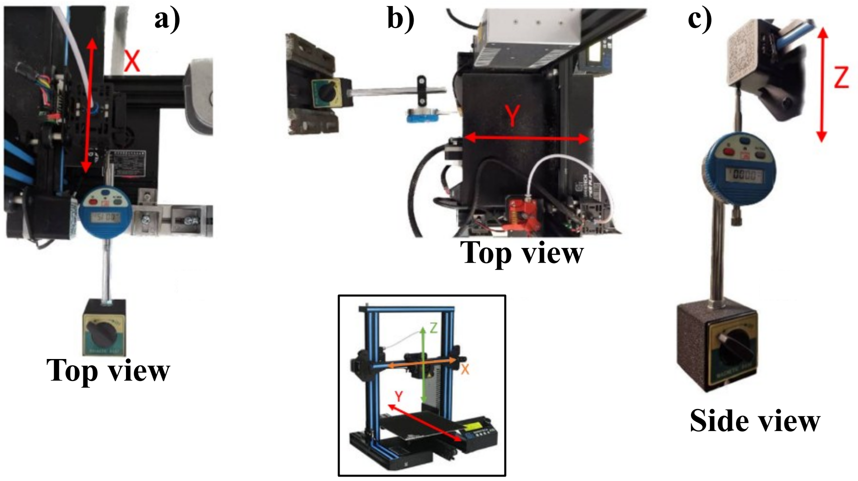

Fig. 18: a) X, b) Y and c) Z stepper Step/mm calibration method based on comparator measurements.

The aforementioned calibration procedure focused on correcting cinematic errors in distances along all three directions, but this did not address potential inaccuracies in the speed. As previously explained, the BLP requires additional movement along the scanning direction, perpendicular to the laser line, to collect 3D point clouds. To ensure accurate registration of 2D profiles, the scan speed needs to be precisely known because discrepancies between the nominal scan speed (5 mm/s) and the actual speed could introduce systematic errors into the measurements. In this case the scan speed coincides with the printing bed speed (Y-axis), which was set to 5 mm/s, thus a second calibration on the Y-axis speed accuracy was necessary.

To evaluate errors induced by imprecision in speed a different approach was applied. A proper artefact was designed by following two requirements: geometric (the geometry of the artefact should allow an easy evaluation of distances along the scanning direction, which is Y axis, to compute the correction factor *C)* and dimensional (the overall dimensions should cover the entire scanning volume). Based on these two criteria, the calibration artefact (Fig. 19) was composed by a support plate characterized by 50x70x8 mm^3 and six steel spheres (ø12 mm) placed at specific distances, and it was 3D printed by MEX using ABS white material. The six spheres were shiny and highly reflective and for this reason they were sprayed with a sublimation matting spray before executing the scanning operation both on the BLP and the structured light scanner (SL).

The calibration plate was scanned using the BLP and the structured light scanner (SL) for reference. The BLP was operated by following the scanning parameters listed in Table 2, such as a profile frequency of 135 profiles/s and a scanning speed of 5 mm/s. Instead, the reference was scanned using the SL GOM Atos Q 8M equipped with a 100MV lenses, having a measuring volume of 100x70x60 mm3 and a certified accuracy of 0.005 mm of Length Measurement Error (assessed according to the VDI/VDE 2634- Part 3).

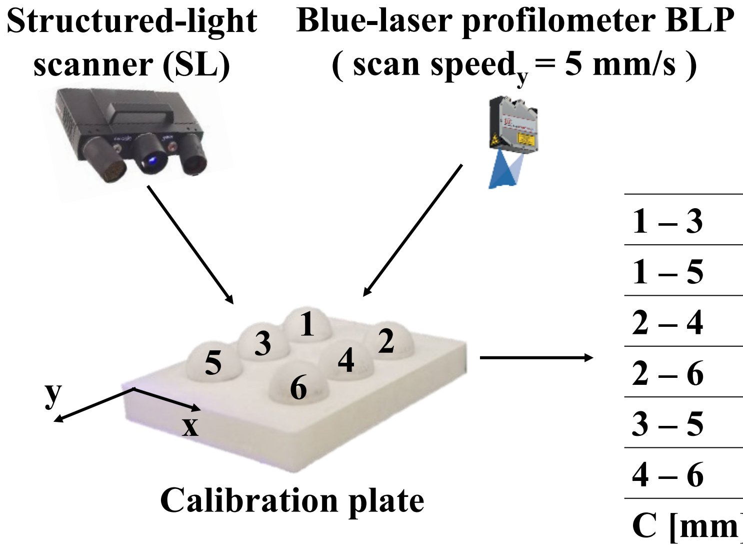

	$\Delta y_{SL,i}$ [mm]	$\Delta y_{BLP,i}$ [mm]	Dev. [mm]	C_i [mm]
1 – 3	17.38	17.18	0.20	1.011
1 – 5	34.70	34.29	0.41	1.012
2 – 4	17.34	17.15	0.19	1.011
2 – 6	34.72	34.31	0.41	1.012
3 – 5	17.33	17.11	0.22	1.013
4 – 6	17.38	17.16	0.22	1.013
C [mm]				**1.012**

Fig. 19: Calibration artefact used to compute the correction factor. The artefact was scanned both with SL and BLP and the distances between the sphere centers are reported in the table in the figure.

Once obtained the point clouds, the analysis was done using metrology software. Using the 3sigma Gaussian method, 6 spheres were fitted on each point cloud and the coordinates of their center points were extracted. Distances along the Y direction were computed and compared. The correction factor C was computed according to equations (2) and (3), and the results are shown in Fig. 19:

$$C_i = \frac{\Delta y_{SL,i}}{\Delta y_{BLP,i}} \qquad (2)$$

$$C = \frac{1}{N}\sum_{i=1}^{N} C_i \qquad (3)$$

where, $\Delta y_{BLP,i}$ was the i-th distance measured on the point cloud obtained with the BLP, while $\Delta y_{SL,i}$ was the same quantity measured on the mesh obtained from the structured light scanner, and N represents the number of the distances measured, which is six in this case. The correction factor C was found to be 1.012 and this value will be applied to all the point clouds obtained during the experiments, because the scanning parameters were kept constant.

4.5. MEX layerwise in-situ monitoring method based on quality indexes

4.5.1. *Method description.*

The main goal of the proposed in-situ monitoring method was to correctly evaluate layer-by-layer surface quality during a MEX process providing insights into current conditions of the printed part. The monitoring operation started with an initial scan by the BLP of the printing bed to establish a reference plane. The scanning operations followed the g-code discussed in paragraph 4.3. This reference plane was fitted to the build platform point cloud using the Gaussian method (3sigma criterion) and set as $z = 0$. The bed scan served two critical purposes because, first, it provided a baseline height map that served to calculate the absolute height points in subsequent later scans by simply subtracting the bed point cloud. And second, the bed fitted plane was used as the foundation for generating a series of nominal planes, each spaced along z-direction by the layer height (0.2 mm). These nominal planes were used to evaluate the overall average height of each layer and determine whether the printing process is stable. For each printed layer, the surface was scanned immediately after material deposition using the BLP. The end-stop switch was a critical component of the system, enabling automatic alignment of all point clouds. This alignment ensured that the x and y coordinates of points in subsequent layers correspond precisely to the same grid, facilitating the point clouds subtraction of the z-coordinate values to compute the absolute height of the layer points relative to the bed. The monitoring operations described above are summarized and represented in Fig. 20.

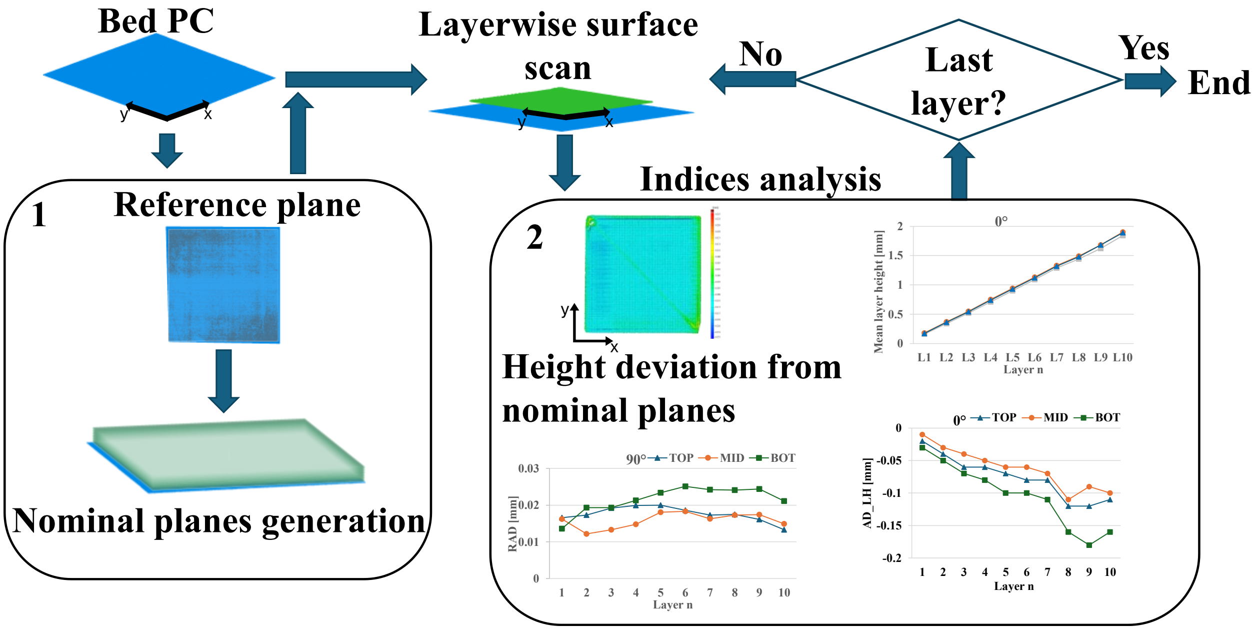

Fig. 20: Monitoring workflow

4.5.2. *Proposed quality indexes.*

The point clouds obtained from the BLP, as already explained, contains many topological information, but for monitoring purposes and future real-time application it is necessary to summarize the content of these dataset by selecting proper process indexes easier and faster to compute and to interpret. For this reason, as a preliminary study, the proposed monitoring setup and method was evaluated through the observation of four indexes, and some result examples are shown in Fig. 20 -2. The first index considered is a simple average cumulative layer height, computed as the means of the distances between the points belonging to the layer surface point cloud with their relative nominal plane. The other three proposed indexes are: Layer Height Average Deviation (**AD_{LH}**), Residual Absolute Deviation (**RAD**) and the Slope of the AD_{LH} graph ($\boldsymbol{s}$).

The AD_{LH} quantifies the deviation of the layer surface from the nominal plane, which is a parallel plane spaced by the current layer height (0.2 mm) from the reference printing bed plane. This parameter was computed as the average signed distance between all points of the layers' point cloud and the nominal plane, following the equation (4):

$$\boldsymbol{AD_{LH} = \frac{1}{N}\sum_{i=1}^{N} \pm d_i} \qquad (\mathbf{4})$$

Here, d_i represents the distance along z-direction between the i-th layer-belonging point with respect to its relative nominal plane, and N represents the number of the total points considered. These distances were kept with their sign because it is the first indicator of the type of deviation: negative sign means that the actual layer surface point lies under the nominal plane; on the other hand, a positive d_i means that the layer surface lies above the nominal plane. This index provided critical insights into the surface conditions of the printed layer, paving the basis for potential process control. The RAD was computed as the average value of the distances between each actual layer points and the plane fitted (Gaussian method, 3σ criteria), using the same points. This index allowed to emphasize the occurrence of surface defects and geometric inaccuracies with respect to dimensional issues, such as surface roughness or inconsistencies in material deposition. Finally, the stability of the process was evaluated using the slope s of the line connecting AD_{LH} values of two consecutive layers. This dimensionless index provided trends in surface quality changing across subsequent layers. Also, this index was considered with its sign, where a positive value indicated improvement in surface quality and height accuracy, and negative values indicated worsening conditions.

4.5.3. *Experimental plan.*

The experimental plan was developed using prism-shaped samples with overall dimensions of 15 × 15 × 2 mm^3, as shown in Fig. 21, a. The first step involved creating an STL file based on the CAD model of the object. This file was then imported into Ultimaker Cura, one of the most used slicing software for MEX printing. The material selected for the experiment was white PLA provided by Fabbrix®. The main printing parameters were as follows: a layer height of 0.2 mm, a nozzle temperature of 210 °C, a build plate temperature of 60 °C, solid infill (100%), and a printing speed of 40 mm/s. These are not the optimal parameters for the 3D printer used, but are parameters usually used when PLA filament is printed with a consumer 3D printer. To thoroughly evaluate the performance of the in-process monitoring system, different process conditions were intentionally introduced to create variations in surface quality and induce process deviations. These variations were achieved by altering the location of the samples on the build platform (TOP, MID and BOT) and changing the raster deposition angle (ɵ, 0°, ± 45° and 90°), following the experimental plan detailed in Fig. 21, b and c. This approach ensured that surface quality could be evaluated under a range of conditions while maintaining consistent printing parameters. A total of 12 samples were fabricated, resulting from the combination of three build platform positions (TOP, MID, and BOT, as shown in Fig. 21, b) and four raster deposition angles (ɵ = 0°, +45°, −45°, and 90°, as shown in Fig. 21, c). Each sample was then monitored on a layer-by-layer basis using the methodology described in Fig. 20. The results are discussed below.

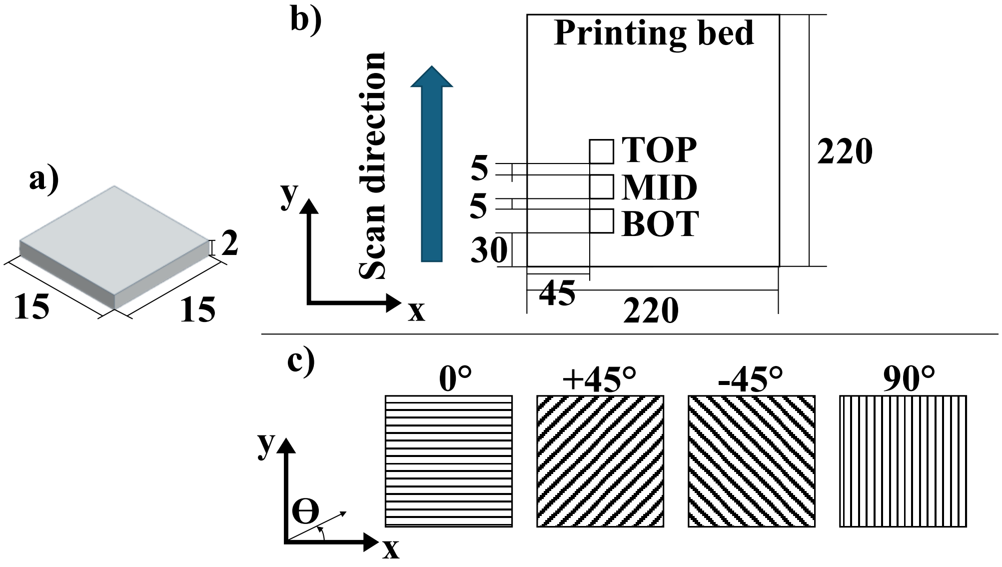

Fig. 21: a) prism-shaped specimens; b) location on the printing bed chosen for the experiment; c) raster deposition strategies.

4.5.4. ***Results.***

The analysis of the experimental results focused on evaluating the cumulative height, AD_{LH}, RAD and AD_{LH} slope *s* as monitoring tools and key indicators of surface quality and process performance. The cumulative height was calculated for each layer and sample, revealing variations influenced by both the raster deposition angle and the sample's position on the printing bed. Generally, all the specimens showed to be shorter than the nominal height, which is represented by green lines in Fig. 22. Samples positioned at the MID location generally exhibited heights closest to the nominal values (1.9–1.96 mm), while those at the TOP and BOT locations displayed greater variability and dimensional deviations, with the largest deviation observed at 1.84 mm. These results highlighted the sensitivity of cumulative height to factors such as platform flatness, Z-axis precision, and material flow rate. Notably, a pronounced deviation was observed between Layers 7 and 8 for samples with a 0° raster angle, particularly at the BOT location, suggesting the potential onset of process instabilities. In Fig. 23 the geometric deviation from the nominal plane of the layer surface is shown, it is possible to observe how this worsen in cumulative layer height is represented by darker blue color on the entire layer surface. The overall results relative to the cumulative layer height can be found in Fig. 22.

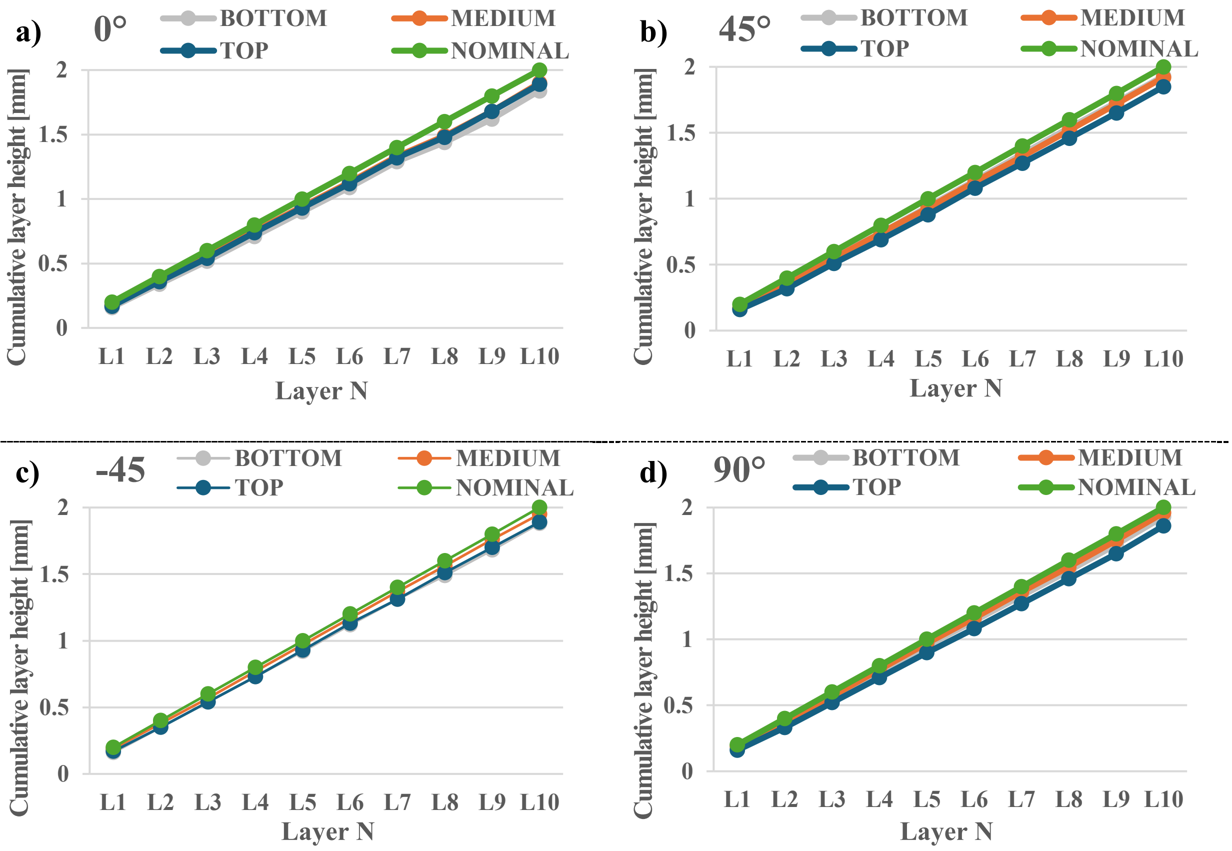

Fig. 22: Average cumulative layer height results divided by raster deposition angle: a) 0°; b) 45°; c) -45°; d) 90°. The green line indicates the nominal trend that the measure should have.

While cumulative height provided an overview of layer-by-layer growth, it was insufficient to assess surface quality or pinpoint the sources of deviation. To address this, the AD_{LH} was computed, quantifying the deviation of each layer surface from its relative nominal plane. AD_{LH} values demonstrated that the early layers consistently had the smallest deviations, while deviations tended to increase with layer number, sometimes approaching the absolute layer height (0.2 mm). Samples printed at -45°-MID and 90°-MID exhibited the most accurate heights (AD_{LH} values between 0 and 0.05 mm, as it demonstrated in Fig. 24, c and d, respectively), whereas other configurations displayed greater variability, with deviations nearing 0.2 mm in some cases. Conversely, other raster angles and position combinations displayed wider AD_{LH} ranges, with deviations nearing 0.2 mm in some cases, such as Layer 9 for samples printed at

0°-BOT. The slope of AD_{LH} across consecutive layers was also analyzed to assess process stability and values are presented in Table 3, with positive slopes indicating improvements and negative slopes signaling worsening conditions.

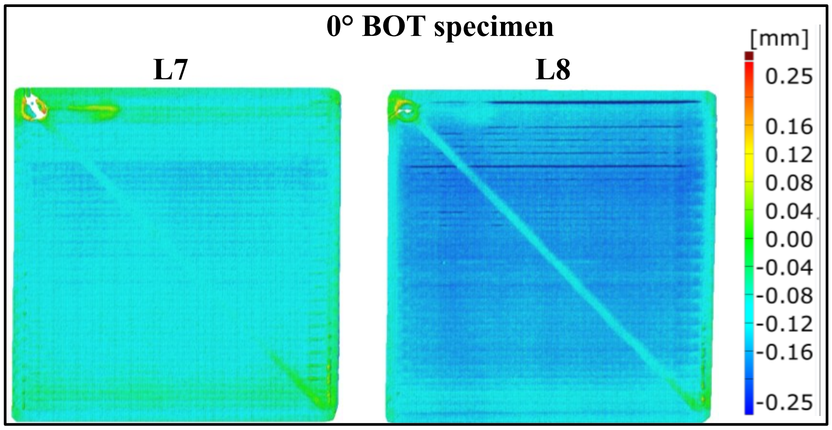

Fig. 23: Worsening of surface height related to high variation in cumulative height from layer 7 to layer 8 for the specimen printed at the BOT position with 0° raster angle.

For instance, significant slope changes were observed between Layers 7 and 8 in 0°-BOT samples, highlighting a marked process shift, in accordance with what was found by analyzing the cumulative layer height and displayed in Fig. 22. This behavior contrasted with samples such as -45°-MID and 90°-MID, which showed minimal slope variations, indicating stable printing conditions. The effect of the slope variation is clearer by looking to Fig. 25, where the most unstable case was considered, which is the specimen printed with 0° of raster angle and BOT location on the printing bed, and the layer surface condition proved that with a negative slope value can be associated to a worsening in the surface quality. A larger slope magnitude indicates greater change, which could signify a significant process shift and potentially the occurrence of defects. Negative slope values correspond to a deterioration in the AD_{LH} index, signifying worsening height accuracy, whereas positive slope values indicate improvement. When the slope is close to zero, no substantial change in the AD_{LH} is observed, suggesting stable process conditions. For reference, samples at -45°-MID and 90°-MID positions, which exhibited the smallest AD_{LH} deviations, demonstrated slope values within a range of ±0.05, which can be considered indicative of stable process conditions (see Table 3). It is important to emphasize that the slope is sensitive to changes between consecutive layers, making it a valuable tool for identifying process shifts. However, analyzing only the slope between two layers may not reveal all instances of sustained negative trends or severe height deviations. For example, samples printed at 90°-TOP and +45°-TOP exhibited persistent height deviations despite registering slope values of only 0.05 to 0.1. This highlighted the importance of examining not just individual slope values but also their signs and trends across multiple layers. In these cases, the consistent sequence of negative slope values indicated a progressive worsening of height accuracy. While the slope index effectively detects process instability, it does not provide information on the type of defect present. Therefore, it could be utilized as an early warning indicator of potential issues in the printing process. To complement the AD_{LH} analysis, the RAD index was employed to evaluate the surface quality of individual layers. Unlike AD_{LH}, which measures dimensional accuracy relative to the nominal plane, RAD reflected the geometric accuracy of the layer's surface by quantifying deviations from a fitted plane. Lower RAD values indicated smoother, more uniform surfaces, while higher values suggested the presence of surface defects, such as blobs or areas of material deficiency. The analysis of RAD values (Fig. 26) revealed a stable trend for the sample printed at -45°-MID, with values consistently between 0.01 and 0.019 mm, indicating smooth and defect-free surfaces. In contrast, other samples exhibited more variable RAD values.

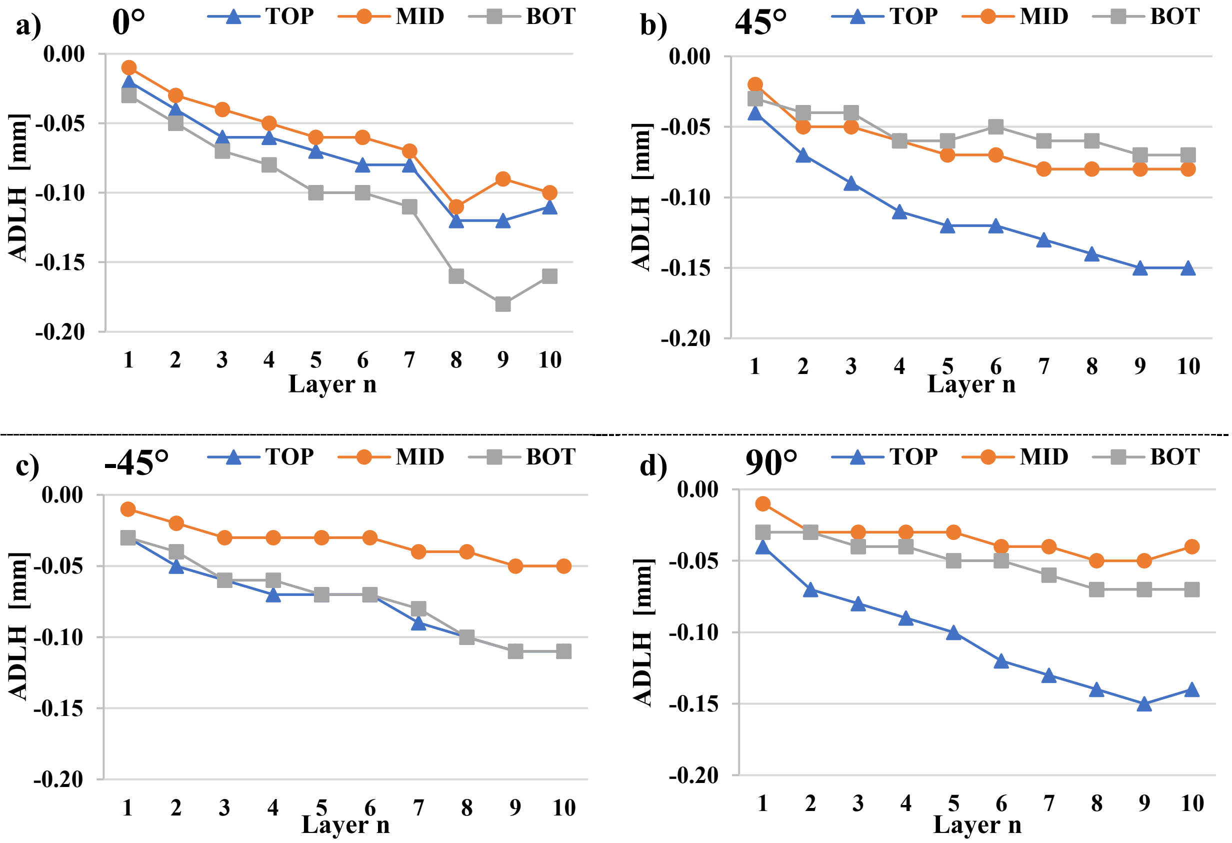

Fig. 24: Results from the AD_{LH} analysis for a) 0°; b) 45°; c)-45°; d) 90°deposition strategies.

The highest values were observed in samples printed at -45°-BOT and +45°-TOP, particularly during Layers 1 through 6. Additionally, samples with a 0° raster angle displayed a noticeable worsening in RAD values from Layer 7 onwards, a pattern that aligned with the observations made for AD_{LH} in similar conditions, as it is shown in Fig. 24. Unlike AD_{LH}, which measures dimensional deviations relative to the nominal plane, RAD is independent of height accuracy, as it evaluates surface deviations from a fitted reference plane. This independence makes RAD a valuable tool for detecting surface defects without being influenced by overall dimensional errors. Both indices, AD_{LH} and RAD, proved effective in identifying process anomalies, each providing unique insights into distinct aspects of layer quality.

AD_{LH} highlighted deviations in dimensional accuracy, while RAD captured surface-level irregularities such as material accumulations or voids.

Table 3: Slope s results obtained for each layer. The red values indicate when high variation of AD_{LH} is detected. Orange values indicate not completely out-of-control values and green values indicate s values that are in control and do not shown to have consequences on subsequent layer.

Slope s

	0°			**+45°**			**-45°**			**90°**		
	TOP	**MID**	**BOT**	**TOP**	**MID**	**BOT**	**TOP**	**MID**	**BOT**	**TOP**	**MID**	**BOT**
1_2	-0.1	-0.1	-0.1	-0.15	-0.15	-0.05	-0.1	-0.05	-0.05	-0.15	-0.1	0
2_3	-0.1	-0.05	-0.1	-0.1	0	0	-0.05	-0.05	-0.1	-0.05	0	-0.05
3_4	0	-0.05	-0.05	-0.1	-0.05	-0.1	-0.05	0	0	-0.05	0	0
4_5	-0.05	-0.05	-0.1	-0.05	-0.05	0	0	0	-0.05	-0.05	0	-0.05
5_6	-0.05	0	0	0	0	0.05	0	0	0	-0.1	-0.05	0
6_7	0	-0.05	-0.05	-0.05	-0.05	-0.05	-0.1	-0.05	-0.05	-0.05	0	-0.05
7_8	-0.2	-0.2	-0.25	-0.05	0	0	-0.05	0	-0.1	-0.05	-0.05	-0.05
8_9	0	0.1	-0.1	-0.05	0	-0.05	-0.05	-0.05	-0.05	-0.05	0	0
9_10	0.05	-0.05	0.1	0	0	0	0	0	0	0.05	0.05	0

By examining these indices together, a more comprehensive understanding of process stability and defect occurrence was achieved, making this cross analysis more suitable for in-situ monitoring purposes as will be discussed below. To illustrate the complementary nature of AD_{LH} and RAD, their values are plotted together for selected samples, as shown in Fig. 27. In these graphs, the left vertical axis corresponds to RAD, while the right axis represents the absolute value of AD_{LH}. Geometric deviation maps are also matched with the combined graphs in Fig. 27, e to provide a visual reference to better interpret the results, with RAD maps representing deviations from the fitted reference plane and AD_{LH} maps highlighting deviations from the nominal plane.

During the cross-analysis of AD_{LH} and RAD, in Fig. 27 , all the possible configurations that can result during a monitoring process are analyzed and are divided into blocks. This analysis will be helpful to understand how these two indexes interact. Block A corresponds to Layer 1 relative the printing strategy 90°-TOP in Fig. 27, a.

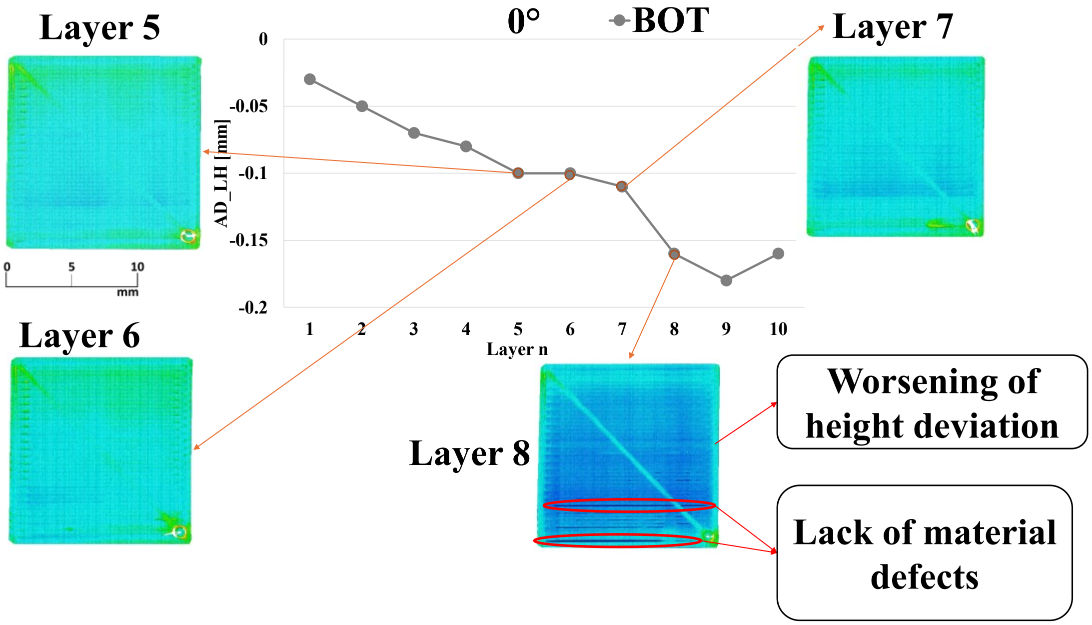

Fig. 25: Effect of slope s on layer surface quality measured on the most unstable case.

In this region, the AD_{LH} value was found low, indicating good height accuracy for the layer. However, the RAD value, approximately 0.017 mm, suggested the presence of localized surface defects. These defects were probably caused by small material accumulations due to the change of direction of the extruder, as confirmed from the A block in Fig. 27, e-A. Despite the slight surface irregularities, the overall dimensional accuracy of the layer was satisfactory. This result highlighted the sensitivity of the RAD index in detecting minor surface anomalies even when height deviations are minimal. Block B on the same sample but on the 5th layer, showed higher AD_{LH} value, reflecting a significant deviation from the nominal height, coupled with a slightly increased RAD value. This combination indicated both poor dimensional accuracy and a broader distribution of surface defects. The increase in RAD suggested that surface conditions have deteriorated, potentially due to uneven material flow or slight misalignments during the printing process. Block C presents an interesting case in Fig. 27, a, where the RAD value remained low at 0.016 mm, indicating good surface quality, while the AD_{LH} value was significantly higher, nearing 0.15 mm. This suggested that while the layer exhibited substantial height deviations, the surface itself was smooth and free of localized defects. Such conditions may arise from systematic issues like uneven Z-axis movement or platform leveling errors, which do not necessarily impact surface quality directly. This result underscored the importance of using both indices to gain a holistic view of the layer's dimensional and surface characteristics. Block D, shown in Fig. 27, b and related to the last layer of the 90°-MID strategy part, represented a scenario where both RAD and AD_{LH} values are low. This indicated that the layer achieved both good surface quality and height accuracy. Such results were indicative of stable and optimal printing process conditions, where material deposition was consistent, and the process was free of mechanical or material-related disturbances. This block served as a benchmark for evaluating the performance of the monitoring system under non-defective conditions. In Fig. 27, block E corresponds to Layer 1 of the strategy 0°-BOT, where a low AD_{LH} value (<0.05mm) was found with a high RAD value (0.026mm).

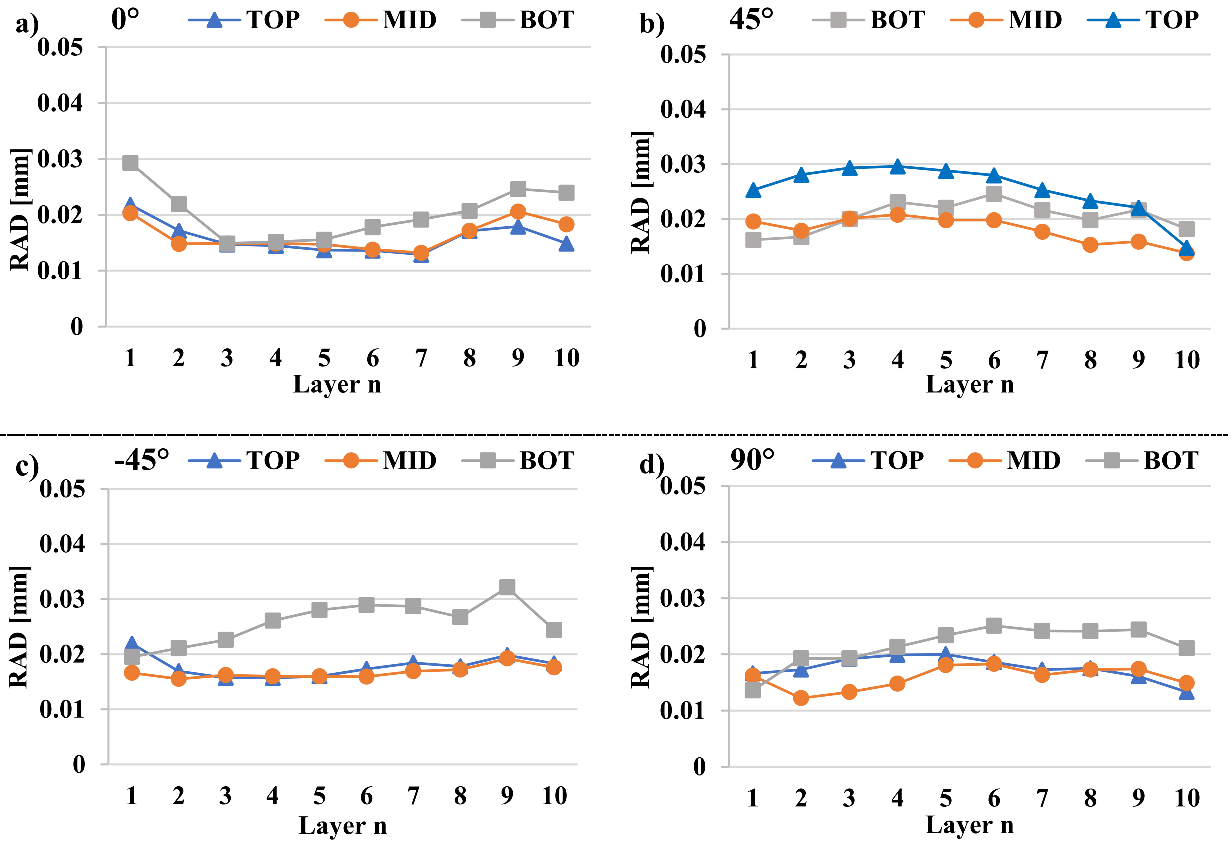

Fig. 26: RAD results for a) 0°, b) 45°, c) -45° and d) 90°.

This combination suggested that the layer has minimal height deviations but suffered from widespread surface defects, such as blobs and material accumulations. These defects were likely caused by factors such as over-extrusion during initial layers or inconsistent nozzle movements. This block highlighted the utility of RAD in identifying surface defects that would not be considered from the AD_{LH}. Block F, corresponding to Layer 9 in Fig. 27, c, exhibited both high RAD and AD_{LH} values, signaling the presence of severe surface defects alongside significant height deviations. This indicated dangerous conditions for process stability. Such conditions were indicative of substantial process instability, emphasizing the importance of a real-time monitoring method to identify and address issues before they propagate. Last, block G in Fig. 27, d presented another case where both RAD and AD_{LH} values were high, although at different magnitudes. This suggested a combination of surface defects and height inaccuracies, similarly to the condition discussed for the block F. The patterns of these deviations may arise from variations in raster deposition or material inconsistencies because of the incorrect operation of the nozzle. Further observations need to be made about RAD. This index was demonstrated to be able to detect various types of surface defects, such as material accumulation and lack of material. An example is displayed in Fig. 28 where a severe buildup of material was caused by prolonged nozzle dwell time at that specific place, resulting in a high RAD value. When a severe defect like that occurs, missing data points can be observed in areas where the sensor failed to detect the laser line, which can occur due to vertical walls or unexpected surface protrusions that prevent the laser line from being correctly reflected into the CCD sensor of the BLP. It follows that if missing data are found inside the layer surface point cloud it means that a severe defect occurred, signaling that the printing process should be stopped.

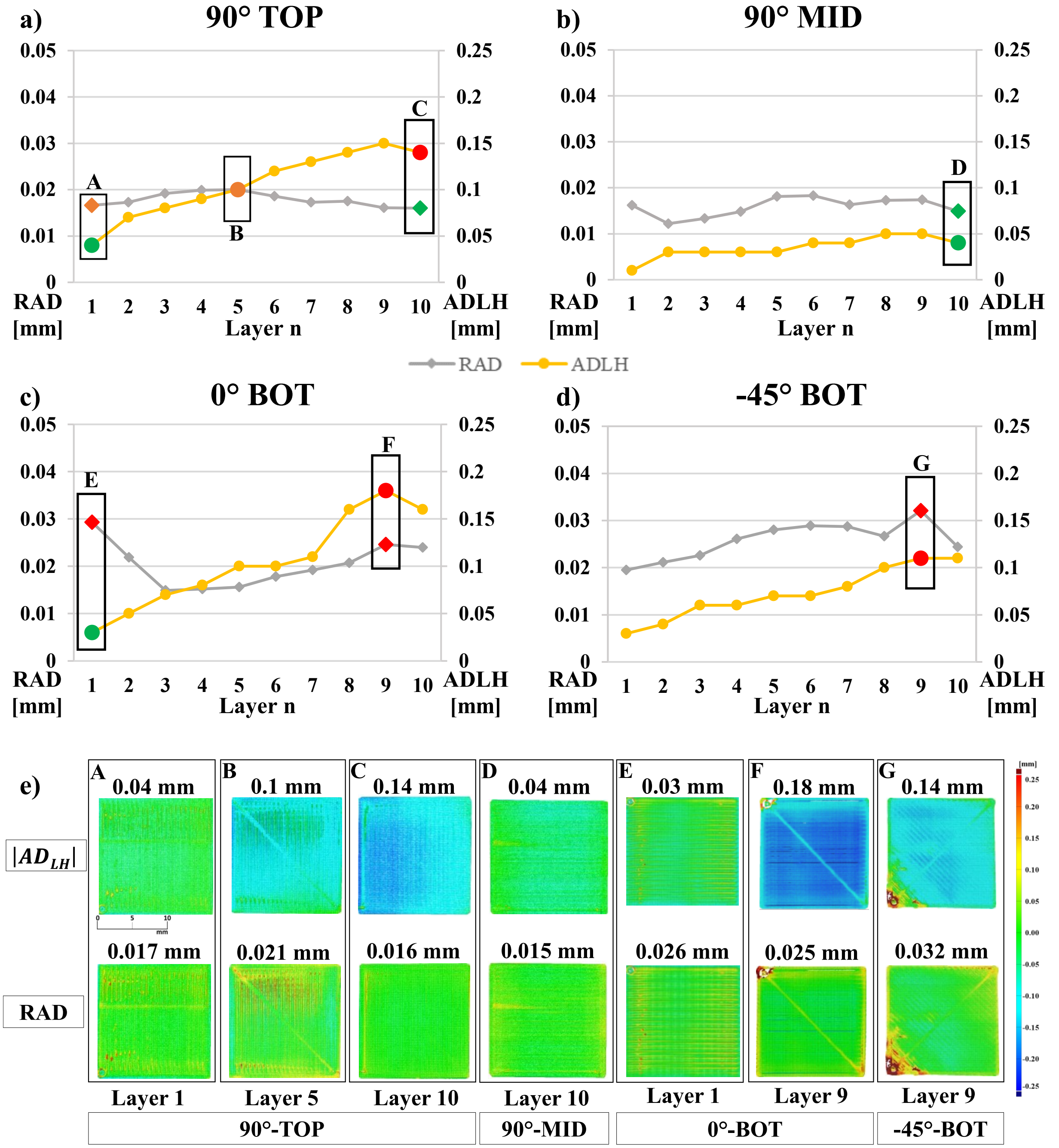

Fig. 27: Example of cross analysis for AD_{LH} and RAD for different specimens. e) represent the layer geometrical deviation based on the indexes combination to provide a fast and easy way to correlate values with surface quality.

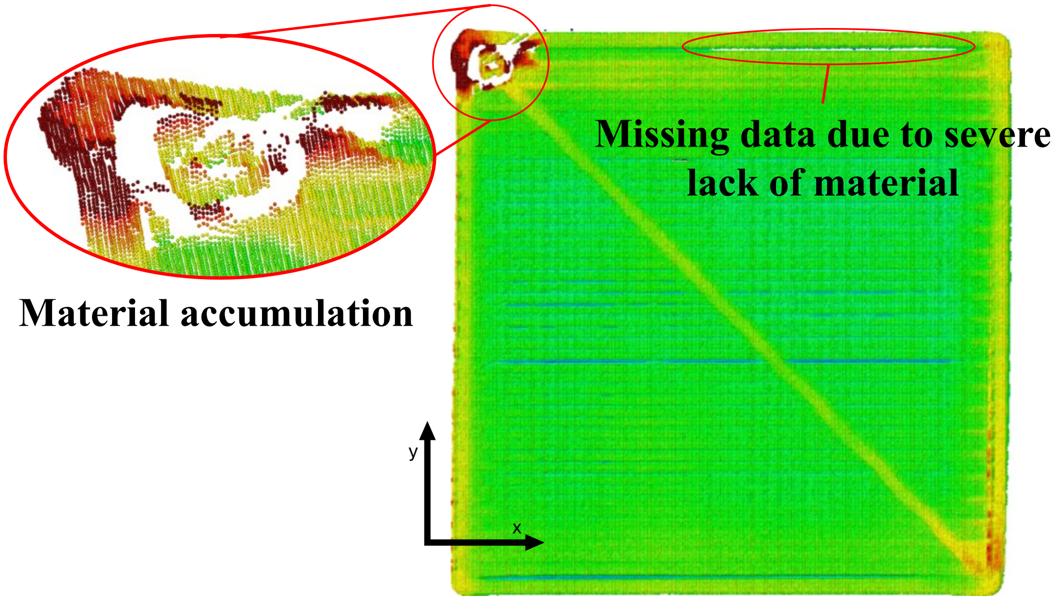

Fig. 28: Defects related to high RAD value for the 9th layer of the specimen 0° BOT.

4.5.5. ***Validation of the results.***

Validating the obtained results is a critical step to ensure the reliability of the data acquired and processed by the proposed monitoring method. After completing the fabrication of the samples, their dimensions were measured using a GOM Atos Q 8M, the same structured-light scanner (LS) used during the calibration phase and shown in Fig. 19. The validation process involved comparing the average height of the fabricated samples, as measured offline by the SL, with the corresponding height data obtained from the monitoring procedure. The comparison focused specifically on the last layer of each sample, as it represents the overall height of the printed object. Every produced part was scanned, and the average height error was computed. The point cloud reference was obtained from the LS. The results of the validation revealed an average error of 0.014 mm, with a standard deviation of 0.007 mm. These findings confirm the reliability of the monitoring method and demonstrate the effectiveness of the calibration process. To further reinforce the validation, a comparison of deviation maps corresponding to the AD_{LH} index was done and the results are shown in Fig. 29. This analysis included several relevant cases to assess the method’s performance under varying process conditions. The deviation maps, all corresponding to the final printed layer, provided additional confirmation of the effectiveness of the monitoring system. The results, as illustrated in Fig. 29, showed a strong correlation between the deviation maps produced by the monitoring system and those obtained from the SL across all analyzed conditions.

This research activity was published in the following research paper: [210].

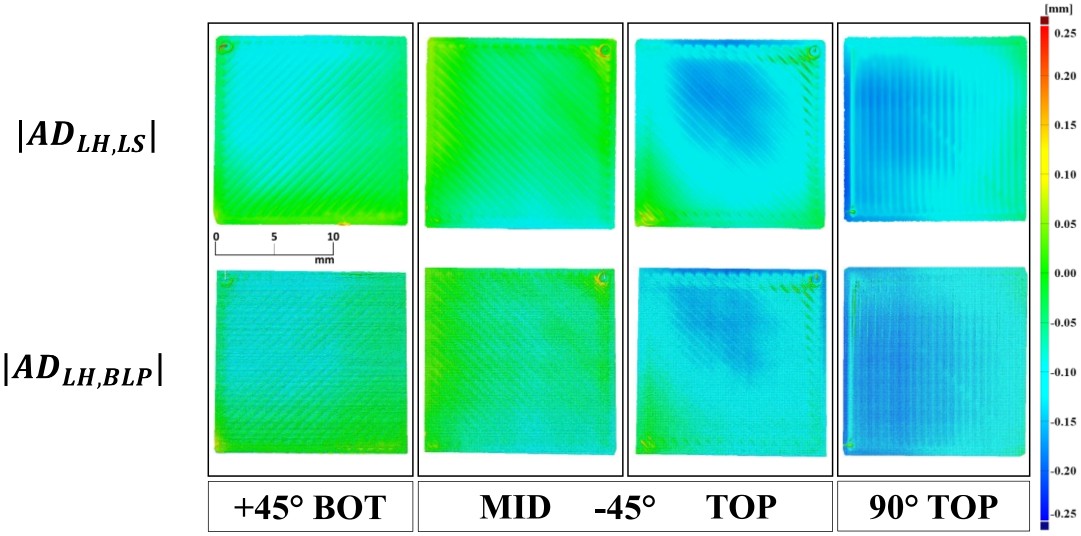

Fig. 29: AD_{LH} measured from the BLP and the LS. This comparison has the purpose of validating the measurement from the BLP sensor.

4.6. In process evaluation of layer defects and surface topography through a novel point cloud functional analysis

The results discussed above have been published in [211].

4.6.1. *Method description.*

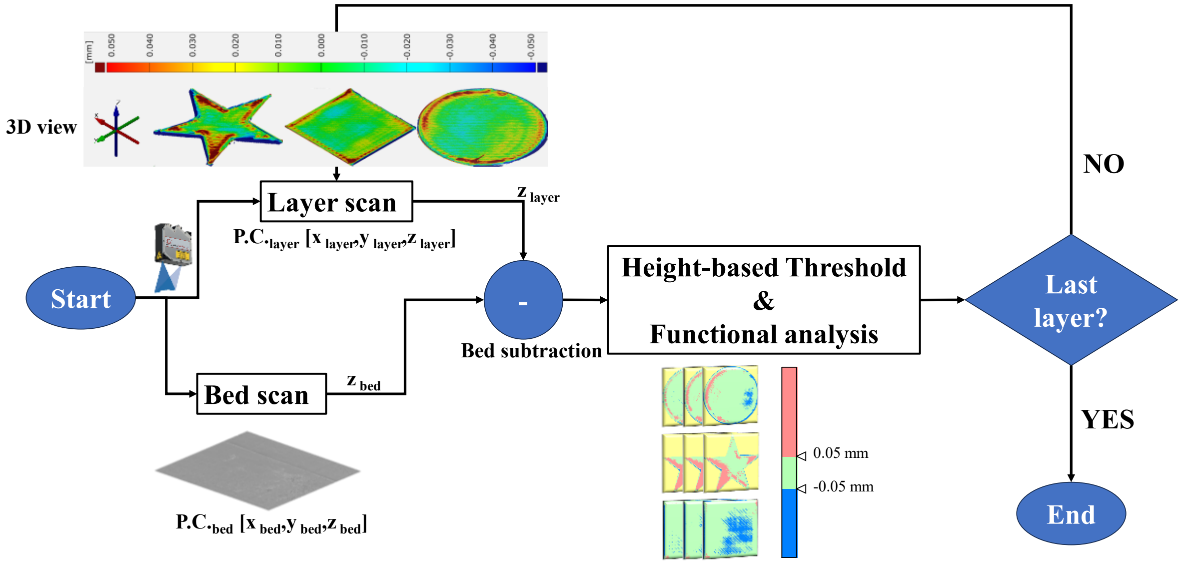

Fig. 30: Second proposed monitoring method workflow. This method is based on functional analysis tools and height measurements.

The goal of this experiment is to prove the effectiveness of a high-resolution monitoring system for MEX parts. Similarly to previous activity, the initial step in the monitoring workflow (see Fig. 30) involved scanning the build plate before the printing process began. This operation was essential for establishing a reference plane. Once the build plate scan was complete, the layer deposition commenced. After the completion of each layer, the printhead was programmed to move and activate the end-stop circuit, triggering the collection of profile data. Once the point cloud for the layer was acquired, it was processed by subtracting the build plate's point cloud. This operation ensured that the z-coordinates of the layer's point cloud were referenced to the build plate. Following data acquisition, specialized surface analysis software (TalyMap v. 7.4 by Digital Surf) was employed for detailed point cloud analysis. Functional analysis tools embedded within the software were used to evaluate the surface conditions of each layer. After subtracting the build plate's point cloud, the layer point cloud was segmented by applying two height thresholds set to ±0.05 mm from the nominal height. The lower threshold corresponded to the nominal height minus 0.05 mm, while the upper threshold was set at the nominal height plus 0.05 mm, as detailed in Table 4. Using these thresholds, the layer surface was divided into three distinct regions: the acceptable region (AR), the upper region (UR), and the lower region (LR) (see Fig. 31). Points with heights falling within the range of nominal height ± 0.05 mm were classified as part of the acceptable region. Points exceeding the upper threshold (*h*>nominal height+0.05 mm) were assigned to the upper region (UR), while points below the lower threshold (h<nominal height-0.05mm) were assigned to the lower region (LR). Points classified in the upper and lower regions corresponded to overfill (OF) and underfill (UF) conditions, respectively.

Table 4:Region definition

Layer Number	**Layer Height *h* [mm]**	**Considered Regions**
n	$h < (n \; * 0,2) - 0,05$	Lower Region (LR)
	$(n \cdot 0,2) - 0,05 \leq h \leq (n \cdot 0,2\,) + 0,05$	Acceptable Range (AR)
	$h > n \cdot 0,20 + 0,05$	Upper Region (UR)

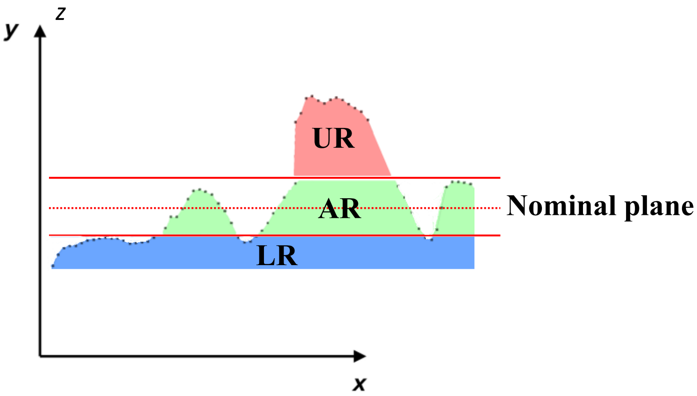

Fig. 31: Image representation of the defined region based on the 2D profile.

4.6.2. *Functional analysis tools.*

The first result of the "slicing" operation on the layer point cloud was an image that visually distinguished the three regions described above. These regions were represented using different colors (see Fig. 31): the acceptable range (AR) in green, overfill (UR) in red, and underfill (LR) in blue. From these images, a quantitative index known as the Projected Percentage Area (PPA) was extracted. This index quantifies, in percentage terms, the proportion of the total layer area occupied by points within each region (acceptable range, overfill, or underfill), as shown in equation (5):

$$\boldsymbol{PPA_{UR\backslash AR\backslash LR}}[\%] = \left(\frac{\boldsymbol{Area_{(UR\backslash AR\backslash LR)}}}{\boldsymbol{Area_{Tot}}}\right) * \mathbf{100} \qquad (\mathbf{5})$$

The concept of PPA is illustrated in Fig. 32, a. Once a defective layer was identified through the slicing process, additional indices related to surface functional analysis were employed to gain deeper insights into the layer's characteristics. These indices focused on evaluating the volume of material or voids and the mean thickness of material or voids within each region (AR, UR, and LR), as shown in Fig. 32, b. These parameters were found to be suitable for surface quality characterization of additively manufactured parts [91]. In the context of the present work, this analysis was used to quantify how the material and voids were distributed in each layer, gathering precious information about the amount of material exceeding the upper acceptable limit, or the number and entity of voids when the UF condition was induced. The application of the above-mentioned analysis on layer surfaces produced by MEX provided a more comprehensive picture of the surface conditions

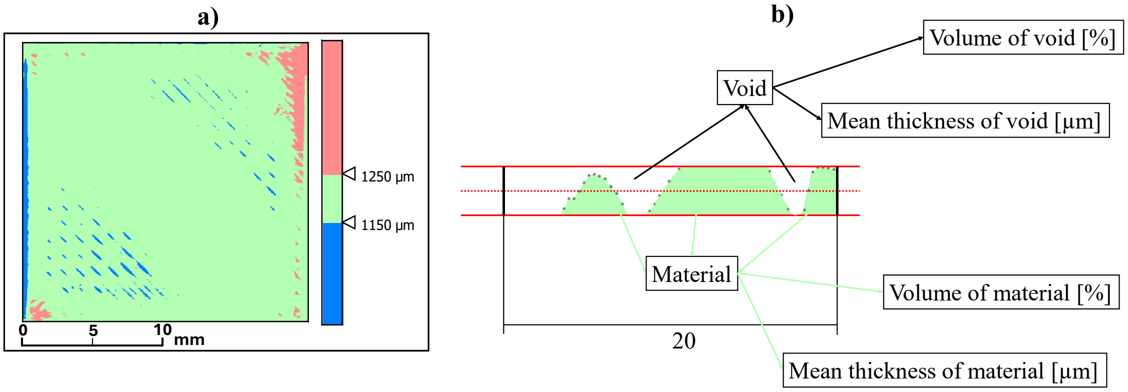

Fig. 32:a) Example of PPA output after the thresholding on the layer surface; b) definition of functional analysis parameters that will be used for the layerwise surface monitoring.

4.6.3. ***Experimental plan.***

The monitoring system was tested on samples fabricated using white PLA filament provided by Fabbrix®. To assess the robustness of the monitoring methodology, three distinct cross-section geometries were selected: a circle, a square, and a five-edged star (see Fig. 33). These shapes were chosen to evaluate the system's ability to reliably monitor and analyze layer quality regardless of the complexity or symmetry of the printed geometry. The maximum dimension of each sample in the xy-plane was set to 20 mm, and all parts were printed at the same location on the build plate. The nominal height of the samples was 2 mm, with a layer height of 0.2 mm, which is a standard parameter for Material Extrusion (MEX) printers equipped with a 0.4 mm nozzle. The printing parameters (PP) used in this study are summarized in Table 5. To simulate a variety of common surface defects, three distinct process conditions were implemented: the optimal condition (OC), representing the use of optimized process parameters, from manufacturer specifications, and two defective conditions typical of MEX processes, which are underfill (UF) and overfill (OF). These conditions were intentionally induced to evaluate the system's capability to detect and analyze defects.

- *Underfill (UF)*: This condition, characterized by insufficient material deposition, was achieved by reducing the flow rate to 95% of the optimal value, increasing the printing speed by 60% relative to the nominal (50 mm/s), and increasing the raster width beyond the nozzle diameter. The result was a shortage of material in areas where a solid layer should form.

- *Overfill (OF)*: This condition, involving excess material deposition, was induced by increasing the flow rate, reducing the printing speed, and using a narrower raster width compared to the optimal parameters.

Each cross-section geometry was printed under the three process conditions, resulting in a total of nine specimens (Table 6). This experimental design allowed for a comprehensive evaluation of the monitoring system across varied geometric and process scenarios. The inclusion of different geometries and process conditions ensured that the methodology was rigorously tested for its ability to identify and characterize defects, regardless of shape or parameter variations.

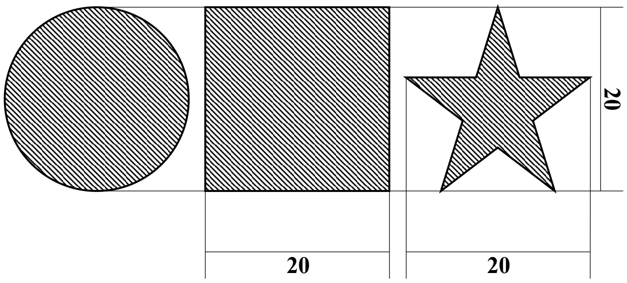

Fig. 33: Specimens cross-sections considered for the experiment.

Table 5: Printing parameters

PP	Over-Fill (OF)	Optimal Condition (OC)	Under-Fill (UF)
Printing speed [mm/s]	30	50	80
Flow rate[%]	105	100	95
Raster width [mm]	0.3	0.4	0.5

Table 6: Nomenclature for specimens.

Cross-section	Samples nomenclature		
Circle	C_OF	C_OC	C_UF
Square	Sq_OF	Sq_OC	Sq_UF
Five edges star	St_OF	St_OC	St_UF

4.6.4. ***Results***

Projected Percentage Area PPA. From the segmented point clouds, the PPA values corresponding to points in the upper region (UR), acceptable range (AR), and lower region (LR) were computed for each layer and sample, and their trends were subsequently analyzed (Fig. 34). These three PPA values collectively represent the overall surface condition of the layer, with the sum of $PPA_{LR}+PPA_{AR}+PPA_{UR}=100\%$. In the proposed monitoring framework, these indices provide an efficient and rapid method for determining whether the surface of a layer meets quality standards. To begin, the PPA results for samples printed under optimized conditions were analyzed. A key observation was that the Percentage of Points in the Acceptable Range (PPA_{AR}) consistently exceeded 65% for circular and square cross-sections, indicating that the majority of points fell within the acceptable range for these geometries. However, the star-shaped cross-section exhibited a lower PPA_{AR}, highlighting its more complex geometry. Among the circular and square samples, PPA_{AR} values were the highest, with most layers exceeding 90%. In contrast, the star sample showed a higher concentration of points in the upper region, particularly in areas of overfill.

Examining the circular sample further, the PPA_{UR} remained below 10% across layers, with overfill defects predominantly observed at the junctions between infill lines and the wall layer. Similarly, the square sample maintained PPA_{UR} below 10%, except for a slight increase in layers 8 and 9. In comparison, the star-shaped sample exhibited the highest PPA_{UR} among the three geometries, attributed to its angular features. Visual analysis of the sliced images revealed that material accumulation was most pronounced at the intersections between infill and wall lines, as well as at narrow corners and tips (Fig. 35). This behavior can be explained by the deceleration of the nozzle at the end of raster tracks, which results in localized material buildup, particularly in the square and star specimens.

Regarding the lower region, PPA_{LR} values averaged 12% for circular samples and 8% for square samples, with maximum values reaching 20%. The star-shaped sample, however, consistently exhibited the lowest PPA_{LR}, typically below 4%, consistent with the higher complexity of its geometry and its sensitivity to sharp corners and tips. When analyzing defective conditions induced intentionally (Fig. 36), distinct trends emerged. For overfill conditions, all samples displayed material accumulation that worsened with successive layers. The circular sample reached a PPA_{UR} of 70%, while the square and star samples exhibited even greater material excess, with PPA_{UR} exceeding 95%. In the circular sample, the overfill was primarily driven by process parameter variations, as its simple geometry lacked the sharp features observed in the other specimens. Underfill conditions were also examined (third column of Fig. 34). The circular sample demonstrated the highest PPA_{LR}, approximately 40%, with underfill zones appearing consistently across layers. Despite this, PPA_{UR} values for the circular sample remained low, never exceeding 6%. In contrast, square and star samples showed underfill defects in the initial layers, which diminished as the layer count increased. These samples eventually exhibited increased PPA_{UR}, with material accumulation occurring primarily at tips and infill-wall connections (Fig. 36). Notably, even with modified process parameters to reduce material deposition, overfill regions were still more prevalent in square and star specimens, highlighting the complex interplay of geometry and process conditions.

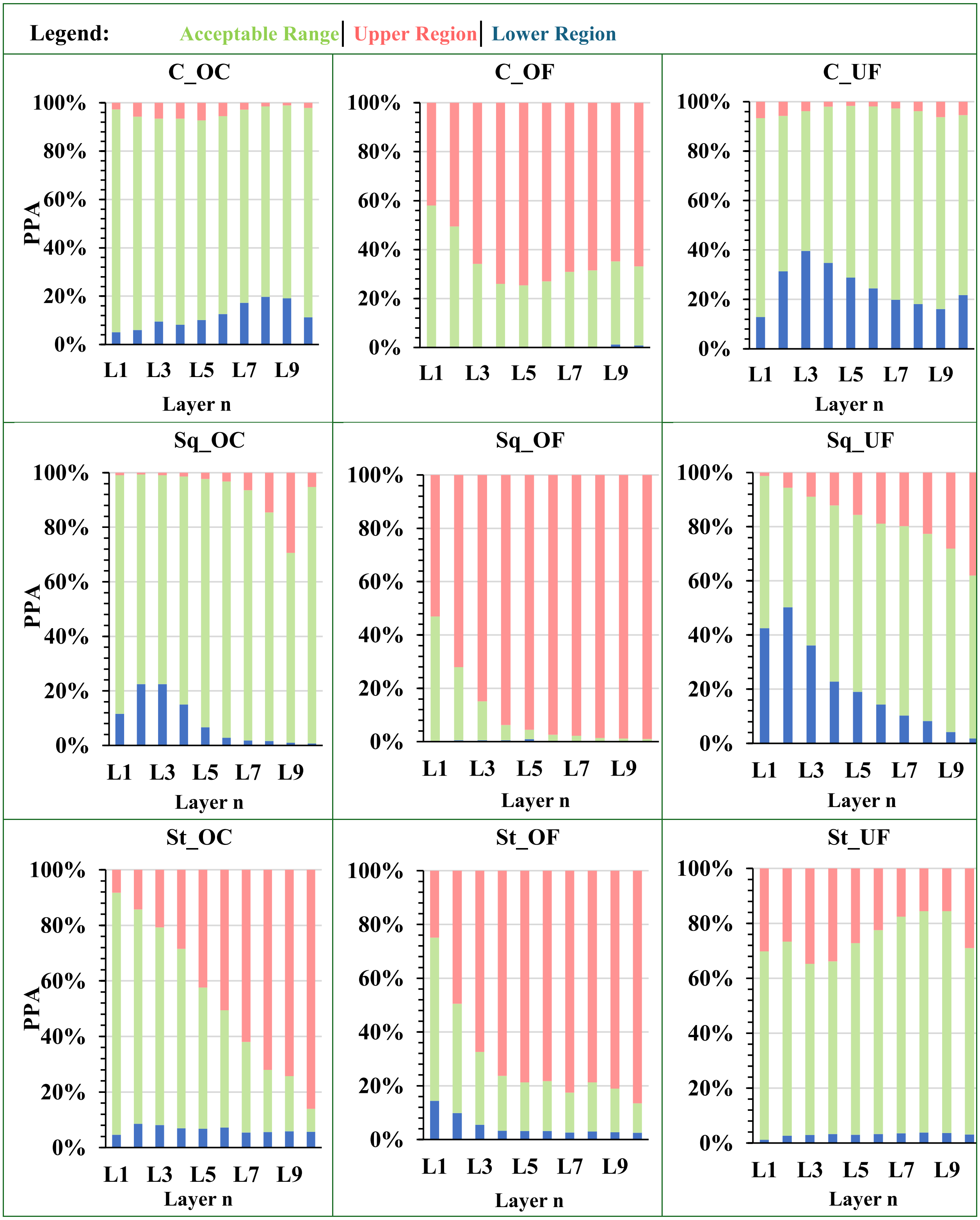

Fig. 34:PPA results divided by strategy.

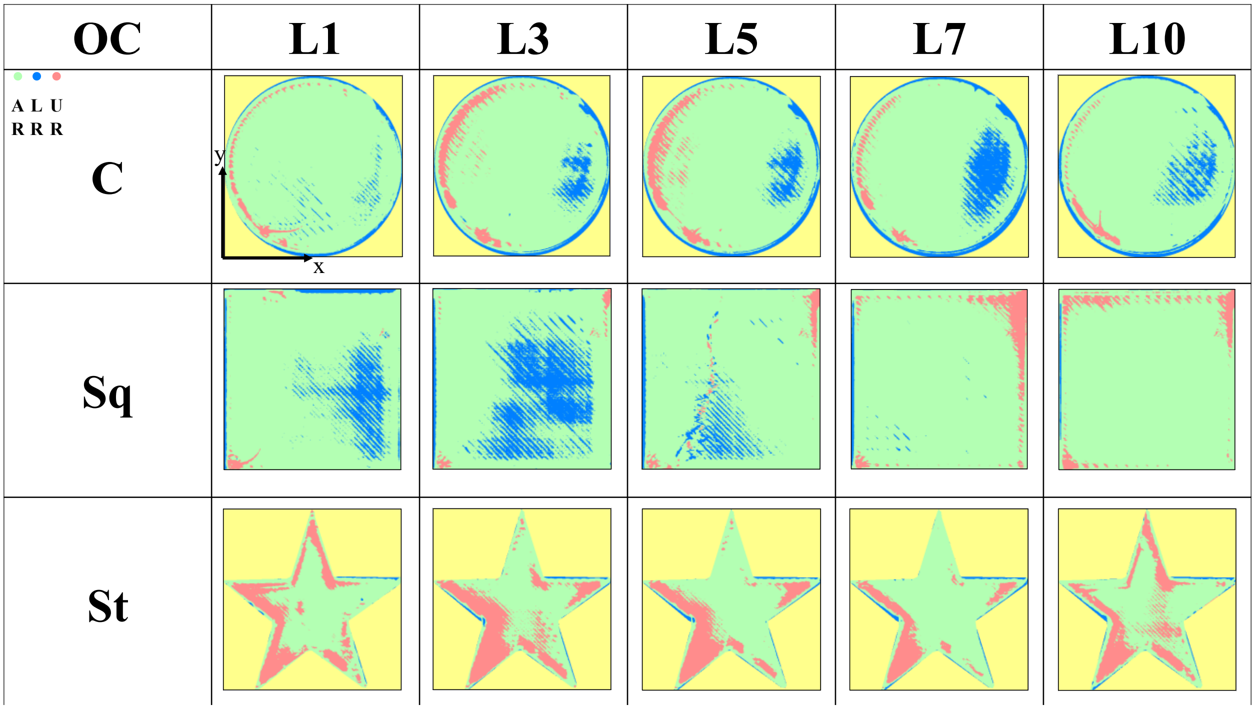

Fig. 35: 'Tip/corner effect' showed for specimens printed with OC parameters. In yellow the not measured points are represented. Print direction was kept constant for each layer, and it was chosen to be −45 degrees.

Material and void. Unlike the rasterization method, where point heights within the same node are typically averaged [37,90], the proposed monitoring methodology retained the height information of each point, enabling a more detailed analysis. This study explored the feasibility of performing a functional analysis on each layer, focusing on the distribution of material and voids. This approach provided critical insights into the severity of defects, offering a deeper understanding of the printing process. The volumes of voids (VV) and material (VM) in each region were calculated and analyzed. To streamline the discussion, both VV and VM were expressed as percentages, recognizing their complementary relationship ($VV+VM=100\%$). To avoid redundancy, only the void volume percentages (VV) are reported. Results were grouped by sample geometry (Fig. 37, a for the circle, Fig. 37, b for the square, and Fig. 37, c for the five-edged star) and examined across three process conditions: underfill (UF), optimal condition (OC), and overfill (OF). The void percentages in the lower region (VV_{LR}) ranged from 0–5%, indicating that these regions predominantly contained material. Under induced underfill conditions, VV_{LR} values were more dispersed but generally remained around 5%, irrespective of sample geometry. In the acceptable range, the void percentages (VV_{AR}) varied more significantly. Circular samples (Fig. 37, a) exhibited less dispersion (20% of the maximum range) but were concentrated at higher void percentages (60–80% for UF, 50–70% for OC). Square and star samples (Fig. 37, b and Fig. 37, c) showed a consistent decrease in VV_{AR} as layer numbers increased. For example, in square samples printed under UF conditions (Sq_{UF}), VV_{AR} decreased from 80% in the initial layers to 20% in later layers. Star-shaped samples consistently recorded the lowest VV_{AR} values across all process conditions. Due to the definition of the acceptable

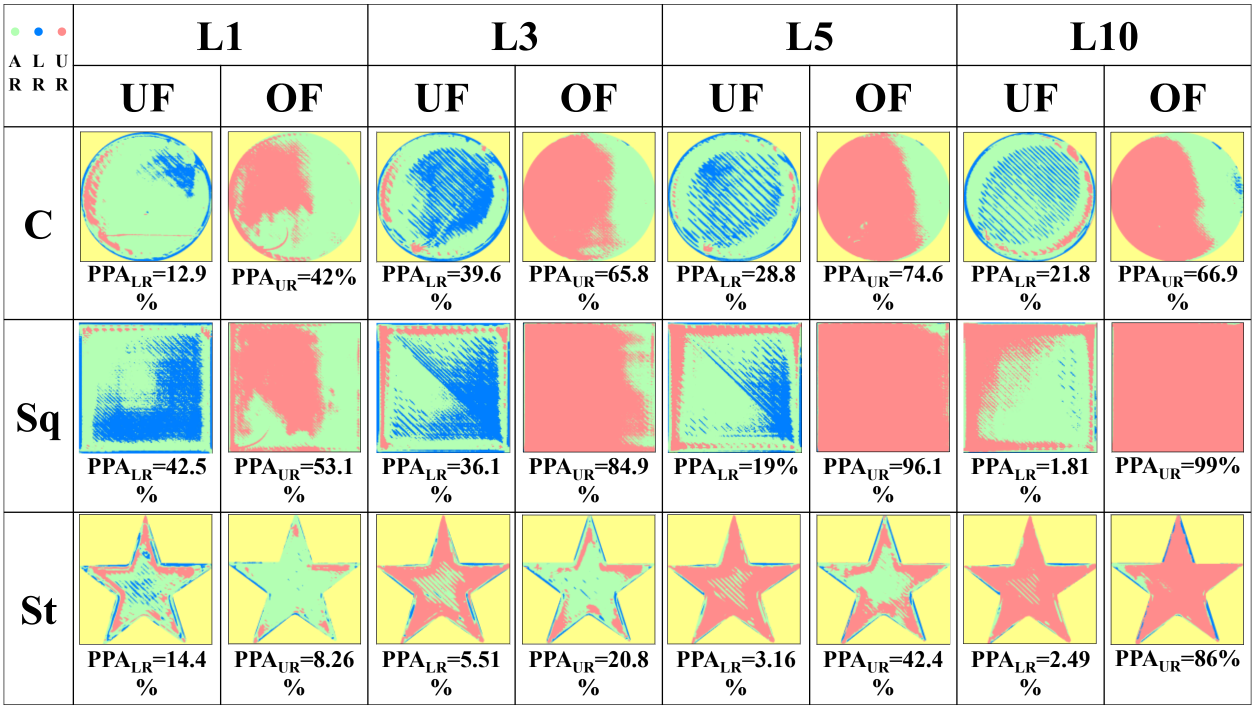

Fig. 36: Sliced point clouds showing the evolution of the PPA$_{UR}$ and PPA$_{LR}$ for samples realized with induced overfill and underfill.

range, achieving the ideal layer condition, with height values close to the nominal, requires VV$_{AR}$ to equal 50%, as illustrated in Fig. 37, d.

To further characterize the defects, the mean thickness of material and voids in each region (lower region (LR), acceptable range (AR), and upper region (UR)) were computed. This thickness was calculated as the ratio of defect volume (μm^3) to the defective area (μm^2). Table 7 and Table 8 reported the mean void thickness in the LR and mean material thickness in the UR, respectively. Voids in the LR were significant because they are less likely to be filled by subsequent layer deposition. In this study, the mean void thickness in the LR never exceeded 40 µm (20% of the layer height), remaining within acceptable limits for most conditions. Under induced overfill, void thickness in the LR was consistently below 10 µm. Conversely, the mean material thickness in the UR reflected the extent of excess material. Across all samples, material thickness in the UR increased with layer number, with the highest values observed in square and star specimens under OF conditions.

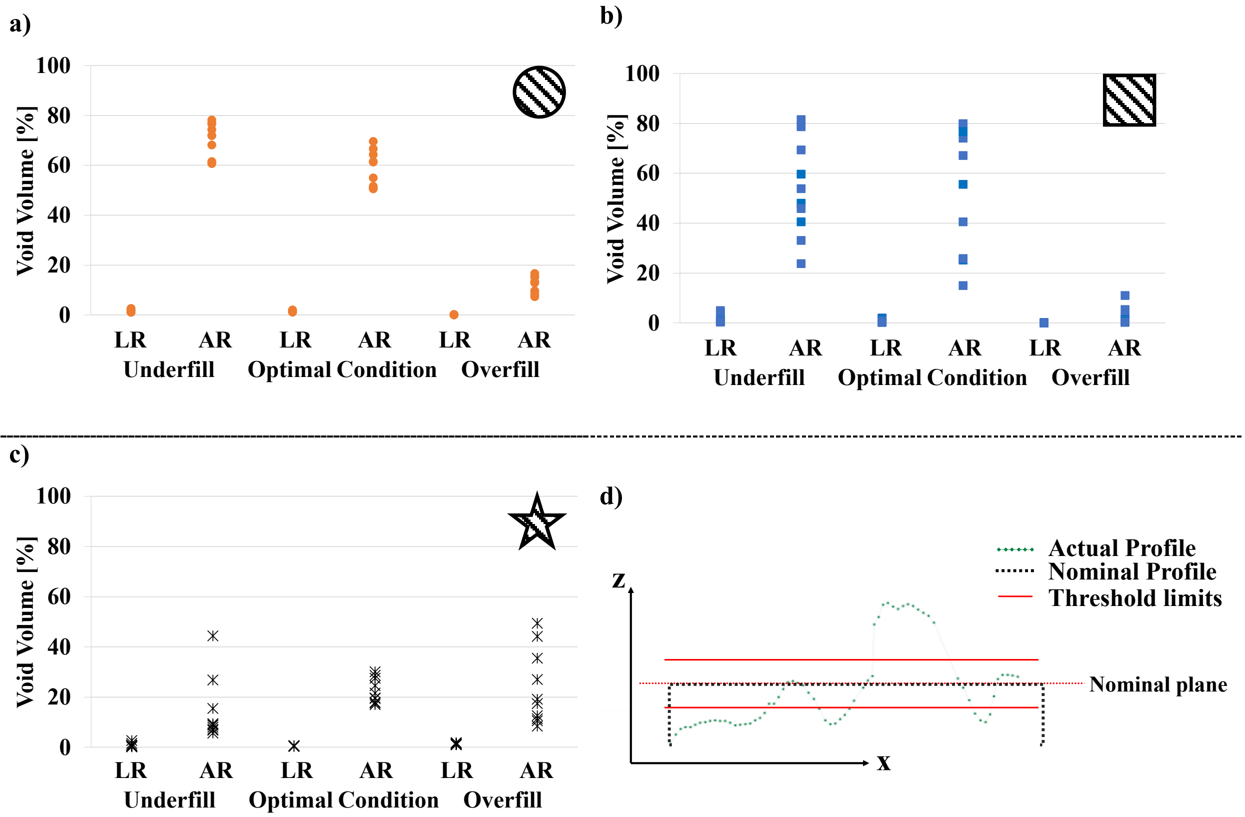

Fig. 37: Volume of Void results from functional analysis for: a) Circle, b) squared and c) five-edge star specimens. d) represent the theoretical result expected from this type of analysis.

In contrast, specimens printed under UF conditions exhibited lower material thickness in the UR. For the final layer, material thickness values were used to compute the average height of the sample obtained through the monitoring system (AH-BLP). These results were compared with the Average Height (AH-SL) calculated from offline measurements using the GOM ATOS Q 8M structured-light scanner, equipped with a 100 mm lens and certified accuracy, as already mentioned in section 4.4 relative to the calibration phase. Results are shown in Table 9. The mean thickness of material in the UR was computed using points above the threshold set 50 µm above the nominal height. Thus, AH-BLP was calculated as the upper limit of the acceptable range (2.05 mm) plus the mean thickness of material in the UR. Comparing AH-BLP with AH-SL revealed good agreement when excess material was more evenly distributed, as indicated by higher PPA_{UR}. This alignment was particularly notable for samples printed under OF conditions and in a few other cases characterized by pronounced PPA_{UR}. Conversely, the largest discrepancies were observed when material thickness in the UR was minimal (approximately 1 µm) and PPA_{UR} ranged between 2.12% and 5.5% (e.g., samples C_{OC} and C_{UF}). It is important to note that the material thickness in the UR reflects only points above the upper threshold, whereas the AH-SL measurement encompasses the entire layer surface, including points below the threshold.

Table 7: Mean thickness of voids in the lower region.

	Mean thickness of voids in the lower region [µm]								
	C_OF	Sq_OF	St_OF	C_OC	Sq_OC	St_OC	C_UF	Sq_UF	St_UF
L1	<1	<1	6	2	2	<1	3	8	1
L2	<1	<1	5	4	2	1	9	20	4
L3	<1	<1	5	8	2	2	14	17	6
L4	<1	<1	5	12	1	3	14	7	9
L5	<1	<1	6	15	1	3	12	6	12
L6	<1	<1	6	20	1	4	14	6	15
L7	<1	<1	6	26	1	6	16	4	16
L8	<1	<1	8	31	1	7	17	6	20
L9	<1	<1	9	34	1	6	18	6	28
L10	<1	<1	9	38	1	7	22	5	36

Table 8: Mean thickness of material in the upper region.

	Mean thickness of material in the upper region [µm]								
	C_OF	Sq_OF	St_OF	C_OC	Sq_OC	St_OC	C_UF	Sq_UF	St_UF
L1	8	10	10	1	<1	2	2	<1	8
L2	15	21	22	1	<1	4	1	2	8
L3	25	35	39	1	<1	7	1	3	10
L4	36	49	46	1	<1	9	1	5	9
L5	44	62	50	1	1	15	1	6	8
L6	47	71	48	1	1	17	1	7	6
L7	46	76	52	1	1	22	1	7	5
L8	49	84	48	<1	2	27	1	8	3
L9	49	90	52	<1	5	30	1	11	3
L10	54	101	67	<1	1	45	1	15	5

Table 9: Data validation through Average Height (AH) obtained from the SL and the BLP.

	C_OF	**Sq_OF**	**St_OF**	**C_OC**	**Sq_OC**	**St_OC**	**C_UF**	**Sq_UF**	**St_UF**
AH-M [mm]	2.104	2.151	2.117	2.050	2.051	2.095	2.050	2.065	2.055
AH-SL [mm]	2.076	2.147	2.108	1.993	2.067	2.093	1.976	2.059	2.04
AH_dev. [µm]	28	4	9	57	16	2	74	6	15
PPA$_{UR}$ [%]	66.9	99	86	2.12	5.19	86	5.42	38	29

4.6.5. *Defect coordinates extraction for possible corrective action*

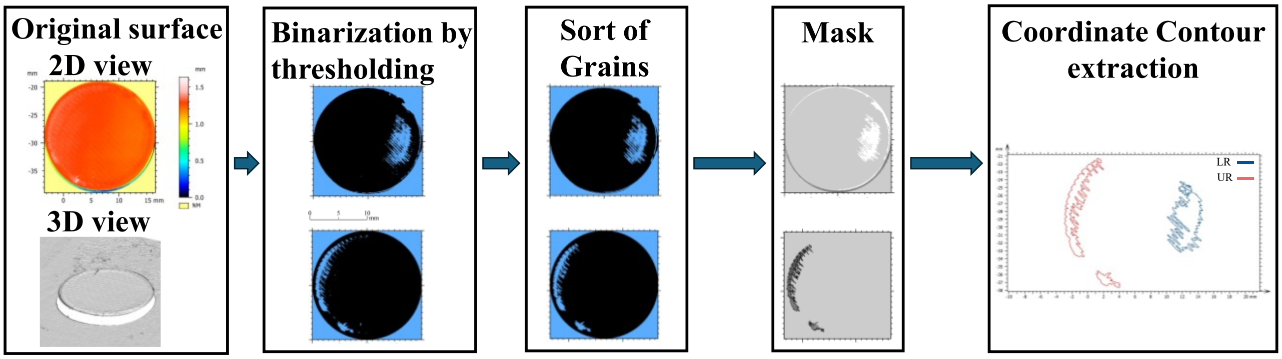

Fig. 38: Contour extraction workflow for future developments.

The proposed methodology for extracting the coordinates of defective regions, illustrated in Fig. 38, began with a binary height thresholding process applied to the point cloud of each layer. This involved segmenting the original surface at a predetermined height threshold, resulting in a binary representation of the surface. The segmented point cloud consisted of clusters of points, or called grains, that corresponded to areas above or below the defined threshold. To facilitate potential corrective actions, certain modifications were applied to the binarized point cloud. In the case of underfill regions, isolated grains smaller than 0.4 mm, which corresponded to the nozzle diameter of the extruder, were removed. The remaining grains were then merged to form a coherent representation of the defective areas. For overfill regions, there were fewer constraints, particularly if machining the entire layer is an option. In such cases, grains can be selected based on the height of the points within the defective region, providing justification for corrective actions such as material removal. Following these adjustments, the contours of the defective areas were overlaid on the original layer surface as a mask. This masking process facilitated the execution of the contour extraction algorithm, which identified and extracted the coordinates of points outlining the defective regions. These coordinates are then made available for further analysis or corrective interventions. An example of contour extracted for different geometry cross-section is shown in Fig. 39.

The proposed approach demonstrates significant potential for detecting, identifying, and quantifying defects that arise during the printing process. By applying height thresholds to generate sliced representations of layer surfaces, the method facilitates the extraction of contours that define defective regions. This enables precise localization of defective zones on the layer surface, allowing for accurate identification of problem areas. Furthermore, integrating additional data, such as the mean thickness of material and voids, provides deeper insights into the extent and dimensions of these defects. This detailed understanding is particularly valuable for implementing targeted corrective actions, such as adding material in underfilled areas or removing excess material in overfilled regions. These adjustments ultimately optimize the printing process and enhance the quality of the final printed objects. For underfilled areas, the extracted coordinates of defective regions could be used to generate toolpaths, directing the printhead to deposit material in these specific zones, when the dimensions of the defect allow. This process could leverage the calculated mean thickness of voids to ensure precise and efficient material addition. For overfilled regions, a potential solution involves equipping the printer with a small milling tool mounted near the printhead. This tool could be used to remove excess material from overfilled areas when a material accumulation is detected, with the depth of the cut determined by the mean thickness of material in the upper regions, as outlined in Table 8. While hybrid systems combining additive and subtractive manufacturing are already available in the market, the ability to integrate in-process monitoring data with targeted corrective actions remains a key advancement. This integration would ensure that corrective measures are implemented both effectively and efficiently, leading to improved print quality and greater process optimization.

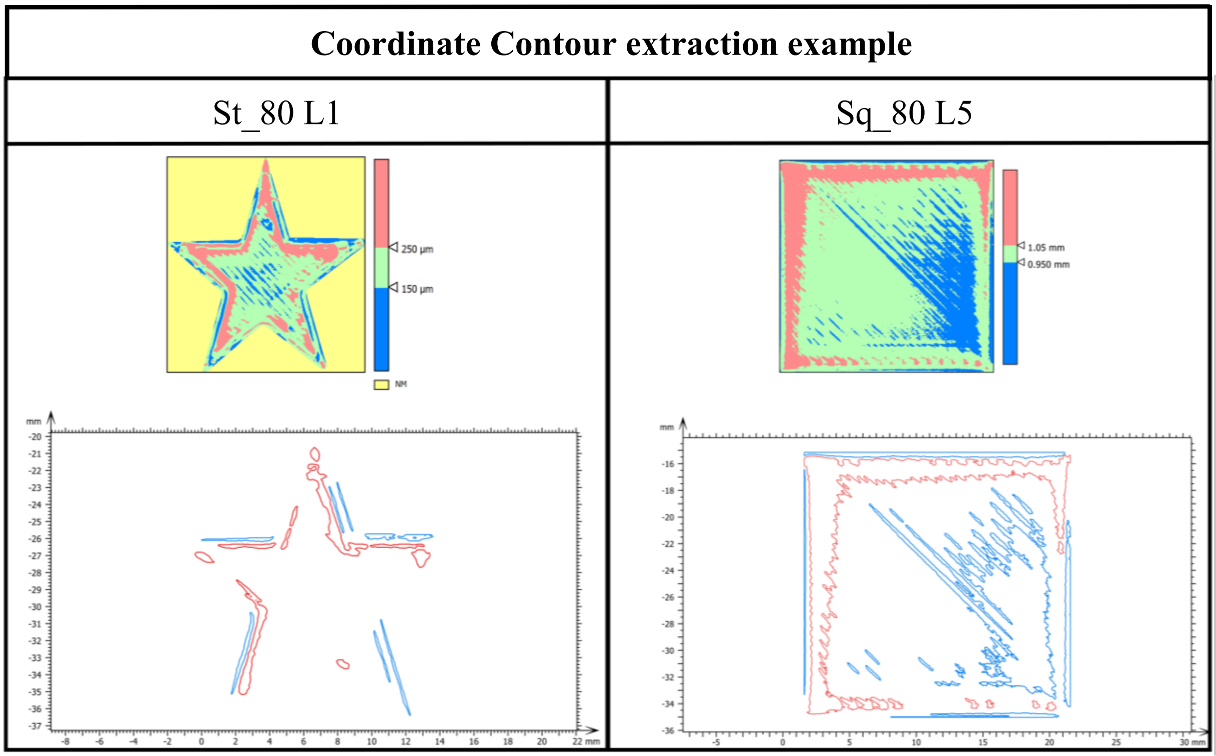

Fig. 39: Example of contour extraction applied on a squared section specimen.

4.7. Conclusion about MEX monitoring activities

This thesis presented robust and innovative in-situ monitoring methodologies aimed at detecting, localizing, and quantifying surface defects commonly encountered in Material Extrusion (MEX) processes, such as underfill, overfill, blobs, and voids. By integrating a high-resolution blue laser profilometer into a consumer-grade MEX printer, the proposed system provided detailed layer-by-layer surface data, unaffected by ambient light conditions, enabling precise in-process defect detection and quality evaluation. One of the most significant challenges in AM metrology is the lack of standardized and reliable metrics to evaluate part quality during manufacturing. For this reason, several quality indices, including the Cumulative Height, Layer Height Average Deviation (AD_{LH}) and its slope (s), and

Residual Absolute Deviation (RAD), were employed to evaluate layer dimensional accuracy, surface conditions, and process stability. Together, these indices revealed the relationship between dimensional and surface defects, showing that high AD_{LH} values were often associated with significant dimensional deviations, while high RAD values highlighted the presence of widespread surface defects, even when dimensional errors were minimal. The stability of the process was further assessed through the slope of AD_{LH} trends, which provided insights into process shifts and layer-to-layer consistency.

Alongside proposing reliable monitoring methods, this thesis addressed also critical gaps in the field of metrology for Material Extrusion (MEX) processes, focusing on the development and validation of consistent indexes that can be used for monitoring purposes. This was made possible thanks to the high-resolution profilometer used as main sensor for the monitoring setup and integrated into the 3D printer. In the second research activity was successfully demonstrated the feasibility of functional surface analysis as a powerful tool for monitoring layer morphology and defect characterization in MEX processes. Unlike traditional rasterization methods, the proposed approach retained raw point cloud data, preserving critical surface details and enabling a more precise analysis of defect morphology. Through the integration of functional analysis tools, quantitative indices such as Projected Percentage Area (PPA), Volume of Void (VV), and Volume of Material (VM) were developed to evaluate the distribution and severity of defects. These indices provided actionable insights into process performance, enabling accurate defect detection, localization, and quantification.

By addressing the lack of universally recognized process signatures in MEX, this work introduced robust and reliable metrics, to assess dimensional accuracy, surface quality, and process stability. The results highlighted the ability of these indices to distinguish between dimensional deviations and surface defects, offering a comprehensive framework for in-situ quality monitoring. Furthermore, the contour extraction algorithm proposed in this study demonstrated the potential for real-time corrective actions, such as targeted material deposition in underfilled areas and material removal in overfilled regions. These corrective strategies align with the zero-defect manufacturing paradigm, reducing waste and enhancing resource efficiency. The methodologies were rigorously tested on specimens with varying geometries and process parameters to evaluate their robustness and versatility. The findings revealed that sharp geometries, such as star shapes, were more prone to material accumulation and defects, especially at tips and corners, while circular geometries exhibited better surface control. These insights underscore the importance of integrating process-specific metrics with real-time monitoring to address challenges posed by complex geometries.

In addition to its applications in MEX, the proposed systems put the basis for broader adoption in other AM technologies, such as L-PBF and L-DED, where real-time monitoring and functional analysis are equally critical. Indeed, by looking at section 3.3.5, the laser profilometer has been already proposed as a monitoring sensor for metal AM, because of its precision and its ease of use. By exploiting the versatility of the high-resolution BLP and by utilizing the raw point cloud data, this research provides a pathway for achieving higher precision in AM metrology. The introduction of robust process signatures and actionable defect metrics addresses a key need identified in the literature, laying the groundwork for future advancements in AM monitoring systems.

In summary, this work contributes significantly to broadening the metrological side in MEX processes by introducing a comprehensive, in-situ monitoring methodologies based on surface quality indexes. It advances both the understanding and the practical application of in-situ functional analysis, offering a scalable solution for defect detection and process optimization. These findings not only enhance the reliability and repeatability of MEX processes but also establish a foundation for advancing metrology across the broader field of additive manufacturing.

4.8. Critical review of MEX proposed monitoring methods

Despite all the advantages discussed in section 4.7, the proposed monitoring systems were characterized by some limitations which should be addressed in future works. One key limitation lies in the fixed position of the BLP, which is secured to the 3D printer's frame. This setup inherently restricts the maximum height of the parts that can be printed, as the BLP operates within a predefined field of view (FOV) where measurements maintain certified accuracy. Beyond this range, the reliability of measurements reduces, effectively defining a fixed scanning volume that cannot be changed with the current setup. To solve this issue, a possible improvement would be to mount the BLP on a movable axis synchronized with the printer. Such a configuration would enable the sensor to move upward at the end of each scan, expanding the system's effective scanning volume and allowing for taller parts to be monitored.

Another important factor to consider is the test of the monitoring system on a real-time case. Despite it was demonstrated that point cloud can be used as real-time monitoring tool for AM [212], additional experiments are necessary to validate the proposed quality indices under more complex and realistic conditions. During these preliminary experiments the feasibility and potential of the quality indexes were demonstrated but no information about the computational cost of these algorithms was conducted. This represents a critical step that must precede the full integration of the monitoring system into the printing process. Understanding the computational requirements is essential to ensure the system operates efficiently and does not hinder the printing workflow. In the context of real-time monitoring, it would also be valuable to explore the integration of the computed quality indices into neural network models. Such an approach could significantly expand the range of monitoring applications, enabling advanced defect prediction and process optimization. By leveraging machine learning, the monitoring system could provide deeper insights into the printing process, enhancing its utility and scalability for broader additive manufacturing applications.

5. L-PBF monitoring for lattice structures characterization

Despite the extensive literature on monitoring systems and techniques L-PBF-related, lightweight structures remain particularly challenging in terms of in-process monitoring due to their complex nature and their intricate features. Offline inspection methods (such as XCT and SEM) have been proved to be highly effective by evaluating dimensional accuracy, surface quality, and porosity. However, these methods are typically costly, and time-consuming, making them not suited for real-time monitoring purposes. This poses a critical limitation to AM processes, where defects can lead to significant material and energy waste.

Current research highlighted the need for in-process monitoring systems for lightweight structures that can capture process signatures, such as strut diameter, and axis waviness. These are crucial for assessing the mechanical properties and overall quality of lattice structures. In response to these challenges, the work presented in this chapter leverages promising HR-OT monitoring system, to provide a robust and reliable solution for real-time defect detection in lattice structures production. In this section the monitoring activities performed to evaluate lattice structures produced by L-PBF are discussed. First, the lattice design and production are described. The monitoring setup is illustrated consequently, followed by the image processing algorithm description. Results obtained from the experiment are discussed and final, the section concludes with conclusions and a critical review section. This research work was conducted in collaboration with Prof. Sabina Luisa Campanelli's research team, which carried out the activities related to the fabrication of the lattice structure using the L-PBF process. The results of this work have been published in the following research paper: [38].

5.1. Lattice design and production

The lightweight structural element investigated in this study is the Octet-Truss (OCT) elementary cell, known for its symmetrical geometry in all three dimensions. Each unitary OCT cell, with dimensions of 8 mm and strut diameters of 2 mm, was replicated periodically to occupy a parallelepiped volume with a square base measuring 24 × 24 mm^2 and a total height of 47 mm and the final result is displayed in Fig. 40. Additionally, two skins were incorporated into the design: a bottom layer of 5 mm thickness and a top layer of 2 mm thickness. These dimensions, particularly the strut diameter and cell size, were carefully selected to align with the printability limitations and processing constraints established in prior studies [213], which emphasize factors such as powder particle size, laser beam focusing capabilities, and the challenges associated with generating detachable supports without inducing distortions in the specimen. The CAD model for the OCT structure was created using nTopology software, employing specific discretization parameters to ensure a high level of accuracy in the resulting model. Following this, the STL file was imported into Materialize Magics for further preparation, including optimal placement on the building platform and slicing operations. The manufacturing process utilized L-PBF technology, executed on a Concept Laser M1 Cusing machine equipped with a solid-state Nd:YAG laser with a wavelength of 1060 nm, a laser spot diameter of 200 µm, and a maximum power output of 100 W. The process parameters were set with the laser power at 100 W, a scanning speed of 180 mm/s, a layer thickness of 40 µm, and a hatch distance of 140 µm. The structure was oriented at a 45° angle relative to the recoater blade to prevent interference during the recoating process. A contour infill scanning strategy was employed, involving random 5 × 5 mm scanning islands to minimize thermal stress [213]. AISI 316L gas-atomized metal powder, characterized by its spherical shape and particle size distribution of 15–45 µm, was used as the material for manufacturing. Together with the lattice structure, four cylinders with 14 mm diameter were printed at specific location on the substrate as shown in Fig. 40. These will be necessary during the perspective correction phase.

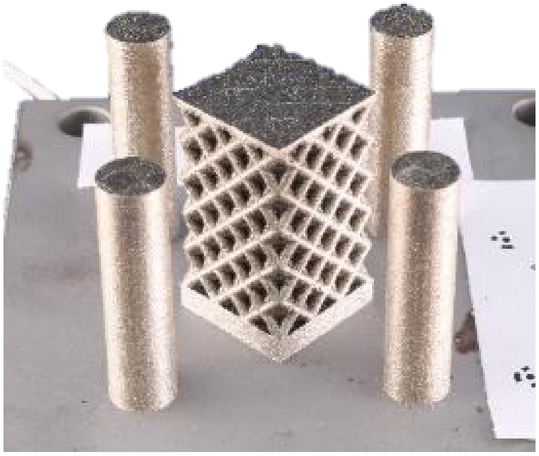

Fig. 40: OCT lattice structure produced during the proposed experiment.

5.2. Monitoring setup

The monitoring system employed in this study was designed to capture high-resolution images of the layer-by-layer L-PBF process using a consumer-grade DSLR camera, the Canon EOS 760D, equipped with a 24.2 megapixel APS-C sensor (22.2 × 14.8 mm), in the configuration shown in Fig. 41. The setup configuration employed a Canon EF 105 mm macro lens, achieving an optical resolution of 18 µm/pixel. This resolution aligns with comparable high-resolution optical tomography (HR-OT) systems and represents an improvement over earlier setups [107].

The system was configured to record light emissions resulting from the laser-material interaction during the scanning of each layer. The exposure time for each frame was synchronized with the time required to complete the laser scan of a layer, ensuring that the camera captured the full scanning trace of the laser. The camera is shooting in bulb mode. This synchronization was achieved using a trigger mounted on the recoater system, allowing the camera to adjust exposure times dynamically for layers with varying geometries, as commonly observed in lattice structures.

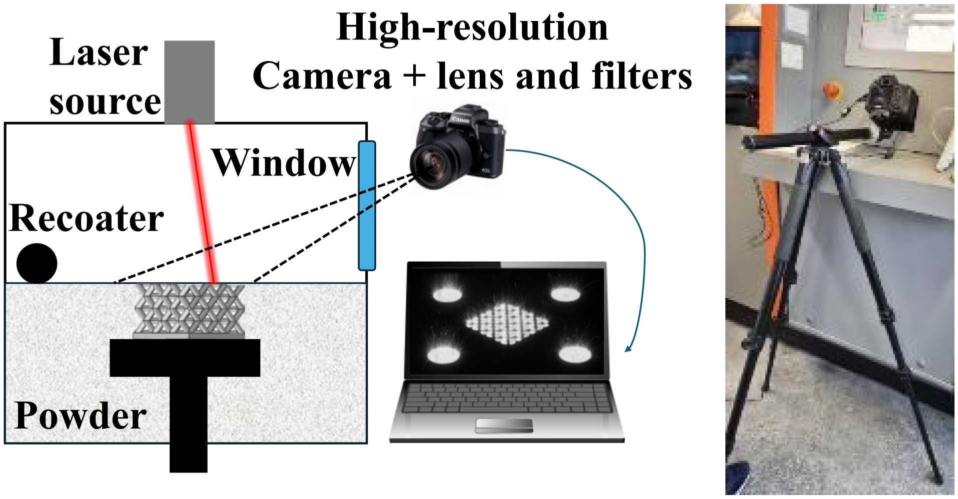

Fig. 41: HR-OT setup.

The acquisition process began immediately after the recoater completed spreading the powder and ceased just before the blade initiated spreading for the next layer. To maximize the depth of field and ensure all slices of the specimen were in focus, the aperture was set to f/29. ISO sensitivity was kept at 100 to maintain image sharpness and avoid noise. Neutral Density (ND) filters were mounted on the lens to control the light intensity and prevent overexposure during image acquisition. Since the AM machine was not equipped with dedicated monitoring equipment, the camera was placed externally with an off-axis configuration, inclined at a specific angle to capture the build area through the single window available on the front panel of the printing chamber. A telescopic tripod was employed to position and stabilize the camera at the correct angle. Because of the off-axis nature of the monitoring setup, perspective corrections were necessary to ensure accurate geometric representation in the captured images.

5.3. Perspective correction

As explained in the previous chapter, the camera is tilted of a specified angle to the bed. This off-axis nature introduced perspective phenomena in the resulting images that cannot be neglected. Therefore, before applying the image processing algorithm, a perspective correction needs to be done, ai it is shown in Fig. 42. The initial phase focused on performing the perspective correction of images by identifying the coordinates of reference cylinders positioned at the extremities of the plate. These coordinates were obtained using a coordinate measuring machine (CMM Demeet 400, with a resolution of µm X/Y/Z 3.9+L/150). A contact measurement system was employed, consisting of a ruby-tipped probe with a 2 mm diameter, manually operated via a joystick. The process began by defining a reference plane coinciding with the upper surface of the specimen base. Eight points were probed on the surface to establish this plane. A reference system was then set up by defining two points along the x-axis and one along the y-axis. With the reference system established, the coordinates of the cylinder centers were measured by taking three readings for each cylinder. Each measurement involved acquiring ten points: four points on a plane at a random height z relative to the specimen's reference plane, four on a different plane, and two randomly selected points. This multi-point approach minimized measurement uncertainty. The cylinder center coordinates were determined by averaging the three sets of measurements.

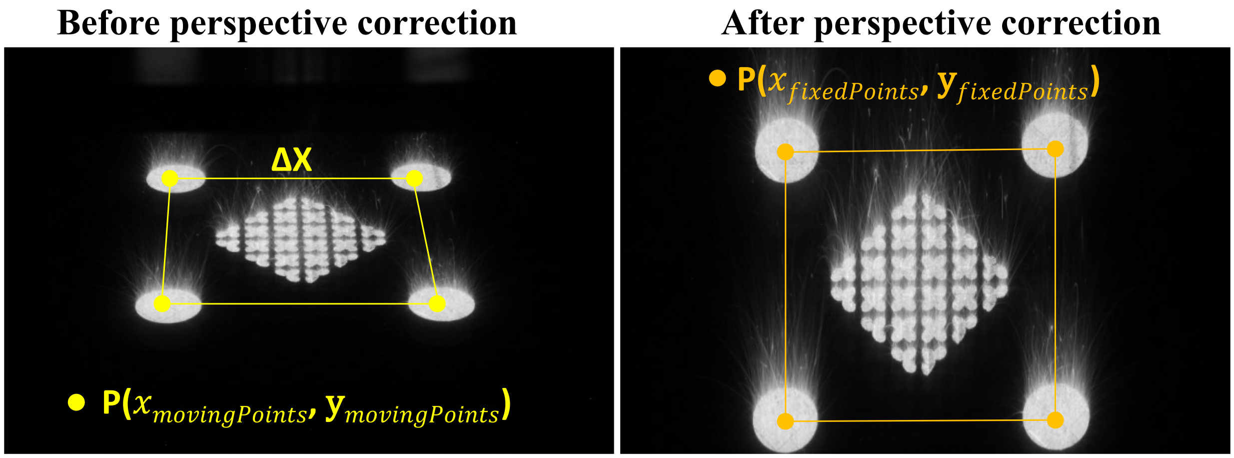
Before perspective correction

After perspective correction

Fig. 42: Perspective correction process.

Subsequently, the pixel-based coordinates of the cylinder centers were extracted from optical monitoring images. Five sample images were selected from the total dataset of 1175 images to compute an average of the extracted coordinates. This is possible because the cylinders displayed in every image theoretically should have the same location in the picture, unless camera movements. The distance between the camera sensor and the powder bed remains unchanged because after the deposition of each layer, the platform is lifted down to leave space for the new layer production. Following this, it was possible to consider only some images to generate average coordinates for the centers of the calibration cylinders. The software ImageJ was utilized for the task of perform the perspective correction of the images, following these steps:

- Image binarization using the "Make Binary" command in the "Process" menu.
- Noise removal via the "Remove Outliers" command.
- Edge detection with the "Find Edges" function.
- Data extraction using the "Analyze Particles" command in the "Analyze" menu.

In this phase ImageJ was used for its simplicity, as only 5 images were required to obtain the necessary data useful for the perspective correction. Indeed, compared to MARTLAB, ImageJ offers a more straightforward method for extracting pixel coordinates. The pixel-based coordinates from each sample image were averaged, resulting in a single pair of x, y values for each cylinder. In the subsequent phase, the real-world mm-based coordinates derived from the

CMM measurements and the pixel-based coordinates from the optical images (prior to perspective correction) were used to compute the corrected pixel coordinates. The transformation was defined in equations (6) and (7) as:

$$x_{fixedPoints} = x_{movingPoints} + \left(\frac{dx}{ris}\right) \qquad (6)$$

$$y_{fixedPoints} = y_{movingPoints} + \left(\frac{dy}{ris}\right) \qquad (7)$$

Where $x_{fixedPoints}$ and $y_{fixedPoints}$ are the corrected pixel coordinate, $x_{movingPoints}$ and $y_{movingPoints}$ are the uncorrected pixel coordinates, dx and dy are the differences along x and y axes between CMM-measured coordinates in mm and ris is the resolution, computed in equation (8) as:

$$ris = \frac{\Delta x}{\Delta X}\left[\frac{mm}{pixel}\right] \qquad (8)$$

Here, Δx represents the distance in mm between two cylinders along the same y-coordinate from the CMM measurements, while ΔX is the corresponding pixel distance in the optical image.

Once established the average centers pixel coordinates for the perspective correction, based on the 5 sample images, and the processing workflow for each image was finalized, MATLAB was employed to batch process and to apply perspective correction to all the optical monitoring images (Fig. 43). In other words, the ImageJ software was initially used as a mean to evaluate if the algorithm proposed was reliable or not and, when the best solution was identified, it was transferred to MATLAB software to automate the entire image processing phase.

The corrected pixel coordinates were multiplied by the resolution to convert them into mm. This allowed a comparison between the optical monitoring-derived cylinder distances (69.942 mm) and the CMM-measured values (70.225 mm). The minimal difference confirmed the accuracy of the perspective correction process. When satisfying coordinated for the four points were found, the perspective correction phase was concluded. Indeed, the same coordinates will be used to correct every image of the dataset.

5.4. HR-OT applied for lattice structure monitoring

5.4.1. *Image processing algorithm*

The image processing method developed in this study aims to enhance the resolution of the existing High-Resolution Optical Tomography (HR-OT) system [214] by improving the extraction and analysis of the geometric contours from images. This process enables the generation of accurate 3D point clouds for dimensional analysis and geometric comparisons with 3D scans or CAD models. Initially, perspective-corrected images were used as the basis for extracting the laser scan contours. A systematic selection process was employed to identify five representative images from the total dataset of 1175 images, chosen at intervals to provide a general sample. These images underwent a sequence of filtering and processing steps, as illustrated in Fig. 43, to isolate the geometric contours while excluding noise and artifacts, such as spatter generated during the laser fusion process. Special attention was given to mitigate the influence of artifacts amplified by the perspective correction process.

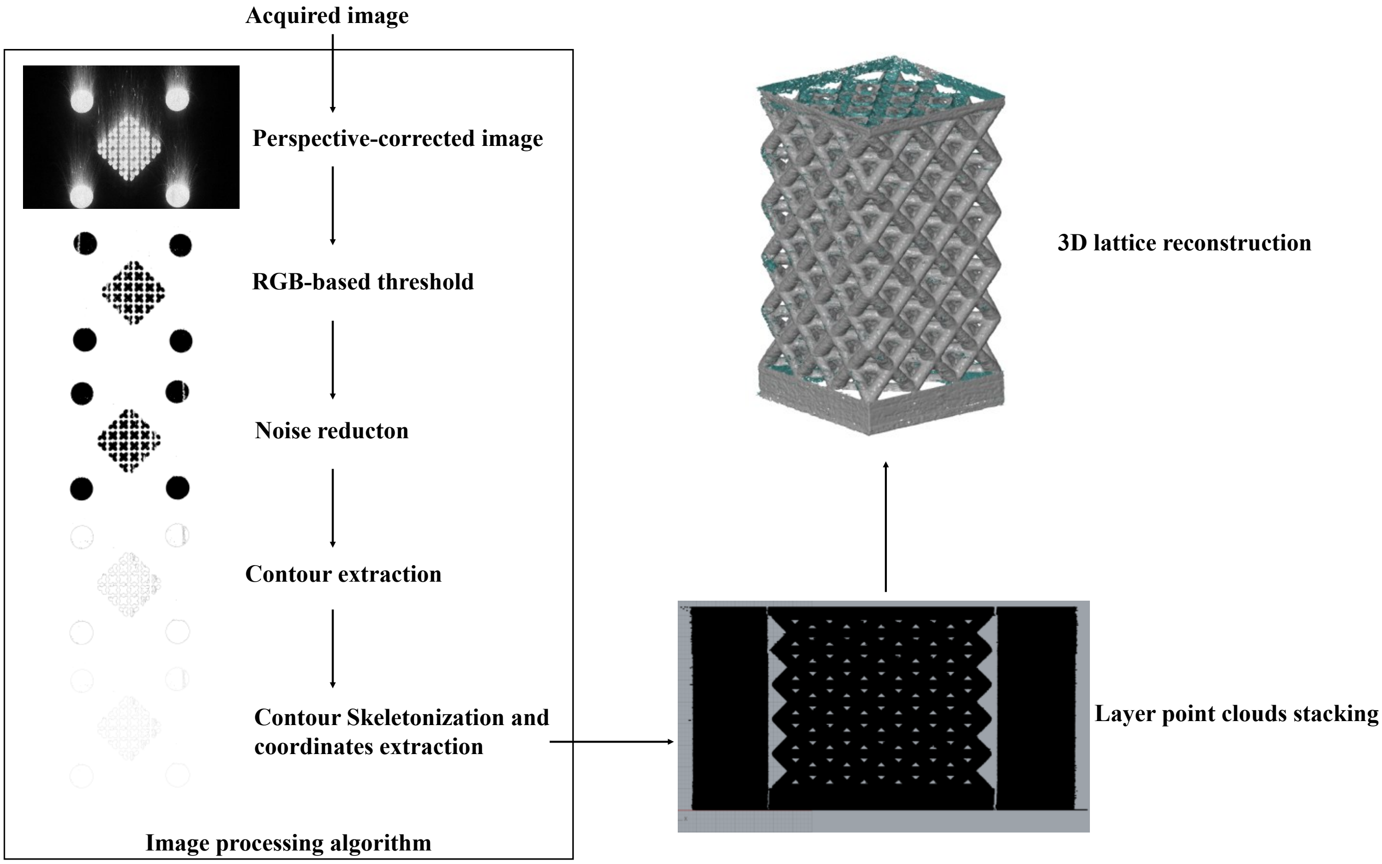

Fig. 43: Image processing workflow for HR-OT monitoring.

The image processing method began with the application of color thresholds based on RGB values to emphasize the laser-scanned areas, ensuring that the parameters were tailored to different groups of images to account for variations in lighting and exposure. Following this, the images were converted into a binary format, isolating regions of interest while minimizing the inclusion of irrelevant features, such as for example the spatter influence. A noise reduction filter was then applied to remove pixel-level noise, enhancing the clarity of the binary images and ensuring a clean dataset for better contour extraction. Subsequently, an edge-finding algorithm was used to detect the contours of the images, which were then skeletonized to reduce their width to a single pixel, providing a precise representation of the geometric boundaries. Once the correct contour of each layer was extracted, the x, y coordinates of each point belonging to the contour were extracted. Subsequently, the point clouds relative to each layer were stacked by automatically adding the z coordinate and the 3D reconstruction was done. The final step involved segmenting the processed images into contours corresponding to external geometries and potential internal defects, enabling separate analyses of geometric imperfections and material anomalies.

To streamline the processing of a large dataset (1175 images), a MATLAB script was developed. This script automated the extraction of x, y coordinates for each pixel in the contours and assigned a z coordinate corresponding to the layer height. The resulting data were saved as a .txt file for further analysis.

Irrelevant elements, such as spatter and internal cylinders, were manually removed to refine the dataset. To enhance efficiency, the point cloud was uniformly downsampled, reducing the total points to approximately 8 million. The refined point cloud was then converted into a mesh using Geomagic Wrap. The maximum number of triangles in the mesh was capped at 2.5 million to optimize dimensional characteristics while maintaining computational efficiency. This enhanced image processing method demonstrated improved accuracy and efficiency in generating point clouds, providing a reliable basis for dimensional analysis and geometric comparison in the HR-OT system. The system developed operates in two main stages: the acquisition of frames and the subsequent image processing. The frame acquisition phase was seamlessly integrated into the printing process, without adding delays, as the camera was automatically triggered by a sensor linked to the recoater mechanism. Once the recoating phase was completed with a new powder layer, the sensor activated the camera to capture the image. The image processing stage followed immediately, including grayscale conversion, binary transformation, contour detection, and skeletonization. The duration of this processing phase depends on the computational capacity of the system but typically remains shorter than the time required to complete the scanning of each layer. This allows the analysis of data from one layer to be completed before the subsequent layer is printed. As a result, the system is highly suitable for real-time monitoring and facilitates effective process control during additive manufacturing.

5.4.2. *Data analysis methodology*

The methodology for data analysis was designed to evaluate the dimensional and geometric accuracy of the as-built lattice structure and to identify critical defects generated during the L-PBF process. The in-situ data analysis involved comparing the slice contours extracted from HR-OT images with the corresponding CAD model contours. This comparison was conducted using software capable of generating colored deviation maps and histograms, highlighting the differences between homologous points from the CAD and HR-OT data for representative layers and overall geometry. The average of the absolute deviations was computed layer-by-layer, allowing for the analysis of trends in dimensional accuracy with respect to the sample height. By evaluating 2D sections, it was possible to assess the geometric conformity of the as-built layers to the nominal design and to identify critical regions prone to deviations, an example is illustrated in Fig. 44.

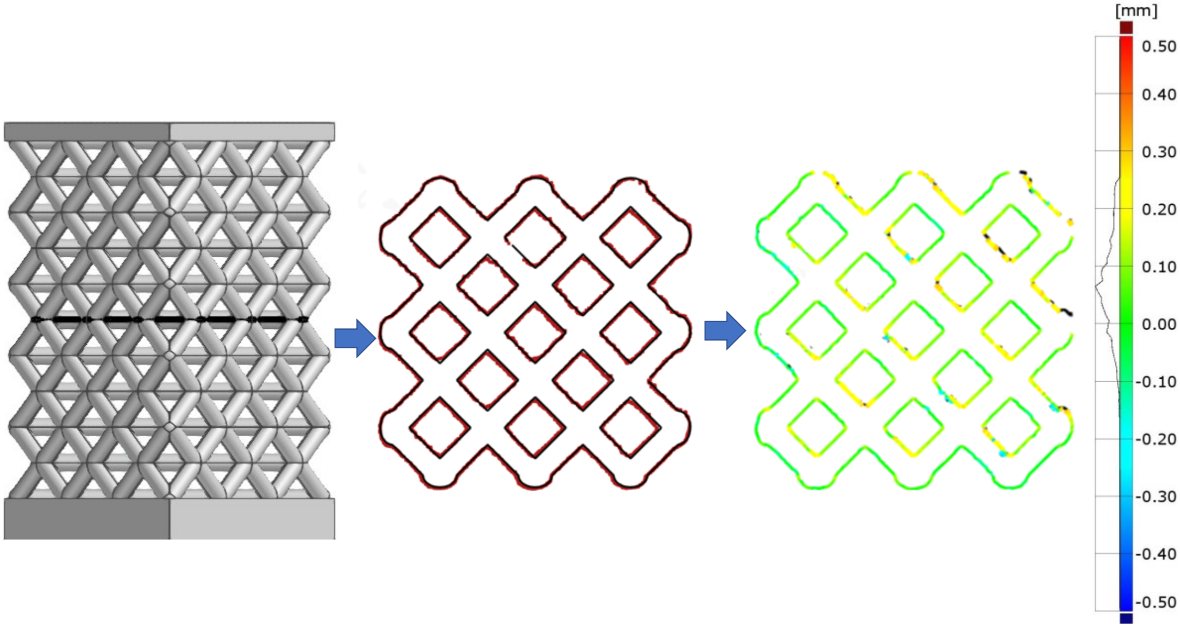

Fig. 44: Example of 2D profile geometric deviation analysis.

A local analysis of the lattice structure's geometry was performed to investigate key parameters such as strut thickness and waviness. These parameters are critical as strut waviness can lead to eccentric loading, causing premature collapse below nominal loads, while deviations in strut thickness significantly affect the mechanical and energy absorption properties of the structure [48,215]. The analysis focused on two representative struts with different orientations: one aligned with the recoating direction and the other oriented opposite to it. Layer-by-layer contours were extracted from HR-OT images, and the strut cross-sections, elliptical due to their 45° inclination, were analyzed. Strut thickness was estimated from the minor axis of the fitted ellipse, while strut waviness was determined by measuring the Euclidean distance between the centers of the ellipses fitted to the as-built and nominal sections. At the conclusion of the manufacturing process, the extracted layer-by-layer contour points were compiled into a high-resolution point cloud, which was converted into a detailed 3D mesh. This mesh allowed for a comprehensive 3D comparison with the CAD model, including both external and internal features. The comparisons enabled an in-depth evaluation of dimensional deviations and provided data for further numerical simulations or post-process analyses, as will be demonstrated in the next section. For analyzing the lattice structure's internal geometry, including strut diameters and axes deviations, cross-sectional data from the HR-OT-derived mesh was utilized. Sections perpendicular to the strut axes were created to measure strut diameters, while deviations in the beam axes were evaluated by comparing the actual positions of circle centers in the as-built structure to their nominal positions from the CAD model. The graphical explanation of how the strut thickness and waviness were computed is shown in Fig. 45. This approach enabled precise identification of geometric imperfections, such as beams over or under-sizing, axis waviness and thickness, providing valuable insights into the structural integrity and potential weaknesses of the lattice. The results of these analyses, including deviation maps, strut dimension evaluations, and axis comparisons, will be detailed in the following section to highlight the efficiency and accuracy of the proposed monitoring system and its ability to detect and quantify defects in-situ and in real-time.

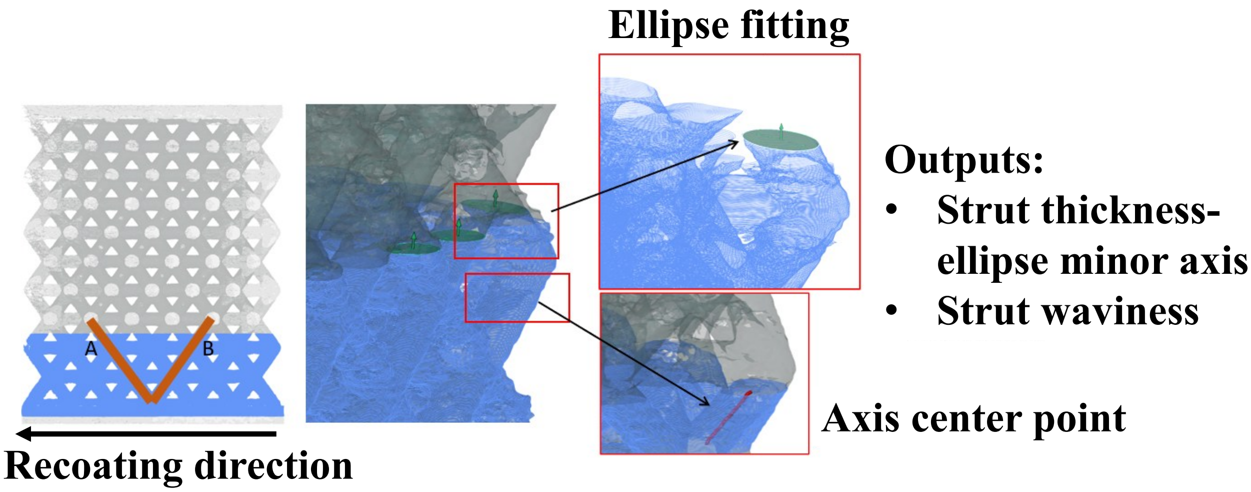

Fig. 45: Computation of strut thickness and waviness.

5.4.3. ***Results***

The results of in-situ monitoring for L-PBF produces lattice structure provided both qualitative and quantitative insights into the dimensional accuracy, geometric deviations, and critical defects encountered during the manufacturing process. These findings were analyzed layer-by-layer and supplemented with 3D geometric comparisons to provide a comprehensive assessment about the capabilities of the High-Resolution Optical Tomography (HR-OT) system.

The 2D deviation analysis focused on comparing the contours extracted from HR-OT images, based on the proposed image processing algorithm, with corresponding CAD data for three representative layers at varying heights. Colored deviation maps and histograms were generated to visualize the dimensional discrepancies for each layer (Fig. 44). These tools proved to be highly effective in identifying critical deviations and provided quantitative feedback on the geometric and dimensional accuracy of the as-built structure. Layer-by-layer trends of the absolute deviations were analyzed (Fig. 46). Most deviations were within 0.1 mm, demonstrating good agreement between the as-built structure and the CAD model for most layers. However, layers corresponding to the strut sections (Fig. 47, a) and external nodes (Fig. 47, c) showed higher deviations, with values reaching up to 0.2 mm. These increased deviations were particularly prominent in the top skin layer, where geometric distortions were observed. The results highlighted those critical areas, such as overhanging struts and external nodes, are prone to greater inaccuracies, necessitating further refinement in the L-PBF process. At the end of the process, a 3D comparison was carried out between the HR-OT-derived mesh and the CAD model, providing a comprehensive assessment of the structure's overall quality.

As shown in the colored maps (Fig. 48), deviations were predominantly within ±0.1 mm, confirming the consistency of the in-situ 2D deviation analysis.

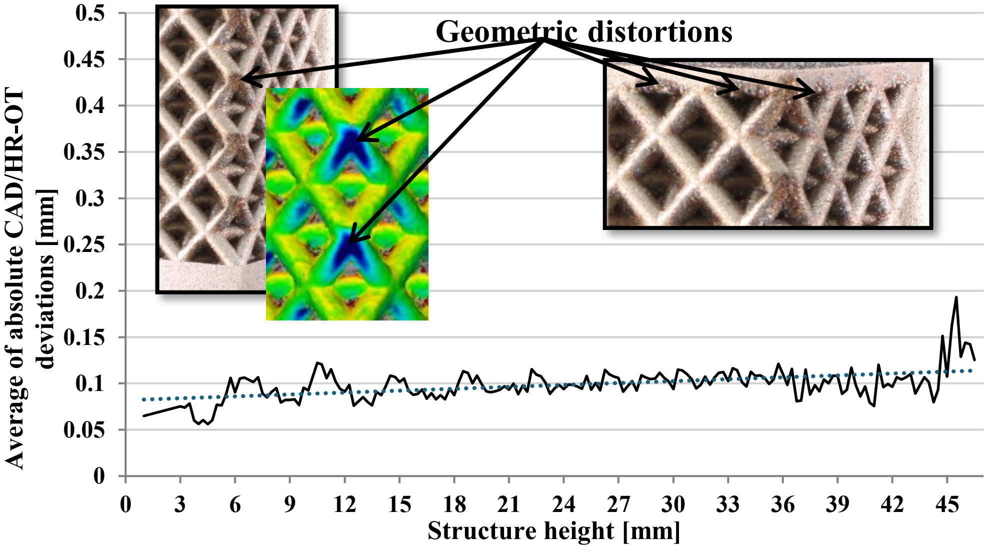

Fig. 46: In-process 2D deviation analysis between the HR-OT and CAD data. As a reference, the colored map, showing the comparison between the photogrammetric model and the CAD, is reported in the picture.[38]

Though critical areas were identified on external surfaces, especially at overhanging struts and external nodes, which are represented by the blue areas observable in Fig. 46. These findings were consistent with observations from the 2D deviation analysis. While the 3D comparison was performed offline and is similar to XCT analysis for characterizing geometric and dimensional properties, HR-OT offers the unique advantage of collecting layer-by-layer data during the process, with significantly lower costs. This makes HR-OT particularly suitable for real-time monitoring of complex geometries, such as lattice structures.

A localized analysis of the struts geometry was conducted to examine key features, such as strut thickness and waviness. The thickness of the struts, measured as the minor axis of fitted ellipses, revealed distinct trends for two differently oriented struts, labeled A and B in Fig. 45. Strut A, aligned with the recoater movement, exhibited an average thickness of 1.98 mm with a standard deviation of 0.03 mm. The absolute percentage errors for this strut ranged from 1.60% to 5.22%, with most values falling between 1.97 mm and 1.99 mm. Conversely, strut B, growing in the opposite direction to the recoater, showed greater deviations, with an average thickness of 1.89 mm and a standard deviation of 0.06 mm. The absolute percentage errors for strut B ranged from 1.43% to 16.80%, with most values between 1.89 mm and 1.93 mm (Fig. 49, a and b). The waviness analysis further highlighted differences between the two struts. Strut A exhibited an average waviness of 0.10 mm with a standard deviation of 0.03 mm, while strut B displayed an average waviness of 0.13 mm with a standard deviation of 0.07 mm.

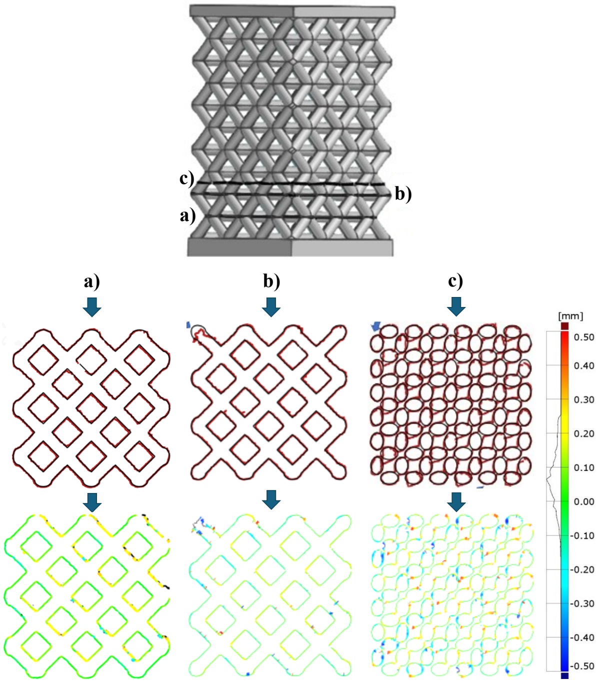

Fig. 47: HR-OT (red) and CAD (black) contours superimposed and 2D deviations analysis at layer n 575 (a), layer n 625 (b) and layer n 725 (c)

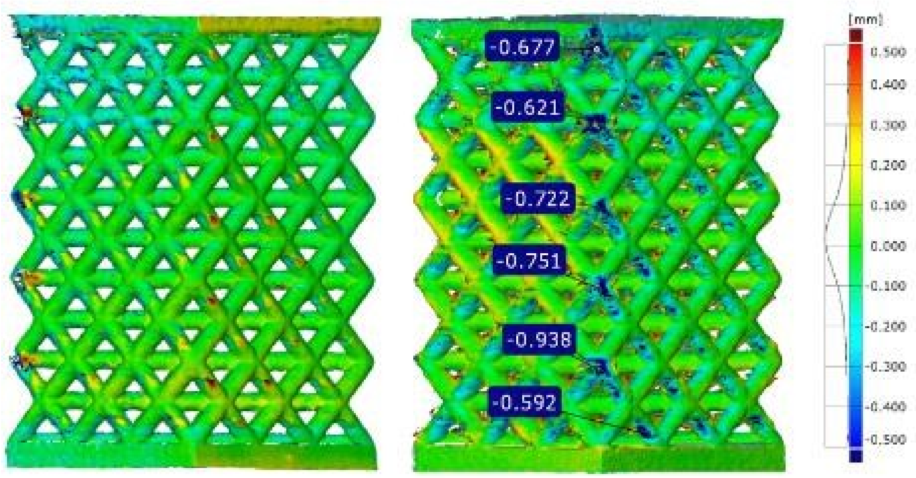

Fig. 48: 3D geometric deviation map between the HR-OT point cloud and the CAD model.

The discrepancies can be attributed to the growth direction of the struts relative to the recoater, with strut B, oriented towards the recoater movement, experiencing greater instability (Fig. 49, c and d). As highlighted in the literature [107,142], optical tomography is a widely used technique for detecting internal defects, utilizing visible and near-infrared camera sensors. This technique indeed acquires a single image per layer which represents a collection of signals, imaged into the corresponding pixel detector, proportional to the radiation intensity emitted from the laser-powder interaction. Through this approach, the hatching pattern and scanning strategy become visible, within the constraints of the system's resolution capabilities. Furthermore, variations in the laser-powder interaction are detectable as changes in emitted radiation intensity, allowing anomalies in the melting process, potentially linked to defects, to be identified by analyzing pixel gray value variations. These intensity changes depend on the material state influenced by the laser; for instance, regions with unmelted powder emit higher intensity compared to areas of melted and resolidified material. This difference in emitted light is likely caused by the distinct cooling rates and thermal conductivity of unmelted versus melted and resolidified material. The proposed HR-OT technique proved effective in capturing anomalies related to the laser-powder interaction, offering valuable insights into layer-specific deviations and defect occurrence.

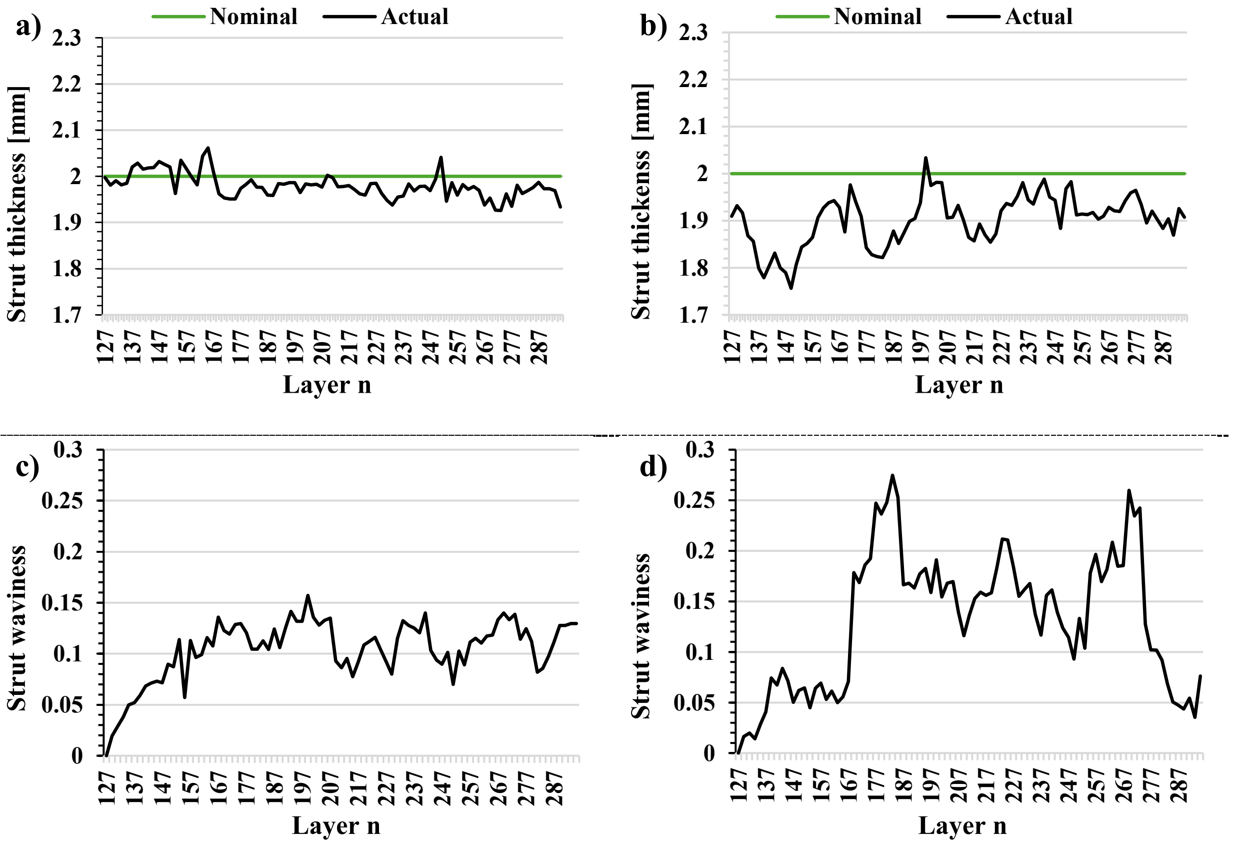

Fig. 49: Results obtained after the strut waviness and thickness evaluation. a) represents the strut thickness of the A strut, while b) is related to the thickness of the B strut. c) refers to A strut in terms of waviness and d) is related to B strut waviness.

For instance, gray value analyses of HR-OT images revealed differences in radiation intensity emitted from the laser interaction zone when defective process conditions happened, enabling the detection of process anomalies. These variations were linked to differences in thermal conductivity between unmelted powder and resolidified material, with superelevated areas and distortions most pronounced in strut edges growing against the recoater direction (Fig. 50). A profile plot illustrating pixel gray values along a straight line revealed differences between regions with unmelted powder underneath (red areas), showing values near 255, and those with melted and resolidified material (corresponding to the lattice structure section), which displayed lower gray values. Examining the same layer, regions with significant geometric distortions, such as superelevated areas and edges visible in the colored map (Fig. 50, a), were linked to pixels with lower intensity (lower gray values) caused by the remelting of previously melted material. This occurred due to its higher thermal conductivity compared to unmelted powder, leading to reduced heat accumulation. The intricate geometry of the lattice structure makes these designs susceptible to superelevated edge defects, which are particularly prominent in the strut sections because of their reduced size (Fig. 50, b). Between two struts, labeled A and B (Fig. 50, b), a notably larger distortion was observed on strut B, as it was the first area of the layer impacted by the recoater. Superelevated regions and geometric distortions were heavily concentrated on edges growing opposite to the recoating direction (Fig. 50, c), which, in some cases, could result in the failure of the building process.

Overall, the HR-OT system demonstrated its potential for in-process quality control, providing layer-by-layer data to detect geometric distortions and critical defects. These findings lay the groundwork for further statistical analyses and integration into process control strategies to enhance the reliability of LPBF processes for complex lattice structures.

5.5. Conclusion about L-PBF monitoring activities

This work introduced an innovative, cost-efficient in-situ optical monitoring system based on High-Resolution Optical Tomography (HR-OT) for layer-by-layer dimensional and geometric characterization of lattice structures manufactured via L-PBF. The proposed system demonstrated its capability to identify process inaccuracies and geometric distortions in real-time, utilizing 2D and 3D comparisons and localized analyses. At the conclusion of the manufacturing process, the system provided a detailed 3D reconstruction of the fabricated structure, enabling comprehensive quality assessments and potential integration with numerical simulation frameworks. The layerwise analysis highlighted critical insights into the geometric and dimensional accuracy of the fabricated structure by comparing actual data with nominal CAD specifications. Localized evaluations of strut geometry further underlined the system's utility, as these features significantly influence the structural performance of lattice geometries. The ability to measure key parameters such as strut thickness and waviness allowed for an in-depth assessment of features most susceptible to deviations during the L-PBF process. The accuracy of the implemented system was validated through comparisons with standard geometries, with average deviations of approximately 0.05 mm, aligning well with the inherent precision of the L-PBF process. These findings underscore the system's effectiveness in monitoring the fabrication of complex geometries and lattice structures. By reconstructing both external and internal features, the HR-OT system offers a cost-effective, faster and simpler alternative to X-ray Computed Tomography (XCT) for dimensional, geometric, and surface quality evaluations. In summary, the HR-OT system proves to be a powerful tool for in-process monitoring of LPBF, combining real-time capability, precision, and affordability. Its ability to capture internal structural details makes it an invaluable solution for ensuring the quality and performance of complex additive manufacturing builds, paving the way for improved reliability and reduced post-process inspection costs.

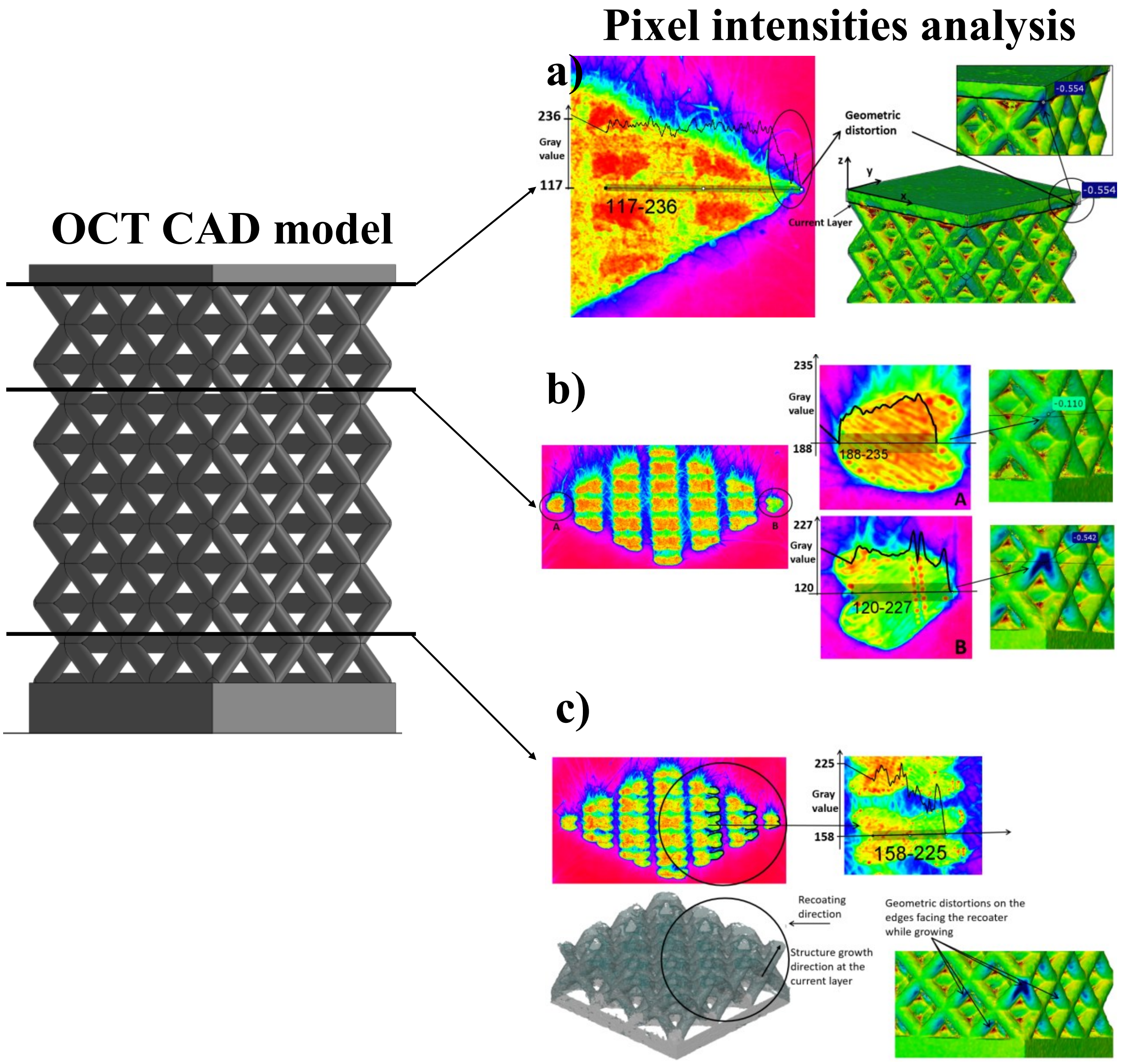

Fig. 50: False color image analysis based on the pixel gray values. In a) the focus is on a geometric distortion detected on the same layer. In b) layer representing the struts sections when approaching the nodes. In c) strut sections with the indication of their growth direction with respect to the recoating direction

5.6. Critical review on L-PBF monitoring method

The proposed monitoring method offers several advancements over existing state-of-the-art techniques for monitoring complex geometries produced via LPBF. However, some limitations must be acknowledged, as addressing these challenges is crucial for the widespread implementation of the proposed in-situ monitoring system. One primary area for improvement is the development of a closed-loop control algorithm. Such an algorithm would enable real-time testing to definitively demonstrate the effectiveness of HR-OT as a real-time monitoring system. Without this capability, the system remains primarily a diagnostic tool rather than a fully integrated real-time quality assurance method. Another challenge lies in the variability of spatter influence on the captured images. The spatter's effect can vary significantly between different manufacturing processes, making it necessary to optimize threshold limits for each application. At present, there is no standardized or rapid method for determining these parameters, which necessitates system calibration at the start of each production run. Similarly, the perspective correction must also be recalibrated for every new manufacturing setup. This process, while essential for ensuring data accuracy, adds a layer of complexity and preparation time to the system. An additional limitation is characterized by the use of physical markers, such as the four cylinders included in the field of view of the camera. These markers are crucial for both perspective correction and data validation. Given the inherent difficulty of performing measurements on lattice structures or freeform shapes, these markers serve as essential reference points. However, their inclusion requires material usage and design considerations that may not be feasible for every application. The single-camera setup of the system introduces another constraint. Measuring distortions along the building direction (z-axis) proved challenging, as the system struggled to differentiate between certain types of geometric deviations. For example, super-elevated edges might be misinterpreted as planar distortions due to the lack of depth information. This limitation highlights the need for a multi-camera system or additional depth-sensing technologies to enhance the system's ability to characterize three-dimensional deviations accurately. Despite these limitations, the HR-OT system remains a valuable tool for the characterization of lattice structures. Its ability to provide detailed insights into dimensional and geometric accuracy, along with its cost-effectiveness compared to other techniques like XCT, makes it an important starting point for developing advanced in-situ real-time monitoring systems. Addressing these challenges will further enhance the system’s reliability and expand its applicability, paving the way for broader adoption in industrial settings.

6. L-DED multi-directional monitoring based on a dual-camera system

Following the discussion in section 3.3.6, despite the wide range of monitoring systems discussed for L-DED, they still face critical limitations. Several techniques have been proposed to develop closed-loop systems that adjust parameters in real-time during powder deposition. Although, because of high computational demands, many systems only execute correction intermittently (e.g., every two layers as seen in [10]). It follows the need for monitoring systems that are fast enough to capture the process signatures on every layer and capable of correcting defects as soon as they occur. In addition, most current systems focus on simple, 2D single-direction thin wall geometries, which are far from complex, multi-directional shapes typically produced in L-DED applications. In this section the method proposed for L-DED multi-direction monitoring will be discussed. First, the design phase of the camera frame will be discussed. Consequently, the monitoring setup will be shown and the calibration method proposed for this system will be validated. The calibration turned out to be necessary to interpret correctly the measurements obtained from the monitoring system, which relies on a novel image processing technique tailored to melt pool height measurements. After explaining the data analysis methodology, the definition of the region considered reliable in terms of measurements will be shown. The results will be discussed and, finally, the conclusion about this activity and the critical review will be discussed. Before starting the discussion, it is important to highlight that the proposed monitoring system is based on two cameras monitoring the melt pool at the same time, but despite the image processing algorithm was designed for both cameras, the frame for X camera was already designed for monitoring purposes, as explained in [10].

The following research activities were executed in collaboration with Prof. Masakazu Soshi and Weijun Zhang, at ARMS LABS (University of California, Davis 95616, CA, USA).

6.1. Frame design

The monitoring system proposed relied on an off-axis dual-camera to enable multi-directional monitoring along the substrate plane. For this reason, the initial phase of the research activities focused on designing a robust frame to securely hold the second camera on the laser head of the L-DED machine. The requirements identified for the fixture design were as follows:

- Minimize camera movements during the deposition phase to ensure stable data acquisition.
- Protect the camera from excessive light emissions generated during laser-powder interactions.
- Facilitate easy maintenance operations for both the camera and the laser head.
- Allow precise alignment of the camera with the melt pool for accurate monitoring.
- Ensure a stable and easily attachable connection between the X and Y camera fixtures.

Based on these requirements, the design of the frame was executed on the software SolidWorks 2023 The primary structure, referred to as the "main body" (as seen in the Fig. 51), provides a robust interface between the laser head and the monitoring camera. Its cantilevered design necessitated the inclusion of stiffeners, which are securely connected to the laser head via a triangular support structure. This feature effectively reduces vibrations caused by the laser head's movement during operation. Additionally, an aperture was incorporated into the main body to allow for quick and convenient removal of the black panel holding the laser focusing lenses, a component subject to frequent maintenance because of paramount importance. Furthermore, the main body was connected to the laser head by only two screws, and this made the mounting and dismantling phases very easy and fast. To protect the camera lens, a welding glass holder was positioned between the camera and the melt pool. This holder is mounted using an L-bracket and a stand, both of which include adjustable sockets. These sockets enable manual alignment of the camera with the melt pool, compensating for potential production inaccuracies in the frame. The camera is considered correctly aligned with the melt pool when it is located at the center of the image resulting from the camera acquisition, explaining why it was important to consider an adjustable setup instead of fixed one. To enhance stability and robustness, a connector was designed to link the pre-existing X camera fixture with the newly developed Y camera fixture. This interconnection improves the structural integrity of the dual-camera system. The final assembly of the dual-camera system frame, as illustrated in the Fig. 51, represents the configuration used for the subsequent experiments detailed in the following sections. The integration of these design features ensures a stable, accessible, and efficient monitoring system, tailored to the requirements of the L-DED process. To provide the right robustness to the fixture it was decided to produce it with the same material used for the X camera fixture, which is stainless steel. But, to speed up the experimental phase, a prototype of this frame was 3D printed by means of a MEX printer, such as the Prusa i3 Mk3, using PLA. The PLA fixture, despite the high sensitivity to high temperature of the thermoplastic filament, proved to be effective for the purpose of the experiments. It is important to say that during the tests, the temperature never reached too high values because only six layers were printed.

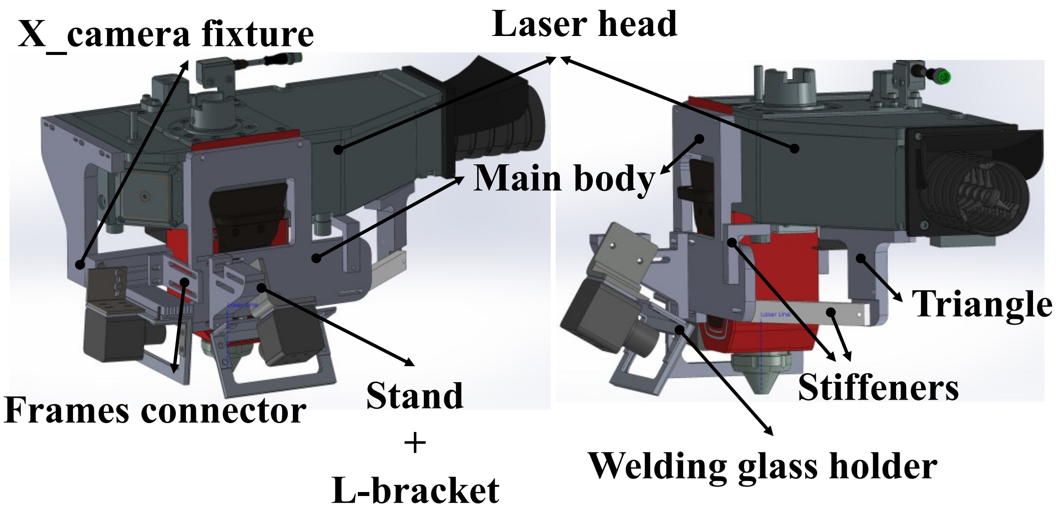

Fig. 51: Fixture components.

6.2. Monitoring setup

The experiments were conducted using a DMG MORI LaserTec 65 3D Hybrid machine, a versatile industrial system integrating three distinct modules: Laser Directed Energy Deposition (L-DED), milling, and Coordinate Measuring Machine (CMM) capabilities. The L-DED module enables precise layer-by-layer material deposition, while the milling module supports high-accuracy post-processing. The integrated CMM module, equipped with a RENISHAW OMP60 Optical touch probe, allows for detailed in-situ measurement and inspection. During the research activities were used the L-DED and the CMM modules. The L-DED module utilized gas-atomized 316L stainless steel powder with particle sizes ranging from 45 to 105 µm, with argon gas employed both as the shielding and carrier gas. A 2.5 kW fiber-guided diode laser, focused on a 2.96 mm diameter spot, was used to fuse the powder. The laser's energy delivery is optimized through a Fraunhofer COAX9 deposition nozzle, with a nominal stand-off distance of 11 mm from the top surface of the clad, ensuring consistent melt pool dynamics. For the monitoring system, two orthogonal digital cameras (designated as X and Y cameras) were employed to observe and analyze the melt pool's height during the deposition process. These cameras were strategically positioned using custom-built fixtures designed to ensure stable and precise alignment with the laser head, as discussed in the previous section and demonstrated in Fig. 52 where two examples of resulting images showed how the melt pool result centered. The X-camera fixture was fabricated from stainless steel for enhanced robustness, while the Y-camera fixture was 3D-printed in PLA using a Prusa i3 Mk3 Material Extrusion (MEX) printer. Despite PLA's moderate mechanical properties, the fixture's design proved sufficient for maintaining stability during low-height experiments, where heat generation remained within manageable limits. The monitoring setup with the centered images are illustrated in Fig. 52. The cameras used were ELP-USB130W01MT-MF40 digital models, equipped with complementary metal-oxide-semiconductor (CMOS) sensors. They offered a resolution of 1280×720 pixels, a 4 mm lens, and a frame rate of up to 30 Hz. While these cameras are relatively limited in frame rate and resolution, they provided a cost-effective and compact solution for real-time monitoring, which resulted in very easy implementation inside the machine building volume. To protect the cameras from intense reflections caused by high-temperature laser-powder interactions, welding glass was incorporated into the setup. This setup was critical for maintaining the accuracy of melt pool monitoring. The custom fixtures and their alignment ensured that the melt pool remained centered in each captured frame, optimizing the effectiveness of the image processing algorithm. The cameras were connected to two different laptops by USB cables to provide fast data exchange.

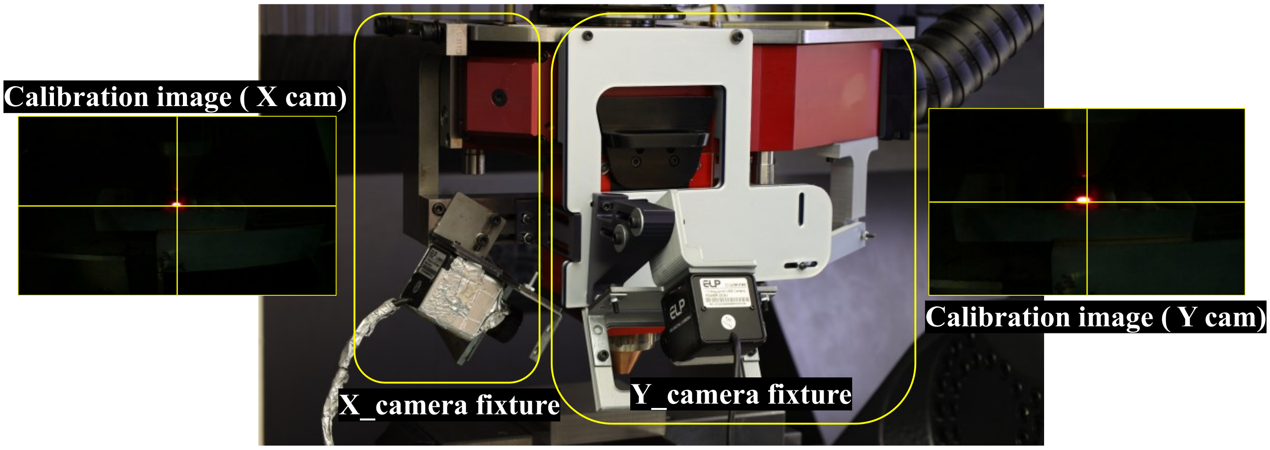

Fig. 52: Off-axis Dual-camera setup. The calibration images show how the melt pool is centered inside the image.

6.3. Camera calibration

As previously discussed in the context of L-PBF, the off-axis configuration introduces unavoidable perspective phenomena that can significantly affect measurements accuracy if left uncorrected. These perspective distortions necessitate a calibration process to ensure reliable melt pool height measurements. Calibration also serves, usually, to compute critical pixel-to-millimeter conversion factors (C.F.), which are essential for translating image data into meaningful physical dimensions. On the other hand, fisheye distortion can be neglected in this setup due to the dual-camera system's operational principle, where the melt pool is consistently centered in the captured images. Deviation from the image center rarely exceeds 1 mm, considering both upward and downward directions during deposition. Based on literature [216], such minimal deviations justify the exclusion of fisheye distortion corrections, provided the melt pool remains at the image center throughout the process. This precise positioning is ensured by custom-designed camera fixtures, which have been tailored specifically to maintain the cameras aligned and steady during operation. Furthermore, neglecting the fish-eye distortion notably simplifies the image processing algorithm by saving computational time destined for the fish-eye distortion correction.

A reliable calibration process for both cameras is critical to achieving accurate melt pool height measurements. This calibration is conducted prior to initiating the experiments to ensure that all measurement systems are properly aligned and configured. A novel calibration method, developed and validated specifically for this setup, is illustrated in Fig. 53. This method is based on the assumption that the melt pool is consistently centered in the image and that lens distortion effects are negligible for the measurement range under consideration. To simulate the production conditions, a 1 mm step gauge was employed as a reference. The gauge's mid-step was positioned at the nominal working stand-off distance of 11 mm from the nozzle, replicating the ideal deposition environment. Images of this setup were captured from both cameras after the laser pilot was turned on. The idea is that the pilot laser spot can be considered as the melt pool, because theoretically, when the nozzle is moved on the mid step, the laser spot is located at the same position the melt pool is supposed to be.

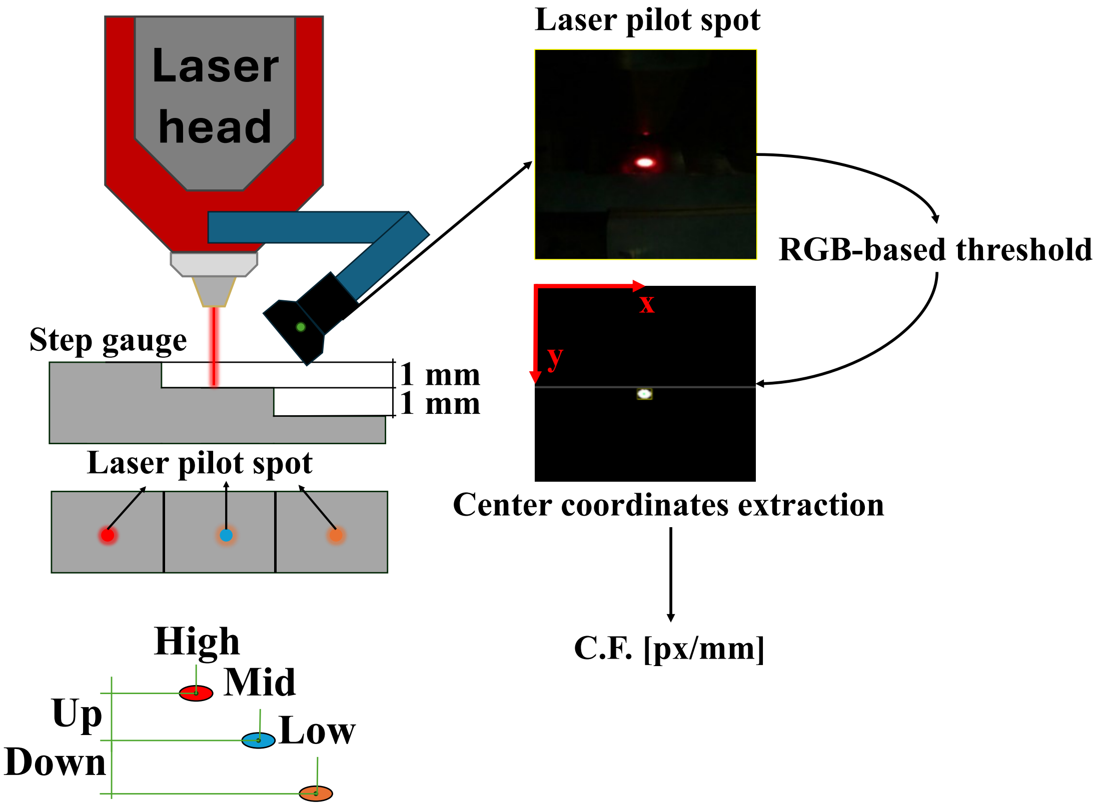

Fig. 53: Proposed calibration method.

Subsequently, the pilot laser spot was systematically moved on the other steps (High and Low, in Fig. 53), which are distant along the building direction (z-axis) by ±1 mm, with additional images taken at each position. The steps were previously grinded to ensure the correct step height of 1 mm. These images were processed using an RGB-based thresholding technique to isolate the laser spot, and the pixel coordinates of the spot's center were extracted for calibration purposes for all three cases. After measuring the pixel coordinates of each laser spot center, the pixel distances between these points were measured and compared with the real distance to compute the C.F. following the equations (9), (10) and (11):

$$C.F. = \frac{C.F._{up} + C.F._{down}}{2} \tag{9}$$

$$C.F._{up} = \frac{1\ [mm]}{y_{high} - y_{mid}\ [pixel]} \tag{10}$$

$$C.F._{down} = \frac{1\ [mm]}{y_{mid} - y_{low}\ [pixel]} \tag{11}$$

Where y_{high}, y_{mid} and y_{low} represent the pixel ordinates of the center of the laser pilot spot measured on the higher, the mid and the lower step of the gauge, respectively. To validate the proposed calibration method, the pixel-to-millimeter conversion factor (C.F.) derived from this approach was compared with results obtained using the Zhang method [217]. This calibration method, commonly referred to as chessboard calibration, is a widely used technique for calibrating cameras to correct geometric distortions because of the curvature of lenses and compute intrinsic (e.g., focal length, principal point) and extrinsic (e.g., camera position and orientation) camera parameters. This method uses a flat calibration target, typically printed with a grid of alternating black and white squares, which resembles a chessboard pattern. The pattern provides a series of well-defined corner points, which serve as reference features for the calibration. The process involves capturing multiple images of the chessboard, which usually should be less than twenty as suggested in [217], at different orientations and distances relative to the camera. By analyzing the positions of the corners in the captured images, the method estimates the camera's intrinsic parameters (such as focal length, principal point, and lens distortion coefficients) and extrinsic parameters (position and orientation of the camera relative to the target). The Zhang method accounts for lens distortion by modeling it mathematically and compensating for its effects. This is particularly valuable in ensuring accurate measurements when using wide-angle lenses or when perspective effects are significant. Once the calibration is complete, the method provides the corrected camera parameters, enabling accurate mapping of image pixels to real-world dimensions. In the context of this study, the Zhang method also computes the Euler angles, based on the values of the Rotation matrix, including the critical Pitch angle, which is used to adjust for perspective errors in melt pool height measurement. Euler angles, shown in Fig. 54, are a set of three rotational angles that describe the orientation of a rigid body in a three-dimensional space relative to a fixed reference coordinate system. They define how an object is rotated about the axes of the coordinate system in a specific sequence. The three angles are typically referred to as:

- *Yaw (ψ)*: The rotation about the vertical Z-axis.
- *Pitch (θ)*: The rotation about the horizontal Y-axis.
- *Roll (ϕ)*: The rotation about the longitudinal X-axis.

Table 10: Pitch angles for each experiment.

Experiment No.	**List of three experiment tests**	**Pitch θ [degrees]**	
		X camera	**Y camera**
1	**5Lines-1Layer**	37	25
2	**9Lines-1Layer**	35	25
3	**9Lines-6Layer**	35	33

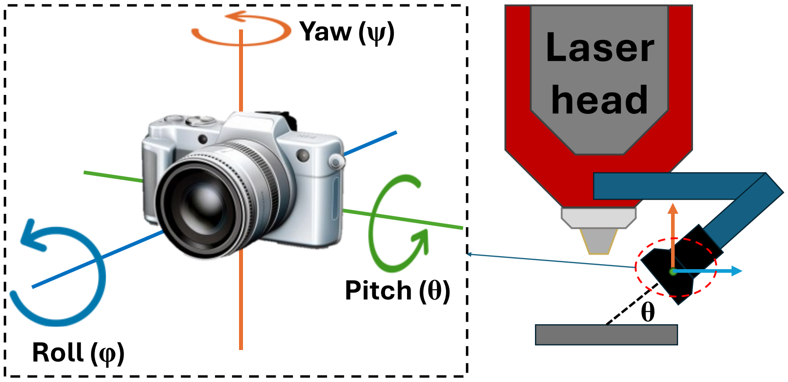

Fig. 54: Euler angles

The order of these rotations is important and depends on the chosen convention (e.g., Z-Y-X or Z-X-Y). In this study, the Pitch angle (rotation about the Y-axis) is of particular interest, as it represents the tilting of the camera relative to the horizontal plane. Any misalignment in the Pitch angle introduces perspective distortions, which can affect the accuracy of measurements like melt pool height. By calibrating the camera and determining these angles, corrections can be applied to compensate for perspective errors, ensuring reliable and precise measurements in the experimental setup. This calibration method was implemented using a 50x40 mm^2 chessboard, with a 5 mm squares, based on OpenCV library for Python through a custom script and for each camera ten chessboard images were used. After the camera parameters were obtained it was possible to undistort and correct the image perspective, based on the computed Pitch angle. In Table 10 the angles measured for both cameras before the experiments are displayed. These values will be fundamental for the final melt pool height measurements. The calibration process revealed that the presence of a Pitch angle introduced a perspective error in the melt pool height measurements. Specifically, as depicted in Fig. 55, the measured height AC exceeded the nominal height BF due to this angular misalignment. To mitigate this error, the Pitch angle was incorporated into the measurement as a correction factor. During the experiments, the sine of the Pitch angle was used to calculate the corrected height CD to substitute the perspective correction algorithm on the images. While this adjustment did not eliminate the error entirely, it ensured that the height measurements are sufficiently accurate for real-time control of the process. A slight underestimation of the clad height resulting from this correction is acceptable, as it produces a final part that is marginally higher than programmed, leaving a small allowance for post-machining operations. This operation further simplified the image processing algorithm because the prospective correction must be done on each frame during the production phase, leading to an increase of computational time which could prevent real-time measurements. Following the proposed calibration method, the C.F. from the Zhang method for each camera was determined within a 5 mm × 5 mm area at the center of the corrected image, by measuring the edges of a single square belonging to the chessboard that was located into the center of the image, and was compared with the one computed from the proposed calibration and the results are shown in Table 11.

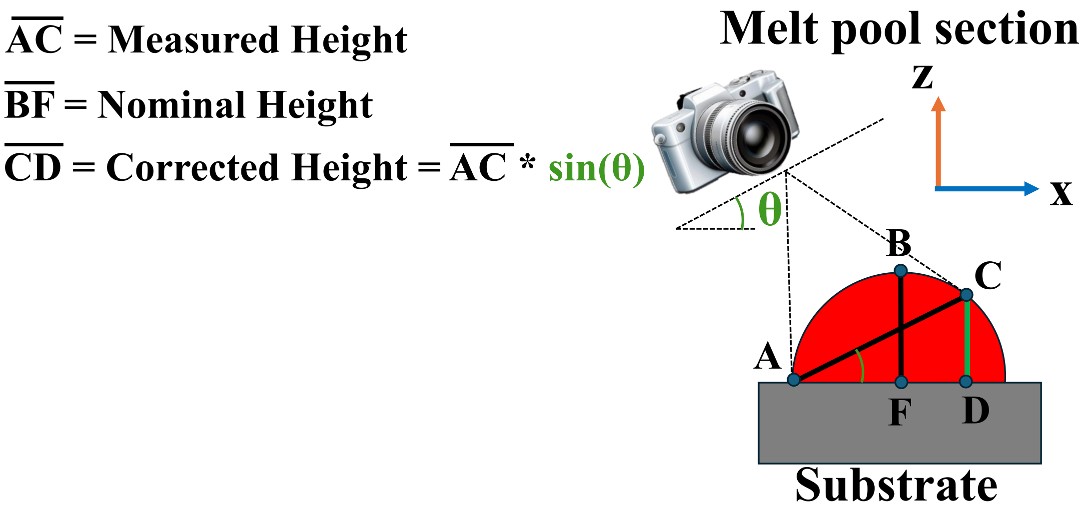

Fig. 55: Perspective correction factor based on the clad height.

The results shown in tab that the proposed calibration method provide reliable C.F. values, based on the C.F. obtained from the Zhang method, which can be considered as a valuable calibration instrument. In this calibration setup, complex distortion and perspective corrections were deliberately excluded from the real-time processing algorithm to reduce computational time. This simplification was justified by the consistent centering of the melt pool within each frame, which minimized distortion effects and ensured reliable measurements without extensive computational adjustments. This comprehensive calibration process not only enhances the accuracy of the melt pool height measurement but also demonstrates the feasibility of implementing real-time corrections for perspective errors, thereby supporting the reliability and repeatability of the additive manufacturing process. The results from the C.F. comparison in the two methods for the three performed experiments are displayed in Table 11.

Table 11: Conversion factor computed using two different calibration methods to validate the proposed calibration technique.

C.F. [mm/px]	**X camera**			**Y camera**		
	Zhang	**New**	**Diff.**	**Zhang**	**New**	**Diff.**
#1	0.1282	0.1256	0.0026	0.1316	0.1275	0.0041
#2	0.1191	0.1189	0.0002	0.1515	0.1431	0.0084
#3	0.1111	0.1083	0.0028	0.1351	0.1315	0.0036

6.4. Off-axial dual-camera multi-directional melt pool height monitoring system

6.4.1. *Experiments description*

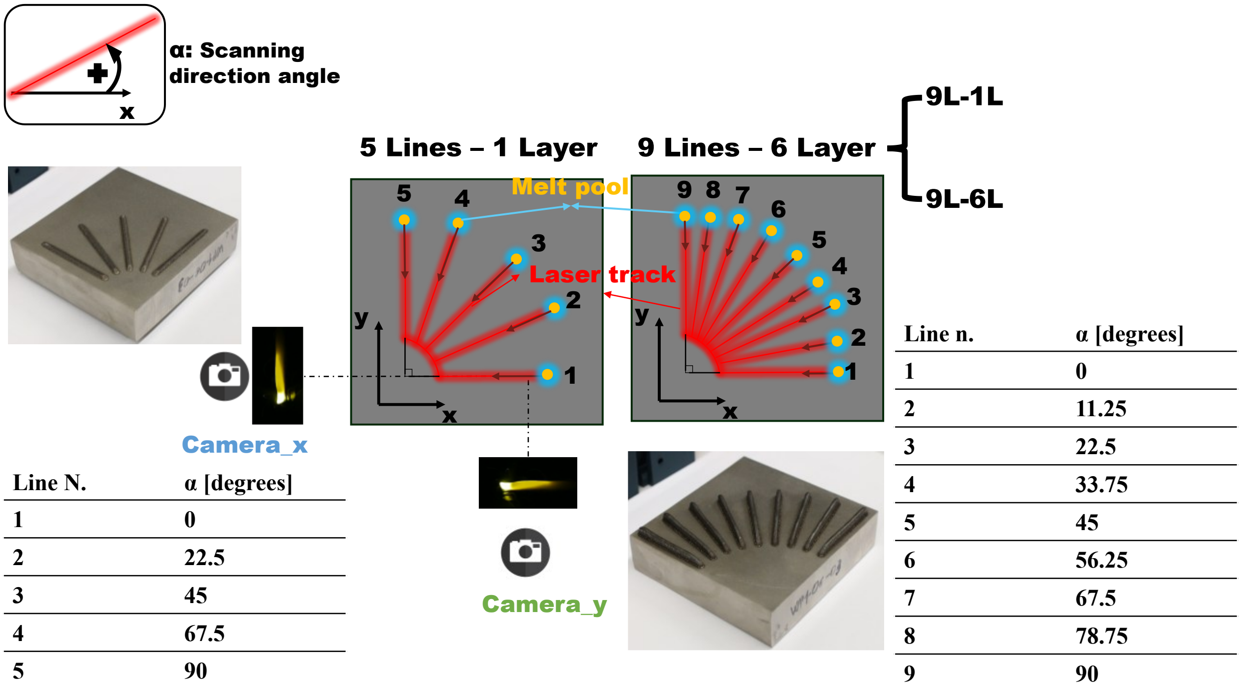

Line N.	α [degrees]
1	0
2	22.5
3	45
4	67.5
5	90

Line n.	α [degrees]
1	0
2	11.25
3	22.5
4	33.75
5	45
6	56.25
7	67.5
8	78.75
9	90

Fig. 56: Part produced during the three experiments. The number of lines for the #2 and #3 experiments were increased to provide more reliable results.

The dual-camera system was designed to enable three-dimensional monitoring and control of the melt pool height during the L-DED process over the substrate plane. To validate its performance across various printing directions and evaluate its accuracy, a series of experiments were conducted, as summarized in Fig. 56. These experiments included two single-layer tests, referred to as "5Lines-1Layer" (#1) and "9Lines-1Layer" (#2), and a multi-layer experiment, "9Lines-6Layer" (#3). The purpose of these tests was to assess the dual-camera system under different deposition directions and track the melt pool height measurements across diverse toolpath configurations. The geometries under exam were single-track thin walls directed inclined with different angles, as shown in Fig. 56. In the first experiment, "5Lines-1Layer" (#1), five single-layer clad lines were deposited, each measuring 45 mm in length. The tilt angle of each line increased incrementally by a step of 22.5°, covering a range from 0° to 90°, as shown in Fig. 56. This test provided a preliminary dataset for validating the system's ability to handle varying deposition angles. The height of six reference points along the tracks was measured using the L-DED machine touch probe module, ensuring precise height data for comparison with the data obtained from the monitoring system. The second experiment, "9Lines-1Layer" (#2), involved printing nine single-layer lines with an angle increment of 11.25° between consecutive lines, resulting in a more refined angular dataset than the first experiment. Height measurements were taken at ten equidistant points along each track to enhance the reference dataset. This dataset was critical for evaluating the system's accuracy with increased printing directions and the part was used as the starting point for the third experiment where six layers were printed. Building upon the second experiment, the third test, "9Lines-6Layer" (#3), consisted of a six-layer thin wall deposited with a programmed layer height of 0.83 mm, same used for previous experiment, a length of 45 mm, and a zigzag toolpath. This multi-layer experiment studied the system's response to increased layer count and cumulative height. The thin wall was deposited on top of the "9Lines-1Layer" (#2), resulting in only two as-built parts, as depicted in Fig. 56. Height measurements were performed at ten reference points along the thin wall to capture variations across multiple layers. During all experiments, the dual-camera system continuously monitored the melt pool geometry, capturing data necessary for calculating the melt pool height. The height measurements obtained from the cameras were compared with the reference values provided by the touch probe module integrated into the L-DED machine, as it demonstrated in Fig. 57. This comparison ensured a robust validation of the system's accuracy under various deposition scenarios.

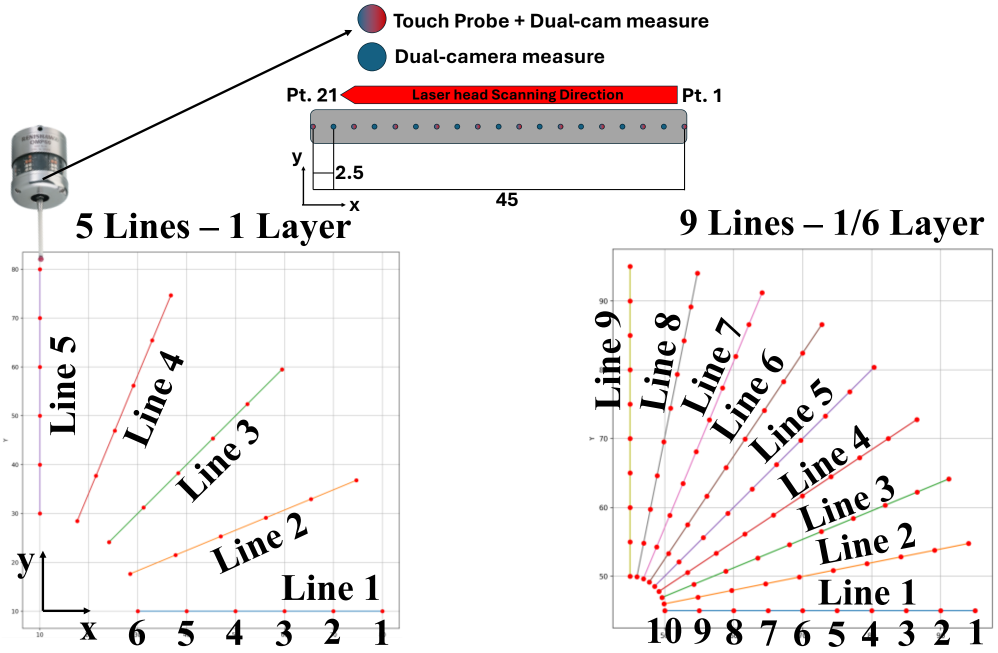

Fig. 57: Touch probe measuring strategy. The red points on each line indicate the location where the touch probe is measuring the clad height. The distance between the red points is set to 5 mm

The printing parameters utilized in the experiments are detailed in Table 12. Despite the cameras' maximum frame rate of 30 Hz, the actual frame rate during experiments was reduced to 7.15 Hz. This reduction was necessary due to poor lighting conditions in the setup, which required an increase in exposure time to ensure image quality. The trade-off between frame rate and exposure time was carefully managed to maintain the reliability of the captured data. The results of these experiments provided a comprehensive dataset to evaluate the dual-camera system's performance across different deposition angles, toolpaths, and layer configurations. By examining the melt pool height data under these varying conditions, the experiments validated the system's capability to deliver precise and consistent monitoring for 3D L-DED applications.

Table 12: L-DED printing parameters.

L-DED parameters	**LP (W)**	**PFR (g/min)**	**FR (mm/min)**	**Carrier gas (L/min)**	**Shield gas (L/min)**
Values	1000	23.5	1000	6	5

6.4.2. *Image processing algorithm*

Two image processing algorithms were developed to support the monitoring system: one focused on detecting the melt pool height (Fig. 58) using a blue-channel method inspired by the approach detailed in [203], and the other aimed at evaluating the so-called "ellipse angle" (Fig. 58). Both algorithms were designed to work concurrently during the deposition process to extract key geometric characteristics of the melt pool from the captured frames and to work with both cameras.

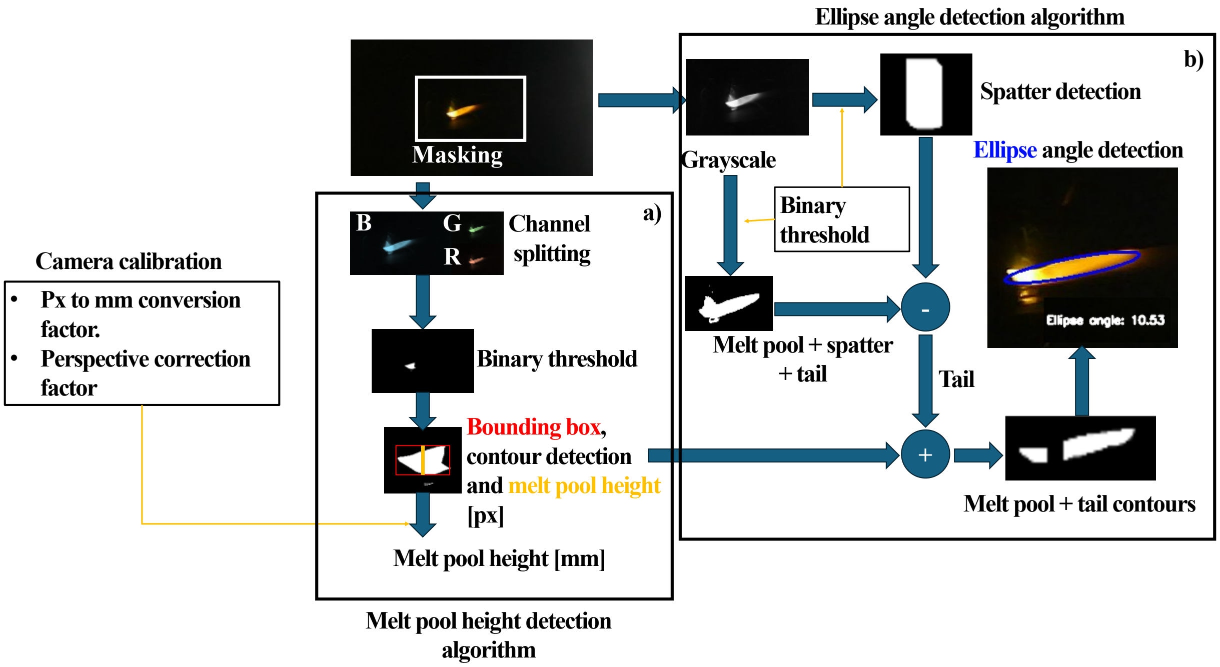

Fig. 58: Image processing workflow.

The blue channel method was specifically chosen for melt pool detection due to its suitability in highlighting the spectral characteristics of the melt pool. In [203] has shown that melt pools emit a significant amount of light in the blue wavelength range, which provides high contrast when isolated. This property makes the blue channel particularly effective for distinguishing the melt pool from surrounding material, spatter, and tail regions. By focusing on the blue channel of captured images, the algorithm ensures precise identification of the melt pool's geometry and dimensions, critical for accurate height measurements and real-time monitoring during the L-DED process. Additionally, applying a binary threshold to the blue channel effectively filters out non-relevant elements, simplifying the image processing workflow and reducing computational load, which can be considered as an advantage in real-time applications.

During the image preprocessing step, each frame was cropped to a region of interest (ROI) using a rectangular mask to focus the processing on the melt pool while excluding unnecessary areas of the frame. This preprocessing step reduced computational load and increased efficiency. The blue channel of the frame, extracted using *cv.split()*, was used for subsequent analysis due to its suitability for capturing the spectral characteristics of the melt pool, based on the findings proposed in [203]. To isolate the melt pool from its surroundings, a binary threshold was applied to the blue channel, setting pixel intensities above a specific threshold which can range between white (255) and black (0). Experimentally determined threshold values were used for different experiments and cameras. For example, during the third experiment (#3), thresholds of 250 and 160 were applied to the X and Y cameras, respectively, while for the first and second experiments (#1 and #2), thresholds of 254 and 145 were used to detect the melt pool geometry. This thresholding step produced a binary image where the melt pool's contour was clearly defined. Morphological operations, such as closing, were applied to the binary mask using *cv.morphologyEx* with a rectangular kernel to fill small gaps and ensure a smoother representation of the melt pool. The contours of the melt pool were then extracted using the OpenCV contour detection function, and the melt pool height was calculated in pixel units. These measurements were converted into millimeters using pre-calibrated conversion factors (C.F.) and perspective correction factors, based on the Pitch angle of each camera. Following the melt pool height detection algorithm (Fig. 58), the ellipse angle detection algorithm (Fig. 58) was applied to analyze the melt pool geometry further and proposed an automatic way to retrieve the deposition direction of the laser head. This process began by duplicating the greyscale frame after the ROI detection and applying two distinct binary thresholds to create two separate binary images for tail extraction. The first binary image, generated with a lower threshold value (e.g., 50), included the melt pool, spatter, and tail. The second binary image, produced with a higher threshold value (e.g., 175), isolated only the melt pool and spatter. The spatter region was enhanced using the *cv.dilate* function, which smoothed the contour of the tail and improved its representation. The tail was then extracted by subtracting the second binary image from the first, resulting in a binary image highlighting only the tail. The extracted tail contour was combined with the melt pool contour to generate a comprehensive representation of the entire melt pool region, without the spatter influence. An ellipse was fitted to this combined contour using the *cv.fitEllipse* function. The fitted ellipse provided key geometrical information about the melt pool, with its angle relative to the horizontal X-axis offering insights into directional properties. The two algorithms, working contemporary, provided a robust and detailed analysis of the melt pool's geometry. Both algorithms were applied independently to the frames captured by the X and Y cameras for every instance where the melt pool was detected. This dual-camera approach enabled a comprehensive view of the melt pool's height, tail, and dynamic behavior, ensuring accurate and consistent monitoring throughout the deposition process along multiple directions. By leveraging the light emission of the melt pool and implementing efficient image processing techniques, the system achieved a high level of precision suitable for real-time applications in L-DED monitoring.

6.4.3. *Evaluation indexes*

This section introduces two performance indices devised to evaluate the dual-camera system's reliability and accuracy in measuring melt pool height during the 3D L-DED process. These indices, derived from processed melt pool height data obtained via the image processing algorithms applied to both cameras, were compared against reference height measurements to assess the system's performance. A representative comparison is illustrated in Fig. 59. The two metrics, Average Height Percentage Error (AHPE) and Ellipse Angle Sum (EAS), are proposed as quantitative measures to characterize the system's accuracy and robustness. The AHPE, mathematically defined in equation (12), represents the percentage error in the melt pool height measurements obtained from the cameras compared to the reference clad height determined by the touch probe. The formula is as follows:

$$\boldsymbol{AHPE}[\%] = \left(\frac{\sum_{i=1}^{n}(H_{cam}^{i} - H_{TP}^{i})}{\sum_{i=1}^{n} H_{TP}^{i}}\right) \boldsymbol{x\ 100} \qquad (\mathbf{12})$$

Where n denotes the number of measurement points, H^{i}_{cam} is the melt pool height measured by the camera for the i-th point, and H^{i}_{TP} is the corresponding reference clad height measured by the touch probe. This metric serves as a direct indicator of the system's accuracy, with AHPE values close to zero indicating more precise and reliable measurements that align closely with the reference data. The sign of the AHPE carries critical information: a positive value indicates the measured melt pool height exceeds the reference height (overbuilt), while a negative value indicates an underestimation (underbuilt). The average AHPE provides a quick overview of the system's overall accuracy, while its standard deviation (σ) offers insight into the consistency of the measurements. Variations in σ can highlight the influence of factors such as spatter or changes in lighting conditions on the accuracy of the system. Additionally, this metric accounts for errors stemming from perspective distortions and environmental variations, emphasizing its role as a comprehensive performance evaluator for the dual-camera system. The second metric, the Ellipse Angle Sum (EAS), is designed to complement the AHPE by providing insight into the deposition direction of the melt pool as captured by both cameras. The EAS is calculated as the sum of the ellipse angles determined from the ellipse angle detection image processing algorithms (Fig. 58) applied to the X and Y cameras and illustrated in Fig. 60.

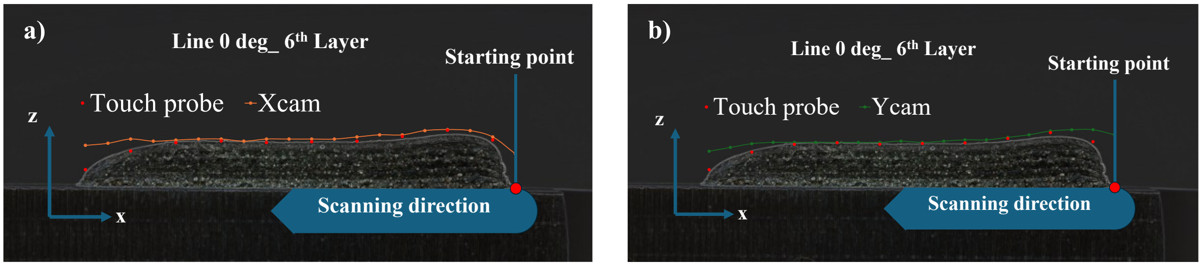

Fig. 59: a) AHPE obtained from X camera after applying the proposed image processing algorithm; b) AHPE obtained from Y camera.

This metric has been observed to correlate strongly with the deposition scanning angle (DSA), and it was found to be a critical parameter in selecting the most suitable camera view at any given time and deposition direction, as will be discussed in subsequent section. Given that different scanning angles affect the perspective and visibility of the melt pool for each camera, the EAS serves as a robust criterion for camera selection. By evaluating the EAS, the system can dynamically identify which camera provides the most reliable view of the melt pool under varying scanning conditions (ranging from 0° to 90° in the experiments). This adaptability enhances the dual-camera system's ability to monitor the melt pool effectively across a wide range of angles, thereby improving its overall performance and robustness.

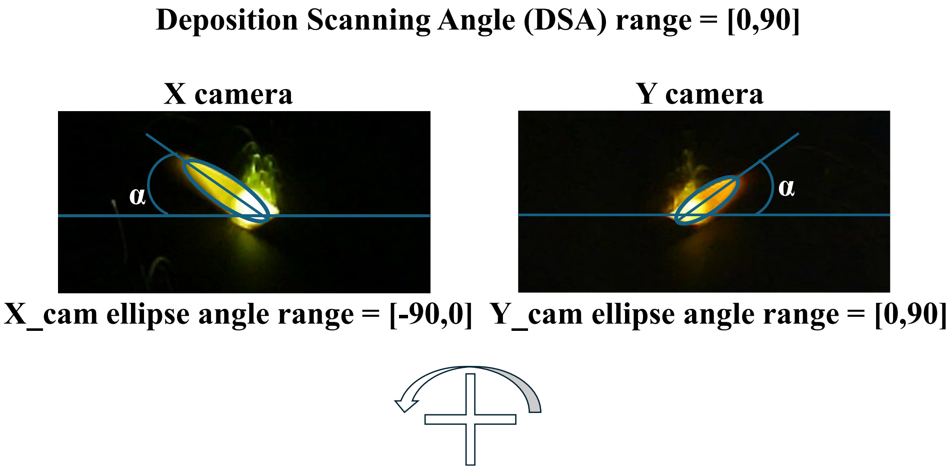

Fig. 60: Ellipse angle representation measured form each camera.

6.4.4. ***Reliable region***

As illustrated in Fig. 59, the melt pool height measured by the cameras (green and orange line in Fig. 59, respectively) exceeds the reference height obtained from the touch probe (red points) at both ends of the thin wall. These deviations, observed at the start and end sections, are typical defects caused by under-deposition due to the acceleration and deceleration of the laser head at the beginning and conclusion of the printing process. Further analysis of the data from camera Y, as shown in Fig. 61,a , reveals that the monitoring system struggled to provide accurate measurements from the 18th point to the end of the line under varying deposition scanning angles (DSAs). For instance, within this range, points near the edges (e.g., Pt. 2, Pt. 18, and Pt. 20 in Fig. 61) exhibited significant local height percentage errors. Specifically, Pt. 2 and Pt. 20 showed errors as high as 26% and 90%, respectively. These discrepancies indicate a consistent overestimation of the melt pool height in these regions. The primary causes of these errors are attributed to the edge effects of the thin wall and the absence of lens distortion corrections, which exacerbate inaccuracies during substantial height variations. Such errors notably impact the Average Height Percentage Error (AHPE), reducing the system's height estimation accuracy.

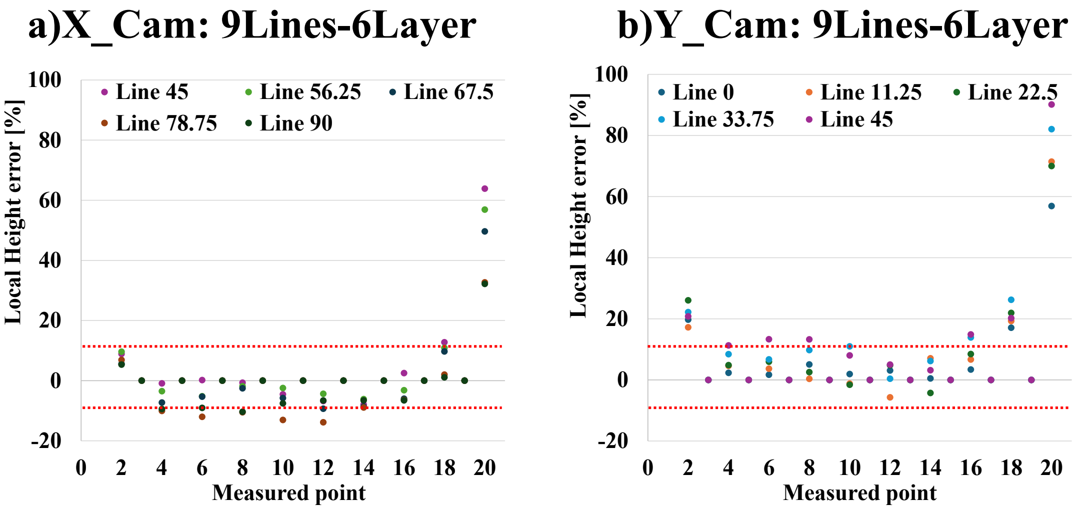

Fig. 61: Results from local height analysis for the #3 experiment.

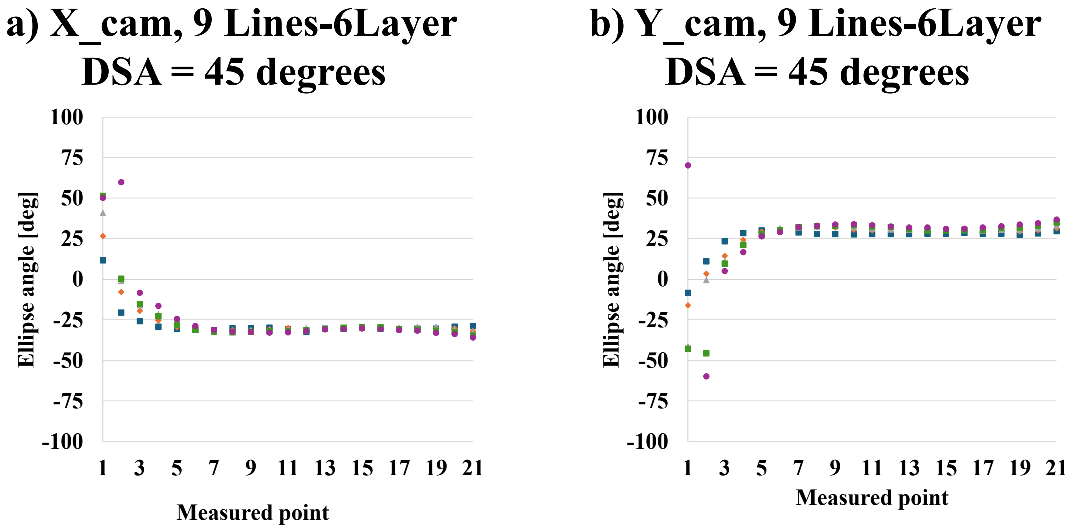

Fig. 62: Ellipse angle measured from the #3 experiment for DSA 45 measured from a) X camera and b) Y camera.

To mitigate this issue, a "Reliable Region" was defined, where only measurements within a ±10% height percentage error are considered. For an average clad height of 0.83 mm, this threshold corresponds to an acceptable error margin of ±0.083 mm. Within this reliable region, approximately 80% of the local height errors fell within the acceptable ±10% range for both cameras. Although occasional outliers were observed, the accuracy of the system remained satisfactory within this region. Fig. 62 presents the ellipse angle measure captured by both X (Fig. 62, a) and Y (Fig. 62, b) camera along a line with a DSA of 45 degrees for the 9Line-6Layer experiment. Considering that for each produced line and layer the ellipse angle was measured, the dataset is composed of 54 diagrams. The other results about the ellipse angles were omitted because of their similarity with the data. The ellipse angle measurements are notably influenced by edge effects, particularly at the start of the deposition process (Pt. 1 to Pt. 4). A logarithmic trend was observed, with the ellipse angles stabilizing after Pt. 4 and remaining consistent across layers deposited with the same DSA. To improve reliability, measurements from Pt. 1 to Pt. 4 were excluded for both cameras, as the edge effect introduced variability that compromised accuracy. By integrating the findings from the melt pool height error analysis and the ellipse angle evaluation, the reliable region was identified. This region begins approximately 10 mm from the start of the deposition and extends to 10 mm before the end. A schematic representation of this reliable region is provided in Fig. 63, highlighting the areas where the monitoring system demonstrates robust performance and reliability.

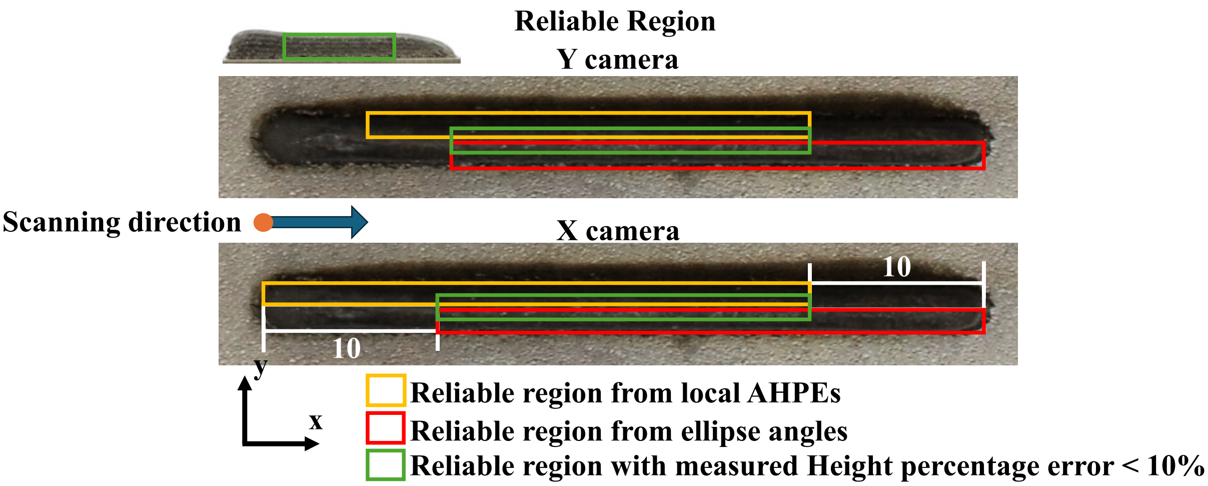

Fig. 63: Reliable region identification

6.4.5. ***Results***

The experimental results were grouped into two distinct categories: single-layer depositions, represented by *5Lines-1Layer and 9Lines-1Layer,* and multi-layer depositions, represented by *9Lines-6Layer*. This categorization facilitated a more precise analysis of layer-specific effects, highlighting the differences in process dynamics between initial and subsequent layer depositions. The findings put in evidence notable differences in process conditions between single and multi-layer depositions, which significantly influence the reliability of the proposed dual-camera monitoring approach. Producing the first layer in an L-DED process is inherently more challenging than subsequent layers due to several factors. First, without pre-heating the substrate, the rapid cooling of the first layer destabilizes the melt pool, increasing the likelihood of spatter caused by the ejection of unmelted particles. This spatter can lead to poor adhesion and challenges in achieving consistent deposition. As shown in Fig. 64, a, spatter is visibly more pronounced in the first layer, while by the sixth layer (Fig. 64, b), spatter production is significantly reduced, indicating a more stable melt pool. Additionally, lighting conditions during deposition vary between layers. The first layer's melt pool appears brighter due to the higher reflectivity of the substrate compared to subsequent layers, where the deposited material changes the surface properties. This contrast in lighting is evident when comparing images of the first and sixth layers in Fig. 64. The increased spatter production and variability in lighting conditions during the first layer make extracting accurate melt pool information more challenging than in multi-layer scenarios. Despite these challenges, the results obtained using the proposed method are promising and demonstrate the potential for future development of a height control algorithm capable of adapting to the differences between single and multi-layer deposition processes. These observations also justify the use of different threshold parameters for melt pool detection in the first layer compared to multi-layer depositions.

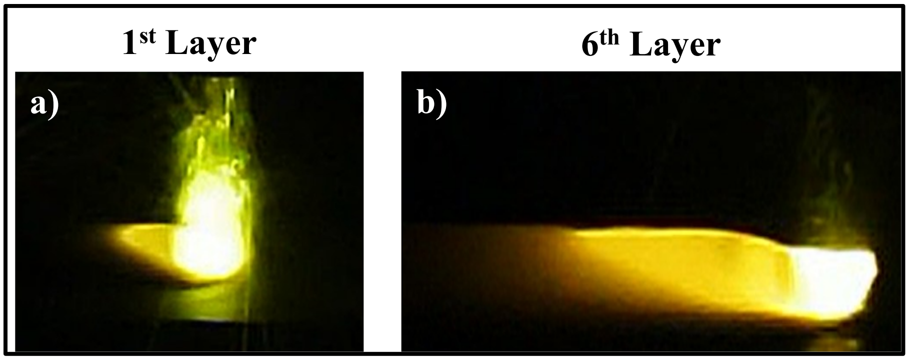

Fig. 64: Melt pool geometry for a) first layer and b) sixth layer.

6.4.6. ***Melt pool height errors results***

First Layer results. The results for the melt pool height measurements during the first single-layer deposition from the first two experiments are presented in Fig. 65. The measured height values, originally in pixel units, were converted to millimeters using the calibration factors derived in Fig. 53, with values of 6.99 px/mm for the Y camera and 8.41 px/mm for the X camera. After applying the proposed image processing algorithms, distinct trends in height errors were observed for each camera, with the error varying as a function of the deposition scanning angle (DSA). As shown in Fig. 65 a, b, and c, the Y camera measurements (represented by the orange line) exhibit a steadily increasing height error. A substantial gap between the Y camera's measured height and the reference height (green points) is observed as the DSA changes from 22.5° to 67.5°, with the AHPE rising from 7.44% to 57.20%. In contrast, the X camera measurements (blue line) show smaller errors at DSAs of 22.5° and 67.5° but display a higher error at 45°. The presence of large peaks in the measurements, evident in the Fig. 65, c, d, e, f, are identified as outliers, caused by high levels of spatter and reflections during the first single-layer deposition, which reduced the stability of the measurements. Furthermore, as seen in Fig. 65 a, d, and f, when the standard deviation exceeds 0.15, the height error measurements were notably affected by multiple peaks. The AHPE values across DSAs ranging from 0° to 90° for two independent single-layer experiments are displayed in Fig. 66. The Y camera measurements in experiment #1 and #2, as well as the X camera in experiment #2, exhibited a linear trend. In contrast, the X camera in experiment #1 followed a parabolic trend. The cause of this discrepancy in X camera behavior between experiments #1 and #2 remains unclear and requires further investigation. One possible explanation is that increasing the number of reference points (measured with the touch probe) improved the data reliability. However, the AHPE values recorded by the X camera in experiment #2 when the DSA was at 0 degrees and 11.25 degrees requires further study, as it directly impacts the observed linear AHPE trend for the X camera.

Despite these differences, both experiments demonstrated consistent behavior in the performance of the two cameras. For DSAs below 45°, the Y camera exhibited a smaller AHPE compared to the X camera. However, for DSAs above 45°, the X camera outperformed the Y camera in terms of accuracy, exhibiting lower AHPE values. This suggests that each camera has an optimal range of DSAs where its performance is maximized. Based on this observation, a camera selection approach was developed: for DSAs less than 45°, the Y camera is used, whereas for DSAs greater than 45°, the X camera is selected. This strategy allowed the AHPE to remain below 55% during single-layer deposition experiments (#1 and #2). The smallest errors were observed when the scanning direction was perpendicular to the camera's optical axis—0° DSA for the Y camera and 90° DSA for the X camera. As shown in Fig. 66, the lowest AHPE values recorded were -11% for the Y camera and 22% for the X camera, demonstrating that the image processing methodology achieves a high degree of accuracy, even during the challenging conditions of first-layer deposition.

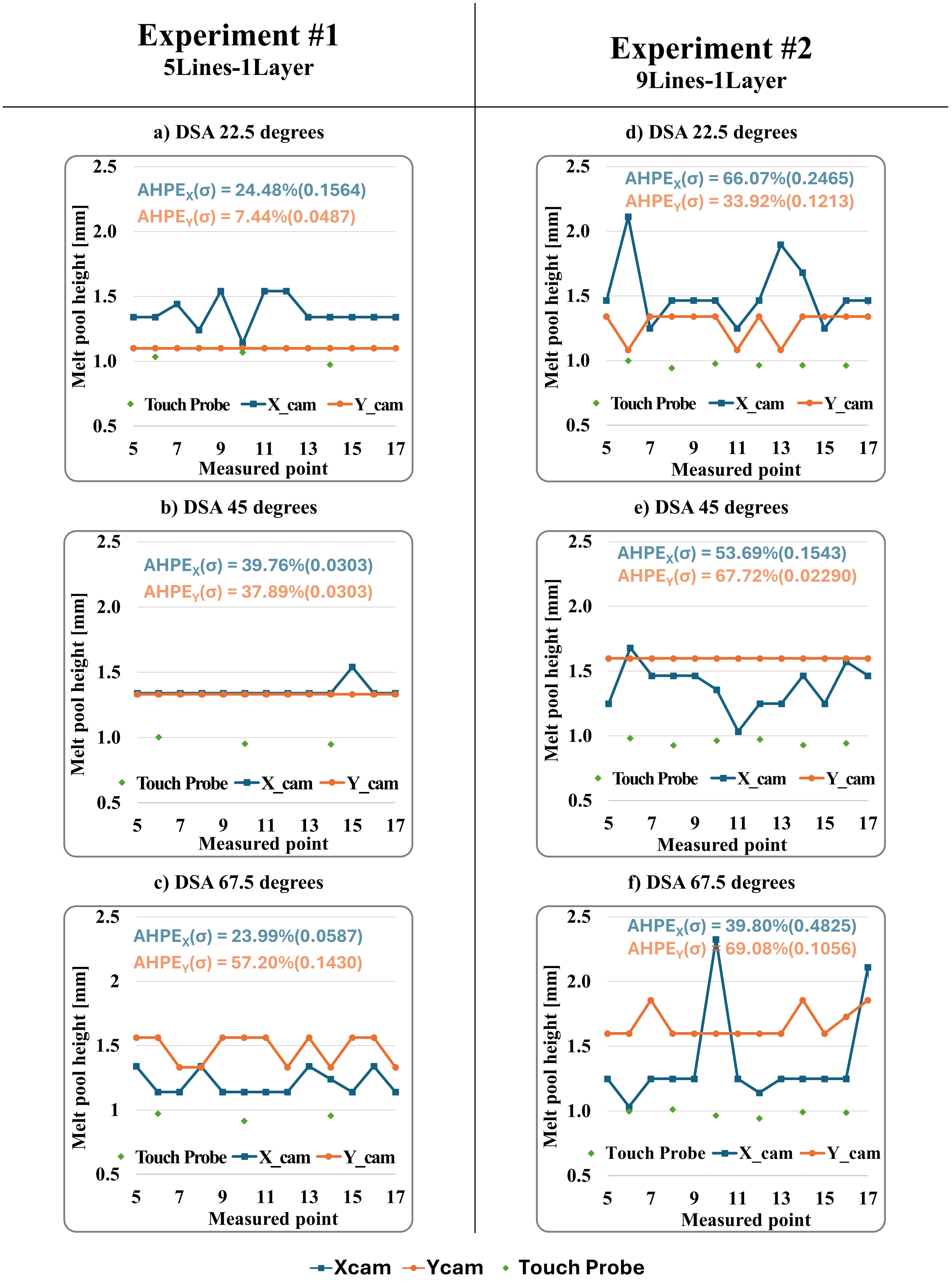

Fig. 65: Melt pool height results obtained from the dual-camera system.

Third experiment (#3) results. Like the single-layer experiments, the results from Experiment #3, 9Lines-6Layer illustrated the height profiles of the six-layer thin walls, as depicted in Fig. 67. The measured heights from both cameras were converted from pixels to millimeters using calibration factors of 7.60 px/mm for the Y camera and 9.23 px/mm for the X camera. The melt pool height profiles captured by the cameras closely matched the reference clad height profile, indicated by green points in Fig. 67. Unlike the single-layer experiments, no significant outlier peaks were detected at any measured DSA, indicating a reduction in spatter effects and a more stable melt pool condition during the multi-layer deposition process. Consequently, for both cameras, the magnitude of the AHPE percentage in the sixth layer is lower than that in the first layer. Furthermore, as indicated by the values in parentheses for X and Y camera, the standard deviations are on the same scale and similar for each DSA.

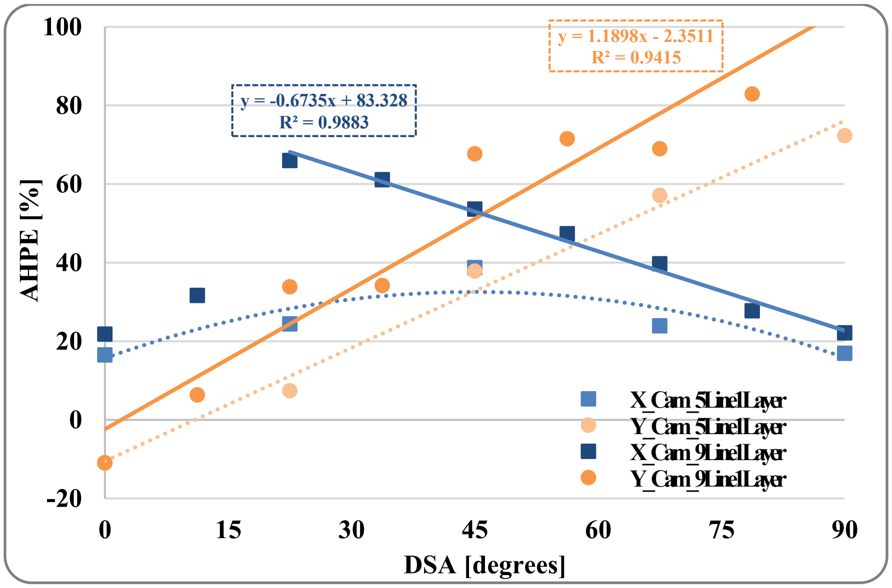

Fig. 66: AHPE diagram comparison.

The variation between the two cameras is less pronounced than in the first layer deposition, likely due to the reduced influence of spatter with no outlier peaks, which indicates that the measured height errors in the 6th layer are similarly distributed with comparable precision. Fig. 68 shows the AHPE values calculated for different DSA configuration, using data from the reliable region (points 5 to 17) to exclude edge effects at the start and end sections. It indicates that the Y camera shows a trend of linearly increasing AHPE, as the measured height diverges from the reference height between 0 degrees and 90 degrees DSA, consistent with observations from the single-layer experiments. For the X camera, AHPE increase as the DSA decreases from 45 to 0 degrees and follows the same trend as the DSA increases from 45 to 90 degrees, though with negative sign, presenting a similar linear AHPE trend compared to the linear pattern observed in the first single-layer experiment. Overall, the measurements from both the X and Y cameras demonstrate higher accuracy in terms of AHPE than the first single layer clad height measurement, as shown in Fig.

68. For instance, the AHPE for the X camera remains within ±11% (91 µm), whereas it reached up to around 60% in the first single-layer experiment.

These findings reinforced the conclusions from the single-layer experiments, highlighting the importance of selecting the appropriate camera based on the DSA to achieve optimal accuracy in a dual-camera system. The relationships identified between AHPE and DSA offer predictive capabilities for height compensation at different DSAs, enhancing the potential of the monitoring and height control system for reliable performance during L-DED processes.

Experiment #3 (9Lines-6Layer)

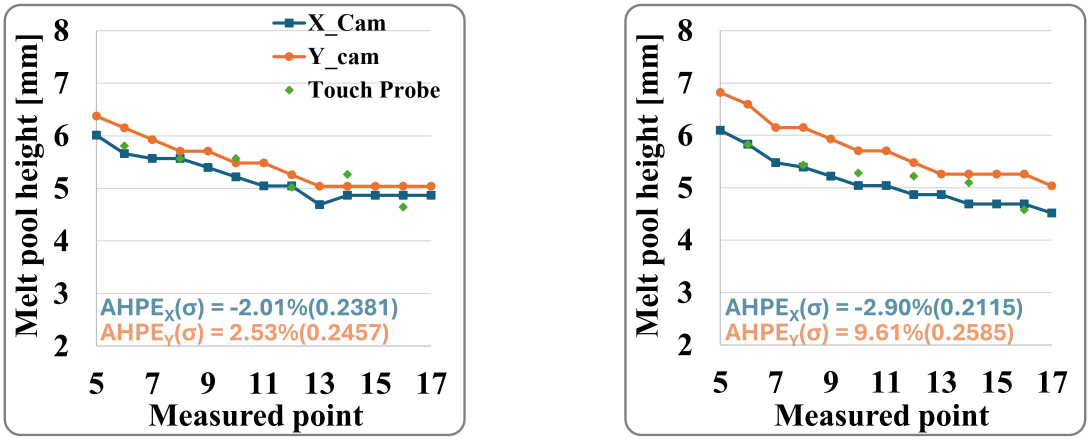

a) DSA 22.5 degrees

b) DSA 45 degrees

c) DSA 67.5 degrees

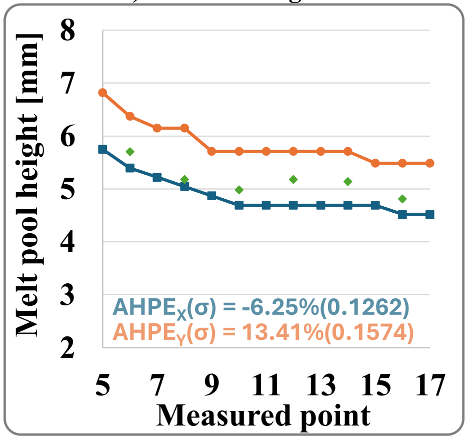

Fig. 67: Results for the melt pool height measured from the dual camera systems for the #3 experiment where six layers were printed.

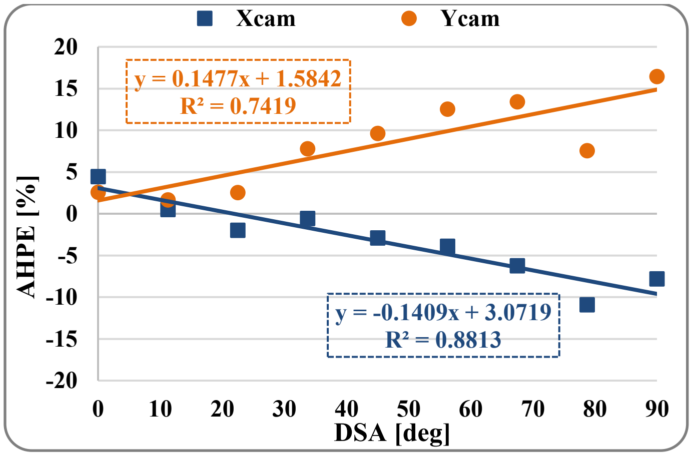

Fig. 68: AHPE resulted from the #3 experiment relative to the sixth layer.

6.4.7. ***Ellipse angle results***

First layer results. The ellipse angle was determined by the orientation of the melt pool tail. Fig. 69 illustrates the ellipse angles measured during the deposition of the first layer. A comparison of the two experiments showed that the Y camera (orange line) recorded relatively stable angles when the DSA ranged from 22.5° to 45°, but the measurements became increasingly random as the DSA increased from 45° to 67.5°. A similar trend was observed for the X camera, where the ellipse angle measurements became less consistent as the scanning angle decreased from 67.5° to 22.5°. This behavior was attributed to the changing perspective of the camera as the DSA transitions between 0° and 45°. In this range, the camera gradually captured more of the side view of the clad, and the tail of the melt pool became less visible in the frame. The reduced visibility resulted in shorter detected tails, which introduced greater calculation errors and contributed to the instability observed in Fig. 69. These results highlighted a limitation of the dual-camera system for ellipse angle measurements during the first layer deposition. Specifically, both cameras became less reliable for capturing ellipse angles when the DSA exceeds 45°. This underscored the importance of carefully selecting the appropriate camera and optimizing the measurement process to account for these perspective-related challenges during deposition.

Third experiment (#3). Like the observations from the first single-layer experiment, the multi-layer results reveal that the cameras operate within their reliable range only after the measured ellipse angle stabilizes following the initial four frames. During the multi-layer experiment, the measurements remained consistent overall, except when the DSA was 0 degrees for the X camera and 90 degrees for the Y camera. As shown in Fig. 706 a, b, and c, the X camera (blue points) produced highly inconsistent values in layers 2, 4, and 6 when the DSA was at 0 degrees, indicating instability and reduced accuracy in measuring the ellipse angle. A similar pattern is evident in Fig. 70 d, e, and f, where the Y camera (orange points) showed comparable instability at a DSA of 90 degrees. Additionally, it was noted that the magnitude of the unstable ellipse angle measurements decreased as the DSA approached an orientation perpendicular to the optical axis of each camera. These findings suggest that the reliability of ellipse angle measurements is strongly influenced by the alignment of the camera relative to the scanning direction.

Experiment #1

5Lines-1Layer

Experiment #2

9Lines-1Layer

a) DSA 22.5 deg

d) DSA 22.5 deg

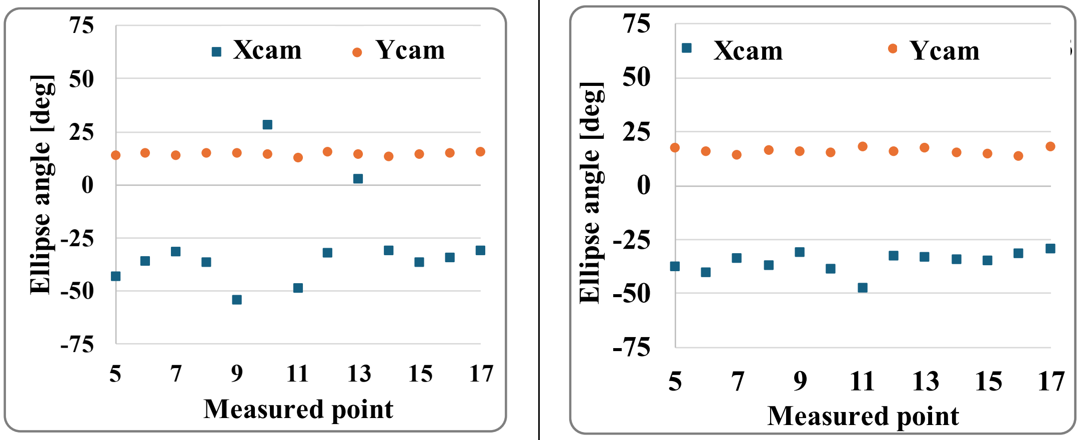

b) DSA 45 deg

e) DSA 45 deg

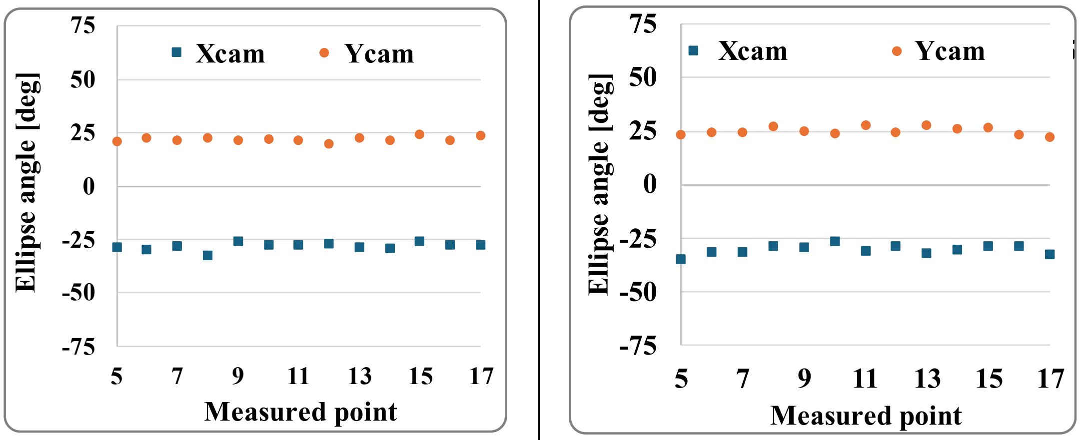

c) DSA 67.5 deg

f) DSA 67.5 deg

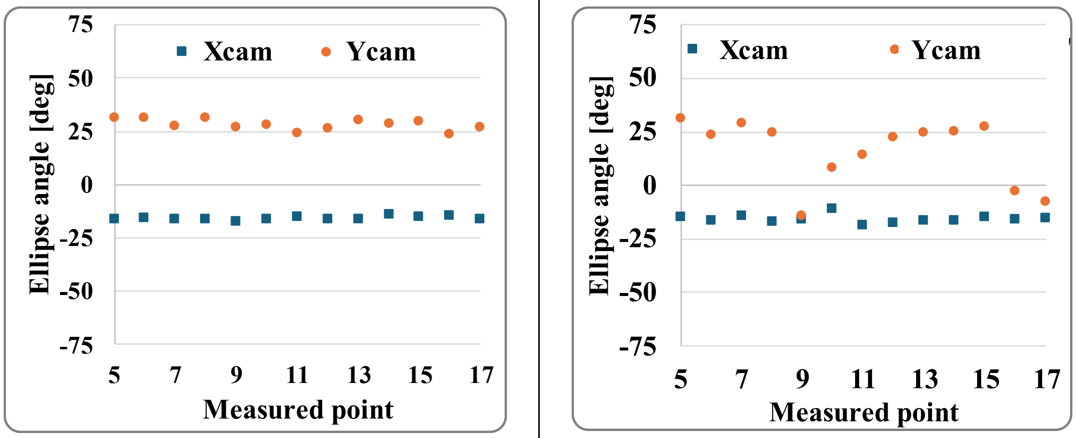

Fig. 69: Results from the #1 and #2 experiments related to the ellipse angle measured from the dual camera system.

DSA 0 deg | DSA 90deg

a) Layer 2 | d) Layer 2

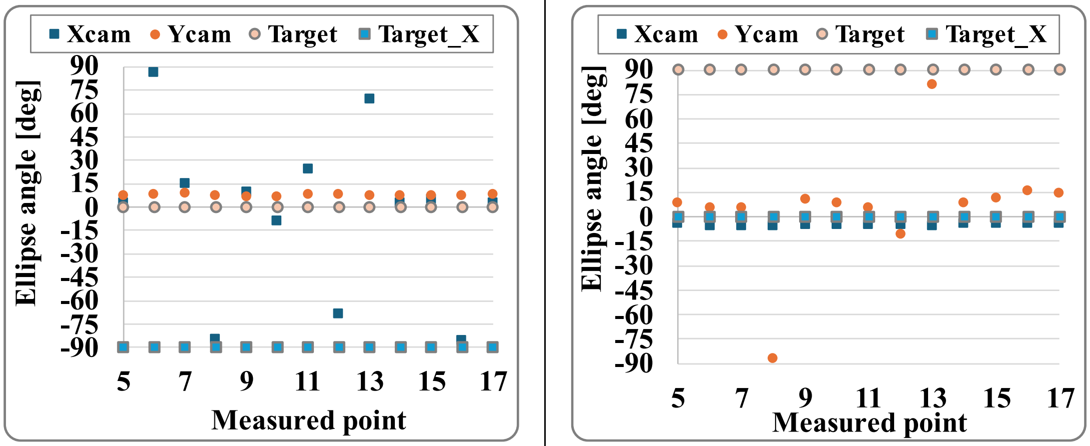

b) Layer 4 | e) Layer 4

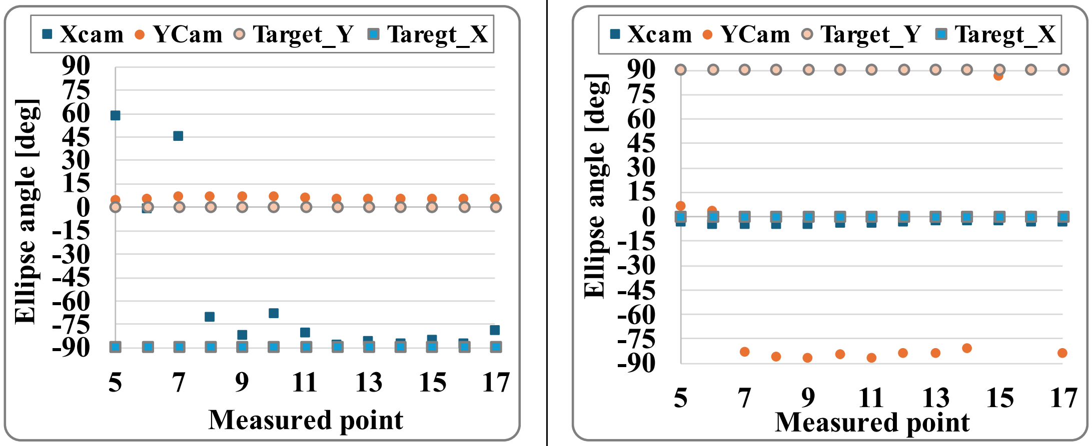

c) Layer 6 | e) Layer 6

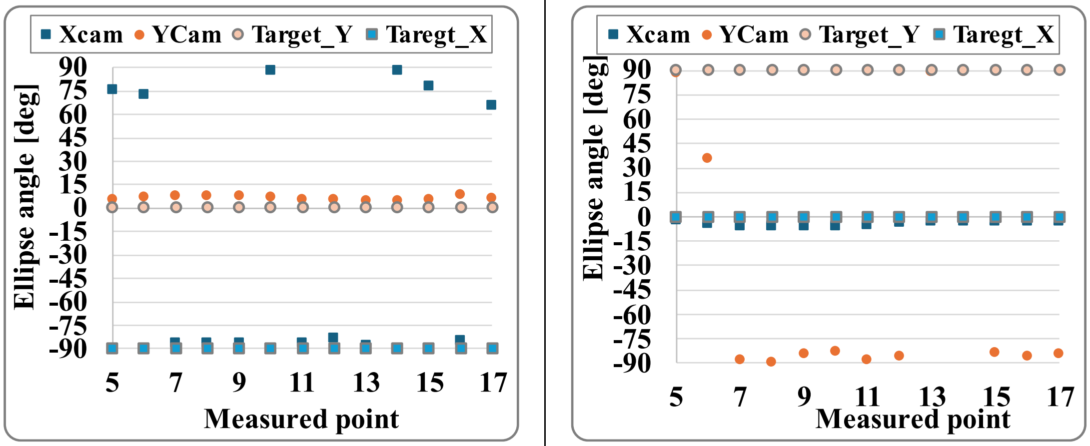

Fig. 70: Results obtained from the #3 experiment relative to the ellipse angle measured from the dual camera system.

6.4.8. *Ellipse angle sum results*

To complement the analysis of individual camera data, a combined metric called the "ellipse angle sum" (EAS) was developed. Measuring the ellipse angle using data from a single camera can be hard, particularly when the DSA lies outside the camera's optimal working range. In such cases, measurements became less stable, reducing reliability, as illustrated in Fig. 69. The EAS addresses this limitation by integrating data from both cameras, providing a more robust and stable representation of the DSA. As shown in Fig. 71, the EAS exhibits a linear relationship with the DSA, emphasizing its potential as a reliable metric for real-time monitoring and control. The EAS analysis also highlighted a high level of consistency across different layers. Apart from DSAs of 0° and 90°, and minor variability observed in the second layer due to the instability of the melt pool, the EAS values measured during layers 3 to 6 remained remarkably stable. This consistency was maintained even within the same frame across these layers, indicating that the EAS metric is unaffected by the number of layers. These findings suggested that the EAS can be effectively used as a reliable predictor of the DSA. Furthermore, the linear fitting model applied to EAS data demonstrated its capability for accurate and consistent predictions, making it a valuable tool for the monitoring and control of the L-DED process.

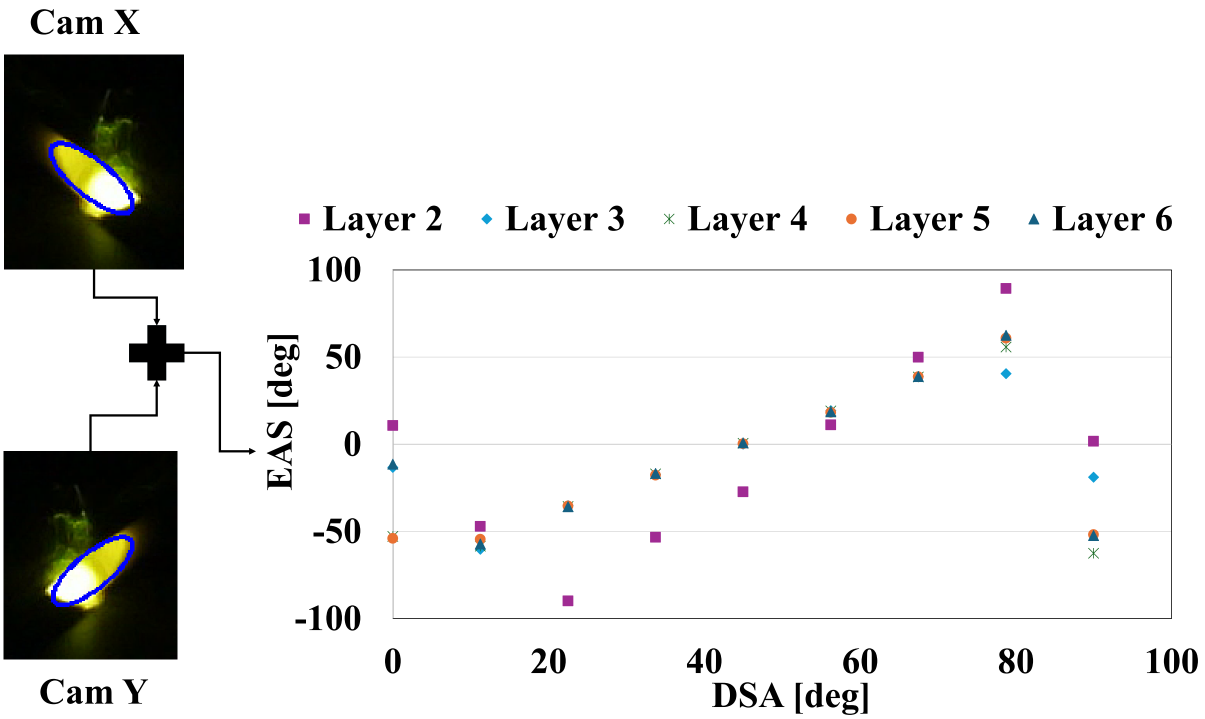

Fig. 71:Ellipse angle sum (EAS).

6.4.9. *Camera matching algorithm*

To achieve 3D monitoring with the proposed system, a height error compensation strategy for L-DED height control was introduced, based on the relationship between the Ellipse Angle Sum (EAS), Deposition Scanning Angle (DSA), and Average Height Percentage Error (AHPE), as illustrated in Fig. 71 and Fig. 72. The monitoring process began with the calculation of the melt pool height and EAS using the two image processing algorithms, shown in Fig. 58. Subsequently, the DSA is determined using the correlation between the EAS and the DSA, as shown in Fig. 71. The system uses the DSA for two main purposes: first, to identify the current optimal working range (Fig. 72), enabling appropriate camera selection; and second, to estimate the potential height error associated with the selected camera. This preliminary study revealed that AHPE served as a reliable predictor of the measurement errors in the dual-camera system for different DSAs. Consequently, the AHPE can be used as a correction factor to refine the estimated melt pool height obtained from the monitoring system. If the calculated DSA was 45 degrees or greater, the system selects Camera X; if the DSA was less than 45 degrees, Camera Y is chosen. The AHPE value corresponding to the selected camera was then applied as a correction factor to the measured melt pool height. This adjustment accounted for errors arising from the camera's relative position to the melt pool and was valid under identical printing conditions. This camera selection methodology aimed to optimize measurement accuracy by dynamically selecting the camera based on the scanning angle and applying the appropriate correction factor, thereby improving the reliability of real-time melt pool monitoring.

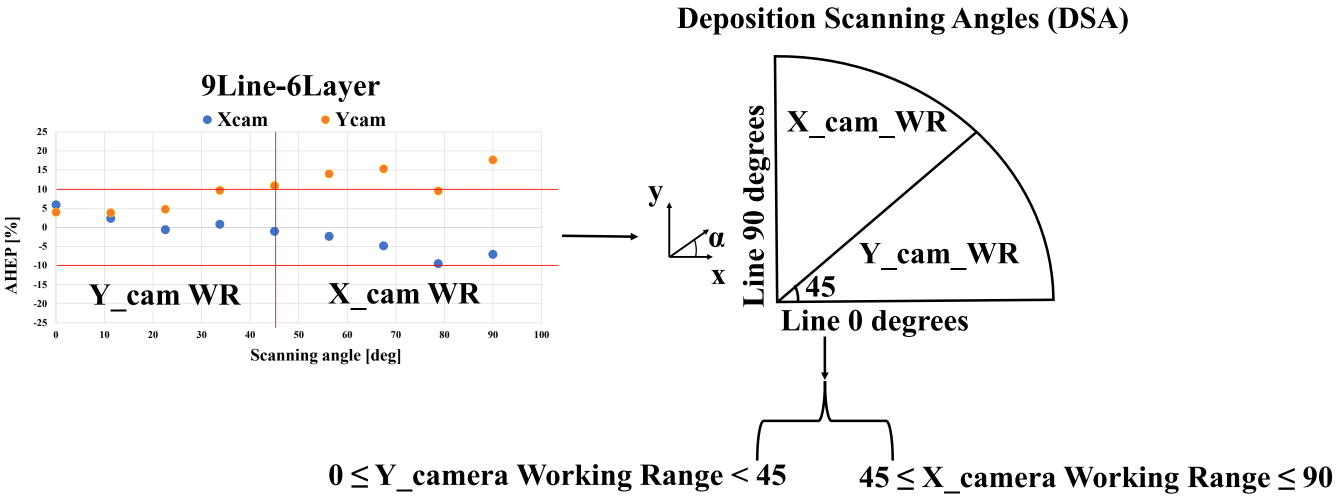

Fig. 72: Camera working range description.

During the deposition process, the system excluded the first and second layers from the height control due to the inconsistent results observed in these layers. Height control is designed to commence from the third layer, where the proposed methodology has demonstrated reliability. The input to the height control system is the melt pool height measured by the selected camera, corrected by the AHPE according to the DSA determined using the EAS. This workflow, Fig. 73, ensured that perspective-induced inaccuracies were mitigated, enabling more accurate and dependable real-time monitoring during the L-DED process.

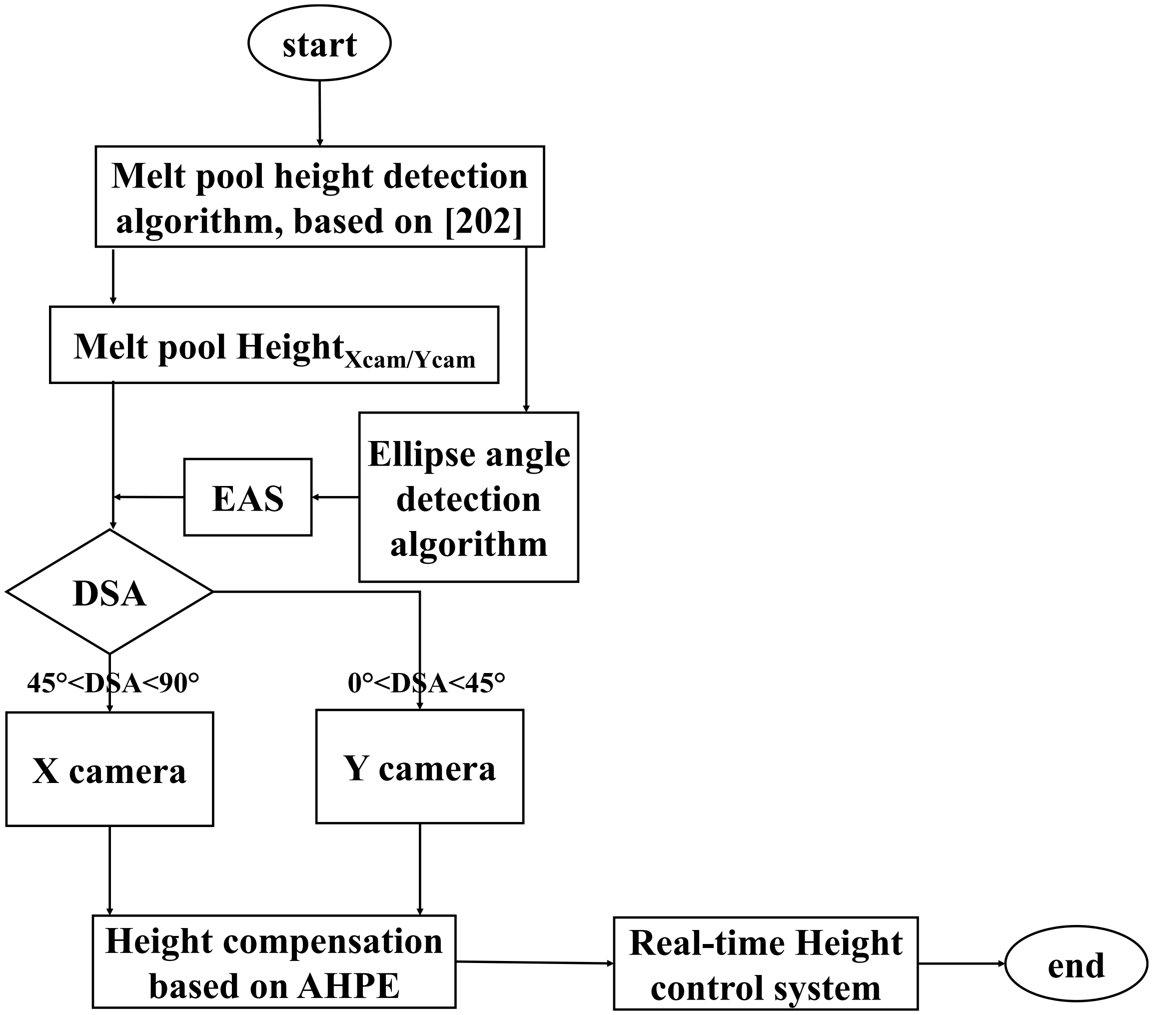

Fig. 73: Off-axis dual camera monitoring system workflow

6.5. Conclusion about L-DED monitoring activities

This study presents a cost-effective dual-camera off-axis monitoring system designed for measuring melt pool height across various printing directions in the 3D L-DED process. While a preliminary evaluation of the system has been conducted, additional studies are required to further validate its effectiveness. The analysis of experimental data led to the development of a height error detection method based on an image processing algorithm capable of handling multi-directional geometries. This methodology begins by measuring melt pool height using both cameras and calculating the Ellipse Angle Sum (EAS) via the ellipse angle detection algorithm. The EAS serves to identify and select the camera that provides the most reliable height measurement. Using the AHPE and DSA fitting model, a height error compensation mechanism is applied, which adjusts the measured height. The corrected height is then used as input for a real-time height control system. This approach effectively detects the laser head scanning angle and adjusts the melt pool height measurements for varying deposition angles. The key findings from this study indicate that the image processing algorithms successfully measure melt pool height and detect the ellipse angle for multi-directional geometries. The results showed that height measurement during the initial layer is particularly challenging due to spatter production and melt pool instability. In contrast, multi-layer depositions exhibited greater stability, reduced spatter, and improved accuracy. For multi-layer deposition, the proposed dual-camera system achieved a height measurement error within 11% (equivalent to 91 μm) across different scanning angles. Furthermore, the EAS was demonstrated to be a reliable indicator of the deposition scanning angle. When combined with the AHPE, it formed a predictive model for clad height errors, enabling the dynamic selection of the most suitable camera for accurate melt pool height measurements during the deposition process.

6.6. Critical review of L-DED proposed monitoring method

While this study demonstrates the potential of the dual-camera monitoring system, it also identifies several areas requiring further development and investigation. To confirm the system's broader applicability, additional experiments encompassing a wider range of deposition angles and process conditions are necessary. Addressing challenges related to first-layer deposition is particularly important, as the spatter and melt pool instability during this phase affect the reliability of real-time monitoring. Furthermore, a dedicated verification test of the dual-camera height measurement methodology for height control is essential to fully validate its performance and facilitate its integration into industrial applications. The use of low-cost CMOS cameras in this study posed limitations for the monitoring system. Specifically, the inability to adjust critical camera parameters such as ISO and exposure time restricted the system's adaptability to varying conditions. Although the system proved effective for melt pool height monitoring, further tests with cameras capable of parameter control are recommended to evaluate how these settings influence accuracy. Additionally, employing cameras with higher resolution could theoretically enhance the spatial resolution of the dual camera monitoring system, potentially improving its overall precision. Another key area for improvement is the calibration process, which is essential for ensuring reliable and precise melt pool height measurements and accurate determination of the deposition scanning angle. The calibration procedure, as described, must be performed prior to each deposition. Future work should explore methods to streamline and automate this process to improve efficiency and consistency. Moreover, the experiments were conducted using a single material with threshold parameters optimized for this specific test case. This highlights the need to investigate how optical properties and threshold parameters vary when different materials and printing conditions are introduced. Finally, the prototype fixture used for Camera Y, which was fabricated via 3D printing, proved stable during the experiments. However, testing with a finalized fixture is necessary to enhance the system's stiffness and ensure consistent results across a broader range of conditions. A more robust and durable fixture would contribute significantly to the reliability and repeatability of the dual-camera monitoring system.

7. Conclusion

This dissertation has addressed critical challenges in the field of AM quality inspection and process monitoring, focusing with particular emphasis on MEX, L-PBF and L-DED, which are the most commonly used AM technologies. The primary objective was the development of robust, in-situ monitoring methodologies to assess process stability, evaluate product quality and pave the basis for adaptive control systems, eventually. Given the increasing complexity of AM systems and their industrial applications, this research aimed to bridge the gap between current monitoring capabilities and the need for reliable, repeatable high-quality and high -performance part production. AM technologies have demonstrated many advantages for the production industry thanks to their flexibility in design freedom and material portfolio. Compared to conventional technologies, and in certain industrial fields and products, they can help reduce material waste and energy consumption. By integrating in-situ monitoring methodologies based on optical sensors, this study aimed to enlarge boundaries of AM technologies toward wider adoption in industry. Particularly for critical applications, reliability and repeatability remain key challenges in AM. This research introduced innovative monitoring methodologies tailored for MEX, L-PBF and L-DED and the conclusions will be discussed below.

For what concerns MEX process, a novel in-situ layerwise monitoring system was developed using a high-resolution blue laser line profilometer applied to raw point cloud data. This system was first used to provide effective evaluation of layer quality through custom quality indexes, such as Layer Height Average Deviation (AD_{LH}), the AD_{LH} Slope s and Residual Absolute Deviation (RAD), which were proven effective in detecting surface defects and assessing process stability. The cumulative height metric was utilized to monitor layer-by-layer accuracy, and specific defects like overfill (OF) and underfill (UF) were identified with high precision. Another methodology was developed using the same monitoring system combined with functional analysis tools. Key indexes such as the Projected Percentage Area (PPA) and void/material volume and mean thickness were used to quantify the dimensions of defects and understanding layer stability. Notably, the proposed methodologies measured surface irregularities with a resolution of 4 µm, demonstrating its potential to enhance both in-situ monitoring and metrology practices. The developed procedure enabled detailed characterization of surface and defect morphology, including the extraction of defect coordinates, which could be used to implement corrective actions in real-time. This research also highlighted the possibility to broaden the applicability of the proposed methods to other AM technologies. All the results obtained from the MEX monitoring activities were validated by means of certified structured-light scanner and the average error committed by the system was found to be on the order of 0.014 mm.

The monitoring procedure developed for L-PBF focused on applying High-Resolution Optical Tomography (HR-OT) for the in-situ characterization of complex lattice structure. An HR-OT system was implemented and improved in accuracy compared to other in-situ monitoring system and optical tomography-based proposed in the literature. This was achieved by refining the image processing algorithm, enabling the detection of geometric errors and distortion layer by layer. The HR-OT provided dimensional and geometrical assessments with an average deviation of 0.05 mm from the reference, proving the accuracy of the proposed method. The 3D point cloud obtained from the HR-OT was compared directly with the CAD, considered as reference. The 3D reconstruction provided valuable results because it has a double function: it can be used for offline quality assessment and, eventually, as input for numerical simulation. Additionally, to the 3D reconstruction of the lattice structure, thanks to the proposed monitoring system it was also possible to evaluate surface defective condition based on the analysis on the false color image of each layer, enabling the detection of superelevated edges and geometric distortions. The main advantage of this proposed system is that it can be considered as a cost-effective alternative to XCT, especially for evaluating both internal and external features.

Finally, the monitoring activity on L-DED consisted in the development of a dual-camera multi direction monitoring system, together with the used image processing algorithm, to measure the melt pool height across different printing directions during the deposition process. The driver of this research was the lack of in-situ dual-camera monitoring systems able to perform correct melt pool measurements when the clad deposition occurs over multiple printing directions. By combining image processing algorithms and a predictive model based on the Ellipse Angle Sum (EAS) and Average Height Percentage Errors (AHPE), the system predicted the measurement error committed by each camera, based on the angle of the deposition direction, and selected the optimal camera to perform real-time measurement of the melt pool height. The system demonstrated a 11% height error range (which is approximately 91 μm) during the multi-layer multi-direction deposition. Additionally, challenges associated with the initial layer, including spatter and melt pool geometry, were noted, whilst subsequent layer melt pool geometry showed improved accuracy and stability. This monitoring approach represents a starting point towards the development of a reliable real-time monitoring system able to evaluate the melt pool height regardless of the deposition direction.

In conclusion, this dissertation has made substantial contributions to advancing the state-of-the-art in AM process monitoring. By addressing the critical need for reliable, in-situ and real-time defect detection and process control, it paves the way for broader industrial adoption of AM technologies. These innovations not only enhance the quality and reproducibility of AM-produced parts but also fosters AM as a sustainable, efficient manufacturing solution for the future.

8. Bibliography

[1] T. Peng, Y. Zhu, M. Leu, D. Bourell, Additive manufacturing-enabled design, manufacturing, and lifecycle performance, Addit Manuf 36 (2020). https://doi.org/10.1016/j.addma.2020.101646.

[2] M. Faes, W. Abbeloos, F. Vogeler, H. Valkenaers, K. Coppens, T. Goedemé, E. Ferraris, Process Monitoring of Extrusion Based 3D Printing via Laser Scanning, (2016). https://doi.org/10.13140/2.1.5175.0081.

[3] T. Maconachie, M. Leary, B. Lozanovski, X. Zhang, M. Qian, O. Faruque, M. Brandt, SLM lattice structures: Properties, performance, applications and challenges, Mater Des 183 (2019). https://doi.org/10.1016/j.matdes.2019.108137.

[4] S. El Baakili, A. Baghad, M. Bricha, K. El Mabrouk, Additive Manufacturing of Titanium Alloys for Aerospace and Biomedical Applications, in: R.V. Vignesh, R. Padmanaban, M. Govindaraju (Eds.), Advances in Processing of Lightweight Metal Alloys and Composites: Microstructural Characterization and Property Correlation, Springer Nature Singapore, Singapore, 2023: pp. 433–442. https://doi.org/10.1007/978-981-19-7146-4_24.

[5] P.I. Pradeep, V.A. Kumar, A. Sriranganath, S.K. Singh, A. Sahu, T.S. Kumar, P.R. Narayanan, M. Arumugam, M. Mohan, Characterization and Qualification of LPBF Additively Manufactured AISI-316L Stainless Steel Brackets for Aerospace Application, Transactions of the Indian National Academy of Engineering 5 (2020) 603–616. https://doi.org/10.1007/s41403-020-00159-x.

[6] L. Fernando Velásquez-García, Y. Kornbluth, Biomedical Applications of Metal 3D Printing, (2021). https://doi.org/10.1146/annurev-bioeng-082020.

[7] S.K. Everton, M. Hirsch, P.I. Stavroulakis, R.K. Leach, A.T. Clare, Review of in-situ process monitoring and in-situ metrology for metal additive manufacturing, Mater Des 95 (2016) 431–445. https://doi.org/10.1016/j.matdes.2016.01.099.

[8] Y. AbouelNour, N. Gupta, In-situ monitoring of sub-surface and internal defects in additive manufacturing: A review, Mater Des 222 (2022). https://doi.org/10.1016/j.matdes.2022.111063.

[9] H.D. Vora, S. Sanyal, A comprehensive review: metrology in additive manufacturing and 3D printing technology, Progress in Additive Manufacturing 5 (2020) 319–353. https://doi.org/10.1007/s40964-020-00142-6.

[10] V. Zhou, K. Odum, M. Soshi, K. Yamazaki, Development of a height control system using a dynamic powder splitter for directed energy deposition (DED) additive manufacturing, Progress in Additive Manufacturing 7 (2022) 1085–1092. https://doi.org/10.1007/s40964-022-00283-w.

[11] F. Caltanissetta, M. Grasso, B.M. Colosimo, In-Situ Defect Detection and Correction in Laser Powder Bed Fusion, n.d.

[12] J.M. Waller, B.H. Parker, K.L. Hodges, E.R. Burke, J.L. Walker, E.R. Generazio, Nondestructive Evaluation of Additive Manufacturing State-of-the-Discipline Report, 2014. http://www.sti.nasa.gov.

[13] A. Oleff, B. Küster, M. Stonis, L. Overmeyer, Process monitoring for material extrusion additive manufacturing: a state-of-the-art review, Progress in Additive Manufacturing 6 (2021) 705–730. https://doi.org/10.1007/s40964-021-00192-4.

[14] R.K. Leach, D. Bourell, S. Carmignato, A. Donmez, N. Senin, W. Dewulf, Geometrical metrology for metal additive manufacturing, CIRP Annals 68 (2019) 677–700. https://doi.org/10.1016/j.cirp.2019.05.004.

[15] C. Dou, D. Elkins, Z. (James) Kong, C. Liu, Online Monitoring and Control of Polymer Additive Manufacturing Processes, in: Additive Manufacturing Design and Applications, ASM International, 2023: pp. 413–425. https://doi.org/10.31399/asm.hb.v24a.a0006968.

[16] Y. Li, W. Zhao, Q. Li, T. Wang, G. Wang, In-situ monitoring and diagnosing for fused filament fabrication process based on vibration sensors, Sensors (Switzerland) 19 (2019). https://doi.org/10.3390/s19112589.

[17] Y. Li, W. Zhao, Q. Li, T. Wang, G. Wang, In-situ monitoring and diagnosing for fused filament fabrication process based on vibration sensors, Sensors (Switzerland) 19 (2019). https://doi.org/10.3390/s19112589.

[18] K. Tzimanis, M.S. Koutsokeras, N. Porevopoulos, P. Stavropoulos, ScienceDirect-NC-ND license (https://creativecommons.org/licenses/by-nc-nd/4.0) Peer-review under responsibility of the scientific A Load Cell-based Monitoring System for In-line Over Build Detection in wire Laser-based DED process-NC-ND license (https://creativecommons.org/licenses/by-nc-nd/4.0) Peer-review under responsibility of the scientific, n.d. www.sciencedirect.comwww.elsevier.com/locate/procedia2212-8271.

[19] M. Grasso, B.M. Colosimo, Process defects and in situ monitoring methods in metal powder bed fusion: A review, Meas Sci Technol 28 (2017). https://doi.org/10.1088/1361-6501/aa5c4f.

[20] E. Malekipour, H. El-Mounayri, Common defects and contributing parameters in powder bed fusion AM process and their classification for online monitoring and control: a review, International Journal of Advanced Manufacturing Technology 95 (2018) 527–550. https://doi.org/10.1007/s00170-017-1172-6.

[21] W. He, W. Shi, J. Li, H. Xie, In-situ monitoring and deformation characterization by optical techniques; part I: Laser-aided direct metal deposition for additive manufacturing, Opt Lasers Eng 122 (2019) 74–88. https://doi.org/10.1016/j.optlaseng.2019.05.020.

[22] A. Selot, R.K. Dwivedi, Machine learning and sensor-based approach for defect detection in MEX additive manufacturing process- A Review, Journal of the Brazilian Society of Mechanical Sciences and Engineering 45 (2023). https://doi.org/10.1007/s40430-023-04425-1.

[23] M. Moretti, F. Bianchi, N. Senin, Towards the development of a smart fused filament fabrication system using multi-sensor data fusion for in-process monitoring, Rapid Prototyp J 26 (2020) 1249–1261. https://doi.org/10.1108/RPJ-06-2019-0167.

[24] ISOASTM 52900_AM terminology, (n.d.).

[25] K. Rajan, M. Samykano, K. Kadirgama, W.S.W. Harun, M.M. Rahman, Fused deposition modeling: process, materials, parameters, properties, and applications, International Journal of Advanced Manufacturing Technology 120 (2022) 1531–1570. https://doi.org/10.1007/s00170-022-08860-7.

[26] A. Pellegrini, M.E. Palmieri, F. Lavecchia, L. Tricarico, L.M. Galantucci, Auxetic behavior of 3D-printed structure made in acrylonitrile butadiene styrene and carbon fiber-reinforced polyamide, Progress in Additive Manufacturing (2023). https://doi.org/10.1007/s40964-023-00465-0.

[27] F.T. Jahromi, M. Nikzad, K. Prasad, J. Norén, M. Isaksson, A. Arian, I. Sbarski, Additive manufacturing of polypropylene micro and nano composites through fused filament fabrication for automotive repair applications, Polym Adv Technol 34 (2023) 1059–1074. https://doi.org/10.1002/pat.5952.

[28] A. Pellegrini, M.E. Palmieri, M.G. Guerra, Evaluation of anisotropic mechanical behaviour of 316L parts realized by metal fused filament fabrication using digital image correlation, International Journal of Advanced Manufacturing Technology 120 (2022) 7951–7965. https://doi.org/10.1007/s00170-022-09303-z.

[29] J. Haley, J. Karandikar, C. Herberger, E. MacDonald, T. Feldhausen, Y. Lee, Review of in situ process monitoring for metal hybrid directed energy deposition, J Manuf Process 109 (2024) 128–139. https://doi.org/10.1016/j.jmapro.2023.12.004.

[30] L. Fernando Velásquez-García, Y. Kornbluth, Biomedical Applications of Metal 3D Printing, (2021). https://doi.org/10.1146/annurev-bioeng-082020.

[31] S. El Baakili, A. Baghad, M. Bricha, K. El Mabrouk, Additive Manufacturing of Titanium Alloys for Aerospace and Biomedical Applications, in: R.V. Vignesh, R. Padmanaban, M. Govindaraju (Eds.), Advances in Processing of Lightweight Metal Alloys and Composites: Microstructural Characterization and Property Correlation, Springer Nature Singapore, Singapore, 2023: pp. 433–442. https://doi.org/10.1007/978-981-19-7146-4_24.

[32] Z.-J. Tang, W.-W. Liu, Y.-W. Wang, & Kaze, M. Saleheen, Z.-C. Liu, & Shi-Tong Peng, Z. Zhang, H.-C. Zhang, A review on in situ monitoring technology for directed energy deposition of metals, (n.d.). https://doi.org/10.1007/s00170-020-05569-3/Published.

[33] M.G. Guerra, V. Errico, A. Fusco, F. Lavecchia, S.L. Campanelli, L.M. Galantucci, High resolution-optical tomography for in-process layerwise monitoring of a laser-powder bed fusion technology, Addit Manuf 55 (2022) 102850. https://doi.org/https://doi.org/10.1016/j.addma.2022.102850.

[34] M. Doshi, A. Mahale, S.K. Singh, S. Deshmukh, Printing parameters and materials affecting mechanical properties of FDM-3D printed Parts: Perspective and prospects, in: Mater Today Proc, Elsevier Ltd, 2021: pp. 2269–2275. https://doi.org/10.1016/j.matpr.2021.10.003.

[35] D. Jiang, F. Ning, Anisotropic deformation of 316L stainless steel overhang structures built by material extrusion based additive manufacturing, Addit Manuf 50 (2022). https://doi.org/10.1016/j.addma.2021.102545.

[36] K. Günaydın, H. Süleyman Türkmen, Common FDM 3D Printing Defects, 2018. https://www.researchgate.net/publication/326146283.

[37] W. Lin, H. Shen, J. Fu, S. Wu, Online quality monitoring in material extrusion additive manufacturing processes based on laser scanning technology, Precis Eng 60 (2019) 76–84. https://doi.org/10.1016/j.precisioneng.2019.06.004.

[38] M. Grazia Guerra, M. Lafirenza, V. Errico, A. Angelastro, In-process dimensional and geometrical characterization of laser-powder bed fusion lattice structures through high-resolution optical tomography, Opt Laser Technol 162 (2023). https://doi.org/10.1016/j.optlastec.2023.109252.

[39] W.J. Sames, F.A. List, S. Pannala, R.R. Dehoff, S.S. Babu, The metallurgy and processing science of metal additive manufacturing, International Materials Reviews 61 (2016) 315–360. https://doi.org/10.1080/09506608.2015.1116649.

[40] M. Liu, A. Kumar, S. Bukkapatnam, M. Kuttolamadom, A review of the anomalies in directed energy deposition (DED) processes & potential solutions - Part quality & defects, in: Procedia Manuf, Elsevier B.V., 2021: pp. 507–518. https://doi.org/10.1016/j.promfg.2021.06.093.

[41] Z. Li, X. Liu, S. Wen, P. He, K. Zhong, Q. Wei, Y. Shi, S. Liu, In situ 3D monitoring of geometric signatures in the powder-bed-fusion additive manufacturing process via vision sensing methods, Sensors (Switzerland) 18 (2018). https://doi.org/10.3390/s18041180.

[42] B. Cheng, J. Lydon, K. Cooper, V. Cole, P. Northrop, K. Chou, Infrared thermal imaging for melt pool analysis in SLM: a feasibility investigation, Virtual Phys Prototyp 13 (2018) 8–13. https://doi.org/10.1080/17452759.2017.1392685.

[43] L.J. Gibson, M.F. Ashby, Cellular Solids, Cambridge University Press, 1997. https://doi.org/10.1017/CBO9781139878326.

[44] B.M. Colosimo, M. Grasso, F. Garghetti, B. Rossi, Complex geometries in additive manufacturing: A new solution for lattice structure modeling and monitoring, Journal of Quality Technology 54 (2022) 392–414. https://doi.org/10.1080/00224065.2021.1926377.

[45] D. Li, R. Qin, B. Chen, J. Zhou, Analysis of mechanical properties of lattice structures with stochastic geometric defects in additive manufacturing, Materials Science and Engineering A 822 (2021). https://doi.org/10.1016/j.msea.2021.141666.

[46] E.W. Jost, D.G. Moore, C. Saldana, Evolution of global and local deformation in additively manufactured octet truss lattice structures, Additive Manufacturing Letters 1 (2021) 100010. https://doi.org/10.1016/j.addlet.2021.100010.

[47] B. Lozanovski, D. Downing, R. Tino, P. Tran, D. Shidid, C. Emmelmann, M. Qian, P. Choong, M. Brandt, M. Leary, Image-Based Geometrical Characterization of Nodes in Additively Manufactured Lattice Structures, 3D Print Addit Manuf 8 (2021) 51–68. https://doi.org/10.1089/3dp.2020.0091.

[48] E.W. Jost, D.G. Moore, C. Saldana, Evolution of global and local deformation in additively manufactured octet truss lattice structures, Additive Manufacturing Letters 1 (2021) 100010. https://doi.org/10.1016/j.addlet.2021.100010.

[49] C. Zhao, K. Fezzaa, R.W. Cunningham, H. Wen, F. De Carlo, L. Chen, A.D. Rollett, T. Sun, Real-time monitoring of laser powder bed fusion process using high-speed X-ray imaging and diffraction, Sci Rep 7 (2017). https://doi.org/10.1038/s41598-017-03761-2.

[50] T. Wischeropp, C. Emmelman, M. Brandt, A. Pateras, Measurement of actual powder layer height and packing density in a single layer in selective laser melting, Addit Manuf 28 (2019) 8. https://doi.org/10.1016/j.addma.2019.04.019.

[51] L. Chen, X. Yao, P. Xu, S.K. Moon, G. Bi, Rapid surface defect identification for additive manufacturing with in-situ point cloud processing and machine learning, Virtual Phys Prototyp 16 (2021) 50–67. https://doi.org/10.1080/17452759.2020.1832695.

[52] M. Samie Tootooni, A. Dsouza, R. Donovan, P.K. Rao, Z. (James) Kong, P. Borgesen, Classifying the Dimensional Variation in Additive Manufactured Parts From Laser-Scanned Three-Dimensional Point Cloud Data Using Machine Learning Approaches, J Manuf Sci Eng 139 (2017). https://doi.org/10.1115/1.4036641.

[53] S. Khan, K. Joshi, S. Deshmukh, A comprehensive review on effect of printing parameters on mechanical properties of FDM printed parts, in: Mater Today Proc, Elsevier Ltd, 2021: pp. 2119–2127. https://doi.org/10.1016/j.matpr.2021.09.433.

[54] H. Wu, Y. Wang, Z. Yu, In situ monitoring of FDM machine condition via acoustic emission, International Journal of Advanced Manufacturing Technology 84 (2016) 1483–1495. https://doi.org/10.1007/s00170-015-7809-4.

[55] M.S. Hossain, H. Taheri, In Situ Process Monitoring for Additive Manufacturing Through Acoustic Techniques, J Mater Eng Perform 29 (2020) 6249–6262. https://doi.org/10.1007/s11665-020-05125-w.

[56] H. Wu, Z. Yu, Y. Wang, Experimental study of the process failure diagnosis in additive manufacturing based on acoustic emission, Measurement 136 (2019) 445–453. https://doi.org/10.1016/j.measurement.2018.12.067.

[57] S.R. Chhetri, A. Canedo, M.A. Al Faruque, KCAD, in: Proceedings of the 35th International Conference on Computer-Aided Design, ACM, New York, NY, USA, 2016: pp. 1–8. https://doi.org/10.1145/2966986.2967050.

[58] Y. Tlegenov, Y.S. Wong, G.S. Hong, A dynamic model for nozzle clog monitoring in fused deposition modelling, Rapid Prototyp J 23 (2017) 391–400. https://doi.org/10.1108/RPJ-04-2016-0054.

[59] Y. Tlegenov, G.S. Hong, W.F. Lu, Nozzle condition monitoring in 3D printing, Robot Comput Integr Manuf 54 (2018) 45–55. https://doi.org/10.1016/j.rcim.2018.05.010.

[60] C.-T. Yen, P.-C. Chuang, Application of a neural network integrated with the internet of things sensing technology for 3D printer fault diagnosis, Microsystem Technologies 28 (2022) 13–23. https://doi.org/10.1007/s00542-019-04323-4.

[61] I. Cummings, E. Hillstrom, R. Newton, E. Flynn, A. Wachtor, In-Process Ultrasonic Inspection of Additive Manufactured Parts, in: 2016: pp. 235–247. https://doi.org/10.1007/978-3-319-30249-2_20.

[62] E.C. Koskelo, E.B. Flynn, Scanning laser ultrasound and wavenumber spectroscopy for in-process inspection of additively manufactured parts, in: T. Yu, A.L. Gyekenyesi, P.J. Shull, H.F. Wu (Eds.), 2016: p. 980418. https://doi.org/10.1117/12.2222130.

[63] H.R. Vanaei, M. Shirinbayan, M. Deligant, S. Khelladi, A. Tcharkhtchi, In-Process Monitoring of Temperature Evolution during Fused Filament Fabrication: A Journey from Numerical to Experimental Approaches, Thermo 1 (2021) 332–360. https://doi.org/10.3390/thermo1030021.

[64] J.E. Seppala, K.D. Migler, Infrared thermography of welding zones produced by polymer extrusion additive manufacturing, Addit Manuf 12 (2016) 71–76. https://doi.org/10.1016/j.addma.2016.06.007.

[65] J.E. Seppala, S. Hoon Han, K.E. Hillgartner, C.S. Davis, K.B. Migler, Weld formation during material extrusion additive manufacturing, Soft Matter 13 (2017) 6761–6769. https://doi.org/10.1039/C7SM00950J.

[66] B.G. Compton, B.K. Post, C.E. Duty, L. Love, V. Kunc, Thermal analysis of additive manufacturing of large-scale thermoplastic polymer composites, Addit Manuf 17 (2017) 77–86. https://doi.org/10.1016/j.addma.2017.07.006.

[67] H. Prajapati, D. Ravoori, A. Jain, Measurement and modeling of filament temperature distribution in the standoff gap between nozzle and bed in polymer-based additive manufacturing, Addit Manuf 24 (2018) 224–231. https://doi.org/10.1016/j.addma.2018.09.030.

[68] E. Ferraris, J. Zhang, B. Van Hooreweder, Thermography based in-process monitoring of Fused Filament Fabrication of polymeric parts, CIRP Annals 68 (2019) 213–216. https://doi.org/10.1016/j.cirp.2019.04.123.

[69] V.E. Kuznetsov, A.N. Solonin, A. Tavitov, O. Urzhumtsev, A. Vakulik, Increasing strength of FFF three-dimensional printed parts by influencing on temperature-related parameters of the process, Rapid Prototyp J 26 (2020) 107–121. https://doi.org/10.1108/RPJ-01-2019-0017.

[70] A. Lepoivre, N. Boyard, A. Levy, V. Sobotka, Heat Transfer and Adhesion Study for the FFF Additive Manufacturing Process, Procedia Manuf 47 (2020) 948–955. https://doi.org/10.1016/j.promfg.2020.04.291.

[71] C. Basgul, F.M. Thieringer, S.M. Kurtz, Heat transfer-based non-isothermal healing model for the interfacial bonding strength of fused filament fabricated polyetheretherketone, Addit Manuf 46 (2021) 102097. https://doi.org/10.1016/j.addma.2021.102097.

[72] J. Yin, C. Lu, J. Fu, Y. Huang, Y. Zheng, Interfacial bonding during multi-material fused deposition modeling (FDM) process due to inter-molecular diffusion, Mater Des 150 (2018) 104–112. https://doi.org/10.1016/j.matdes.2018.04.029.

[73] D. Xu, Y. Zhang, F. Pigeonneau, Thermal analysis of the fused filament fabrication printing process: Experimental and numerical investigations, International Journal of Material Forming 14 (2021) 763–776. https://doi.org/10.1007/s12289-020-01591-8.

[74] H.R. Vanaei, M. Shirinbayan, S.F. Costa, F.M. Duarte, J.A. Covas, M. Deligant, S. Khelladi, A. Tcharkhtchi, Experimental study of <scp>PLA</scp> thermal behavior during fused filament fabrication, J Appl Polym Sci 138 (2021). https://doi.org/10.1002/app.49747.

[75] S. Nuchitprasitchai, M. Roggemann, J.M. Pearce, Factors effecting real-time optical monitoring of fused filament 3D printing, Progress in Additive Manufacturing 2 (2017) 133–149. https://doi.org/10.1007/s40964-017-0027-x.

[76] Q.Y. Lu, C.H. Wong, Additive manufacturing process monitoring and control by non-destructive testing techniques: challenges and in-process monitoring, Virtual Phys Prototyp 13 (2018) 39–48. https://doi.org/10.1080/17452759.2017.1351201.

[77] J. Li, W. Quan, L.-K. Shark, H. Laurence Brooks, A Vision-based Monitoring System for Quality Assessment of Fused Filament Fabrication (FFF) 3D Printing, in: 2022 the 5th International Conference on Image and Graphics Processing (ICIGP), ACM, New York, NY, USA, 2022: pp. 242–250. https://doi.org/10.1145/3512388.3512424.

[78] A. Rossi, M. Moretti, N. Senin, Layer inspection via digital imaging and machine learning for in-process monitoring of fused filament fabrication, J Manuf Process 70 (2021) 438–451. https://doi.org/10.1016/j.jmapro.2021.08.057.

[79] M. Moretti, A. Rossi, N. Senin, In-process monitoring of part geometry in fused filament fabrication using computer vision and digital twins, Addit Manuf 37 (2021) 101609. https://doi.org/10.1016/j.addma.2020.101609.

[80] C. Liu, A.C.C. Law, D. Roberson, Z. (James) Kong, Image analysis-based closed loop quality control for additive manufacturing with fused filament fabrication, J Manuf Syst 51 (2019) 75–86. https://doi.org/10.1016/j.jmsy.2019.04.002.

[81] T. Huang, S. Wang, S. Yang, W. Dai, Statistical process monitoring in a specified period for the image data of fused deposition modeling parts with consistent layers, J Intell Manuf 32 (2021) 2181–2196. https://doi.org/10.1007/s10845-020-01628-4.

[82] K. He, Q. Zhang, Y. Hong, Profile monitoring based quality control method for fused deposition modeling process, J Intell Manuf 30 (2019) 947–958. https://doi.org/10.1007/s10845-018-1424-9.

[83] U. Delli, S. Chang, Automated Process Monitoring in 3D Printing Using Supervised Machine Learning, Procedia Manuf 26 (2018) 865–870. https://doi.org/10.1016/j.promfg.2018.07.111.

[84] G.P. Greeff, M. Schilling, Comparing Retraction Methods with Volumetric Exit Flow Measurement in Molten Material Extrusion, n.d. www.euspen.eu.

[85] G.P. Greeff, M. Schilling, Closed loop control of slippage during filament transport in molten material extrusion, Addit Manuf 14 (2017) 31–38. https://doi.org/10.1016/j.addma.2016.12.005.

[86] A. Malik, H. Lhachemi, J. Ploennigs, A. Ba, R. Shorten, An Application of 3D Model Reconstruction and Augmented Reality for Real-Time Monitoring of Additive Manufacturing, Procedia CIRP 81 (2019) 346–351. https://doi.org/10.1016/j.procir.2019.03.060.

[87] O. Holzmond, X. Li, In situ real time defect detection of 3D printed parts, Addit Manuf 17 (2017) 135–142. https://doi.org/10.1016/j.addma.2017.08.003.

[88] Z. Ye, C. Liu, W. Tian, C. Kan, In-situ point cloud fusion for layer-wise monitoring of additive manufacturing, J Manuf Syst 61 (2021) 210–222. https://doi.org/10.1016/j.jmsy.2021.09.002.

[89] P. Charalampous, I. Kostavelis, C. Kopsacheilis, D. Tzovaras, Vision-based real-time monitoring of extrusion additive manufacturing processes for automatic manufacturing error detection, (n.d.). https://doi.org/10.1007/s00170-021-07419-2/Published.

[90] J. Lyu, S. Manoochehri, Online Convolutional Neural Network-based anomaly detection and quality control for Fused Filament Fabrication process, Virtual Phys Prototyp 16 (2021) 160–177. https://doi.org/10.1080/17452759.2021.1905858.

[91] S. Lou, Z. Zhu, W. Zeng, C. Majewski, P.J. Scott, X. Jiang, Material ratio curve of 3D surface topography of additively manufactured parts: An attempt to characterise open surface pores, Surf Topogr 9 (2021). https://doi.org/10.1088/2051-672X/abedf9.

[92] R. McCann, M.A. Obeidi, C. Hughes, É. McCarthy, D.S. Egan, R.K. Vijayaraghavan, A.M. Joshi, V. Acinas Garzon, D.P. Dowling, P.J. McNally, D. Brabazon, In-situ sensing, process monitoring and machine control in Laser Powder Bed Fusion: A review, Addit Manuf 45 (2021). https://doi.org/10.1016/j.addma.2021.102058.

[93] H. Rieder, M. Spies, J. Bamberg, B. Henkel, On- and offline ultrasonic characterization of components built by SLM additive manufacturing, in: AIP Conf Proc, American Institute of Physics Inc., 2016. https://doi.org/10.1063/1.4940605.

[94] S.A. Shevchik, C. Kenel, C. Leinenbach, K. Wasmer, Acoustic emission for in situ quality monitoring in additive manufacturing using spectral convolutional neural networks, Addit Manuf 21 (2018) 598–604. https://doi.org/10.1016/j.addma.2017.11.012.

[95] J. Bamberg, A. Dillhöfer, H. Rieder, M. Spies, T. Hess, Online Monitoring of Additive Manufacturing Processes Using Ultrasound, 2014. https://www.researchgate.net/publication/271850494.

[96] D. Ye, G.S. Hong, Y. Zhang, K. Zhu, J.Y.H. Fuh, Defect detection in selective laser melting technology by acoustic signals with deep belief networks, International Journal of Advanced Manufacturing Technology 96 (2018) 2791–2801. https://doi.org/10.1007/s00170-018-1728-0.

[97] B. Zhang, Y. Li, Q. Bai, Defect Formation Mechanisms in Selective Laser Melting: A Review, Chinese Journal of Mechanical Engineering (English Edition) 30 (2017) 515–527. https://doi.org/10.1007/s10033-017-0121-5.

[98] E. Rodriguez, J. Mireles, C.A. Terrazas, D. Espalin, M.A. Perez, R.B. Wicker, Approximation of absolute surface temperature measurements of powder bed fusion additive manufacturing technology using in situ infrared thermography, Addit Manuf 5 (2015) 31–39. https://doi.org/10.1016/j.addma.2014.12.001.

[99] A.J. Dunbar, E.R. Denlinger, J. Heigel, P. Michaleris, P. Guerrier, R. Martukanitz, T.W. Simpson, Development of experimental method for in situ distortion and temperature measurements during the laser powder bed fusion additive manufacturing process, Addit Manuf 12 (2016) 25–30. https://doi.org/10.1016/j.addma.2016.04.007.

[100] S. Berumen, F. Bechmann, S. Lindner, J.-P. Kruth, T. Craeghs, Quality control of laser- and powder bed-based Additive Manufacturing (AM) technologies, Phys Procedia 5 (2010) 617–622. https://doi.org/10.1016/j.phpro.2010.08.089.

[101] T. Craeghs, S. Clijsters, Jean.-P. Kruth, F. Bechmann, Marie.-C. Ebert, Detection of Process Failures in Layerwise Laser Melting with Optical Process Monitoring, Phys Procedia 39 (2012) 753–759. https://doi.org/10.1016/j.phpro.2012.10.097.

[102] T. Craeghs, F. Bechmann, S. Berumen, J.-P. Kruth, Feedback control of Layerwise Laser Melting using optical sensors, Phys Procedia 5 (2010) 505–514. https://doi.org/10.1016/j.phpro.2010.08.078.

[103] S. Clijsters, T. Craeghs, S. Buls, K. Kempen, J.-P. Kruth, In situ quality control of the selective laser melting process using a high-speed, real-time melt pool monitoring system, The International Journal of Advanced Manufacturing Technology 75 (2014) 1089–1101. https://doi.org/10.1007/s00170-014-6214-8.

[104] M.A. Doubenskaia, I.V. Zhirnov, V.I. Teleshevskiy, P. Bertrand, I.Y. Smurov, Determination of True Temperature in Selective Laser Melting of Metal Powder Using Infrared Camera, Materials Science Forum 834 (2015) 93–102. https://doi.org/10.4028/www.scientific.net/MSF.834.93.

[105] Y. Chivel, Optical In-Process Temperature Monitoring of Selective Laser Melting, Phys Procedia 41 (2013) 904–910. https://doi.org/10.1016/j.phpro.2013.03.165.

[106] U. Thombansen, A. Gatej, M. Pereira, Process observation in fiber laser–based selective laser melting, Optical Engineering 54 (2014) 011008. https://doi.org/10.1117/1.OE.54.1.011008.

[107] G. Mohr, S.J. Altenburg, A. Ulbricht, P. Heinrich, D. Baum, C. Maierhofer, K. Hilgenberg, In-Situ Defect Detection in Laser Powder Bed Fusion by Using Thermography and Optical Tomography—Comparison to Computed Tomography, Metals (Basel) 10 (2020) 103. https://doi.org/10.3390/met10010103.

[108] H. Krauss, C. Eschey, M.F. Zaeh, Thermography for Monitoring the Selective Laser Melting Process, n.d.

[109] H. Krauss, T. Zeugner, M.F. Zaeh, Layerwise Monitoring of the Selective Laser Melting Process by Thermography, Phys Procedia 56 (2014) 64–71. https://doi.org/10.1016/j.phpro.2014.08.097.

[110] B. Lane, S. Moylan, E.P. Whitenton, L. Ma, Thermographic measurements of the commercial laser powder bed fusion process at NIST, Rapid Prototyp J 22 (2016) 778–787. https://doi.org/10.1108/RPJ-11-2015-0161.

[111] M. Islam, T. Purtonen, H. Piili, A. Salminen, O. Nyrhilä, Temperature Profile and Imaging Analysis of Laser Additive Manufacturing of Stainless Steel, Phys Procedia 41 (2013) 835–842. https://doi.org/10.1016/j.phpro.2013.03.156.

[112] J. Schwerdtfeger, R.F. Singer, C. Körner, In situ flaw detection by IR-imaging during electron beam melting, Rapid Prototyp J 18 (2012) 259–263. https://doi.org/10.1108/13552541211231572.

[113] M. Grasso, V. Laguzza, Q. Semeraro, B.M. Colosimo, In-Process Monitoring of Selective Laser Melting: Spatial Detection of Defects Via Image Data Analysis, J Manuf Sci Eng 139 (2017). https://doi.org/10.1115/1.4034715.

[114] B. Yuan, B. Giera, G. Guss, M. Matthews, S. McMains, Semi-supervised convolutional neural networks for in-situ video monitoring of selective laser melting, in: Proceedings - 2019 IEEE Winter Conference on Applications of Computer Vision, WACV 2019, Institute of Electrical and Electronics Engineers Inc., 2019: pp. 744–753. https://doi.org/10.1109/WACV.2019.00084.

[115] J. Mi, Y. Zhang, H. Li, S. Shen, Y. Yang, C. Song, X. Zhou, Y. Duan, J. Lu, H. Mai, In-situ monitoring laser based directed energy deposition process with deep convolutional neural network, J Intell Manuf 34 (2023) 683–693. https://doi.org/10.1007/s10845-021-01820-0.

[116] L. Scime, J. Beuth, Using machine learning to identify in-situ melt pool signatures indicative of flaw formation in a laser powder bed fusion additive manufacturing process, Addit Manuf 25 (2019) 151–165. https://doi.org/10.1016/j.addma.2018.11.010.

[117] M. Bugatti, B.M. Colosimo, Towards real-time in-situ monitoring of hot-spot defects in L-PBF: a new classification-based method for fast video-imaging data analysis, J Intell Manuf 33 (2022) 293–309. https://doi.org/10.1007/s10845-021-01787-y.

[118] L. Scime, B. Fisher, J. Beuth, Using coordinate transforms to improve the utility of a fixed field of view high speed camera for additive manufacturing applications, Manuf Lett 15 (2018) 104–106. https://doi.org/10.1016/j.mfglet.2018.01.006.

[119] L. Caprio, A.G. Demir, B. Previtali, Observing molten pool surface oscillations during keyhole processing in laser powder bed fusion as a novel method to estimate the penetration depth, Addit Manuf 36 (2020) 101470. https://doi.org/10.1016/j.addma.2020.101470.

[120] H.-C. Yang, C.-H. Huang, M. Adnan, C.-H. Hsu, C.-H. Lin, F.-T. Cheng, An Online AM Quality Estimation Architecture From Pool to Layer, IEEE Transactions on Automation Science and Engineering 18 (2021) 269–281. https://doi.org/10.1109/TASE.2020.3012622.

[121] J.P. Kruth, P. Mercelis, J. Van Vaerenbergh, T. Craeghs, Feedback control of selective laser melting, in: Proceedings of the 3rd International Conference on Advanced Research in Virtual and Rapid Prototyping, TAYLOR & FRANCIS LTD, Leiria, 2007: pp. 521–527.

[122] J.A. Kanko, A.P. Sibley, J.M. Fraser, In situ morphology-based defect detection of selective laser melting through inline coherent imaging, J Mater Process Technol 231 (2016) 488–500. https://doi.org/10.1016/j.jmatprotec.2015.12.024.

[123] G. Guan, M. Hirsch, Z.H. Lu, D.T.D. Childs, S.J. Matcher, R. Goodridge, K.M. Groom, A.T. Clare, Evaluation of selective laser sintering processes by optical coherence tomography, Mater Des 88 (2015) 837–846. https://doi.org/10.1016/j.matdes.2015.09.084.

[124] J. Zur Jacobsmuhlen, S. Kleszczynski, D. Schneider, G. Witt, High Resolution Imaging for Inspection of Laser Beam Melting Systems, n.d.

[125] E. Yasa, J.-P. Kruth, K.U. Leuven, Online quality control of selective laser melting, 2011. https://www.researchgate.net/publication/268293509.

[126] M. Aminzadeh, T. Kurfess, IN-SITU QUALITY INSPECTION OF LASER POWDER-BED FUSION USING HIGH-RESOLUTION VISUAL CAMERA IMAGES, n.d.

[127] S. Kleszczynski, J. Sehrt, G. Witt, zur Jacobsmühlen, Error detection in laser beam melting systems by high resolution imaging, 2016. www.lfb.rwth-aachen.de.

[128] B. Shen, W. Xie, Z. James Kong, Clustered Discriminant Regression for High-Dimensional Data Feature Extraction and Its Applications in Healthcare and Additive Manufacturing, IEEE Transactions on Automation Science and Engineering 18 (2021) 1998–2010. https://doi.org/10.1109/TASE.2020.3029028.

[129] A. Caggiano, J. Zhang, V. Alfieri, F. Caiazzo, R. Gao, R. Teti, Machine learning-based image processing for on-line defect recognition in additive manufacturing, CIRP Annals 68 (2019) 451–454. https://doi.org/10.1016/j.cirp.2019.03.021.

[130] F. Wasserfall, D. Ahlers, N. Hendrich, Optical In-Situ Verification of 3D-Printed Electronic Circuits, in: 2019 IEEE 15th International Conference on Automation Science and Engineering (CASE), IEEE, 2019: pp. 1302–1307. https://doi.org/10.1109/COASE.2019.8842835.

[131] L. Scime, J. Beuth, A multi-scale convolutional neural network for autonomous anomaly detection and classification in a laser powder bed fusion additive manufacturing process, Addit Manuf 24 (2018) 273–286. https://doi.org/10.1016/j.addma.2018.09.034.

[132] L. Scime, D. Siddel, S. Baird, V. Paquit, Layer-wise anomaly detection and classification for powder bed additive manufacturing processes: A machine-agnostic algorithm for real-time pixel-wise semantic segmentation, Addit Manuf 36 (2020) 101453. https://doi.org/10.1016/j.addma.2020.101453.

[133] C. Gobert, E.W. Reutzel, J. Petrich, A.R. Nassar, S. Phoha, Application of supervised machine learning for defect detection during metallic powder bed fusion additive manufacturing using high resolution imaging., Addit Manuf 21 (2018) 517–528. https://doi.org/10.1016/j.addma.2018.04.005.

[134] Q.Y. Lu, N.V. Nguyen, A.J.W. Hum, T. Tran, C.H. Wong, Identification and evaluation of defects in selective laser melted 316L stainless steel parts via in-situ monitoring and micro computed tomography, Addit Manuf 35 (2020) 101287. https://doi.org/10.1016/j.addma.2020.101287.

[135] J. zur Jacobsmühlen, J. Achterhold, S. Kleszczynski, G. Witt, D. Merhof, In situ measurement of part geometries in layer images from laser beam melting processes, Progress in Additive Manufacturing 4 (2019) 155–165. https://doi.org/10.1007/s40964-018-0068-9.

[136] F. Caltanissetta, M. Grasso, S. Petrò, B.M. Colosimo, Characterization of in-situ measurements based on layerwise imaging in laser powder bed fusion, Addit Manuf 24 (2018) 183–199. https://doi.org/10.1016/j.addma.2018.09.017.

[137] M. Abdelrahman, E.W. Reutzel, A.R. Nassar, T.L. Starr, Flaw detection in powder bed fusion using optical imaging, Addit Manuf 15 (2017) 1–11. https://doi.org/10.1016/j.addma.2017.02.001.

[138] M. Erler, A. Streek, H. Exner, Novel Machine and Measurement Concept for Micro Machining by Selective Laser Sintering, n.d. https://www.researchgate.net/publication/308968522.

[139] J.L. Bartlett, B.P. Croom, J. Burdick, D. Henkel, X. Li, Revealing mechanisms of residual stress development in additive manufacturing via digital image correlation, Addit Manuf 22 (2018) 1–12. https://doi.org/10.1016/j.addma.2018.04.025.

[140] J.L. Bartlett, A. Jarama, J. Jones, X. Li, Prediction of microstructural defects in additive manufacturing from powder bed quality using digital image correlation, Materials Science and Engineering: A 794 (2020) 140002. https://doi.org/10.1016/j.msea.2020.140002.

[141] B. Zhang, J. Ziegert, F. Farahi, A. Davies, In situ surface topography of laser powder bed fusion using fringe projection, Addit Manuf 12 (2016) 100–107. https://doi.org/10.1016/j.addma.2016.08.001.

[142] J. Bamberg, G. Zenzinger, A. Ladewig, In-Process Control of Selective Laser Melting by Quantitative Optical Tomography, 2016. http://creativecommons.org/licenses/by/3.0/.

[143] I. Echeta, X. Feng, B. Dutton, R. Leach, S. Piano, Review of defects in lattice structures manufactured by powder bed fusion, International Journal of Advanced Manufacturing Technology 106 (2020) 2649–2668. https://doi.org/10.1007/s00170-019-04753-4.

[144] W. Liu, T. Wang, B. Liu, W. Li, G. Hu, Z. Lyu, Research of on-line monitoring technology and control strategy for laser-directed energy deposition: a review, The International Journal of Advanced Manufacturing Technology 133 (2024) 3105–3132. https://doi.org/10.1007/s00170-024-13893-1.

[145] S.J. Wolff, S. Webster, N.D. Parab, B. Aronson, B. Gould, A. Greco, T. Sun, In-situ Observations of Directed Energy Deposition Additive Manufacturing Using High-Speed X-ray Imaging, JOM 73 (2021) 189–200. https://doi.org/10.1007/s11837-020-04469-x.

[146] P. Lhuissier, X. Bataillon, C. Maestre, J. Sijobert, E. Cabrol, P. Bertrand, E. Boller, A. Rack, J.-J. Blandin, L. Salvo, G. Martin, In situ 3D X-ray microtomography of laser-based powder-bed fusion (L-PBF)—A feasibility study, Addit Manuf 34 (2020) 101271. https://doi.org/10.1016/j.addma.2020.101271.

[147] Z. Ren, L. Gao, S.J. Clark, K. Fezzaa, P. Shevchenko, A. Choi, W. Everhart, A.D. Rollett, L. Chen, T. Sun, Machine learning–aided real-time detection of keyhole pore generation in laser powder bed fusion, Science (1979) 379 (2023) 89–94. https://doi.org/10.1126/science.add4667.

[148] S.J. Wolff, H. Wu, N. Parab, C. Zhao, K.F. Ehmann, T. Sun, J. Cao, In-situ high-speed X-ray imaging of piezo-driven directed energy deposition additive manufacturing, Sci Rep 9 (2019) 962. https://doi.org/10.1038/s41598-018-36678-5.

[149] A. Lindenmeyer, S. Webster, M.F. Zaeh, K.F. Ehmann, J. Cao, Template-bayesian approach for the evaluation of melt pool shape and dimension of a DED-process from in-situ X-ray images, CIRP Annals 70 (2021) 183–186. https://doi.org/10.1016/j.cirp.2021.03.011.

[150] Y. Chen, S.J. Clark, L. Sinclair, C.L.A. Leung, S. Marussi, T. Connolley, R.C. Atwood, G.J. Baxter, M.A. Jones, I. Todd, P.D. Lee, Synchrotron X-ray imaging of directed energy deposition additive manufacturing of titanium alloy Ti-6242, Addit Manuf 41 (2021) 101969. https://doi.org/10.1016/j.addma.2021.101969.

[151] Y. Chen, S.J. Clark, D.M. Collins, S. Marussi, S.A. Hunt, D.M. Fenech, T. Connolley, R.C. Atwood, O. V. Magdysyuk, G.J. Baxter, M.A. Jones, C.L.A. Leung, P.D. Lee, Correlative Synchrotron X-ray Imaging and Diffraction of Directed Energy Deposition Additive Manufacturing, Acta Mater 209 (2021) 116777. https://doi.org/10.1016/j.actamat.2021.116777.

[152] C. Ioannidou, H.-H. König, N. Semjatov, U. Ackelid, P. Staron, C. Körner, P. Hedström, G. Lindwall, In-situ synchrotron X-ray analysis of metal Additive Manufacturing: Current state, opportunities and challenges, Mater Des 219 (2022) 110790. https://doi.org/10.1016/j.matdes.2022.110790.

[153] J.J. Valdiande, J. Mirapeix, J. Nin, E. Font, C. Seijas, J.M. Lopez-Higuera, Laser Metal Deposition On-Line Monitoring via Plasma Emission Spectroscopy and Spectral Correlation Techniques, IEEE Journal of Selected Topics in Quantum Electronics 27 (2021) 1–8. https://doi.org/10.1109/JSTQE.2021.3075489.

[154] B. Chen, Y. Yao, C. Tan, Y. Huang, J. Feng, A study on spectral characterization and quality detection of direct metal deposition process based on spectral diagnosis, The International Journal of Advanced Manufacturing Technology 96 (2018) 4231–4241. https://doi.org/10.1007/s00170-018-1889-x.

[155] J. Choi, M. Wooldridge, J. Mazumder, Spectroscopy-based smart optical monitoring system in the applications of laser additive manufacturing, J Laser Appl 35 (2023). https://doi.org/10.2351/7.0000910.

[156] W. Ren, J. Mazumder, In-situ porosity recognition for laser additive manufacturing of 7075-Al alloy using plasma emission spectroscopy, Sci Rep 10 (2020) 19493. https://doi.org/10.1038/s41598-020-75131-4.

[157] L. Song, W. Huang, X. Han, J. Mazumder, Real-Time Composition Monitoring Using Support Vector Regression of Laser-Induced Plasma for Laser Additive Manufacturing, IEEE Transactions on Industrial Electronics 64 (2017) 633–642. https://doi.org/10.1109/TIE.2016.2608318.

[158] M. Miyagi, T. Tsukamoto, H. Kawanaka, Adaptive shape control of laser-deposited metal structures by adjusting weld pool size, J Laser Appl 26 (2014). https://doi.org/10.2351/1.4869499.

[159] J. Lin, W.M. Steen, Design characteristics and development of a nozzle for coaxial laser cladding, J Laser Appl 10 (1998) 55–63. https://doi.org/10.2351/1.521821.

[160] G. Bi, B. Schürmann, A. Gasser, K. Wissenbach, R. Poprawe, Development and qualification of a novel laser-cladding head with integrated sensors, Int J Mach Tools Manuf 47 (2007) 555–561. https://doi.org/10.1016/j.ijmachtools.2006.05.010.

[161] G. Bi, A. Gasser, K. Wissenbach, A. Drenker, R. Poprawe, Identification and qualification of temperature signal for monitoring and control in laser cladding, Opt Lasers Eng 44 (2006) 1348–1359. https://doi.org/10.1016/j.optlaseng.2006.01.009.

[162] V.N. Lednev, P.A. Sdvizhenskii, R.D. Asyutin, R.S. Tretyakov, M.Ya. Grishin, A.Ya. Stavertiy, S.M. Pershin, In situ multi-elemental analysis by laser induced breakdown spectroscopy in additive manufacturing, Addit Manuf 25 (2019) 64–70. https://doi.org/10.1016/j.addma.2018.10.043.

[163] V.N. Lednev, P.A. Sdvizhenskii, A.Y. Stavertiy, M.Y. Grishin, R.S. Tretyakov, R.D. Asyutin, S.M. Pershin, Online and in situ laser-induced breakdown spectroscopy for laser welding monitoring, Spectrochim Acta Part B At Spectrosc 175 (2021) 106032. https://doi.org/10.1016/j.sab.2020.106032.

[164] C. Ni, Y. Shi, J. Liu, G. Huang, Characterization of Al0.5FeCu0.7NiCoCr high-entropy alloy coating on aluminum alloy by laser cladding, Opt Laser Technol 105 (2018) 257–263. https://doi.org/10.1016/j.optlastec.2018.01.058.

[165] P.A. Sdvizhenskii, V.N. Lednev, R.D. Asyutin, M.Ya. Grishin, R.S. Tretyakov, S.M. Pershin, Online laser-induced breakdown spectroscopy for metal-particle powder flow analysis during additive manufacturing, J Anal At Spectrom 35 (2020) 246–253. https://doi.org/10.1039/C9JA00343F.

[166] J. Shin, J. Mazumder, Composition monitoring using plasma diagnostics during direct metal deposition (DMD) process, Opt Laser Technol 106 (2018) 40–46. https://doi.org/10.1016/j.optlastec.2018.03.020.

[167] L. Song, J. Mazumder, Real Time Cr Measurement Using Optical Emission Spectroscopy During Direct Metal Deposition Process, IEEE Sens J 12 (2012) 958–964. https://doi.org/10.1109/JSEN.2011.2162316.

[168] S. Wang, Y. Wang, C. Liu, J. Mazumder, In-situ Monitoring on Micro-hardness of Laser Molten Zone on AISI4140 Steel by Spectral Analysis, Sci Rep 10 (2020) 4241. https://doi.org/10.1038/s41598-019-55559-z.

[169] S. Wang, C. Liu, Real-Time Monitoring of Chemical Composition in Nickel-Based Laser Cladding Layer by Emission Spectroscopy Analysis, Materials 12 (2019) 2637. https://doi.org/10.3390/ma12162637.

[170] D. De Baere, W. Devesse, B. De Pauw, L. Smeesters, H. Thienpont, P. Guillaume, Spectroscopic monitoring and melt pool temperature estimation during the laser metal deposition process, J Laser Appl 28 (2016). https://doi.org/10.2351/1.4943995.

[171] H. Gaja, F. Liou, Defect classification of laser metal deposition using logistic regression and artificial neural networks for pattern recognition, The International Journal of Advanced Manufacturing Technology 94 (2018) 315–326. https://doi.org/10.1007/s00170-017-0878-9.

[172] H. Gaja, F. Liou, Defects monitoring of laser metal deposition using acoustic emission sensor, The International Journal of Advanced Manufacturing Technology 90 (2017) 561–574. https://doi.org/10.1007/s00170-016-9366-x.

[173] K. Li, T. Li, M. Ma, D. Wang, W. Deng, H. Lu, Laser cladding state recognition and crack defect diagnosis by acoustic emission signal and neural network, Opt Laser Technol 142 (2021) 107161. https://doi.org/10.1016/j.optlastec.2021.107161.

[174] H. Taheri, L.W. Koester, T.A. Bigelow, E.J. Faierson, L.J. Bond, In Situ Additive Manufacturing Process Monitoring With an Acoustic Technique: Clustering Performance Evaluation Using K-Means Algorithm, J Manuf Sci Eng 141 (2019). https://doi.org/10.1115/1.4042786.

[175] A. García de la Yedra, M. Pfleger, B. Aramendi, M. Cabeza, F. Zubiri, T. Mitter, B. Reitinger, E. Scherleitner, Online cracking detection by means of optical techniques in laser-cladding process, Struct Control Health Monit 26 (2019) e2291. https://doi.org/10.1002/stc.2291.

[176] M. Strantza, D. Van Hemelrijck, P. Guillaume, D.G. Aggelis, Acoustic emission monitoring of crack propagation in additively manufactured and conventional titanium components, Mech Res Commun 84 (2017) 8–13. https://doi.org/10.1016/j.mechrescom.2017.05.009.

[177] Y. Li, F. Xu, Structural condition monitoring and identification of laser cladding metallic panels based on an acoustic emission signal feature optimization algorithm, Struct Health Monit 20 (2021) 1052–1073. https://doi.org/10.1177/1475921720945637.

[178] J. Whiting, A. Springer, F. Sciammarella, Real-time acoustic emission monitoring of powder mass flow rate for directed energy deposition, Addit Manuf 23 (2018) 312–318. https://doi.org/10.1016/j.addma.2018.08.015.

[179] D. Svetlizky, M. Das, B. Zheng, A.L. Vyatskikh, S. Bose, A. Bandyopadhyay, J.M. Schoenung, E.J. Lavernia, N. Eliaz, Directed energy deposition (DED) additive manufacturing: Physical characteristics, defects, challenges and applications, Materials Today 49 (2021) 271–295. https://doi.org/10.1016/j.mattod.2021.03.020.

[180] E. Leonidas, S. Ayvar-Soberanis, H. Laalej, S. Fitzpatrick, J.R. Willmott, A Comparative Review of Thermocouple and Infrared Radiation Temperature Measurement Methods during the Machining of Metals, Sensors 22 (2022) 4693. https://doi.org/10.3390/s22134693.

[181] N. Thawari, C. Gullipalli, T.V.K. Gupta, Effect of buffer layer on distortion and temperature in laser cladding, Mater Today Proc 72 (2023) 1792–1797. https://doi.org/10.1016/j.matpr.2022.09.573.

[182] N. Thawari, C. Gullipalli, H. Vanmore, T.V.K. Gupta, In-situ monitoring and modelling of distortion in multi-layer laser cladding of Stellite 6: Parametric and numerical approach, Mater Today Commun 33 (2022) 104751. https://doi.org/10.1016/j.mtcomm.2022.104751.

[183] S. Liu, P. Farahmand, R. Kovacevic, Optical monitoring of high power direct diode laser cladding, Opt Laser Technol 64 (2014) 363–376. https://doi.org/10.1016/j.optlastec.2014.06.002.

[184] N. Thawari, C. Gullipalli, H. Vanmore, T.V.K. Gupta, In-situ monitoring and modelling of distortion in multi-layer laser cladding of Stellite 6: Parametric and numerical approach, Mater Today Commun 33 (2022) 104751. https://doi.org/10.1016/j.mtcomm.2022.104751.

[185] G. Muvvala, D. Patra Karmakar, A.K. Nath, Online assessment of TiC decomposition in laser cladding of metal matrix composite coating, Mater Des 121 (2017) 310–320. https://doi.org/10.1016/j.matdes.2017.02.061.

[186] G. Muvvala, D. Patra Karmakar, A.K. Nath, Online monitoring of thermo-cycles and its correlation with microstructure in laser cladding of nickel based super alloy, Opt Lasers Eng 88 (2017) 139–152. https://doi.org/10.1016/j.optlaseng.2016.08.005.

[187] H. Köhler, C. Thomy, F. Vollertsen, Contact-less temperature measurement and control with applications to laser cladding, Welding in the World 60 (2016) 1–9. https://doi.org/10.1007/s40194-015-0275-7.

[188] M. Doubenskaia, M. Pavlov, S. Grigoriev, I. Smurov, Definition of brightness temperature and restoration of true temperature in laser cladding using infrared camera, Surf Coat Technol 220 (2013) 244–247. https://doi.org/10.1016/j.surfcoat.2012.10.044.

[189] H. Xu, H. Huang, In situ monitoring in laser melt injection based on fusion of infrared thermal and high-speed camera images, J Manuf Process 92 (2023) 466–478. https://doi.org/10.1016/j.jmapro.2023.02.059.

[190] L. Tang, R.G. Landers, Melt Pool Temperature Control for Laser Metal Deposition Processes—Part II: Layer-to-Layer Temperature Control, J Manuf Sci Eng 132 (2010). https://doi.org/10.1115/1.4000883.

[191] L. Song, V. Bagavath-Singh, B. Dutta, J. Mazumder, Control of melt pool temperature and deposition height during direct metal deposition process, The International Journal of Advanced Manufacturing Technology 58 (2012) 247–256. https://doi.org/10.1007/s00170-011-3395-2.

[192] L. Song, J. Mazumder, Feedback Control of Melt Pool Temperature During Laser Cladding Process, IEEE Transactions on Control Systems Technology 19 (2011) 1349–1356. https://doi.org/10.1109/TCST.2010.2093901.

[193] D. Salehi, M. Brandt, Melt pool temperature control using LabVIEW in Nd:YAG laser blown powder cladding process, The International Journal of Advanced Manufacturing Technology 29 (2006) 273–278. https://doi.org/10.1007/s00170-005-2514-3.

[194] L. Tang, R.G. Landers, Melt Pool Temperature Control for Laser Metal Deposition Processes—Part I: Online Temperature Control, J Manuf Sci Eng 132 (2010). https://doi.org/10.1115/1.4000882.

[195] M. Khanzadeh, W. Tian, A. Yadollahi, H.R. Doude, M.A. Tschopp, L. Bian, Dual process monitoring of metal-based additive manufacturing using tensor decomposition of thermal image streams, Addit Manuf 23 (2018) 443–456. https://doi.org/10.1016/j.addma.2018.08.014.

[196] P. Colodron, J. Farina, J.J. Rodriguez-Andina, F. Vidal, J.L. Mato, M.A. Montealegre, Performance improvement of a laser cladding system through FPGA-based control, in: IECON 2011 - 37th Annual Conference of the IEEE Industrial Electronics Society, IEEE, 2011: pp. 2814–2819. https://doi.org/10.1109/IECON.2011.6119758.

[197] W.-W. Liu, Z.-J. Tang, X.-Y. Liu, H.-J. Wang, H.-C. Zhang, A Review on In-situ Monitoring and Adaptive Control Technology for Laser Cladding Remanufacturing, Procedia CIRP 61 (2017) 235–240. https://doi.org/10.1016/j.procir.2016.11.217.

[198] S. Moralejo, X. Penaranda, S. Nieto, A. Barrios, I. Arrizubieta, I. Tabernero, J. Figueras, A feedforward controller for tuning laser cladding melt pool geometry in real time, The International Journal of Advanced Manufacturing Technology 89 (2017) 821–831. https://doi.org/10.1007/s00170-016-9138-7.

[199] J.T. Hofman, D.F. de Lange, B. Pathiraj, J. Meijer, FEM modeling and experimental verification for dilution control in laser cladding, J Mater Process Technol 211 (2011) 187–196. https://doi.org/10.1016/j.jmatprotec.2010.09.007.

[200] J.T. Hofman, B. Pathiraj, J. van Dijk, D.F. de Lange, J. Meijer, A camera based feedback control strategy for the laser cladding process, J Mater Process Technol 212 (2012) 2455–2462. https://doi.org/10.1016/j.jmatprotec.2012.06.027.

[201] K. Lei, X. Qin, H. Liu, M. Ni, Analysis and modeling of melt pool morphology for high power diode laser cladding with a rectangle beam spot, Opt Lasers Eng 110 (2018) 89–99. https://doi.org/10.1016/j.optlaseng.2018.05.022.

[202] R. Sampson, R. Lancaster, M. Sutcliffe, D. Carswell, C. Hauser, J. Barras, An improved methodology of melt pool monitoring of direct energy deposition processes, Opt Laser Technol 127 (2020) 106194. https://doi.org/10.1016/j.optlastec.2020.106194.

[203] H.W. Hsu, Y.L. Lo, M.H. Lee, Vision-based inspection system for cladding height measurement in Direct Energy Deposition (DED), Addit Manuf 27 (2019) 372–378. https://doi.org/10.1016/j.addma.2019.03.017.

[204] M. Mazzarisi, M.G. Guerra, M. Latte, A. Angelastro, S.L. Campanelli, L.M. Galantucci, Off-axis optical system for the monitoring of the Laser Metal Deposition process, in: Procedia Comput Sci, Elsevier B.V., 2024: pp. 3092–3101. https://doi.org/10.1016/j.procs.2024.02.125.

[205] S. Donadello, M. Motta, A.G. Demir, B. Previtali, Monitoring of laser metal deposition height by means of coaxial laser triangulation, Opt Lasers Eng 112 (2019) 136–144. https://doi.org/10.1016/j.optlaseng.2018.09.012.

[206] I. Garmendia, J. Pujana, A. Lamikiz, M. Madarieta, J. Leunda, Structured light-based height control for laser metal deposition, J Manuf Process 42 (2019) 20–27. https://doi.org/10.1016/j.jmapro.2019.04.018.

[207] I. Garmendia, J. Leunda, J. Pujana, A. Lamikiz, In-process height control during laser metal deposition based on structured light 3D scanning, in: Procedia CIRP, Elsevier B.V., 2018: pp. 375–380. https://doi.org/10.1016/j.procir.2017.12.098.

[208] R.G. Dorsch, G. Häusler, J.M. Herrmann, Laser triangulation: fundamental uncertainty in distance measurement, Appl Opt 33 (1994) 1306. https://doi.org/10.1364/AO.33.001306.

[209] D. Ding, W. Ding, R. Huang, Y. Fu, F. Xu, Research progress of laser triangulation on-machine measurement technology for complex surface: A review, Measurement 216 (2023) 113001. https://doi.org/10.1016/j.measurement.2023.113001.

[210] M. Lafirenza, M.G. Guerra, F. Lavecchia, A layerwise monitoring methodology based on blue laser line profilometer for Material Extrusion processes, International Journal of Advanced Manufacturing Technology (2023). https://doi.org/10.1007/s00170-023-11864-6.

[211] M. Lafirenza, M.G. Guerra, F. Lavecchia, L.M. Galantucci, In-process evaluation of layer defects and surface topography on material extruded parts through a novel point cloud functional analysis, Meas Sci Technol 36 (2025) 016229. https://doi.org/10.1088/1361-6501/ad9b41.

[212] E. Binega, L. Yang, H. Sohn, J.C.P. Cheng, Online geometry monitoring during directed energy deposition additive manufacturing using laser line scanning, Precis Eng 73 (2022) 104–114. https://doi.org/10.1016/j.precisioneng.2021.09.005.

[213] F. Scalzo, G. Totis, E. Vaglio, M. Sortino, Experimental study on the high-damping properties of metallic lattice structures obtained from SLM, Precis Eng 71 (2021) 63–77. https://doi.org/10.1016/j.precisioneng.2021.02.010.

[214] M.G. Guerra, V. Errico, A. Fusco, F. Lavecchia, S.L. Campanelli, L.M. Galantucci, High resolution-optical tomography for in-process layerwise monitoring of a laser-powder bed fusion technology, Addit Manuf 55 (2022) 102850. https://doi.org/https://doi.org/10.1016/j.addma.2022.102850.

[215] D. Li, R. Qin, B. Chen, J. Zhou, Analysis of mechanical properties of lattice structures with stochastic geometric defects in additive manufacturing, Materials Science and Engineering A 822 (2021). https://doi.org/10.1016/j.msea.2021.141666.

[216] T.N. Mundhenk, M.J. Rivett, X. Liao, E.L. Hall, <title>Techniques for fisheye lens calibration using a minimal number of measurements</title>, in: Intelligent Robots and Computer Vision XIX: Algorithms, Techniques, and Active Vision, SPIE, 2000: pp. 181–190. https://doi.org/10.1117/12.403762.

[217] Z. Zhang, A Flexible New Technique for Camera Calibration, 2000.